UNIVERSITY OF CALIFORNIA
RIVERSIDE

Phenomenology of Axion Fields and Topological Defects

A Dissertation submitted in partial satisfaction
of the requirements for the degree of

Doctor of Philosophy

in

Physics

by

Chia-Feng Chang

September 2023

Dissertation Committee:

Dr. Yanou Cui, Chairperson
Dr. Simeon Bird
Dr. Hai-Bo Yu

The Dissertation of Chia-Feng Chang is approved:

Committee Chairperson

University of California, Riverside

感謝李淑美、詹媛媛和張瑞瑜陪我度過這ㄐㄅ的日子。
ㄏㄏ

ABSTRACT OF THE DISSERTATION

Phenomenology of Axion Fields and Topological Defects

by

Chia-Feng Chang

Doctor of Philosophy, Graduate Program in Physics
University of California, Riverside, September 2023
Dr. Yanou Cui, Chairperson

In the conventional misalignment mechanism, the axion field is assumed to start with zero initial velocity. However, we introduce an alternative scenario in which the axion field possesses a nonzero initial velocity, potentially due to the breaking of the Peccei–Quinn (PQ) symmetry during the early Universe. Depending on the initial velocity and the sequence of events between PQ symmetry breaking and inflation, this novel scenario can amplify or diminish the expected axion relic abundance compared to the conventional prediction. Consequently, this opens up new parameter regions for axion dark matter models.

Global cosmic strings, anticipated in various non-standard models, generate primordial gravitational waves detectable by instruments. We refine the analytical Velocity-dependent One-Scale (VOS) model through recent simulation outcomes, revealing the gravitational wave spectrum produced by global string networks, including Goldstone emission. Our findings present a technique to detect signals from the early universe before Big Bang nucleosynthesis, impacted by the non-standard pre-BBN equation of state and new relativistic particles.

Early dark energy, relieving the Hubble tension, imprints discernible characteristics on the primordial stochastic gravitational wave background originating from cosmic string networks. This signal stands out in planned gravitational wave experiments, distinctly separate from other cosmological and astrophysical signals in the gravitational wave frequency spectrum.

In the context of axion-like particle (ALP) dark matter theories, we explore enhanced early galaxy formation through the kinetic misalignment mechanism. This has potential relevance to the excess observed by the James Webb Space Telescope (JWST) while adhering to constraints. Viable parameter space is identified for ALP mass within the range of $10^{-22}\text{eV} < m_a < 10^{-19}\text{eV}$. Additionally, ALP parameter regions offer complementary insights into the small-scale structure of dark matter halos and ongoing ALP searches.

Through advanced simulations and analytical modeling, we conduct an updated analysis of long-lived axion domain wall (DW) networks. By scrutinizing energy loss mechanisms and calculating axion emissions from the DW network, we determine their contribution to axion dark matter density. While our results are consistent with prior research, disparities arise, particularly in predicting DM abundance. These disparities could profoundly impact axion phenomenology on a larger scale.

Contents

List of Figures

List of Tables

Chapter 1

A Review of Axion Physics

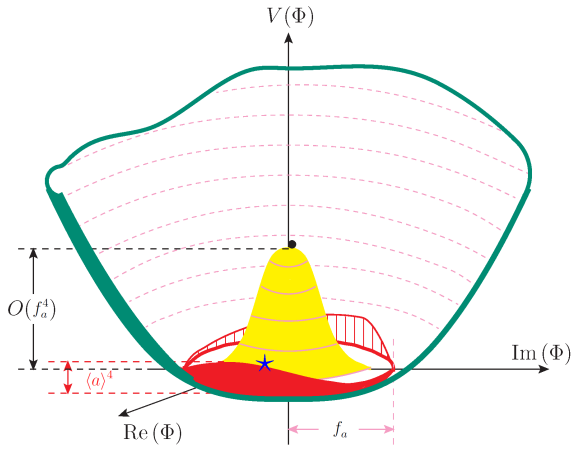

As the Φ^4 theory, the green part is the potential at high energy, it carried the $U(1)_{PQ}$ symmetry $\Phi \to \Phi e^{i\alpha}$. Then the symmetry is broken at $\langle \phi \rangle \sim f_a$ (the yellow part), and an associated Goldstone-boson-axion shows up. Finally, the instanton provides a non-perturbative vacuum $\langle a \rangle \simeq \Lambda_{\mathrm{QCD}}$ (the red circle) to break the shift symmetry i.e. the red circle, it is an example for $N_{DW} = 2$ (two minima in the red circle), this plot is cited from [32].

1.1 The $U(1)_A$ Problem and Its Resolution

• The QCD Lagrangian for N flavors in the limit of vanishing quark masses $m_f \to 0$ has a large global symmetry: $U(N)_V \times U(N)_A$. Since at a scale $\Lambda \gg \{m_u, m_d, m_s \cdots\}$, at least for these quarks, the limit of sending the quark masses to zero is sensible. Therefore we have an approximately symmetry $U(3)_V \times U(3)_A$ invariant under u, d, and s quarks if $\Lambda \simeq \Lambda_{QCD}$.[1]

• Since the vector part $U(3)_V = SU(3)_I \times U(1)_B$, where $SU(3)_I$ is isospin-like under $\{u, d, s\}$, $U(1)_B$ is baryon number. They are good approximate symmetry on the hadron spectrum.

• However, since the quark condensates $\langle \bar{u}u \rangle = \langle \bar{d}d \rangle = \langle \bar{s}s \rangle \equiv -V^3 \neq 0$[2] at $\Lambda \leq \Lambda_{QCD}$, it breaking the axial symmetry $U(3)_A$ down spontaneously by QCD confinement.

• Since the $d.o.f.$ of $U(3)_A$ is $3^3 = 9$, there should have nine Nambu-Goldstone bosons associated with the breakdown of $U(3)_A$. They would be $\{\pi^0, \pi^\pm, K^0, \bar{K}^0, K^\pm, \eta, \eta'\}$. But Weinberg proved that the mass $m_{\eta'} < \sqrt{3} m_\pi$, it is not consistent to experiment.

1.2 Calculation of U(1) Problem

This section is mainly following [34]. We have the flavor symmetries in the standard model fermion framework as

$$\mathcal{G} = U(3)_V \times U(3)_A = SU(3)_V \times SU(3)_A \times U(1)_V \times U(1)_A. \tag{1.1}$$

[1] It is not good if we only consider the $U(2)_V \times U(2)_A$ under u, d as [33], then we only need $2^2 = 4$ Goldstone i.e. π^0, π^+, π^- and η. Because the η has a mixing with η' from the experiment result, the η' is not ignorable. On the other hand, the η cannot be Goldstone, because its mass $m_\eta = 497\text{MeV} > \sqrt{3} m_\pi$.

[2] The minus at font of V^3 is used to makes the sign of Goldstone mass correctly, see Eq.(1.9).

In order to break the $U(3)_V \times U(3)_A$ one can consider the linear sigma model [35]

$$\mathcal{L} = |\partial_\mu \Sigma|^2 + m^2|\Sigma|^2 - \frac{\lambda}{4}|\Sigma|^4, \tag{1.2}$$

where Σ transformation under $\mathcal{G}$, i.e.

$$\Sigma \to g_L \Sigma g_R^\dagger, \qquad \Sigma \to g_R \Sigma g_L^\dagger, \tag{1.3}$$

and $|\Sigma|^2 = \Sigma_{ij}\Sigma^\dagger_{ji}$, with[3]

$$\Sigma(x) = \frac{v + \sigma(x)}{\sqrt{2}} \exp\left(2i\frac{\pi^a(x)\lambda^a}{F_\pi}\right) \equiv \frac{v + \sigma(x)}{\sqrt{2}} U(x), \tag{1.4}$$

where the $F_\pi = 130\text{MeV} = \sqrt{2} f_\pi = \sqrt{2} \times 92\text{MeV}$ is decay constant,

$$\pi^a\lambda^a = \sqrt{2}\begin{pmatrix} \frac{1}{\sqrt{2}}\pi^0 + \frac{1}{\sqrt{6}}\eta^0 & \pi^+ & K^+ \\ \pi^- & -\frac{1}{\sqrt{2}}\pi^0 + \frac{1}{\sqrt{6}}\eta^0 & K^0 \\ \bar{K}^- & \bar{K}^0 & -\sqrt{\frac{2}{3}}\eta^0 \end{pmatrix} + \sqrt{2}\frac{F_\pi}{F_{\eta'}}\begin{pmatrix} \frac{1}{\sqrt{3}}\eta' & 0 & 0 \\ 0 & \frac{1}{\sqrt{3}}\eta' & 0 \\ 0 & 0 & \frac{1}{\sqrt{3}}\eta' \end{pmatrix}. \tag{1.5}$$

where since the $SU(3)_V \times SU(3)_A/SU(3)$ generators are corresponding to $\{\pi^0,\ \pi^\pm,\ K^0,\ \bar{K}^0,\ K^\pm,\ \eta\}$, except η'. Therefore we have additional decay constant $F_{\eta'}$ for the $U(1)_A$ with Goldstone η', see more detils [36, 34]. Substitute Eq.(1.4) back to Lagrangian then expanding $e^x \to 1 + x + \frac{x^2}{2!} + \cdot$ would get full interaction terms.

[3] There should have an additional factor 2 in exponential, it is not trivial, see Eq.(19.7.8) in [34])

To sum, the quarks transformation under $U(3)_V \times U(3)_A/U(3)_V$ i.e. the broken part $U(3)_A$ is

$$q(x) \equiv \begin{pmatrix} u(x) \\ d(x) \\ s(x) \end{pmatrix} = \exp\left(-i\gamma_5 \pi^a \lambda^a / F_\pi\right) \tilde{q}, \tag{1.6}$$

where $\tilde{q}$ is the state after symmetry breaking, then of course the $U(3)_A$ phase is fixed to be $\pi^a \lambda^a$ after that. The F_π makes the dimension correctly, similar to ϕ_I/v_h in SM. Then we have the mass term as

$$\mathcal{L}_{\text{mass}} = -\bar{q} M_q q = -\bar{\tilde{q}} e^{-i\gamma_5 \pi^a \lambda^a / F_\pi} M_q e^{-i\gamma_5 \pi^a \lambda^a / F_\pi} \tilde{q} \tag{1.7}$$

where we used $\{\gamma_5, \gamma_0\} = 0$ at $\bar{q} \to \bar{\tilde{q}}$ transformation, and

$$M_q = \begin{pmatrix} m_u & 0 & 0 \\ 0 & m_d & 0 \\ 0 & 0 & m_s \end{pmatrix}. \tag{1.8}$$

The Eq.(1.7) contains a purely bosonic part, obtained by replacing the quark bilinear with its vacuum expectation value,

$$\langle \bar{\tilde{q}}_i \gamma_5 \tilde{q}_j \rangle = 0, \qquad \langle \bar{\tilde{q}}_i \tilde{q}_j \rangle = -V^3 \delta_{ij}. \tag{1.9}$$

The Goldstone boson mass term in the Lagrangian is (define $B \equiv \pi^a \lambda^a$), from Eq.(1.7) we obtain

$$
\begin{aligned}
-\frac{1}{2}\frac{V^3}{F_\pi^2}\mathrm{Tr}\{B,\{B,M_q\}\} = -\frac{V^3}{F_\pi^2}\Big[& 4m_u\left(\frac{1}{\sqrt{2}}\pi^0+\frac{1}{\sqrt{6}}\eta^0+\frac{F_\pi}{\sqrt{3}F_{\eta'}}\eta'\right)^2 \\
& + 4(m_u+m_d)\pi^+\pi^- + 4(m_u+m_s)K^+\bar{K}^- \\
& + 4m_d\left(-\frac{1}{\sqrt{2}}\pi^0+\frac{1}{\sqrt{6}}\eta^0+\frac{F_\pi}{\sqrt{3}F_{\eta'}}\eta'\right)^2 \\
& + 4(m_d+m_s)K^0\bar{K}^0 + 4m_s\left(-\sqrt{\frac{2}{3}}\eta^0+\frac{F_\pi}{\sqrt{3}F_{\eta'}}\eta'\right)^2\Big]
\end{aligned}
$$

where we used Baker-Hausdorff lemma[4], and the δ_{ij} in Eq.(1.9) require a trace. Now the neutral mesons have a mass matrix

$$
M_0^2 = 8V^3\begin{pmatrix}\pi^0 & \eta & \eta'\end{pmatrix}\begin{pmatrix}
\frac{m_u+m_d}{2F_\pi^2} & \frac{m_u-m_d}{2\sqrt{3}F_\pi^2} & \frac{m_u-m_d}{\sqrt{6}F_\pi F_{\eta'}} \\
\frac{m_u-m_d}{2\sqrt{3}F_\pi^2} & \frac{m_u+m_d+4m_s}{6F_\pi^2} & \frac{m_u+m_d-2m_s}{3\sqrt{2}F_\pi F_{\eta'}} \\
\frac{m_u-m_d}{\sqrt{6}F_\pi F_{\eta'}} & \frac{m_u+m_d-2m_s}{3\sqrt{2}F_\pi F_{\eta'}} & \frac{m_u+m_d+m_s}{3F_{\eta'}^2}
\end{pmatrix}\begin{pmatrix}\pi^0 \\ \eta \\ \eta'\end{pmatrix}. \tag{1.10}
$$

In the light quarks limit, $m_s \gg \{m_u, m_d\} \to 0$, we have two eigenvectors with zero eigenmasses,

$$
u_a = \begin{pmatrix}1\\0\\0\end{pmatrix}, \qquad u_b = \frac{1}{\sqrt{F_\pi^2+2F_{\eta'}^2}}\begin{pmatrix}0\\F_\pi\\\sqrt{2}F_{\eta'}\end{pmatrix}, \tag{1.11}
$$

[4] $e^A B e^A = B + \{A,B\} + \frac{1}{2!}\{A,\{A,B\}\} + \frac{1}{3}\{\{A,\{A,B\}\}\} + \cdots$.

with masses

$$m_{aa}^2 = \frac{4V^3(m_u + m_d)}{F_\pi^2}, \qquad m_{bb}^2 = \frac{12V^3(m_u + m_d)}{F_\pi^2 + 2F_{\eta'}^2}, \tag{1.12}$$

its off-diagonal term provide a negligible mixing angle $\theta \sim (m_u - m_d)^2/64(m_u + m_d)^2$. If we assume another mass eigenstate is the heaviest state, the second heavier state mass will be m_{bb}^2. Furthermore, if the lightest state is π^0, i.e. $m_{aa}^2 = m_\pi^2$, then we obtain

$$m_b \simeq \sqrt{m_{bb}^2} \simeq \frac{\sqrt{3}m_\pi F_\pi}{\sqrt{F_\pi^2 + 2F_{\eta'}^2}} \leq \sqrt{3}m_\pi. \tag{1.13}$$

It provides a theoretical upper bond for η or η', however, no one of them well fits in this bond, this so-called $U(1)_A$ problem. See section 23.5 of [34] or [37], this problem was eventually solved by a non-perturbative effect that violates the $U(1)_A$ symmetry, in effect, makes $U(1)_A$ not a true symmetry of QCD. So the η' is not THE Goldstone who breaks the symmetry.

1.3 Strong CP problem

Under the $SU(3)^2_{QCD}U(1)_A$ anomaly, it provide the strong CP phase term as

$$\mathcal{L} \supset \theta_{QCD}\frac{g_s^2}{32\pi}\epsilon^{\mu\nu\alpha\beta}F^a_{\mu\nu}F^a_{\alpha\beta}, \tag{1.14}$$

where $F^a_{\mu\nu}$ is QCD field. We have two situations:

• If $U(1)_A$ exists, the anomaly θ term should be removed by the $U(1)_A$ chiral rotations on the quarks mass matrix[5], i.e. $\bar{\theta} = 0$ at high energy. But at lower energy, the $U(1)_A$ should be broken by $\langle\bar{q}q\rangle$, it consequently provide a strong CP phase[38, 39]:

$$\bar{\theta} = \theta_{QCD} - \text{argdet}\,(Y_dY_u) < 0.7 \times 10^{-11}. \tag{1.15}$$

It has no reason to be small. The question is that *Why this phase is super small?* or say *Why is CP not badly broken in QCD?* [33].

• If we have no $U(1)_A$ even at high energy, the $\bar{\theta}$ will be a constant, we still ask the strong CP problem.

[5]It is worth to mention that in SM case, since the $U(1)_Y$ is broken, it is not a symmetry! They cannot cancel the anomaly by rotating the phase term, they should consider the anomaly cancellation.

1.3.1 Kazuo Fujikawa's Chiral Anomaly from path-integral (massless case)

Mainly follow [40], [41], [42]. It is worth mentioning that the fermions in this section, which can be chiral or non-chiral, don't affect the result. A gauge invariant operator in path-integral is

$$\langle \mathcal{O}(x_1, \cdots, x_n) \rangle = \frac{1}{Z[0]} \int \mathcal{D}\bar{\psi}\mathcal{D}\psi \exp\left[i \int d^4x i\bar{\psi}\not{\partial}\psi \right] \mathcal{O}(x_1, \cdots, x_n). \tag{1.16}$$

Under the global/gauge symmetry $\psi(x) \to e^{i\alpha(x)}\psi(x)$, i.e. $\bar{\psi}\not{\partial}\psi \to \bar{\psi}\not{\partial}\psi + i\psi\gamma^\mu\bar{\psi}\partial_\mu\alpha$. Since the path-integral should be invariant, the α term should have vanished. First, we obtain the first order in α

$$\begin{aligned} &\frac{1}{Z[0]} \int \mathcal{D}\bar{\psi}\mathcal{D}\psi \exp\left[i \int d^4x i\bar{\psi}\not{\partial}\psi \right] \left(\int d^4x \bar{\psi}\gamma^\mu\psi\partial_\mu\alpha \right) \mathcal{O}(x_1, \cdots, x_n) \\ =&\frac{1}{Z[0]} \int \mathcal{D}\bar{\psi}\mathcal{D}\psi \exp\left[i \int d^4x i\bar{\psi}\not{\partial}\psi \right] \left(\int d^4z \bar{\psi}(z)\gamma^\mu\psi(z)\partial_\mu\alpha(z) \right) \mathcal{O}(x_1, \cdots, x_n), \end{aligned}$$

where the two parts of the integral are independent, so we replace the $x \to z$. Then integral by part,

$$\frac{1}{Z[0]} \int d^4z\alpha(z) \int \mathcal{D}\bar{\psi}\mathcal{D}\psi \exp\left[i \int d^4x i\bar{\psi}\not{\partial}\psi \right] \frac{\partial}{\partial z^\mu} \left(\bar{\psi}(z)\gamma^\mu\psi(z) \right) \mathcal{O}(x_1, \cdots, x_n), \tag{1.17}$$

where the currents are defined as

$$J_5^\mu = J_a^\mu = \bar{\psi}\gamma^\mu\gamma_5\psi, \qquad J_5 = J_a = \bar{\psi}\gamma_5\psi. \tag{1.18}$$

Since this should be vanished with any $\alpha(z)$, in other word, we have

$$\partial_\mu \langle J^\mu(x)\mathcal{O}(x_1,\cdots,x_n)\rangle = 0. \tag{1.19}$$

In fact, we missed the gauge transformation on the path-integral $\mathcal{D}\bar{\psi}\mathcal{D}\psi$ above. Second, let us consider a general linear transformation

$$\psi(x) \to \Delta(x)\psi(x) \quad \text{and} \quad \bar{\psi}(x) \to \Delta^\dagger(x)\psi(x) \tag{1.20}$$

which generates a Jacobian factor (see, Eq.(2.11) in [40])

$$\boxed{\mathcal{D}\bar{\psi}\mathcal{D}\psi \to |\mathcal{J}|^{-2}\mathcal{D}\bar{\psi}\mathcal{D}\psi}. \tag{1.21}$$

This Jacobian

$$\mathcal{J} = \det\Delta = \exp\left[\mathrm{tr}\ln\Delta\right]. \tag{1.22}$$

The negative power is because the transformed variables are fermionic [40]. For the non-chiral rotation, i.e. $\Delta(x) = e^{i\alpha(x)}$,

$$\mathcal{J} = \exp\left(i\int d^4x\alpha(x)\right) \qquad \to \qquad |\mathcal{J}|^2 = 1. \tag{1.23}$$

On the other hand, the chiral rotation would be $\Delta(x) = e^{i\beta(x)\gamma_5}$, [6]

$$\mathcal{J} = \exp\left(i\int d^4x\beta(x)\mathrm{tr}[\gamma_5]\right). \tag{1.24}$$

Since $\mathrm{tr}[\gamma_5] = 0$, it looks like we got a singular on that rotation. But it would not be the case, we add an $U(1)$ gauge with gauge boson A_μ invariant form (mainly follow Eq.(2.15) [40]),

$$\int \mathcal{D}\bar{\psi}\mathcal{D}\psi\mathcal{D}A\,\exp\left[i\int d^4x\left(-\frac{1}{4}F_{\mu\nu}^2 + i\bar{\psi}\not{D}\psi\right)\right]. \tag{1.25}$$

The gauge boson A_μ do not carry any global symmetries charges, therefore the transform is the same as Eq.(1.17). We then consider a one-particle Hilbert space as

$$\mathcal{J} = \exp\left(i\int d^4x\mathrm{Tr}\left[\langle x|\beta(\hat{x})\gamma_5|x\rangle\right]\right). \tag{1.26}$$

A key point is considering an exponential regulator term

$$\exp\left(-\hat{\not{\Pi}}^2/\Lambda^2\right), \qquad \text{with} \qquad \hat{\not{\Pi}} = \hat{\not{p}} - e\not{A}(\hat{x}), \tag{1.27}$$

[6] The $\beta(x)$*can be a constant*, i.e. the axial transformation is a global symmetry, this wouldn't affect the result, see example in section 30.5 of [43]. The baryon and lepton number global symmetry introduce the anomaly is a good example of global anomalous.

then

$$\begin{aligned}
\hat{\not{\Pi}}^2 &= \left(i\not{\partial} - e\not{A}\right)\left(i\not{\partial} - e\not{A}\right) \\
&= (i\partial_\mu - eA_\mu)(i\partial_\nu - eA_\nu)\gamma^\mu\gamma^\nu \\
&= \left(\frac{1}{4}\{i\partial_\mu - eA_\mu, i\partial_\nu - eA_\nu\}\{\gamma^\mu, \gamma^\nu\} + \frac{1}{4}\left[i\partial_\mu - eA_\mu, i\partial_\nu - eA_\nu\right]\left[\gamma^\mu, \gamma^\nu\right]\right) \\
&= \left((i\partial_\mu - eA_\mu)^2 + \frac{1}{2}(-eF_{\mu\nu})\sigma^{\mu\nu}\right) \\
&= \hat{\Pi}^2 - \frac{e}{2}F_{\mu\nu}\sigma^{\mu\nu},
\end{aligned}$$

where we used $\{\gamma^\mu, \gamma^\nu\} = 2g^{\mu\nu}$ and $\sigma^{\mu\nu} = \frac{i}{2}\left[\gamma^\mu, \gamma^\nu\right]$,

$$\left[i\partial_\mu - eA_\mu, i\partial_\nu - eA_\nu\right] = -e\left[i\partial_\mu A_\nu - i\partial_\nu A_\mu\right] = -i\, eF_{\mu\nu}. \tag{1.28}$$

So that

$$\begin{aligned}
\mathrm{Tr}\left[\langle x|\beta(\hat{x})\gamma^5|x\rangle\right] &= \lim_{\Lambda\to\infty} \mathrm{Tr}\left[\langle x|\beta(\hat{x})\gamma^5 e^{\hat{\not{\Pi}}^2/\Lambda^2}|x\rangle\right] \\
&= \lim_{\Lambda\to\infty} \beta(x)\langle x|\mathrm{Tr}\left[\gamma^5 \exp\left(\frac{\hat{\Pi}^2 - \frac{e}{2}\sigma_{\mu\nu}F^{\mu\nu}}{\Lambda^2}\right)\right]|x\rangle.
\end{aligned} \tag{1.29}$$

The next step is expanding this exponential, we only expend the $\sigma_{\mu\nu}F^{\mu\nu}$ term. However, we only need to focus on $(\gamma_5)^2$ term, since $\mathrm{tr}[\gamma_5] = 0$. In addition, we use the identity

$$\frac{1}{2}\{\sigma^{\mu\nu}, \sigma^{\alpha,\beta}\} = g^{\mu\alpha}g^{\nu\beta} - g^{\nu\alpha}g^{\mu\beta} + i\gamma^5\epsilon^{\mu\nu\alpha\beta}, \tag{1.30}$$

then the squared term can be read

$$(\sigma_{\mu\nu}F^{\mu\nu})^2 = 2F_{\mu\nu}^2 + i\gamma^5\epsilon^{\mu\nu\alpha\beta}F_{\mu\nu}F_{\alpha\beta}. \tag{1.31}$$

The Eq.(1.29) only leaves

$$i\mathrm{Tr}\left[\langle x|\beta(\hat{x})\gamma^5|x\rangle\right] = -\frac{e^2}{2}\beta(x)\epsilon^{\mu\nu\alpha\beta}F_{\mu\nu}(x)F_{\alpha\beta}(x)\lim_{\Lambda\to\infty}\left[\frac{1}{\Lambda^4}\langle x|e^{\Pi^2/\Lambda^2}|x\rangle\right]. \tag{1.32}$$

In order to extract the finite term, we need [7]

$$\begin{aligned}
\frac{1}{\Lambda^4}\langle x|e^{\hat{p}^2/\Lambda^2}|x\rangle =& \frac{1}{\Lambda^4}\langle x|\int\frac{d^4k}{(2\pi)^4}e^{\hat{p}^2/\Lambda^2}|k\rangle\langle k|x\rangle \\
=& \frac{1}{\Lambda^4}\int\frac{d^4k}{(2\pi)^4}e^{k^2/\Lambda^2} \\
=& \frac{i}{\Lambda^4}\int\frac{d^4k_E}{(2\pi)^4}e^{-k_E^2/\Lambda^2} \\
=& \frac{i}{\Lambda^4}\int\Omega_4\int\frac{k_E^3dk_E}{(2\pi)^4}e^{-k_E^2/\Lambda^2} \\
=& -\frac{i}{\Lambda^4}2\pi^2\frac{1}{(2\pi)^4}\frac{1}{2}\Lambda^4 = \frac{-i}{16\pi^2},
\end{aligned}$$

where $\int d\Omega_4 = 2\pi^2$. The Eq.(1.29) become

$$\mathrm{Tr}\left[\langle x|\beta(\hat{x})\gamma^5|x\rangle\right] = \frac{e^2}{32\pi^2}\beta(x)\epsilon^{\mu\nu\alpha\beta}F_{\mu\nu}(x)F_{\alpha\beta}(x). \tag{1.33}$$

[7] same calculation in Eq.(2.21-25) of [40]

So the Eq.(1.26) would be

$$\mathcal{J} = \exp\left[i\int d^4x \left(\frac{e^2}{32\pi^2}\beta(x)\epsilon^{\mu\nu\alpha\beta}F_{\mu\nu}(x)F_{\alpha\beta}(x)\right)\right]. \tag{1.34}$$

In the final, we turn Eq.(1.21) back to Eq.(1.17) and using Eq.(1.34), we have [8]

$$\begin{aligned}
&\int \mathcal{D}\bar{\psi}\mathcal{D}\psi\mathcal{D}A \exp\left[i\int d^4x\mathcal{L}\right] \\
&\to \int \mathcal{D}\bar{\psi}\mathcal{D}\psi\mathcal{D}A \exp\left[i\int d^4x \left(\mathcal{L} - J^5_\mu\partial_\mu\beta - \beta\frac{e^2}{16\pi^2}\epsilon^{\mu\nu\alpha\beta}F_{\mu\nu}F_{\alpha\beta}\right)\right]
\end{aligned}$$

where the $J^5_\mu\partial\beta$ term is from (Eq.(5) of [40])

$$\begin{aligned}
\mathcal{L} \supset\ & i\bar{\psi}\gamma^\mu\partial_\mu\psi \to i\bar{\psi}(e^{+i\beta(x)\gamma_5})\gamma^\mu\partial_\mu(e^{i\beta(x)\gamma_5}\psi) \\
&= i\bar{\psi}(e^{+i\beta(x)\gamma_5})\gamma^\mu e^{i\beta(x)\gamma_5}\partial_\mu\psi + i\bar{\psi}(e^{+i\beta(x)\gamma_5})\gamma^\mu e^{i\beta(x)\gamma_5}(i\partial\beta(x)\gamma_5)\psi \\
&= i\bar{\psi}\gamma^\mu\partial_\mu\psi + i\bar{\psi}\gamma^\mu(i\partial\beta(x)\gamma_5)\psi \\
&= i\bar{\psi}\gamma^\mu\partial_\mu\psi - J^5_\mu\partial^\mu\beta,
\end{aligned} \tag{1.35}$$

where $\{\gamma^5, \gamma^\mu\} = 0$, and don't forget a γ_0 in $\bar{\psi} = \psi^\dagger\gamma_0$ with $\gamma_5^\dagger = \gamma_5$ makes $+$. By the way, if there has a fermion mass term, the transformation gives

$$m\bar{\psi}\psi \to m\bar{\psi}\psi - 2mi\beta(x)\bar{\psi}\gamma_5\psi, \tag{1.36}$$

[8] massive fermion case is only adding a mass term as in Eq.(2.9) of [40].

which is Eq.(5) of [40]. Again, since the gauge invariant, the addition terms should have vanished, i.e. expanding the exponential terms in the first order of β,

$$\partial_\mu \langle J^{5\mu}(x)\mathcal{O}(x_1,\cdots,x_n)\rangle = \frac{e^2}{16\pi^2}\langle \epsilon^{\mu\nu\alpha\beta}F_{\mu\nu}F_{\alpha\beta}\mathcal{O}(x_1,\cdots,x_n)\rangle, \tag{1.37}$$

where we used integral by part on $J^5_\mu \partial_\mu \beta$ again. In short, the result is, under chiral transformation on fermion e.g. $\psi \to e^{i\gamma_5\beta}\psi$, the Lagrangian will transform as[9]

$$\boxed{\delta\mathcal{L} = \beta\partial^\mu J^5_\mu - \beta\frac{e^2}{16\pi^2}\epsilon^{\mu\nu\alpha\beta}F_{\mu\nu}F_{\alpha\beta}}, \tag{1.38}$$

where $\beta(x)$ can be either constant or a local function, this wouldn't change the result. For the non-Abelian, there should be times additional factor $\mathcal{C}$ from their Lie algebra e.g. Eq.(1.93) and Eq.(1.41) for details. As we can see the β terms always be canceled out in the Lagrangian level. In addition, this result means the $U(1)_A$ symmetry is broken, because if we require it isn't broken i.e. $\delta\mathcal{L} = 0$, then we have[10]

$$\partial^\mu J^5_\mu = \frac{e^2}{16\pi^2}\epsilon^{\mu\nu\alpha\beta}F_{\mu\nu}F_{\alpha\beta} \neq 0. \tag{1.39}$$

[9] Another form is the Chern-Simons current, $\epsilon^{\mu\nu\alpha\beta}F_{\mu\nu}F_{\alpha\beta} = \partial^\mu K_\mu$, with $K_\mu = \epsilon_{\mu\nu\alpha\beta}\left(A^a_\nu F^a_{\alpha\beta} - \frac{g}{3}f^{abc}A^a_\nu A^b_\alpha A^c_\beta\right)$.

[10] This is massless anomalous Ward Takahashi identity, see also Eq.(21) of [44] or his lecture [45] Eq.(2.11) for massive one.

Since $\partial^\mu J^5_\mu \neq 0 \rightarrow U(1)_A$ current is not conserved, the symmetry should be broken. The important thing is that we considered the boundary condition on the axial current as

$$\int d^4x J^5_\mu \partial_\mu \beta(x) = \cancelto{0}{\int d^4x \partial_\mu \left(J^5_\mu \beta(x)\right)} - \int d^4x \left(\partial_\mu J^5_\mu\right) \beta(x), \tag{1.40}$$

where if the transformation is global, namely, $\beta(x) =$ constant, the LHS term is zero. Therefore this anomaly requires that the topological term (1st term on RHS) is non-zero. That's why people call the global anomalous is *non-perturbative anomalies* [46]. In addition, the total derivatives never contribute to perturbation theory, since the momenta is conserved at every vertex in the Feynman rule. However, *this can NOT be true if only if the theory includes any non-perturbation effects*. Therefore, we can conclude that the $U(1)_A$ is *not* served in **perturbation** theory[11].

It is worth mentioning that if we consider the non-Abelian gauge fields, Eq.(1.38) has to rewrite as (see, Eq.(12) in [5] or Eq.(221) in [44]),

$$\boxed{\delta\mathcal{L} = \beta \partial^\mu J^5_\mu - \mathcal{C}\, \beta \frac{e^2}{16\pi^2} \epsilon^{\mu\nu\sigma\rho} F_{\mu\nu} F_{\sigma\rho}}, \tag{1.41}$$

(This β can be either local or global) where

$$\frac{1}{2} \epsilon^{\mu\nu\sigma\rho} F_{\mu\nu} \equiv \tilde{F}, \tag{1.42}$$

[11] As shown in Eq.(1.41), this symmetry is exact symmetry at the classical level, but it is intrinsically broken by QCD anomalies, as Wilczek once put it "It is a quasi-symmetry expect for instanton effects". Unlike the chiral symmetry, the PQ invariance is not even an approximate symmetry exhibited by Nature since instanton effects cannot be treated as a small perturbation. This discussion is cited from Page 20 of [47].

with (below Eq.(221) of [44])

$$\mathcal{C} = 2\mathrm{Tr}\left[Q_{\mathrm{axial}} T_a T_b\right] = 2 \times \frac{1}{2}\delta_{ab}\mathrm{Tr}Q_{\mathrm{axial}} = \delta_{ab}\mathrm{Tr}Q_{\mathrm{axial}}, \tag{1.43}$$

where $T_{a,b}$ are color generates, an example for the Q_{axial} is at Eq.(1.120), and the $U(1)_{\mathrm{axial}}$ transformation under fermions is

$$\psi_i \to e^{\pm i Q_{\mathrm{axial},i}{}^{\beta}}\psi_i, \tag{1.44}$$

with $i = \{R, L\}$, the R and L hand fermions should carried opposite sign on that $\pm$. An example can be found in Eq.(1.117). If the $U(1)_{\mathrm{axial}}$ is global symmetry, we can absorb $\mathcal{C}$ into β, on the other hand, if it carried a goldstone e.g. $U(1)_{PQ}$, the factor $\mathcal{C}$ becomes important. Furthermore, if the $F_{\mu\nu}$ corresponds to $SU(3)_c$, the $\mathcal{C}$ is called **colour anomaly** or **domain wall number** i.e. $\mathcal{C} = N_{DW}$. This factor is model dependent, see details in Sec.1.4.4. An example of $\mathcal{C}$ can be found in Eqs.(222-226) of [44], the $\mathcal{C} \simeq 1$.

The Eq.(1.41) is perturbative *axial Ward identity* (adding fermion mass)

$$\partial^{\mu} J^5_{\mu} = 2im\bar{\psi}\gamma_5\psi + \frac{e^2}{16\pi^2}\epsilon^{\mu\nu\alpha\beta}F_{\mu\nu}F_{\alpha\beta}. \tag{1.45}$$

This work on both gauge and global symmetries.

1.3.2 Connect to QCD axion

This subsection is combination of the calculations in Page73-75 of [44], Page16-20 of [47], and page4 of [2]. See also a comparison between two different bases $\beta(x) = 0$ and $\beta(x) = a(x)/f_a$ in Eqs.(5-22) of [1], and Kim's review [48].

Suppose we have the Lagrange[12]

$$\mathcal{L} = -\lambda_i \bar{\psi}_{L,i} H \psi_{R,i} + h.c. + \mathcal{L}_\theta, \tag{1.46}$$

with wind number (QCD anomaly term)

$$\mathcal{L}_\theta = \theta_i \frac{g^2}{16\pi^2} G_{\mu\nu} \tilde{G}_{\mu\nu} \neq 0, \tag{1.47}$$

where λ_i are complex Yukawa couplings, $\psi_i = \psi_1, \psi_2, \psi_3 \cdots$ are a set of Dirac fermion spinor, and the PQ scalar H and axion a is given

$$H = \frac{1}{\sqrt{2}} (f_a + h) \, e^{ia/f_a}, \tag{1.48}$$

with $U(1)_{\rm PQ}$ *global* chiral symmetry [13]

$$H \to e^{i\alpha} H, \quad \psi_L \to e^{i\alpha/2} \psi_L, \quad \psi_R \to e^{-i\alpha/2} \psi_R, \tag{1.49}$$

[12] We have to emphasize that the following calculations are considering the Lagrange Eq.(1.46), but in some cases, an $a\tilde{G}G$ is initially(before rotation) gave by exotic fermion loop, and the phase of H isn't axion, see [2, 44]. In these cases, we need to add an $a\tilde{G}G$ into Eq.(1.46). But all the calculations are the same.

[13] (Important concept) As shown in 1.41, this symmetry is exact symmetry at the classical level, but it is intrinsically broken by QCD anomalies, as Wilczek once put it "It is a quasi-symmetry expect for instanton effects". Unlike the chiral symmetry, the PQ invariance is not even an approximate symmetry exhibited by Nature since instanton effects cannot be treated as a small perturbation [This part is from Page 20 of [47]].

where $\alpha \in [0, 2\pi)$. This $U(1)_{\rm PQ}$ can be decomposed by

$$U(1)_{\rm PQ} \;\to\; U(1)_{\rm vector} \times U(1)_{\rm axial} \;=\; U(1)_V \times U(1)_A. \tag{1.50}$$

The $U(1)_{\rm axial}$ gives a *global* chiral transformation as Eq.(1.41) which can easily remove/change the θ_i in Eq.(1.47), then solve the strong CP problem, see section 2 of [47]. We leave the detail of the calculation in Sec.1.3.2. Before we study the details, we should first introduce *Changing Variable in Path Integral*.

The $U(1)_A$ transformation isn't symmetry - Changing variable in Path integral

Before we start to apply the technique *changing a variable in Path integral* into axion [49, 50]. We should first introduce the concern:

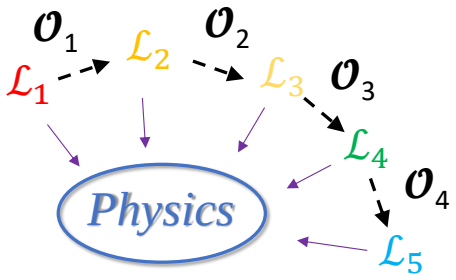

One Physics phenomenon can be described by many different Lagrangians, and those Lagrangians can be transformed to each other by different methods. For example, we initially use $\mathcal{L}_1$ to describe the Physics, then we can do a symmetry transformation, e.g. gauge/global transformation or any to have

$$\mathcal{L}_1 \;\to\; \mathcal{L}_2. \tag{1.51}$$

In definition, we call the transformation as symmetry, it is because of that the Lagrangian are identical after/before the transformation, so we have

$$\mathcal{L}_1 \quad = \quad \mathcal{L}_2. \tag{1.52}$$

On the other hand, we can also be changing the variable as in Eq.(1.21),

$$\mathcal{L}_2 \to \mathcal{L}_3, \qquad \text{but} \qquad \mathcal{L}_2 \neq \mathcal{L}_3, \tag{1.53}$$

to change the Lagrangian. *This changing variable in path integral is unphysical* [50], it is mathematically changing the integration variable, without affecting the integration target. Furthermore, as we use the symmetry transformation on Lagrangian, the changing variable is doing a similar transformation. But it does change the Lagrangian. So we would say:

$$\boxed{\text{Changing Variable in Path Integral} \supset \text{Symmetry Transformation}}. \tag{1.54}$$

The symmetry transformation is a subset of Changing Variable in Path Integral. We can separate all of transformations $\mathcal{O}$ into three parts:

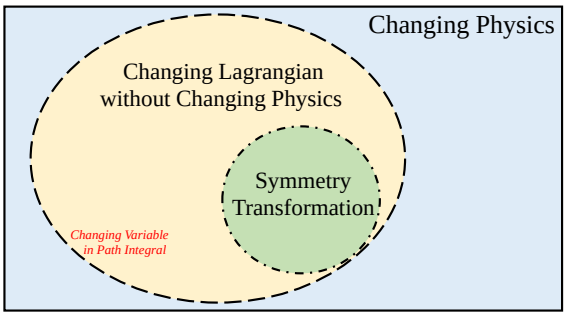

The Blue part shows all of the possible transformation operators $\mathcal{O}$, the Yellow is *Changing variable*, and the Green is for symmetry transformation.

When physics has this property, we can ask a question that *Usually we define a symmetry which introduces some conversation law, however, in this case, we still see a conversation law but it isn't a symmetry?*

A: The symmetries we defined is that its transformation isn't changing the Lagrangian. But, however, Lagrangian is due to classical physics. The quantum effects would remain the physics to be unchanged in those changing variables. For example, applying a redefinition(Changing variable) in fermions to the Lagrangian Eq.(1.46),

$$\psi_i \to e^{i\beta(x)Q_i\gamma_5}\psi_i. \tag{1.55}$$

The charges Q_i are free degrees of freedom. Following the axial ward identity Eq.(1.45), the axion-fermion interaction in Eq.(1.46) can be rewrote by

$$\frac{m_\psi}{f_a}a\bar{\psi}i\gamma_5\psi \quad \to \quad \frac{a}{2f_a}\partial^\mu J^5_\mu - \frac{a}{f_a}\frac{e^2}{16\pi^2}\tilde{G}_{\mu\nu}G^{\mu\nu}. \tag{1.56}$$

This means that we can remove the axion-fermion Yukawa coupling by the unphysical field redefinition, and create the aGG term. The full Lagrangian reads (on tree level) [2, 1],

$$\begin{aligned}\mathcal{L} \to \quad & \lambda_1\bar{\psi}_{L,1}He^{i\beta(x)Q_1}\psi_{R,1} + \lambda_2\bar{\psi}_{L,2}He^{i\beta(x)Q_2}\psi_{R,2} + h.c. \\ & + \beta(x)Q_i\partial_\mu J^\mu_{a,i} - \beta(x)\mathrm{Tr}Q_i\frac{g^2}{16\pi^2}\tilde{G}^{\mu\nu}G_{\mu\nu} + \mathcal{L}_\theta.\end{aligned} \tag{1.57}$$

But, another question is *HOW do we know this transformation wouldn't change the physics?* This is a technique on effective field theory [49, 50]. This paper [1] shows that those two different representations are identical. Further discussion is shown in Sec. 1.3.2.

On the other hand, it is not true that U(1)PQ is made a local symmetry since scalar fields are not transformed. One should think about QED: going from a global to a local symmetry requires the introduction of gauge fields because a true symmetry asks for the Lagrangian to retain its form. Here, the transformation is not leaving the fermion kinetic terms invariant but introduces the derivative interactions. Those are precisely the interaction that would be killed by gauge fields (thanks to the $d_\mu\Lambda$ in $A_\mu \to A_\mu + d_\mu\Lambda$).

Basis: $\beta(x) = 0$

If we have the field redefinition Eq.(1.55), the $\beta(x)$ is unphysical, then we can choose any of $\beta(x)$. But in this subsection, we first choose $\beta(x) = 0$. Then the Lagrange reduces to Eq.(1.46). Then after the fermion condensate (Eq.(2.14) of [47])

$$\langle\theta|\bar{\psi}_L\psi_R|\theta\rangle = \Lambda^3_{\rm QCD}e^{-i\phi_i}, \qquad \langle\theta|\bar{\psi}_R\psi_L|\theta\rangle = \Lambda^3_{\rm QCD}e^{i\phi_i}, \tag{1.58}$$

where $|\theta\rangle$ is QCD state, namely, the minimal of axion potential. In this explanation, we only consider one family of fermion, this gives $\phi_i = \theta_i$, see Eq.(1.73) or Eq.(2.17) in [47]. The QCD ground state is (section 2.1, [47])

$$\langle\theta|\bar{\psi}_L\psi_R|\theta\rangle = \langle\theta|\bar{\psi}_R\psi_L|\theta\rangle = \Lambda^3_{\rm QCD}. \tag{1.59}$$

To rotate into the QCD ground sate (see Sec.1.3.2), the phase $e^{i\theta_i}$ is removed by *global* $U(1)_{\rm PQ}$ rotation $\psi \to e^{i\theta_i/2\gamma_5}\psi$, equivalently, $\psi_R \to e^{i\theta_i/2}\psi_R$ and $\psi_L \to e^{-i\theta_i/2}\psi_L$. When we rotate the phase $e^{i\theta_i}$ away, the θ_i in Eq.(1.47) also be rotated away by Eq.(1.41) with $\mathcal{C} = 1$. This is the key point of the PQ mechanism. Back to Lagrange Eq.(1.46), *before* the $U(1)_{\rm PQ}$ rotation, the original Lagrangian is

$$\begin{aligned}\mathcal{L} &\supset \frac{\lambda}{\sqrt{2}}\bar{\psi}_L(f_a + h)e^{ia/f_a}\psi_R + h.c. \\ &= \frac{\lambda}{\sqrt{2}}\langle\bar{\psi}_L\psi_R\rangle(f_a + h)e^{ia/f_a} + h.c. \\ &= \sqrt{2}\lambda\Lambda^3_{\rm QCD}(f_a + h)\cos(\frac{a}{f_a} - \theta_i).\end{aligned} \tag{1.60}$$

We can redefine the axion by the *global* $U(1)_{\rm PQ}$ Eq.(1.49), namely, $a \to a + \theta_i f_a$ to absorb the θ_i. On the other hand, we can look at the $\tilde{G}G$ anomalous term:

$$\mathcal{L} \supset \left(\theta_i - \frac{a}{f_a}\right)\frac{e^2}{16\pi^2}G^a_{\mu\nu}\tilde{G}^{\mu\nu,a}, \tag{1.61}$$

where the $a\tilde{G}G$ term is from fermion loop, the calculation is in Eq.(7) of [1][14]. We can use $U(1)_{\rm PQ}$ to cancel the θ_i. In this case, we can see that we only need a *global* axial $U(1)_{\rm PQ}$ to solve the strong CP problem. The redefinition Eq.(1.55) isn't necessary.

So we find that both Eq.(1.60) and Eq.(1.61) break the axion shift symmetry. The

[14]The Ref.[1] considers $a\gamma\gamma$ case, but we can simply add the trace of $SU(3)_c$ generators $\mathrm{Tr}[t_a t_b]$ for $a\tilde{G}^a_{\mu\nu}G^{\mu\nu}_b$ case. We don't need to calculate the value of the trace, because it would be written as an effective Lagrangian form as Eq.(1.61).

axion is the same as Higgs in the Higgs mechanism. It would roll into its true vacuum

$$a = \theta_i f_a. \tag{1.62}$$

If we redefine $a \to a + \theta_i f_a$, the potential is shown in Fig.4.3. Furthermore, the $a\tilde{G}G$ term allows the axion interacts to the meson or gluon radiative bath in this toy model. This interaction would provide thermal friction on axion, as in Minimal warm inflation. Once the meson density is hardly diluted in the universe, this effect would be ignorable, i.e. the $a\tilde{G}G$ interaction term isn't affected much. Then the dynamic of axion is the same as the conventional one.

On the other hand, if all of the fermions are massless, i.e. no $a\tilde{G}G$ term Eq.(1.68), and this also means that the H does not spontaneously symmetry breaking. In this case, the axion shift symmetry and $U(1)_{\rm PQ}$ still hold. So if we say the $a\tilde{G}G$ term breaks the axion shift symmetry, which isn't precise. Because all the things (H SSB, fermion get mass, $U(1)_{\rm PQ}$ breaking, axion shift symmetry breaking, $a\tilde{G}G$ term) are all together.

By the way, once the Higgs h rotates to its minimal $h \to 0$, this potential is purely cosine. However, this potential can be modified, e.g. if we assume another component in this term, and it would dominate in the early universe:

$$\mathcal{L} \supset \lambda \left(\frac{\phi}{\Lambda_\phi}\right)^n \bar{\psi}_L H \psi_R \gg \lambda \bar{\psi}_L H \psi_R, \tag{1.63}$$

where ψ is a real field, this term can modify the dynamic of axion in the early universe.

Basis: $\beta(x) = a(x)/f_a$

In the last subsection, we prove that the $U(1)_{\rm PQ}$ can solve the strong CP problem without the field redefinition. But in this section, we use the redefinition. This procedure is more standard [44]. If we secondly pick up the redefinition to be $\beta(x) = a/(f_a {\rm Tr}Q_i)$, the Lagrange becomes [2, 44, 1]

$$\begin{aligned}
\mathcal{L} \to \quad & \lambda_1 \bar{\psi}_{L,1} H e^{i\frac{a}{f_a}} \psi_{R,1} + \lambda_2 \bar{\psi}_{L,2} H e^{i\frac{a}{f_a}} \psi_{R,2} + h.c. \\
& + \frac{a}{2f_a} \partial_\mu J^\mu_{a,i} + \left(-\frac{a}{f_a} + \theta_i \right) \frac{g^2}{16\pi^2} \tilde{G}^{\mu\nu} G_{\mu\nu}, \\
= & \frac{\lambda_1}{\sqrt{2}} \bar{\psi}_{L,1} (f_a + h) \psi_{R,1} + \frac{\lambda_2}{\sqrt{2}} \bar{\psi}_{L,2} (f_a + h) \psi_{R,2} + h.c. \\
& + \frac{a}{2f_a} \partial_\mu J^\mu_{a,i} + \left(-\frac{a}{f_a} + \theta_i \right) \frac{g^2}{16\pi^2} \tilde{G}^{\mu\nu} G_{\mu\nu},
\end{aligned} \tag{1.64}$$

to simplify we simply assume

$$Q_1 = Q_2 = \frac{1}{2}, \qquad {\rm Tr}Q_i = Q_1 + Q_2 = 1, \tag{1.65}$$

this is the same as the case $m_u \simeq m_d$ in Eq.(225) of [44] or see Eq.(14) of [2]. The axion in H is shown in Eq.(1.48), and *the axion in Yukawa terms are exactly canceled by the chiral transformation $\beta(x)$, but we have to emphasize that this cancellation is true only if the charge degenercy* Eq.(1.65)*.If $Q_1 \neq Q_2$, the axion cannot be cencelled in both Yukawa terms, simultaneously.* The Eq.(1.64) is the same as Eq.(1) of [2], i.e. Eq.(1.113). Interestingly, they [2] further do an inverse transformation to rotate the symmetry back to $\beta(x) = 0$ case. In addition, this transformation $\beta(x)$ is the same as using the axial Ward identity Eq.(1.45)

to replace $m_\psi \bar{\psi} i\gamma_5 \psi$ in Eq.(1.67).

It is worth mentioning that the $a\bar{\psi} i\gamma_5 \psi$ term is vanished in this representation Eq.(1.64). But it is checked in [1], the physics (e.g. $a \to \gamma\gamma$) are the same as in the previous representation Eq.(1.60) plus Eq.(1.61).

Comparison of these two bases

A comparison between two different bases is shown on page 4 of [2]. In $\beta = a/(f_a \mathrm{Tr} Q_i)$ basis, the $a\tilde{G}G$ interaction would introduce a quantum loop: This leading order

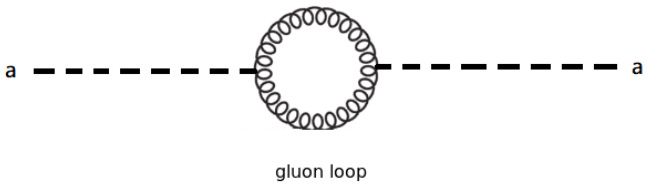

of the loop graph gives the second leading order of the cosine in Eq.(1.60), i.e. $m_a^2 a^2$ term,

$$m_a^2 f_a^2 \cos(\frac{a}{f_a}) \simeq m_a^2 f_a^2 + m_a^2 a^2 + \cdots . \tag{1.66}$$

More axion legs on the loop would give higher order of cosine. By the way, odd axion legs are forbidden by CP-symmetry. On the other hand, on the $\beta(x) = 0$ basis, the $a\tilde{G}G$ term can be introduced by a fermion loop as Fig.4.2, see Eqs.(5-10) in [1], and depiction on below Eq.(3.50) of [47]. Therefore, these two representation bases are Equivalent, see discussion below Eq.(5) of [2].

Furthermore, to expanding the exponential e^{ia/f_a} in Eq.(1.49), we can have an

interaction term as [1],

$$\mathcal{L} \supset \frac{m_\psi}{f_a} a\bar{\psi} i\gamma_5 \psi, \tag{1.67}$$

As shown in [1], this axion-fermions interaction term with a triangle fermion loop can introduce an anomalous term [1]

$$\mathcal{L}_{\text{eff}} = -\frac{a}{f_a}\mathcal{C}\frac{g^2}{16\pi^2}\tilde{G}G \times \begin{cases} 0, & \text{for} \quad m_\psi \to 0 \\ \\ 1, & \text{for} \quad m_\psi \to \infty \end{cases}. \tag{1.68}$$

where $\mathcal{C}$ is a constant, dependent on fermion mass and number of fermions Eq.(1.44). This $a\tilde{G}G$ breaks the axion shift symmetry. They [1] find that those two representations $\beta(x) = 0$ and $\beta(x) = a/f_a$ are identical.

Rotate to the vacuum representation

The charge choosing on [44],

$$Q_1 = \frac{m_1}{m_1 + m_2}, \qquad Q_2 = \frac{m_2}{m_1 + m_2}, \tag{1.69}$$

is in order to rotate the Lagrange into the QCD vacuum[15], which is the same as the redefinition of Higgs field in Higgs mechanism $H \to \frac{1}{\sqrt{2}}(v + h)$. This choice Eq.(1.69) can cancel the axion-pion mixing term $a - \pi$ [44], and rotate the Lagrange into the QCD vacuum presentation [47]. The following is the calculation in section 2.1 of [47]. Suppose

[15]See, section2.1 of [47] and Eq.(14) of [2] and Eq.(225) of [44]

we have fermion mass terms to break the $U(1)_A$ axial symmetry, and this term is very small

$$\epsilon\mathcal{L} = -m_i\bar{q}_i q_i, \tag{1.70}$$

where ϵ is very small. So in the low energy region, the $U(1)_A$ is broken(spontaneously), but it is still an approximate symmetry. Without this symmetry-breaking term, the Lagrange should have vacuum expectation values which are invariant(degenerate) under $U(1)_A$, therefore the vacuum expectation values can be written

$$\langle\theta|\bar{q}_{iL}q_{jR}|\theta\rangle = \Lambda^3_{\mathrm{QCD}}\delta_{ij}e^{-i\phi_i} + \mathcal{O}(\epsilon), \tag{1.71}$$

where ϕ_i is a variable, which corresponds to $U(1)_A$ invariant. The explicit chiral-symmetry breaking term $\epsilon\mathcal{L}$ will pick out a unique vacuum on the $U(1)_A$ circle, i.e. explicit value for the ϕ_i. The $U(1)_A$ vacuum direction is governed by the anomalous Ward identity, see Eq.(2.17) of [47],

$$m_i \sin\phi_i = m_j \sin\phi_j + \mathcal{O}(\epsilon^2), \tag{1.72}$$

$$\sum_{i=1}^{n}\phi_i = \theta_i + \mathcal{O}(\epsilon), \tag{1.73}$$

where θ_i is from Eq.(1.47). If the $|\theta\rangle$ is the correct vacuum, it must satisfy Eqs.(1.72,1.73). Lets consider the *field redefinition* as Eq.(1.55) and the charges in Eq.(1.57), to remove the

phases on Eq.(1.71), we need

$$\beta(x)Q_i = \phi_i. \tag{1.74}$$

Lets consider simple case $i = \{1, 2\}$, and $\phi_i \ll 1$, the Eq.(1.72) becomes

$$m_1 \sin(\beta(x)Q_1) \simeq m_2 \sin(\beta(x)Q_2) \quad \rightarrow \quad m_1 Q_1 \simeq m_2 Q_2. \tag{1.75}$$

The Eq.(1.73) becomes

$$\beta(x)\,(Q_1 + Q_2) = \theta_i \quad \rightarrow \quad \frac{a(x)}{f_a}\frac{1}{\mathrm{Tr}Q}\,(Q_1 + Q_2) = \frac{a(x)}{f_a} = \theta_i, \tag{1.76}$$

where we substitute the basis,

$$\beta(x) = a(x)/(f_a \mathrm{Tr}Q). \tag{1.77}$$

The Eq.(1.76) is the same as what we expected[16], the vacuum is when the $\tilde{G}G$ term disappear, see Eq.(1.64), and solution of Q_1 and Q_2 are exactly Eq.(1.69), where $1 \rightarrow u$ and $2 \rightarrow d$. On the other hand, for the $\beta(x) = 0$ basis, the ϕ_i are global phases. We still can chose ϕ_1 and ϕ_2 to satisfy Eqs.(1.72,1.73)[17]. This is shown in Section 2.1 of [47].

The Eq.(1.72) also says that if one of a fermion is massless, the rotation $\beta(x)$ or say ϕ_i is unphysical, see discussion in Section II-B-2 [48]. Hence, there are no strong CP

[16] We have to emphasize that these calculations are considering the Lagrange Eq.(1.46), but in some case, an $a\tilde{G}G$ is initially(before rotation) gave by exotic fermion loop, and the phase of H isn't axion, see [2, 44]. In these cases, we need to add an $a\tilde{G}G$ into Eq.(1.46). But all the calculations are the same.

[17] Also, if $\theta_i = 0$, we don't need to do redefinition of $\beta(x)$, because we can have $\beta(x) = 0$ as solution of Eqs.(1.72,1.73).

problems.

Similarity with Gauge fixing

The gauge fixing is fixing the gauge transformation function $\beta(x)$, and the unitary gauge requires

$$\beta(x) \equiv \frac{a}{f_a}, \tag{1.78}$$

this is exactly the same as the vacuum representation. In these two cases $\beta(x) = \{0, a/f_a\}$, they both have same physics. This is very similar to gauge fixing.

1.3.3 No Confuse on Anomaly Cancellation - Strong CP Phase do Not Break $SU(3)_c$

First, from Eq.(25.73) of [43], the strong CP phase term

$$\mathcal{L}_\theta \propto \theta \epsilon^{\mu\nu\alpha\beta} F^a_{\mu\nu} F^a_{\alpha\beta} = 2\theta \partial_\mu \left(\epsilon^{\mu\nu\alpha\beta} A^a_\nu F^a_{\alpha\beta} \right), \tag{1.79}$$

is gauge invariance. A non-Abelian gauge field $A_\mu \equiv A^a_\mu T^a$ transformation

$$A_\mu \;\; \rightarrow \;\; A'_\mu = U A_\mu U^{-1} - \frac{i}{g} (\partial_\mu U) U^{-1}, \tag{1.80}$$

where $U^{-1} = U^\dagger$, considering the non-Abelian rotation $U = e^{i\theta_a T^a} \simeq 1 + i\theta_a T^a$,

$$A_\mu \;\; \rightarrow \;\; A'_\mu = A_\mu + i\theta_a \left[T^a, A_\mu \right] - \frac{1}{g} \partial_\mu \theta_a T^a + \mathcal{O}(\theta^2) \tag{1.81}$$

then substituting $A_\mu \equiv A_\mu^a T^a$, we have

$$\boxed{A_\mu^a \;\; \rightarrow \;\; A_\mu^{a\,\prime} = A_\mu^a - f^{abc}\theta^b A_\mu^c - \frac{1}{g}\partial_\mu \theta^a = A_\mu^a - \frac{1}{g} D_\mu^{ab}\theta^b}, \tag{1.82}$$

where we used

$$[T_a, T_b] = i f^{abc} T_c, \qquad D_\mu^{ab} = \delta^{ab}\partial_\mu + g f^{abc} A_\mu^c. \tag{1.83}$$

Let's define non-Abelian field strength

$$F_{\mu\nu}^a = \partial_\mu A_\nu^a - \partial_\nu A_\mu^a - g f^{abc} A_\mu^b A_\nu^c. \tag{1.84}$$

Then using $U = e^{i\theta_a T^a} \simeq 1 + i\theta_a T^a$ again

$$F_\mu \;\; \rightarrow \;\; F'_{\mu\nu} = U F_{\mu\nu} U^\dagger = F_{\mu\nu}^a U T_a U^\dagger = F_{\mu\nu}^a T_a + i\theta^b F_{\mu\nu}^a [T_b, T_a] = (F_{\mu\nu}^a - f^{abc}\theta^b F_{\mu\nu}^c) T_a, \tag{1.85}$$

then we have the field transformation without the operator:

$$\boxed{F_{\mu\nu}^a \;\; \rightarrow \;\; F_{\mu\nu}^{a\,\prime} = F_{\mu\nu}^a - f^{abc}\theta^b F_{\mu\nu}^c} \tag{1.86}$$

Let us check the kinetic term of the gauge boson:

$$\mathcal{L}_A = -\frac{1}{2}\mathrm{tr}(F_{\mu\nu}F^{\mu\nu}) \rightarrow -\frac{1}{2}\mathrm{tr}\left[(F_{\mu\nu}^a - f^{abc}\theta^b F_{\mu\nu}^c) T_a (F_{\mu\nu}^\alpha - f^{\alpha\beta\gamma}\theta^\beta F_{\mu\nu}^\gamma) T_\alpha\right], \tag{1.87}$$

this trace can be just replaced by $\mathrm{tr}[T_a, T_\alpha] = \frac{1}{2}\delta_{a\alpha}$. Consider the $\mathcal{O}(\theta)$ term:

$$
\begin{aligned}
\mathrm{tr}\left[F^a_{\mu\nu}T_a f^{\alpha\beta\gamma}\theta^\beta F^\gamma_{\mu\nu}T_\alpha + f^{abc}\theta^b F^c_{\mu\nu}T_a F^\alpha_{\mu\nu}T_\alpha\right] &\overset{\clubsuit}{=} \mathrm{tr}\left[F^a_{\mu\nu}T_a f^{\alpha bc}\theta^b F^c_{\mu\nu}T_\alpha + f^{abc}\theta^b F^c_{\mu\nu}T_a F^\alpha_{\mu\nu}T_\alpha\right] \\
&\overset{\spadesuit}{=} \mathrm{tr}\left[F^\alpha_{\mu\nu}T_\alpha f^{abc}\theta^b F^c_{\mu\nu}T_a + f^{abc}\theta^b F^c_{\mu\nu}T_a F^\alpha_{\mu\nu}T_\alpha\right] \\
&\overset{\diamondsuit}{=} \mathrm{tr}\left[T_\alpha T_a + T_a T_\alpha\right] f^{abc}\theta^b F^\alpha_{\mu\nu}F^c_{\mu\nu} \\
&\overset{\heartsuit}{=} \mathrm{tr}\left[\{T_\alpha, T_a\}\right] f^{abc}\theta^b F^\alpha_{\mu\nu}F^c_{\mu\nu} \\
&\overset{\circ}{=} \mathrm{tr}\left[\frac{1}{3}\delta_{a\alpha}I_{3\times 3} + \sum_{j=1}^{8} d_{a\alpha j}T_j\right] f^{abc}\theta^b F^\alpha_{\mu\nu}F^c_{\mu\nu} \\
&= f^{abc}\theta^b F^a_{\mu\nu}F^c_{\mu\nu} = 0. \quad \text{Gauge invariant!}
\end{aligned}
$$

where $\clubsuit$, $\spadesuit$ and $\diamondsuit$ just replace the index. The $\heartsuit$ is considering $\{T^a, T^b\} = \frac{1}{3}\delta^{ab} + d^{abc}T^c$, where d^{abc} is a set of constants (hyperlink). The most important is the antisymmetry of structure constant $f^{abc} = -f^{acb}$, therefore the symmetry $a \leftrightarrow c$ on $F^a_{\mu\nu}F^c_{\mu\nu}$ makes the term be vanished. Furthermore, the string CP phase Eq.(1.79) is $SU(3)_c$ gauge invariant as well, since the $\epsilon^{\mu\nu\alpha\beta}$ do not affect color space. So the kinetic mixing term between $U(1)_a \times U(1)_b$ is gauge invariant as well, but kinetic mixing $SU(3)_c \times U(1)$ is not since gluon carried the colors.

Second, a Question: *Why the term $\epsilon^{\mu\nu\alpha\beta}F^b_{\mu\nu}F^a_{\alpha\beta}$ does not break non-Abelian gauge symmetry, but we still need anomaly cancellation?*

Recall the anomaly cancellation term, for example $U(1)_a \times SU(3)_c \times SU(3)_c$

(Eq.(30.80) of [43]):

$$\partial_\mu J^a_\alpha(x) = \left(\sum_{\text{left}} A(R_l) - \sum_{\text{right}} A(R_r) \right) \frac{g_s^2}{128\pi^2} d^{abc} \epsilon^{\mu\nu\alpha\beta} F^b_{\mu\nu} F^a_{\alpha\beta}. \tag{1.88}$$

The key point it that the $U(1)_\alpha$ gauge invariance require $\partial_\mu J^a_\alpha(x) = 0$, this condition is independent to $SU(3)_c$, namely, $\epsilon^{\mu\nu\alpha\beta} F^b_{\mu\nu} F^a_{\alpha\beta}$ in this equation. Therefore the *anomaly cancellation* is only conditions for this $U(1)_a$ symmetry invariance, instead of the condition for $SU(3)$ or $SU(2)$, etc. By the way, for the non-Abelian symmetry the non-Abelian current is NOT defined as Abelian. The non-Abelian current should be covariant, see Eq.(1.91).

Third, another Question: *What is the current gauge invariant condition for non-Abelian gauge symmetry?*

Recalling Chapter 25.3 of [43], in Abelian $U(1)_a$ symmetry we defined

$$Q^a = \int d^3 J^a_0, \tag{1.89}$$

as conserved current. However, it cannot be the case in non-Abelian theory. Since the gauge boson in non-Abelian is carried charges, e.g. gluon has color, $W^\pm$ has weak isospin to change *up* to *down*. So the current should be gauge covariant i.e. carried gauge charge

$$j^a_\mu - \bar{\psi}_i \gamma^\mu T^a_{ij} \psi_j. \tag{1.90}$$

Then the gauge invariant condition to be

$$\boxed{D_\mu j^a_\nu \equiv \partial_\mu j^a_\nu + g f^{abc} A^b_\mu j^c_n u = 0}. \tag{1.91}$$

We will see the application of this gauge invariant in the following sections.

1.3.4 CP violation θ_B, θ_W and θ_{QCD} in SM

Basis on the chiral rotation $\psi \to e^{i\gamma_5\theta}\psi$, we have

$$\int \mathcal{D}\bar{\psi}\mathcal{D}\psi \;\; \to \;\; \int \mathcal{D}\bar{\psi}\mathcal{D}\psi \exp\left(i\theta \int d^4x \frac{g^2}{32\pi^2}\epsilon^{\mu\nu\alpha\beta}F^a_{\mu\nu}F^a_{\alpha\beta}\right), \tag{1.92}$$

where ψ can be chiral e.g. $\psi = \psi_L$, this transformation wouldn't be changed. Furthermore, applied to SM fermions, the chiral transformation provides

$$\mathcal{L}_{SM} \supset \theta_{QCD}\frac{g_s^2}{32\pi^2}\epsilon^{\mu\nu\alpha\beta}F^a_{\mu\nu}F^a_{\alpha\beta} + \theta_W\frac{g^2}{32\pi^2}\epsilon^{\mu\nu\alpha\beta}W^a_{\mu\nu}W^a_{\alpha\beta} + \theta_B\frac{g'^2}{16\pi^2}\epsilon^{\mu\nu\alpha\beta}B_{\mu\nu}B_{\alpha\beta}, \tag{1.93}$$

where $F^a_{\mu\nu}$, $W^a_{\mu\nu}$ and $B_{\mu\nu}$ are the $SU(3)_c$, $SU(2)_L$ and $U(1)_Y$ field strengths, respectively. To connect to the phenomenon, we need to use the chiral rotation is that when the interaction states are not the mass eigenstates, e.g.

$$Y_d = U_{d,L}M_dU^\dagger_{d_R}, \qquad Y_u = U_{u,L}M_uU^\dagger_{u_R}, \tag{1.94}$$

where $Y_{u,d}$ are on the SM interaction eigenstate, the $M_{u,d}$ are on the mass eigenstate i.e. diagonal. One we can do is considering the Dirac basis for fermion, i.e.

$$Y_d = U_d M_d U_d^\dagger K_d^\dagger, \qquad Y_u = U_u M_u U_u^\dagger K_u^\dagger, \tag{1.95}$$

by assuming the chiral rotations on only the K_u and K_d, and they can be removed by right-handed fermions. On the other hand, the U_d and U_u can be removed by non-chiral rotations, i.e. they are real. Considering Eq.(1.92), if we are only chiral rotating the right-hand fermions globally i.e.

$$\int \mathcal{D}\bar{\psi}_R \mathcal{D}\psi_R \;\; \rightarrow \;\; \int \mathcal{D}\bar{\psi}_R \mathcal{D}\psi_R \exp\left(i\theta_F \int d^4x \frac{g^2}{32\pi^2} \epsilon^{\mu\nu\alpha\beta} F^a_{\mu\nu} F^a_{\alpha\beta} \right), \tag{1.96}$$

to cancel the $K_{d,u}$. From Eq.(1.20) and using Eq.(1.22) with $\Delta = K_{d,u}$, the phase θ_F should be read as

$$\arg\det\Delta = \arg\mathcal{J} = \arg e^{-i\theta_F\gamma_5} = -\theta_F, \tag{1.97}$$

and

$$\arg\det\left(K_d\right) + \arg\det\left(K_u\right) = \arg\det\left(K_d K_u\right) = -\arg\left[\det\left(M_d M_u\right)\,\det\left(Y_d Y_u\right)\right] = -\arg\det\left(Y_d Y_u\right).$$

Thus we have[18]

$$\mathcal{L} \supset \bar{\theta}\frac{g_s^2}{32\pi^2}\epsilon^{\mu\nu\alpha\beta}F^a_{\mu\nu}F^a_{\alpha\beta}, \qquad \bar{\theta} \equiv \theta_{QCD} - \theta_F, \tag{1.98}$$

where

$$\theta_F = \arg\det\left(Y_d Y_u\right), \tag{1.99}$$

and the θ_{QCD} is the phase after the $U(1)_A$ symmetry breaking, just like Higgs vacuum v_H in SM, a parameter. It is worth mentioning that only the difference $\bar{\theta} = \theta_{QCD} - \theta_F$ is physical, it is a so-called strong CP phase.

Another two phases θ_W and θ_B can be removed: For the θ_W, considering the lepton Yukawa matrix, e.g.

$$Y_e = U_e M_e U_e^\dagger K_e^\dagger, \tag{1.100}$$

again, since the right-hand lepton does not couple to $SU(2)_L$, the $K_e^\dagger$ can be removed by right-hand lepton without the anomaly term. Similarly, the θ_B can be removed by a right-hand neutrino. You may question that *How about* $U(1)_{em}$*?* Since it is linear combination of $SU(2)_L$ and $U(1)_Y$, the anomaly term should be removed initially. To sum, the anomaly term will be left after $U(1)_A$ SSB only if the gauge-symmetry couple to both left and right-hand massive fermions. We emphasize the **massive** fermions since the $U(1)_A$ is broken by the mass terms. By the way, instantons break the $U(1)_A$ symmetry at $V \sim 260$MeV [51].

[18] In some papers, e.g. [38, 39, 2], they defined the chiral transformation $e^{i\frac{1}{2}\gamma_5\theta}$ with additional factor $\frac{1}{2}$.

1.3.5 Constraint from neutron electric dipole moment

Lets use the sigma model again, rewrite Eq.(1.82) and Eq.(1.4),

$$\mathcal{L} = \frac{F_\pi^2}{4}\,\mathrm{tr}\left[(D_\mu U)\left(D_\mu U^\dagger\right)\right] + \frac{V^3}{2}\,\mathrm{tr}\left[MU + M^\dagger U^\dagger\right] \tag{1.101}$$

where we do the chiral rotation on quarks $u \to e^{i\bar{\theta}\gamma_5}u$ i.e. $M \to M_q e^{i\bar{\theta}}$ at Eq.(1.8), and $-V^3 = \langle\bar{u}u\rangle = \langle\bar{d}d\rangle$. It is worth mentioning that the second term leads to the Gell-Mann-Oakes-Renner relation, i.e. after expanding $U(x) = \exp\left(2i\pi^a(x)\lambda^a/F_\pi\right)$,

$$F_\pi^2 m_\pi^2 = V^3\left(m_u + m_d\right), \tag{1.102}$$

where $V \simeq 260\mathrm{MeV}$ is the $U(1)_A$ SSB scale [51]. As above, the vacuum energy from the mass terms by expanding in first order $U(x) \to 1$, then considering only two flavors $SU(2)$ would be (drop off constant term)

$$E(\bar{\theta}) = -\frac{V^3}{2}\,\mathrm{tr}\left[M + M^\dagger\right] = -V^3(m_u + m_d)\cos\bar{\theta} = F_\pi^2 m_\pi^2\cos\bar{\theta}, \tag{1.103}$$

as we can see the vacuum energy is the function of $\bar{\theta}$-vacuum. Next, lets consider the Baryon $SU(3)$ chiral Lagrangian, see chapter 4.4 in [52] for details, and the original paper [53]

$$\mathcal{L}_{\pi NN} = \pi^a\bar{\Psi}\left(i\gamma_5 g_{\pi NN} + \bar{g}_{\pi NN}\right)\lambda^a\Psi, \tag{1.104}$$

where Ψ is the $P-N$ isospin doublet. The first term is the ordinary Yukawa coupling with $g_{\pi NN} = 13.4$ to the pseudoscalar pions, which provides a Yukawa potential to describe

strong nuclear force among nucleons. The $\bar{g}_{\pi NN}$ is from Eq.(12) of [53],

$$\bar{g}_{\pi NN} = \frac{2m_u m_d}{f_\pi (m_u + m_d)(2m_s - m_u - m_d)} \left(M_\Sigma - M_N\right) \bar{\theta} \simeq 0.023\bar{\theta}. \tag{1.105}$$

then the neutron EDM is $(d_n + d_p = 0)$ [38, 39]

$$d_n = e\frac{g_{\pi NN}\bar{g}_{\pi NN}}{4\pi^2 m_N} \ln\left(\frac{m_N}{m_\pi}\right) \simeq 4.5 \times 10^{-15}\, \bar{\theta}\; e\,\mathrm{cm} < 2.9 \times 10^{-26}\; e\,\mathrm{cm}, \tag{1.106}$$

where the bound is from 2006 [54], i.e. $\bar{\theta} \lesssim 0.7 \times 10^{-11}$, by comparing to $g_{\pi NN} = 13.4 \gg \bar{g}_{\pi NN} \sim 10^{-13}$, we know it is unnaturally small.

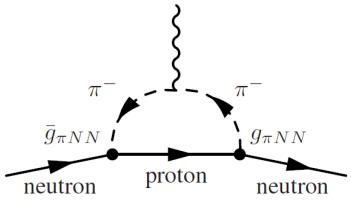

In later sections, we apply the Goldstone field theory to the axion phenomenology.

1.4 Axion: Theory

There have many possibilities to solve the strong CP problem, e.g. a calculable $\bar{\theta}$, the easiest way to do this job is by assuming the SSB phase θ_{QCD} to be zero, then the $\bar{\theta}$ is mainly contributed by Yukawa matrix e.g. [55] or spontaneous CP violation [56] which can be introduced effectively from multi-loop (at least one-loop suppression) diagrams e.g. [57], see [58] and [38, 39] for more examples.

An elegant solution for the strong CP problem is the axion (The axion that solves the strong CP problem is called QCD Axion), introduced by Peccei and Quinn (PQ) [59]. They introduce a global chiral symmetry $U(1)_{PQ}$ on both the quarks and the Higgs multiplets transform same phase as quarks transformed under $U(1)_{PQ}$. Consequently, the phase $\bar{\theta}$ can be dynamically set to zero.

The symmetry breaking procedure of axion is following[19]

$$G \overset{\text{Step-1}}{\to} U(1)_{\text{PQ}} \overset{\text{Step-2}}{\to} Z_N, \tag{1.107}$$

where the G is the symmetry on PQ scalar ϕ, the $U(1)_{PQ}$ is topologically a circle, and Z_N is disconnected points in the circle as shown in the figure in 1.1. The Step-1 and Step-2 are gonna be explained in following paragraphs.

Following the calculation in [33]. Similar to the linear sigma model, the Lagrangian

$$\mathcal{L} = (\partial_\mu \phi^*)(\partial_\mu \phi) + m^2 \phi \phi^* - \frac{\lambda}{4} \phi^2 \phi^{*2}, \tag{1.108}$$

[19] However, the $U(1)_{\text{PQ}}$ is not a explicit symmetry, see an important explanation on page20 of [47] points (a) and (b). This symmetry breaking is also explained mathematically/topologically on page 79 of the book [60]. The axion-string formation depends on whether G isn't simply connect $\pi_1(G) \neq I$.

with $m^2 > 0$, where we have a global $U(1)_{PQ}$ symmetry $\phi(x) \to e^{i\beta}\phi(x)$. Step-1, the G will be broken at $\langle\phi\rangle = v = f_a/\sqrt{2}$ (axion-string has possible to be formed). However, the Goldstone direction does not break (i.e. $U(1)_{\rm PQ}$ not break), so there are an infinite number of equivalent vacua $|\Omega_\theta\rangle$ with $\langle\Omega_\theta|\phi|\Omega_\theta\rangle = \sqrt{\frac{2m^2}{\lambda}}e^{i\theta}$ for any constant θ. Consequently, the θ direction can be parametrized to a real field as

$$\phi(x) = \left(\sqrt{\frac{2m^2}{\lambda}} + \frac{1}{\sqrt{2}}\sigma(x)\right) e^{i\frac{a(x)}{f_a}}. \tag{1.109}$$

Next interesting is expanding the Lagrangian with the field, i.e.

$$\mathcal{L} = \frac{1}{2}(\partial_\mu\sigma)^2 + \left(\sqrt{\frac{2m^2}{\lambda}} + \frac{1}{\sqrt{2}}\sigma(x)\right)^2 \frac{1}{f_a^2}(\partial_\mu a)^2 - \left(-\frac{m^4}{\lambda} + m^2\sigma^2 + \frac{1}{2}\sqrt{\lambda}m\sigma^3 + \frac{1}{16}\lambda\sigma^4\right),$$

if we require a canonical kinetic term for the axion, we have $f_a = \frac{2m}{\sqrt{\lambda}} \equiv \sqrt{2}v$. The axion a is the Goldstone boson of the broken $U(1)_{PQ}$ symmetry, i.e. its transformation in the Goldstone direction do not break

$$e^{i\gamma_5\frac{a}{f_a}}\psi \to e^{i\gamma_5(\frac{a}{f_a}+\alpha)}\psi, \qquad \text{as} \qquad a(x) \to a(x) + \alpha f_a, \tag{1.110}$$

f_a is a real parameter with a mass scale, as the decay constant f_π in the sigma model which is associated with breaking $U(1)_{PQ}$. Step-2, this shift symmetry on axion would be broken by instanton non-perturbative effect i.e. $\langle a\rangle = \Lambda_{\rm inst} \sim \Lambda_{QCD}$, to a $Z_{N_{DW}}$ symmetry e.g.[20]

At step-2, an axion potential from fermions is shown up as Fig.4.3, and the axion-

[20] Here should not be confused, when we say $Z_{N_{DW}}$ is looking around the potential at the original point instead of the minima. This $Z_{N_{DW}}$ is not real symmetry at minima potential, therefore it do not need any *d.o.f.*.

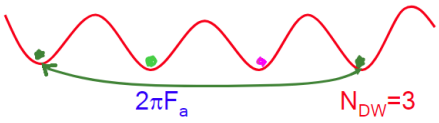

domain walls are formed at this moment. On the other hand, the Noether current is

$$J^{\mu}_{PQ} = \frac{\partial \mathcal{L}}{\partial\left(\partial_{\mu} a\right)} \frac{\delta a}{\delta \alpha} = f_a \partial^{\mu} a + \text{fermion terms}, \tag{1.111}$$

where $\delta a/\delta\alpha = f_a$. If we only require the right(left)-hand fermions carry the $U(1)_{PQ}$ charge, i.e.

$$\psi_R \to e^{i\frac{a}{f_a}}\psi_R, \qquad \psi_L \to e^{-i\frac{a}{f_a}}\psi_L \tag{1.112}$$

this is the same as transformation under of Dirac basis with γ_5 e.g. Eq.(1.110). So the fermion terms will be

$$J^{\mu}_{PQ} = f_a \partial^{\mu} a + f_a \frac{\partial}{\partial\left(\partial_{\mu} a\right)} \left[i\bar{\psi}_R \gamma_{\mu} \partial^{\mu} \psi_R - m\bar{\psi}_R \psi_L - m\bar{\psi}_L \psi_R \right] = f_a \partial^{\mu} a - \bar{\psi}_R \gamma_{\mu} \psi_R.$$

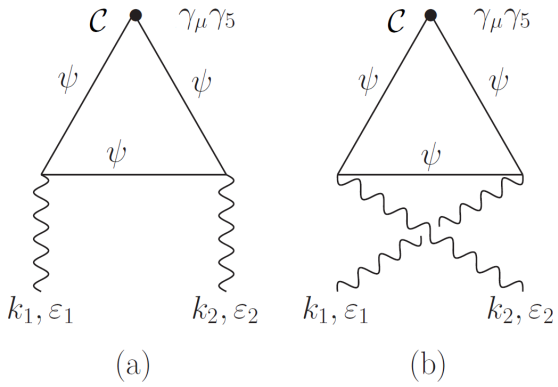

Figure 1.1: The last two terms can be not only obtained by these triangle diagrams but also from Kazuo Fujikawa's path-integral i.e. Eq.(1.38). Only AAA or AVV mode would contribute nonzero amplitude, where the A is axial vector γ_5 and V is a vector. See Eqs.(5-10) in [1].

1.4.1 Axion potential

The detail of the calculation for obtaining the Lagrange Eq.(1.113) is given in 1.3.2. We mainly follow [2] in this section. Including the fermion part, the full Lagrange would be

$$\mathcal{L} \supset \underbrace{\frac{1}{2}(\partial_\mu a)^2}_{\text{from Eq.(1.109)}} + \underbrace{c_q^0 \frac{\partial_\mu a}{f_a} j^\mu_{a,0}}_{\text{from Eq.(1.114)}} + \underbrace{\frac{g_s^2}{16\pi^2}\frac{a}{f_a} G_{\mu\nu}\tilde{G}^{\mu\nu} + \frac{1}{2} g^0_{a\gamma\gamma} a F_{\mu\nu}\tilde{F}^{\mu\nu}}_{\text{from Triangle diagram Fig.4.2}}, \tag{1.113}$$

there has a factor 1/2 difference to Eq.(1) of [2], since a different definition $e^{i\gamma_5 \frac{a(x)}{f_a}}$, where axial current $j^\mu_{a,0} \equiv \bar{q}\gamma^\mu\gamma_5 q$ with a model dependent parameter c_q^0, and the fermion kinetic term under the $U(1)_{PQ}$ transformation, for example,

$$i\bar{q}\gamma^\mu\partial_\mu q \quad \rightarrow \quad i\bar{q}\gamma^\mu\partial_\mu q + \frac{\partial_\mu a}{f_a}\bar{q}\gamma^\mu\partial_\mu q, \tag{1.114}$$

where we used $\{\gamma_\mu, \gamma_5\} = 0$, and $q \to e^{i\gamma_5 \frac{a(x)}{f_a}} q$. The dual gluon field strength $\tilde{G}_{\mu\nu} = \frac{1}{2}\epsilon_{\mu\nu\rho\sigma}G^{\rho\sigma}$, color indices are implicit, and the coupling to the photon field strength $F_{\mu\nu}$ is

$$g^0_{a\gamma\gamma} \equiv \frac{\alpha_{em}}{2\pi f_a}\frac{\mathcal{E}}{\mathcal{C}}, \tag{1.115}$$

where the electromagnetic and the color anomaly ratio: $\mathcal{E}/\mathcal{C} = 8/3$ for a complete $SU(5)$ representation [61] or DFSZ [62], $\mathcal{E}/\mathcal{C} = 0$ for KSVZ [63] (details in Section III.C of [38] and Section 8.1.2 of [39]). Similar to Eq.(1.43), the $\mathcal{E}$ is the EM anomaly

$$\mathcal{E} = 2\mathrm{Tr}Q_a Q^2_{em}. \tag{1.116}$$

In addition, if the quarks transformation under the Yukawa matrix i.e. $\bar{\theta}$ with $U(1)_{PQ}$ and a local $U(1)_A$: $\psi \to e^{i\beta(x)Q_a\gamma_5}\psi$ with redefinition $\beta(x) \equiv a(x)/f_a$ are (similarly Eq.(220) of [44])

$$q = \begin{pmatrix} u \\ \\ d \end{pmatrix} \to e^{i\gamma_5\bar{\theta}Q_a} \begin{pmatrix} u \\ \\ d \end{pmatrix}, \quad \text{and} \quad q = \begin{pmatrix} u \\ \\ d \end{pmatrix} \to e^{i\gamma_5\frac{a}{f_a}Q_a} \begin{pmatrix} u \\ \\ d \end{pmatrix} \tag{1.117}$$

with unitary condition $\mathrm{tr}Q_a = 1$, where $\bar{\theta}$ is the strong CP phase. Then using Eq.(1.38), the Eq.(1.113) becomes

$$\mathcal{L} \supset \frac{1}{2}(\partial_\mu a)^2 + \frac{\partial_\mu a}{f_a} j^\mu_a + \frac{1}{2} a g_{a\gamma\gamma} F_{\mu\nu}\tilde{F}^{\mu\nu} - \bar{q}M_a q + \mathrm{h.c.} \tag{1.118}$$

where

$$g_{a\gamma\gamma} = \frac{\alpha_{em}}{2\pi f_a}\left[\frac{\mathcal{E}}{\mathcal{C}} - 6\,\mathrm{tr}\left(Q_a Q_{em}^2\right)\right], \qquad j_a^\mu = j_{a,0}^\mu - \bar{q}\gamma^\mu\gamma_5 Q_a q,$$
$$M_a = e^{i\left(\bar{\theta}+\frac{a}{f_a}\right)Q_a} M_q e^{i\left(\bar{\theta}+\frac{a}{f_a}\right)Q_a}, \qquad M_q = \begin{pmatrix} m_u & 0 \\ 0 & m_d \end{pmatrix}, \qquad Q_{em} = \begin{pmatrix} \frac{2}{3} & 0 \\ 0 & -\frac{1}{3} \end{pmatrix}, \tag{1.119}$$

where only non-derivative couplings of the axion appear in the quark's mass terms. The important is that the $a\tilde{G}G$ term has been removed, and we have to say those two different bases are *Equivalent* because the rotation(redefinition) Eq.(1.117) is unphysical. In addition, an example for the Q_a as

$$Q_a = \frac{1}{2}\frac{M_q^{-1}}{\mathrm{Tr}M_q^{-1}}, \tag{1.120}$$

see Eq.(50) of [38], in fact, it can be any form e.g. a number Q_a =Diag(X_u, X_d) see Eq.(1.135), it depends on the model. Apply this axial symmetry on the Eq.(1.101) by replacing $M \to M_a$ then considering only 2-flavor $\{u, d\}$ $SU(2)$ effective chiral theory[21], we obtain

$$\mathcal{L} \supset \frac{V^3}{2}\,\mathrm{tr}\left[MU + M^\dagger U^\dagger\right], \tag{1.121}$$

[21] If we do not consider this $SU(2)$ flavor symmetry, the mass term with first order a will provide a potential $V(a) = -\frac{1}{4}m_a^2 f_a^2 \cos(\bar{\theta} + 2a/f_a)$ with the minia $\bar{\theta} = -2\langle a\rangle/f_a$, this exactly cancel the strong CP phase to solve that problem.

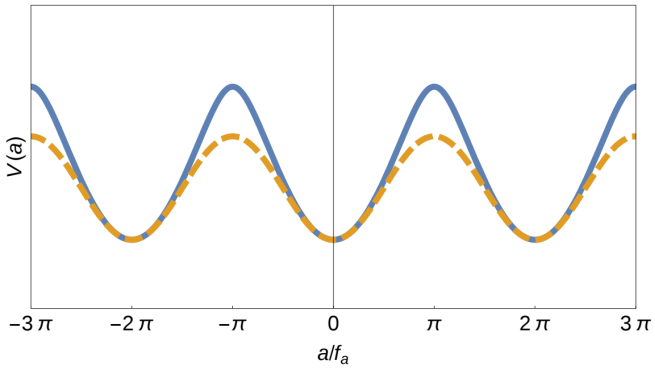

Figure 1.2: This figure is from [2]. Comparison between the axion potential predicted by chiral Lagrangians, Eq.(1.123) (blue solid line) and the single cosine instanton one, $V(a) = -\frac{1}{4}m_a^2 f_a^2 \cos(\mathrm{a})$ with $\mathrm{a} \equiv \bar{\theta} + 2a/f_a$.

where similar to Eq.(1.5) and V^3 at Eq.(1.102),

$$U = e^{i\pi^a \tau^a / F_\pi}, \qquad \pi^a \tau^a = \begin{pmatrix} \pi^0 & \sqrt{2}\pi^+ \\ \sqrt{2}\pi^- & -\pi^0 \end{pmatrix}, \tag{1.122}$$

then do the same as Eq.(1.103), expanding $U \to 1 + i\pi^a \tau^a / F_\pi$ and using M_a in Eq.(1.119),

we have [64] (drop off constant term)

$$\begin{aligned} V(a, \pi^0) &= -V^3 \left[m_u \cos\left(\frac{\pi^0}{F_\pi} - \bar{\theta} - \frac{a}{f_a} \right) + m_d \cos\left(\frac{\pi^0}{F_\pi} + \bar{\theta} + \frac{a}{f_a} \right) \right] \\ &= -m_\pi^2 F_\pi^2 \sqrt{1 - \frac{4 m_u m_d}{(m_u + m_d)^2} \sin^2\left(\bar{\theta} + \frac{a}{f_a} \right)} \cos\left(\frac{\pi^0}{F_\pi} - \phi_a \right), \end{aligned} \tag{1.123}$$

where we defined

$$\tan \phi_a \equiv \frac{m_u - m_d}{m_u + m_d} \tan\left(\bar{\theta} + \frac{a}{f_a} \right). \tag{1.124}$$

As we can see at Eq(1.123) or numerically Fig.(4.3), the minima happen at $\sin^2\left(\bar{\theta}+\frac{a}{f_a}\right)=0$, and $\cos\left(\frac{\pi^0}{f_\pi}-\phi_a\right)=1$ i.e. $\langle\pi^0\rangle=\phi_a F_\pi$, it means that the π^0 vacuum expectation value (VEV) depends on the axion phase. So if we keep $\langle\pi^0\rangle=\phi_a F_\pi$, the potential read as

$$V(a)=-m_\pi^2F_\pi^2\sqrt{1-\frac{4m_um_d}{(m_u+m_d)^2}\sin^2\left(\bar{\theta}+\frac{a}{f_a}\right)}. \tag{1.125}$$

As expected the minimum is at $\langle a\rangle=-\bar{\theta}f_a$ (solving strong CP problem). Just simply expand this within the first order of a, we obtain the well-known formula for the axion mass [65]

$$m_a^2=\frac{1}{2}\frac{m_um_d}{(m_u+m_d)^2}\frac{m_\pi^2F_\pi^2}{f_a^2}=\frac{m_um_d}{(m_u+m_d)^2}\frac{m_\pi^2f_\pi^2}{f_a^2}. \tag{1.126}$$

It is worth mentioning that there would be a 3 by 3 mixing matrix between $\{a,\eta',\pi^0\}$ if a $SU(3)$ $\{u,d,s\}$ chiral Lagrangian was considered i.e. Eq.(1.5), see Eq.(39) in [38] or Section 4 of [33], it solved the $U(1)$ problem. It is worth mentioning that the vacuum of axion $\langle a\rangle$ is called *QCD instanton vacuum* since the non-perturbative instanton effect breaks the axion shift symmetry down to discrete shift symmetry [5, 37]. On the other hand, the $SU(2)_L$ and $U(1)_Y$ were affected by instanton as well, but the effects were suppressed by a factor e.g.

$$V_i(\theta)\propto\cot\theta e^{-S_{\text{inst}}},\qquad\text{with}\qquad S_{\text{inst}}=\frac{8\pi^2}{g_i^2}, \tag{1.127}$$

where $g_s\gg g_1,g_2$, therefore the instanton effects on perturbative theory $SU(2)_L$ and $U(1)_Y$ can be ignored, see Eq.(2.27) in [66] for details. It is worth mentioning that the temperature-

dependent term (Eq.(32) in [67])

$$e^{-S_{\text{inst}}} = e^{-\frac{2\pi}{\alpha_s(T)}} \simeq \left(\frac{\Lambda_{QCD}}{T}\right)^{11-\frac{2}{3}N_f}, \tag{1.128}$$

where N_f is the number of quark flavors with mass less than T.

1.4.2 PQWW/KSVZ/DFSZ Axion Models

- PQWW axion model.

The original axion model is considering a single additional complex scalar field, ϕ, to the SM as a second Higgs doublet, just like 2HDM type(I,II,X,Y). One Higgs couple to u-type quarks, while another couple to d-type quarks. The key point is requiring the quarks transform under the global chiral symmetry $U(1)_{PQ}$, on the other hand, the scalar should rotate the same value on its phase, i.e.

$$q \to e^{i\gamma_5\alpha} q, \qquad H \to e^{i\beta} H, \tag{1.129}$$

where $\alpha = \beta = a/f_a$ at PQ SSB. However, in their model, the symmetry breaking should be at EW scale, i.e. $v_{EW} = f_a = 246\text{GeV}$. Since all the interactions between SM and axion are proportional to at least the order of $1/f_a$, it was excluded by e.g. beam-dump experiments, recently $f_a \geq 10^{12}\text{GeV}$. Under this constraint $f_a \gg v_{EW}$, we call the axion as invisible, e.g. KSVZ and DFSZ models, see Section 2 of [5].

• KSVZ axion model (also called hadronic axion model).

The KSVZ axion model [63] include vector-like heavy quark doublets, Q_L, Q_R, each is in $SU(3)_c$ triplet, the Yukawa term as

$$\mathcal{L}_{KSVZ} = -\lambda_Q \phi \bar{Q}_L Q_R + \text{h.c.}, \tag{1.130}$$

with the global chiral $U(1)_{PQ}$ transformation,

$$Q_L \to e^{i\alpha/2} Q_L, \quad Q_R \to e^{-i\alpha/2} Q_R, \quad \phi \to e^{i\alpha}\phi, \tag{1.131}$$

where the singlet scalar ϕ has to be carried charge 1 under $U(1)_{PQ}$, fermions have charge 1/2. At low energy, after PQ symmetry breaking i.e. redefine the quarks field as,

$$Q_L \to e^{ia/2f_a} Q_L, \quad Q_R \to e^{-ia/2f_a} Q_R, \tag{1.132}$$

then the Lagrangian would be

$$\mathcal{L}_{KSVZ} = -\frac{1}{2}\partial_\mu a \partial^\mu a - \lambda_Q f_a \left(\bar{Q}_L e^{ia/f_a} Q_R + \bar{Q}_R e^{-ia/f_a} Q_L \right) \tag{1.133}$$

where the mass of Q field as $m_Q \sim \lambda_Q f_a \gg v_{EM}$. It suppresses all of the tree-level couplings between axion and SM fields. All SM fermions do **NOT** interact with axion directly. The transformation of field under $U(1)_{PQ}$ are similar to Eq.(1.129).

• DFSZ axion model.

Similar to the PQWW model, the axion couples to the SM via the 2HDM sector, but add an additional singlet complex scalar field ϕ [62],

$$\mathcal{L} \supset \lambda_H \phi^2 H_u^\dagger H_d + \text{h.c.}, \tag{1.134}$$

where ϕ carried charge $-(X_u + X_d)/2$ under $U(1)_{PQ}$, and the Higgs fields have $X_{u,d}$ for each, i.e. (the H_u has additional minus because of duality of $SU(2)_L$)

$$H_u \to e^{-iX_u} H_u, \qquad H_d \to e^{iX_d} H_d, \qquad \phi \to e^{-i(H_u+H_d)/2}\phi \tag{1.135}$$

The transformation of field under $U(1)_{PQ}$ are similar to Eq.(1.129), assuming no charge on left-hand quarks,

$$u_R \to e^{iX_u} u_R, \qquad d_R \to e^{iX_d} d_R, \qquad \ell_R \to e^{-iX_\ell} \ell_R, \tag{1.136}$$

where the ℓ part is flexible, it depends on which type of 2HDM is used. The simplest solution is setting $\{X_u, X_d\} = \{1, 1\}$. On the other hand, the Yukawa as e.g.

$$\mathcal{L} \supset \lambda_u \bar{q}_L H_u u_R + \text{h.c.}, \tag{1.137}$$

it means the SM fermion should be charged under $U(1)_{PQ}$. As the transformation in Eq.(1.129), the interaction between axion and SM fermions after EW SSB, $m_u(a/f_a) i\bar{u}\gamma_5 u$. This term provides the anomaly term i.e. $G\tilde{G}$ term with a triangle diagram. The PQ scale

v_ϕ should be much larger than v_{EM} to avoid experiment constraint. The difference between these two models is that the heavy quarks Q provide anomaly terms on KSVZ, but SM light-fermions provide anomaly terms on DFSZ. In the DFSZ model, all of SM quarks are charged under $U(1)_P Q$, it giving rise to color anomaly $\mathcal{C} = 6$, see Sec.1.4.4 for details.

1.4.3 SM fermions couple to SM

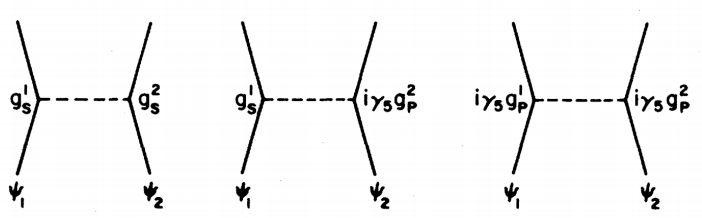

Figure 1.3: Graphs for the potentials [3]. Left to right, monopole-monopole, monopole-dipole, and dipole-dipole.

Mainly follow Section 2.3 of [5], [61], Section 8.1.2 of [39], and more details in Section III.C of [38].

- Couple to fermions, from Eq.(1.114), the interaction is

$$g_{aff} \frac{\partial_\mu a}{f_a} \left(\bar{\psi} \gamma^\mu \gamma_5 \psi \right), \tag{1.138}$$

where γ_5 means that the axion force is *spin-dependent*, see Eq.(6) in [3] as well as Fig.1.3. The potential is only dipole-dipole interaction between particle-i and particle-j,

$$V(r) = \frac{g_i g_j}{16\pi M_i M_j} \left[(\hat{\sigma}_i \cdot \hat{\sigma}_j) \left(\frac{m_a}{r^2} + \frac{1}{r^3} \right) - (\hat{\sigma}_i \cdot \hat{r}) (\hat{\sigma}_j \cdot \hat{r}) \left(\frac{m_a^2}{r} + \frac{3m_a}{r^2} + \frac{3}{r^3} \right) \right] e^{-m_a r}, \tag{1.139}$$

where $\hat{\sigma}$ is a unit vector in the direction of the spin, and $\hat{r}$ is a unit vector along the line of centers. As we can see, the Yukawa-type interaction is suppressed by $e^{-m_a r}$. If we consider the limit $m_a \to 0$, the potential to be $V(r) \propto \frac{1}{r^3}$, it is a short distance force. Thus *NO matter how light the axion, it transmits no long-rangle scalar forces between macroscopic bodies.*

- As an example for axion-SM couplings can be found in Chapter 10.1.1 of [6], considering the DFSZ model as Eq.(1.134) to Eq.(1.137). The effective Lagrangian

$$\mathcal{L}_{int} = i\frac{g_{aNN}}{2m_N}\partial_\mu a\left(\bar{N}\gamma^\mu\gamma_5 N\right) + i\frac{g_{app}}{2m_p}\partial_\mu a\left(\bar{p}\gamma^\mu\gamma_5 p\right) + i\frac{g_{aee}}{2m_e}\partial_\mu a\left(\bar{e}\gamma^\mu\gamma_5 e\right) + g_{a\gamma\gamma}a\vec{E}\cdot\vec{B}; \tag{1.140}$$

with

$$g_{aee} = \left[\frac{X_\ell}{N_{DW}} + \frac{3\alpha_{em}^2}{4\pi}\left(\frac{\mathcal{E}}{N_{DW}}\ln(f_a/m_e) - 1.95\ln(\Lambda_{QCD}/m_e)\right)\right]\frac{m_e}{f_a/N_{DW}}, \tag{1.141}$$

$$g_{a\gamma\gamma} = \frac{\alpha_{em}}{2\pi(f_a/N_{DW})}\left(\frac{\mathcal{E}}{N_{DW}} - 1.95\right), \tag{1.142}$$

$$g_{aNN} = \left[(-F_{A0}+F_{A3})(X_u/2N_{DW}-0.32) - (F_{A0}+F_{A3})(X_d/2N_{DW}-0.18)\right]\frac{m_N}{f_a/N_{DW}}, \tag{1.143}$$

$$g_{aNN} = \left[(-F_{A0}-F_{A3})(X_u/2N_{DW}-0.32) - (F_{A0}-F_{A3})(X_d/2N_{DW}-0.18)\right]\frac{m_p}{f_a/N_{DW}}, \tag{1.144}$$

where $F_{A0} \simeq -0.75$, $F_{A3} \simeq -1.25$ and $\mathcal{E}$ at Eq.(1.116) and $N_{DW} = \mathcal{C}$ at Eq.(1.43). As

above, the axion lifetime is [6]

$$\tau_a = 6.8 \times 10^{24}\text{sec}\frac{(m_a/\text{eV})^{-5}}{[(\mathcal{E}/N_{DW} - 1.95)/0.72]^2}. \tag{1.145}$$

This lifetime is usually longer than the universe's age, thus the axion is a good candidate for dark matter.

1.4.4 Colour Anomaly/Domain Wall Number in Axion Model

Mainly following Section 2.2 [5], Section 7.3 [39] and [61]. Considering Eq.(1.117) and Eq.(1.44), i.e. the $U(1)_{PQ}$ transform as

$$\psi_i \to e^{\pm iQ_i a/f_a}\psi_i, \tag{1.146}$$

where $i = \{L, R\}$, the left and right handed spinor carried opposite $U(1)_{PQ}$ charges. Similar to Eq.(1.41), the matrix Q_i achieve a *colour anomaly* from Eq.(1.43). It turns out that adding a factor on Lagrangian

$$\mathcal{L} \to \mathcal{L} + \frac{\mathcal{C}}{32\pi^2}\frac{a}{f_a}\text{Tr}G_\mu\tilde{G}^{\mu\nu}. \tag{1.147}$$

This factor effectively affects the vacuum energy Eq.(1.125) to (at limit $4m_u m_d/(m_u + m_d)^2 \sim 1$)

$$V(a) \propto -\cos\left(\bar{\theta} + \mathcal{C}\frac{a}{f_a}\right). \tag{1.148}$$

This means that the colour anomaly sets the number of vacua that a has in the range $[0, 2\pi f_a]$. Since the $U(1)_{PQ}$ has the transform symmetry under every 2π shift i.e. $a \to a + 2\pi f_a$, the physics do not charge. Therefore the colour anomaly $\mathcal{C}$ must be an integer [61]. Because the $\mathcal{C}$ corresponds to a number of vacuums during axion shift, it is a number of domain walls i.e. $\mathcal{C} = N_{DW}$. Effectively, it affects the decay constant

$$f_a \to f_a / N_{DW}. \tag{1.149}$$

This also means that the $U(1)_{PQ}$ symmetry was broken into subgroup $Z_{N_{DW}}$, and has degenerated minima at $a = 0, 2\pi/N_{DW}, \cdots, 2\pi(N_{DW} - 1)/N_{DW}$. For example:

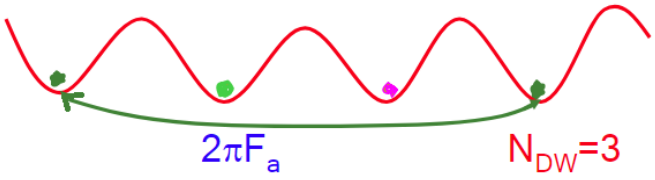

Therefore, Eq.(1.126) can be rewrote as

$$m_a^2 = \frac{m_\pi^2 f_\pi^2}{(f_a/N_{DW})^2} \frac{m_u m_d}{(m_u + m_d)^2} \left\{ 1 + \frac{m_\pi^2}{m_\eta^2} \left[-1 + \mathcal{O}\left(1 - \frac{m_\pi}{m_\eta} \right) \right] \right\} \tag{1.150}$$

where the NLO is considered. This talk to us that if these mesons $\{\eta', \pi\}$ carried the same masses, the axion should be massless. Numerically,

$$m_a \simeq 6 \times 10^{-6}\,\text{eV} \left(\frac{10^{12}\,\text{GeV}}{f_a/N_{DW}} \right). \tag{1.151}$$

• For the Domain Wall number for $U(1)_{PQ}SU(3)_c^2$ [10], from Eq.(1.43) we have (it is the same as the calculation on anomaly cancellation)

$$N_{DW} = \left| 2\sum_{i=L} \mathrm{Tr}\left[Q_{PQ}(q_i)T_a^2(q_i)\right] - 2\sum_{i=R} \mathrm{Tr}\left[Q_{PQ}(q_i)T_a^2(q_i)\right] \right|, \tag{1.152}$$

where $Q_{PQ}(q_i)$ is the $U(1)_{PQ}$ charge for each quark species q_i, and T_a are the generators of $SU(3)_c$ normalized such that $\mathrm{Tr}[T_aT_b] = I\delta_{ab}$ where $I = 1/2$ for fundamental representation of $SU(3)_c$. If we choose the unit $Q_{PQ} = 1$ for the minimum non-vanishing magnitude of PQ quantum numbers. In $KSVZ$ models, from Eq.(1.132) we obtain

$$N_{DW}^{KSVZ} = \left| 2 \times \frac{1}{2} \times \frac{1}{2} - 2 \times \left(-\frac{1}{2}\right) \times \frac{1}{2} \right| = 1, \tag{1.153}$$

while in the $DFSZ$ models, from Eq.(1.136) with $X_u = X_d = 1$,

$$N_{DW}^{DFSZ} = \left| 0 - 2 \sum_{u_R,c_R,t_R} \times 1 \times \frac{1}{2} - 2 \sum_{d_R,s_R,b_R} \times 1 \times \frac{1}{2} \right| = 6. \tag{1.154}$$

It is exactly a number of families. As above, the domain wall number is just the non-canceled ($N_{DW} \neq 0$) anomaly cancellation.

1.5 Axion: Cosmology

Figure 1.4: The PQ complex scalar potential with PQ symmetry breaking, the figure is cited from [4].

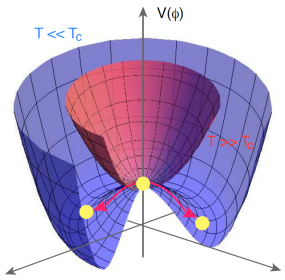

The PQ scalar field ϕ has the Lagrangian, (see Section.3 in [4])

$$\mathcal{L} = \frac{1}{2}|\partial_\mu \phi|^2 - V_{\text{eff}}\left(\phi, T\right), \tag{1.155}$$

where

$$V_{\text{eff}}\left(\phi, T\right) = \frac{\lambda}{4}\left(|\phi|^2 - \eta^2\right)^2 + \frac{\lambda}{6}T^2|\phi|^2. \tag{1.156}$$

This Lagrangian is invariant under global $U(1)_{PQ}$ transformation, $\phi \to \phi e^{i\alpha}$. At high temperature $T > T_c \equiv \sqrt{3}\eta$, the potential has the minimum at $\phi = 0$ and the vacuum has the $U(1)_{PQ}$ symmetry. Then as the cosmic temperature decreases to $T < T_c$, the PQ scalar ϕ obtains vacuum expectation value $|\phi| = \eta$. The axion a is a Goldstone boson associated with this $U(1)_{PQ}$ SSB. Recalling Eq.(1.148), the instanton vacuum $\langle a \rangle$ would cancel the strong CP phase $\bar{\theta}$, leave the field term only i.e.

$$V(a) = \frac{m_a^2 \eta^2}{N_{DW}^2}\left(1 - \cos\frac{N_{DW}a}{\eta}\right), \tag{1.157}$$

where axion mass m_a is temperature dependent, i.e. [68] or Eq.(10.26) of [6]

$$m_a(T) \simeq \begin{cases} 4.05 \times 10^{-4} \times \dfrac{\Lambda_{QCD}^2}{f_a} \left(\dfrac{T}{\Lambda_{QCD}} \right)^{-3.34} & T > 0.26\Lambda_{QCD}, \\ 3.82 \times 10^{-2} \times \dfrac{\Lambda_{QCD}^2}{f_a} & T < 0.26\Lambda_{QCD}, \end{cases} \tag{1.158}$$

where $\Lambda_{QCD} \simeq 400$MeV, and recall to Eq.(1.149) we have $f_a = \eta/N_{DW}$. This is like Eq.(1.149), in the following section, we used $f_a \equiv \eta/N_{DW}$. More clear discussion of this $m_a(T)$ can be also found at [69].

1.5.1 The Kibble Mechanism

During a cosmological phase transition any correlation length is always limited by the particle horizon, see Chapter 7.5 of [6]. The particle horizon is at Chapter 2.2 of [6], it is the maximum distance a massless particle can propagate since the time of the big bang, i.e.

$$d_H(t) = R(t) \int_0^t \frac{dt'}{R(t')} \leq \frac{1}{H(t)} \simeq \frac{T^2}{m_{pl}}. \tag{1.159}$$

If $R \propto t^n$ with $n > 1$, then we have $d_H = t/(1-n)$. Any physical length/correlation length cannot be longer than $d_H(t)$.

1.5.2 Misalignment Mechanism

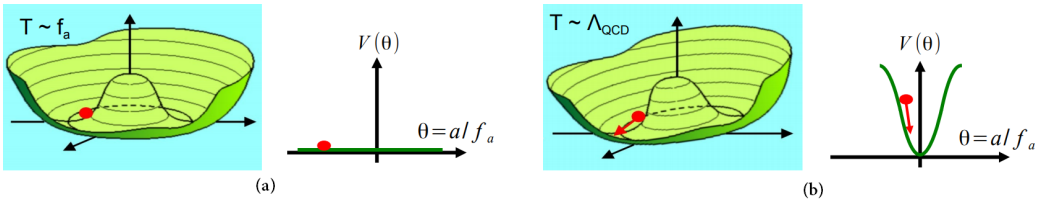

At beginning $T \gg f_a$, the potential is Eq.(1.156). Following the cooling universe in Refs.[70, 71, 72], at the temperature $T \sim f_a$ the $U(1)_{PQ}$ symmetry broken, then the Goldstone axion moving in the circle, shown as (a). However, at $T \sim \Lambda_{QCD} \ll f_a$, instanton break the shift symmetry of axion, the potential looks like (b), i.e. as Eq.(1.125) with $m_a \ll f_a$,

$$V(a) = m_a^2 f_a^2 \left[1 - \cos\left(\frac{a}{f_a}\right)\right] \simeq \frac{1}{2} m_a^2 a^2 + \cdots . \tag{1.160}$$

But the axion is not just rolling down to the minimum, it is oscillating around the minimum point, this motion is called coherent axion oscillation. The oscillation happen when $m_a(T_1) \simeq 3H(T_1)$ (see Eq.(1.170)), this correspond to $T \sim T_1 \sim$ GeV, i.e. radiation dominated era the $H \propto \frac{1}{t} \propto T^2$ [73]. On the other hand, Eq.(1.158) shows $m_a(T) \propto 1/T^{3.34}$. Therefore the fraction term in Eq.(1.162) can be ignored by $H(T) \ll m_a(T)$ at a later time $T \ll T_1$. The Eq.(1.162) can be rewrote as (more precise calculations in [67, 70, 71, 72])

$$\begin{aligned} &\ddot{a} + 3H\dot{a} + V'(a) = 0 \\ &\rightarrow \quad \ddot{a} + m_a^2 a \simeq 0 \quad \rightarrow \quad a(t) = A(t)\cos\left(m_a t + C\right) \quad \text{with} \quad A(t) \sim A \ll f_a, \end{aligned} \tag{1.161}$$

where A and C are constants depends on initial conditions θ_1 and T_1. This is called an Adiabatic condition. Axion is fixed at $\theta \sim 0$, therefore $A \ll f_a$. Kinetic energy can be ignored (substitute this solution back to Lagrange) when axion reaches the minimum, the energy density from Eq.(1.163) will be approximated to $\rho_a \simeq \frac{1}{2} m_a^2 a^2$, it associated density as shown in Eq.(1.177), see also [70, 71, 72, 7]. Since the coherent axion will condensate, it can be cold DM even if it is super light. [74]

1.5.3 Abundance of the Axion

Axion Density in Misalignment Mechanism

The calculations in this section are following Section 4.2 of [5]. The axion equation of motion on FRW metric reads, (This equation of motion ONLY valid when $|\theta| = |a/f_a| \lesssim 1$ in Eq.(1.160))

$$\ddot{a} + 3H\dot{a} + m_a^2 a = 0. \tag{1.162}$$

where the space term $\nabla_x^2 a(x)$ is ignored, see Eq.(29) of [67]. The background energy density and pressure of the axion field are:

$$\rho_a = \frac{1}{2}\dot{a}^2 + \frac{1}{2} m_a^2 a^2, \qquad P_a = \frac{1}{2}\dot{a}^2 - \frac{1}{2} m_a^2 a^2. \tag{1.163}$$

The general at the matter or radiation dominated universe $R(t) \propto t^p$. In this era, the field has an exact solution:

$$a = R^{-3/2} \left(t/t_i\right)^{1/2} \left[C_1 J_n(m_a t) + C_2 Y_n(m_a t)\right], \tag{1.164}$$

where $n = (3p-1)/2$, $J_n(x)$ and $Y_n(x)$ are Bessel functions of the first and second kind, and the t_i is the initial time. The initial conditions are when $H(t_i) \gg m_a$:

$$a(t_i) = f_a \theta_{a,i}, \qquad \dot{a}(t_i) = 0, \tag{1.165}$$

where $\theta_a \equiv \langle a \rangle / f_a$ is at Eq.(1.183). The numerical solution is shown in Fig.4.6.

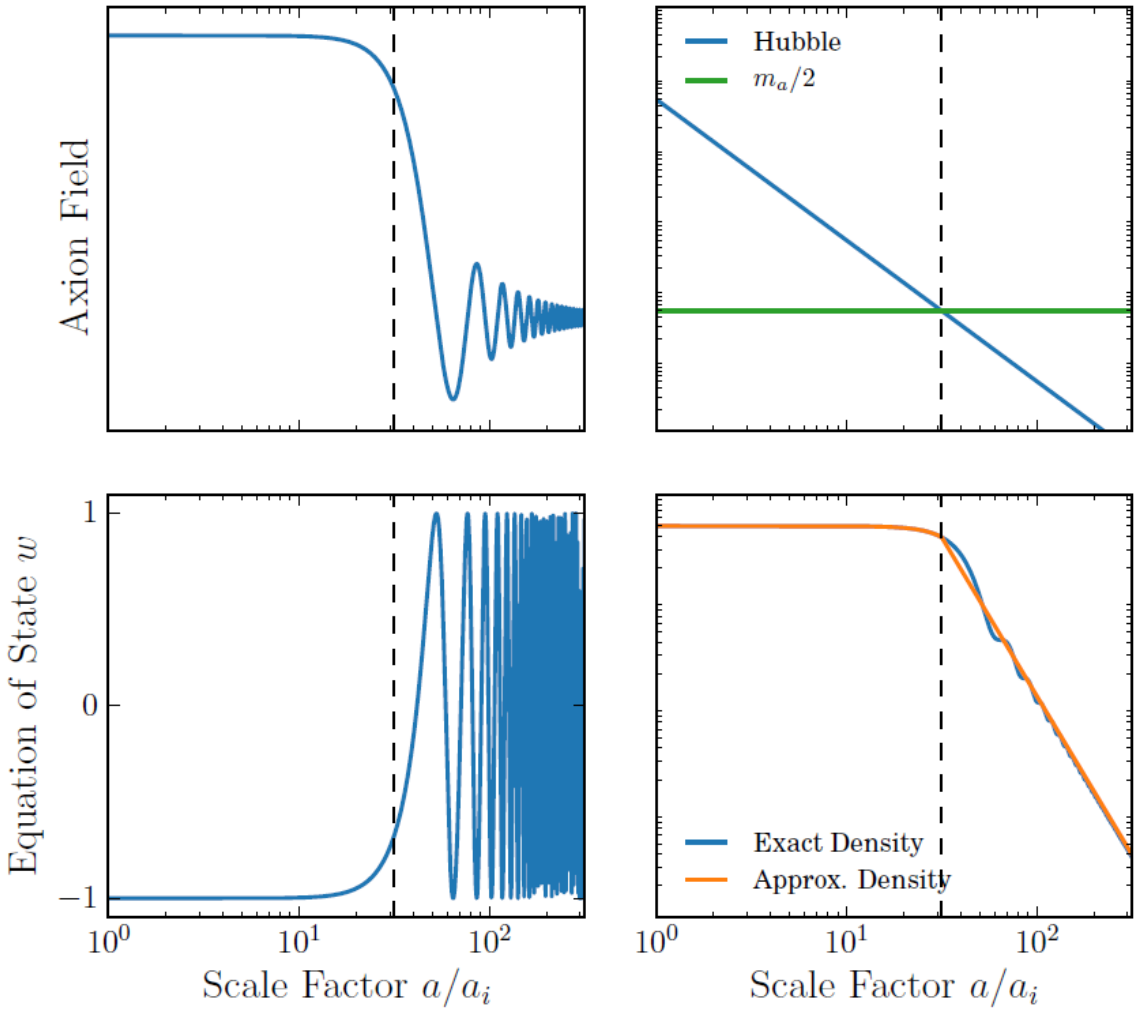

Figure 1.5: This shows Eq.(1.164) with $p = 1/2$. This is from Figure 4 of [5]. Vertical dashed lines show the condition defining $A \equiv m_a/H(R_{\rm osc}) \equiv 2$ as condition in Eq.(1.162) and Eq.(1.163), also used the approximation $\rho_a(R) = \rho_a(R_{\rm osc})(R_{\rm osc}/R)^3$ when $(R > R_{\rm osc})$ as well as $\rho_a(R_{\rm osc}) \simeq m_a^2 a_i^2/2$, hence the axion energy density is controlled by initial conditions. The right-down shows a comparison of $A = 2$ and is fully numerical. On the other hand, if we consider $A = 3$ the result can be fit very well as $A = 2$ did. The important things are (1) upper-left, the axion field frozen when m_a is in of scale-regime ($H > m_a$, see upper-right). (2) lower-right, the axion energy density decays shortly once enters to scale regime.

In initial conditions Eq.(1.165), the factor $C_2 \to 0$. The potential term in Eq.1.163 to be dominated until the oscillation occurs at $T_{\rm OSC}$, namely, the relation holds $3H(T_{\rm OSC}) \simeq m_a(T_{\rm OSC})$. On the other hand, if there has an initial velocity of the field at an early time

e.g. $\dot{a} \sim H(T = f_a)^2$ or the condition when two terms are comparable at QCD phase transition time i.e. $3H\dot{a} \overset{T\sim\Lambda_{\rm QCD}}{\sim} m_a^2 a$, the solution will be different $C_1 \to 0$. The axion will be $w = +1$ during $T > T_{\rm OSC}$, then oscillating at low temperature as usual. This situation can be built by that the early axion was emitted by a cosmic string, those axions have high kinetic energy. A non-zero initial velocity of field is assumed in this reference [75].

By the way, in the limit $m_a t \to 0$, the Eq.(1.164) can be simplified by

$$R^{-3/2}(t/t_i)^{1/2} J_n(m_a t) \sim \text{constant}, \qquad R^{-3/2}(t/t_i)^{1/2} Y_n(m_a t) \propto \frac{1}{\sqrt{m_a t}}. \tag{1.166}$$

So the energy density ρ_a in Eq.(1.163) would be decreasing as $w = +1$, if C_2 is dominated. The $w \equiv P_a/\rho_a$ is the Equation of state. On the other hand, in the limit $m_a t \to \infty$, the asymptotic form reads

$$J_\alpha(z \to \infty) = \sqrt{\frac{2}{\pi z}} \cos\left(z - \frac{\alpha\pi}{2} - \frac{\pi}{4}\right), \qquad Y_\alpha(z \to \infty) = \sqrt{\frac{2}{\pi z}} \sin\left(z - \frac{\alpha\pi}{2} - \frac{\pi}{4}\right). \tag{1.167}$$

So the field solution on Eq.(1.164),

$$a \simeq R^{-3/2} \sqrt{\frac{2}{\pi m_a t_i}} \left(C_1 \cos(m_a t) + C_2 \sin(m_a t)\right). \tag{1.168}$$

The constants C_1 and C_2 from initial conditions Eq.(1.165) with $p = 1/2$ reads

$$C_1 \simeq f_a \theta_{a,i}/27, \qquad C_2 \simeq 0. \tag{1.169}$$

• The history of the axion field is given:

1. At early times when $H > m_a$, the axion field is overdamped and is frozen at its initial value by Hubble friction. The equation of state at early times is $\omega_a = -1$, and it behaves as a contribution to the vacuum energy, see the left-down in Fig.4.6. However, the length of this period depends on the ratio H/m_a when the axion comes to dominate the energy density.

2. Later time, when $H < m_a$ the axion field is underdamped and oscillating. **The equation of state oscillates around $\omega_a = 0$ (after averaged), that's the reason why the axion can work like ordinary matter**, see the left-down in Fig.4.6. It becomes a DM candidate. By the way, the Hubble rate at matter-radiation equality in ΛCDM is approximately $H(a_{eq}) \sim 10^{-28}$eV.

3. For the solution of $H \simeq m_a$ at QCD phase transition (see Chapter 10.3.2 in [6] for more details) i.e. Cold QCD Axion with peV $\lesssim m_a \lesssim \mu$eV and $f_a \gtrsim 10^{12}$ GeV, using the condition $A = 3$ i.e. $m_a(T_1) = 3H(T_1)$ where T_1 corresponds to QCD phase transition, which is the temperature when oscillation starts. Then using Eq.(1.158), we have[22] [4]:

$$T_1 = 0.98 \text{ GeV} \left(\frac{F_a}{10^{12} \text{ GeV}}\right)^{-0.19} \left(\frac{\Lambda_{QCD}}{400 \text{ MeV}}\right). \tag{1.170}$$

where the simplest Cold Axion model is considered i.e. Eq.(1.160) instead of Eq.(1.123). In

[22]Since matter-radiation equality at $T \simeq 0.75$eV, we use radiation domination in this calculation, i.e. $H = 1.66 g_*(T)^{1/2} T^2/m_{pl}$, see Eq.(A5) in [76].

short, the story is that

Axion freeze out at $H \gg m_a$with field value $a \sim f_a$
$\downarrow$
Axionenergy density start to decay as $\rho \propto R^{-3}$when $H \sim m_a$
$\downarrow$
Since astrongoscillationbetween $\omega = \pm 1$, axion is averagely matter-like $\langle \omega \rangle = 0$

- **Adiabatic condition at late time of universe** $H \ll m_a$

Again, using Eq.(1.162) and Eq.(1.163), see details in Section.3.2.1 of [4]. we have

$$\begin{aligned}\dot{\rho}_a &\overset{1.163}{=} \ddot{a}\dot{a} + \dot{m}_a m_a a^2 + m_a^2 \dot{a} a \\ &\overset{1.162}{=} \left(-H\dot{a} - m_a^2 a\right)\dot{a} + \dot{m}_a m_a a^2 + m_a^2 \dot{a} a \\ &= -3H\dot{a}^2 + \dot{m}_a m_a a^2. \end{aligned} \tag{1.171}$$

Since the potential varies much slower than the field itself (i.e. $H, \dot{m}_a/m_a \ll m_a$) [77], we can use the so-called adiabatic invariant theorem (is a WKB approximation [5]), the area in the phase space swept by the periodic motion is unchanged per one axion oscillation [77, 38]. In this case, the Eq.(1.162) can be rewrite as

$$\ddot{a} + 3H\dot{a} + m_a^2 a \;\rightarrow\; \ddot{a} + m_a^2 a = 0, \tag{1.172}$$

so the ansatz solution reads as Eq.(1.161) (Eq.(62) of [5])

$$a(t) = \mathcal{A}(t)\cos\left(m_a t + \theta\right), \tag{1.173}$$

where θ is an arbitrary phase, and using Eq.(1.162) we obtain $\mathcal{A} \propto a^{3/2}$ in RD is slowly varying such that $\dot{\mathcal{A}}/m_a \sim H/m_a \ll 1$. So we have approximately

$$\dot{a}^2 \simeq m_a^2\left(\mathcal{A}^2 - a^2\right). \tag{1.174}$$

The basis of this ansatz solution, we obtain the time-invariant quantity as [4]

$$\frac{\rho_a R^3}{m_a} = \text{constant}. \tag{1.175}$$

The solution with this theorem is shown as the number to entropy ratio [76, 77, 4] (since $s \propto R^{-3}$)

$$Y_a^{\text{cold}} = \frac{n_{a,0}}{s_0} = \beta\left(\frac{\rho_a/m_a}{s}\right)_{T=T_1}, \tag{1.176}$$

where s is the entropy density and s_0 is its present value. The $\beta = 1.85$ [77] is a correction factor from anharmonic terms in axion potential. The anharmonic is just the ratio of the axion energy density obtained by using e.g. $V'(a) = m^2/N\sin(Na)$, to that obtained using the linearized form $V'(a) = m_a^2 a^2$ i.e. higher order terms effect (see Figure 4 in [76]). The numerical result for present cold axion density is given [Anthropic window, i.e. SSB-f_a

before end of inflation]

$$\Omega_a h^2 = 0.18\,\theta_1^2 \left(\frac{f_a}{10^{12}\,\mathrm{GeV}}\right)^{1.19} \left(\frac{\Lambda_{QCD}}{400\,\mathrm{MeV}}\right), \tag{1.177}$$

where we assume that the late-time entropy production after the QCD phase transition is neglected [**?**], and the misalignment mechanism was considered. The $\theta_1 \equiv a_1/\eta$ with $(f_a = \eta/N_{DW})$ is the initial angle at the start of oscillation, see Eq.(1.183). We know the energy density is proportional to $\rho_a \propto V_a \propto m_a^2 f_a^2$, then we know $m_a \propto 1/f_a$. It seems the energy density should be independent to f_a or m_a, however, check the temperature dependence (Eq.(1.158)):

$$m_a(T) \propto \frac{1}{f_a} T^{-n}, \tag{1.178}$$

we also know the temperature

$$3H \simeq m_a(T) \quad \rightarrow \quad \frac{1}{t} \propto T^2 \propto \frac{1}{f_a} T^{-n} \quad \rightarrow \quad f_a \propto T^{-2-n}. \tag{1.179}$$

Then we obtain

$$\rho_a(t_0) = m_a^2(T) f_a^2 \frac{m_a(T=0)}{m_a(T)} \propto T^{-n} \propto f_a^{\frac{n}{2+n}} \propto f_a^{0.625}, \tag{1.180}$$

where $n_a = m_a^2(T) f_a^2 / m_a(T)$ is the number of axions at starting of the oscillation, we also assume that the axion mass changes adiabatically, the number density is conserved. So the

relic density is expressed

$$\Omega_a = \frac{\rho_a(t_0)}{s(T)} \times \frac{s_0}{\rho_0} \propto f_a^{\frac{n}{2+n}} \times T^{-3} \propto f_a^{\frac{n}{2+n}+\frac{3}{2+n}} = f_a^{1.187}, \tag{1.181}$$

where $n = 3.34$ is the QCD axion. [This is how we calculate the Eq.(1.177)]

Axion Isocurvature condition

- If the $U(1)_{PQ}$ SSB after the inflation, we called classic window,

$$f_a < \text{Max}\left[\frac{H_I}{2\pi}, T_{\text{max}}\right], \tag{1.182}$$

where H_I is Hubble parameter during inflation, the T_{max} is maximum temperature after inflation. In this case, the θ_1 is random in the whole space, then we should replace with its spatial average, namely, (Eq.(16) in [78] or Eq.(10.48) in [6])

$$\theta_1^2 \to \langle\theta_1^2\rangle = \frac{c_{\text{anh}}}{2\pi}\int_{-\pi}^{\pi}\theta_1^2 d\theta_1 \simeq c_{\text{anh}}\pi^2/3 \sim 6.85, \tag{1.183}$$

where $c_{\text{anh}} \sim 2$ is the anharmonic correction [77]. The picture of the universe is shown in Fig.1.6.

- If the $U(1)_{PQ}$ SSB before the inflation, we called anthropic window,

$$f_a > \text{Max}\left[\frac{H_I}{2\pi}, T_{\text{max}}\right], \tag{1.184}$$

The θ_1 takes the same value in the whole space, it becomes a free parameter. In this case,

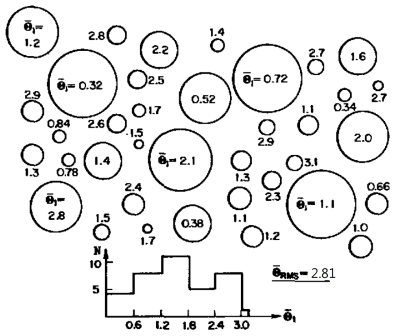

Figure 1.6: Distribution of $|\theta_1|$ in an inflationary Universe, this from Fig. 10.9 of [6].

$\Omega_a h^2$ depends strongly on initial conditions.

In particular, the density of this coherent axion oscillation (Misalignment mechanism) cannot exceed the present DM density i.e. $\Omega_a h^2 \leq \Omega_{\rm CDM} h^2 \simeq 0.11$. If the $U(1)_{PQ}$ SSB after inflation, we obtain an upper bound on

$$f_a \lesssim 1.4 \times 10^{11}\ {\rm GeV}, \tag{1.185}$$

this is the bound from cosmic string radiation. But from PQ-SSB axion is at Figure.5 in [5], the bound on f_a depends on the mass of axion m_a.

Isocurvature bound is from the uniformless that is caused by inflation, which is only applicable when the PQ-SSB is earlier than inflation i.e. the anthropic window. It happens when you have massless particles that have independent quantum fluctuations vs. an inflaton field.

Thermal production of axion

4. For the case $H \gg m_a$ on all period, namely, Hot Axion with $m_a \lesssim$ keV and $10^6\,\text{GeV} \lesssim f_a \lesssim 10^8\,\text{GeV}$. Follow the Lagrangian

$$\begin{aligned}\mathcal{L}_{\text{interation}} = &-\frac{\alpha_s}{8\pi f_a} G^a_{\mu\nu}\tilde{G}^a_{\mu\nu}a - \frac{C_\gamma \alpha_{em}}{8\pi f_a} F_{\mu\nu}\tilde{F}^{\mu\nu}a \\ &+ \frac{C_i}{2f_a}\bar{\Psi}_i\gamma^\mu\gamma_5\Psi_j\partial_\mu a + \frac{C_\pi}{f_a f_\pi}\left(\pi^+\pi^0\partial^\mu\pi^- + \cdots\right)\partial_\mu a + \cdots,\end{aligned}$$

where the Ψ_i are SM fermions, and C_γ, C_i are model-dependent parameters, see [38, 39]. In the following we set $C_\gamma = C_i = 0$. The axion production rate is dominated by these processes as shown in Fig.(4.9).

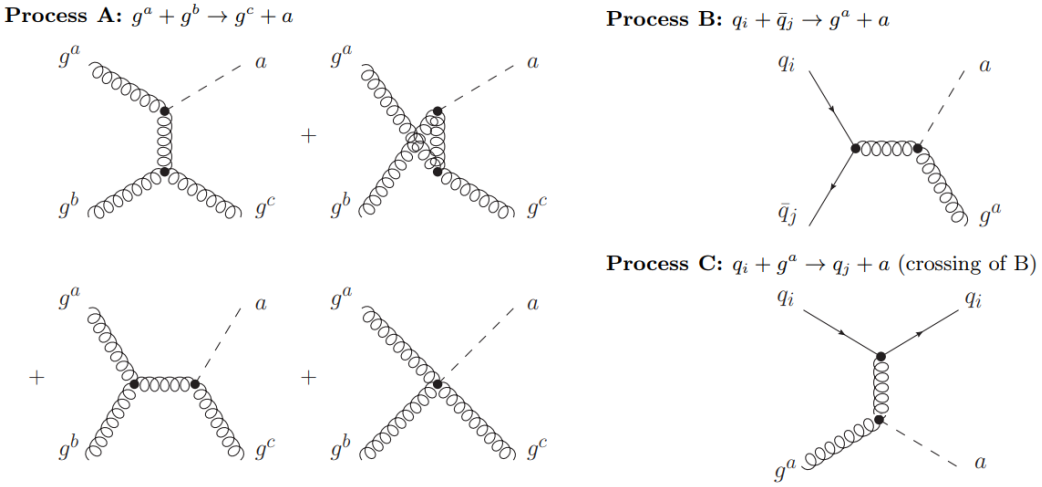

Figure 1.7: The axion production from gluon collision [7].

Those processes correspond to the amplitudes (see Table. I in [7]),

$$|\mathcal{M}_A|^2 = -\frac{g_s^6}{32\pi^4 f_a^2}\frac{(s^2+st+t^2)^2}{st(s+t)}|f^{abc}|^2, \tag{1.186}$$

$$|\mathcal{M}_B|^2 = \frac{g_s^6}{128\pi^4 f_a^2}\left(2\frac{t^2}{s}+2t+s\right)|T^a_{ji}|^2, \tag{1.187}$$

$$|\mathcal{M}_C|^2 = -\frac{g_s^6}{128\pi^4 f_a^2}\left(2\frac{s^2}{t}+2s+t\right)|T^a_{ji}|^2, \tag{1.188}$$

where gluons g^a carried the color index a, then f^{abc} and T^a_{ji} are SU(N_C) color matrces. Then the Boltzmann equation is

$$\frac{dn_a}{dt} + 3Hn_a = -\langle\sigma_a|v|\rangle\left[n_a^2 - \left(n_a^{EQ}\right)^2\right] = W_a \tag{1.189}$$

where using Eq.(5.23) in [6],

$$W_a = \frac{\xi(3)g_s^6T^6}{64\pi^7 f_a^2}\left[\ln\left(\frac{T^2}{m_g^2}+0.406\right)\right], \tag{1.190}$$

where $m_g = g_sT\sqrt{N_c+(n_f/2)}/3$, σ_a is cross-section of axion production. The easier way to find the number to entropy ratio is using Eq.(1.189) with $Y \equiv n_a/s$

$$\frac{dY}{dt} = \frac{dn_a}{dt}\frac{1}{s} - n_a\frac{ds}{dt}\frac{1}{s^2} = \frac{dn_a}{dt}\frac{1}{s} + n_a3H\frac{1}{s} = \left(\frac{dn_a}{dt}+3Hn_a\right)\times\frac{1}{s} = \frac{W_a}{s}, \tag{1.191}$$

where we used $s \propto R^{-3}$ and $H \equiv \dot{R}/R$. If we set the initial condition $Y(T_R) = 0$, where T_R is reheating temperature after inflation, and assumed that axions were never in the thermal

equilibrium with the primordial plasma. So we obtain the relic axion today

$$Y_a^{\rm TP} = \int_{T_{m,\gamma}}^{T_R} dT \frac{W_a(T)}{Ts(T)H(T)} = 18.6\, g_s^6 \ln\left(\frac{1.501}{g_s}\right)\left(\frac{10^{10}\,\text{GeV}}{f_a}\right)^2\left(\frac{T_R}{10^{10}\,\text{GeV}}\right), \quad (1.192)$$

where $T_{m,\gamma}$ is the matter-radiation equality temperature. This is only valid when axion disappearance processes can be neglected, i.e. $T_R < T_D$ and the axion is out of thermal equilibrium. However, if the decoupling temperature is lower the reheating temperature, i.e. $T_R > T_D$, the disappearance processes have to be taken into account, namely, the axion is within thermal equilibrium unit $T \sim T_D$ its behaver is the same as hot thermal relics, the resent yield of that thermal relic axion is then given by[23] $Y_a^{EQ} = n_a^{EQ}/s \simeq 2.6 \times 10^{-3}$. The decoupling temperature T_D can be found by [79], for process $a + j \leftrightarrow 1 + 2$,

$$\begin{aligned}\sqrt{\frac{4\pi^3}{45}g_*(T)}\frac{T^2}{M_{pl}} = H \simeq \Gamma_a &= \frac{1}{n_a^{EQ}}\int \frac{d^3p_a}{(2\pi^3)2E_a}\frac{d^3p_j}{(2\pi^3)2E_j} f_a^{EQ} f_j^{EQ}\ (\sigma_{a+j\leftrightarrow 1+2}\, v\, 2E_a 2E_j) \\ &= n_j\langle\sigma|v|\rangle,\end{aligned}$$

then obtain numerically [7]

$$T_D \simeq 9.6\times 10^6\,\text{GeV}\left(\frac{f_a}{10^{10}\,\text{GeV}}\right)^{2.246}. \quad (1.193)$$

Finally, the density from Thermal Production rate:

$$\Omega_a^{\rm TP}h^2 \simeq \sqrt{\langle p_{a,0}\rangle^2 + m_a^2}\, Y_a^{\rm TP}(\infty)s(T_0)h^2/\rho_c, \quad (1.194)$$

[23] Using Fig.3.5 and Eq.(5.27) in [6] $Y_\infty = Y_{EQ}(x_f) = 0.278 g_{\rm eff}/g_{*S}(x_f)$ with $g_{\rm eff} \sim 1$ and $g_{*S}(x_f) \sim 100$.

where the present average momentum $\langle p_{a,0}\rangle = 2.701\, T_{a,0}$ given by the present axion temperature $T_{a,0} = 0.332\, T_0 \simeq 0.332 \times 0.235 = 0.08\text{meV}$ [7]. The axion mass is at Eq.(1.151). As above we have: [7]

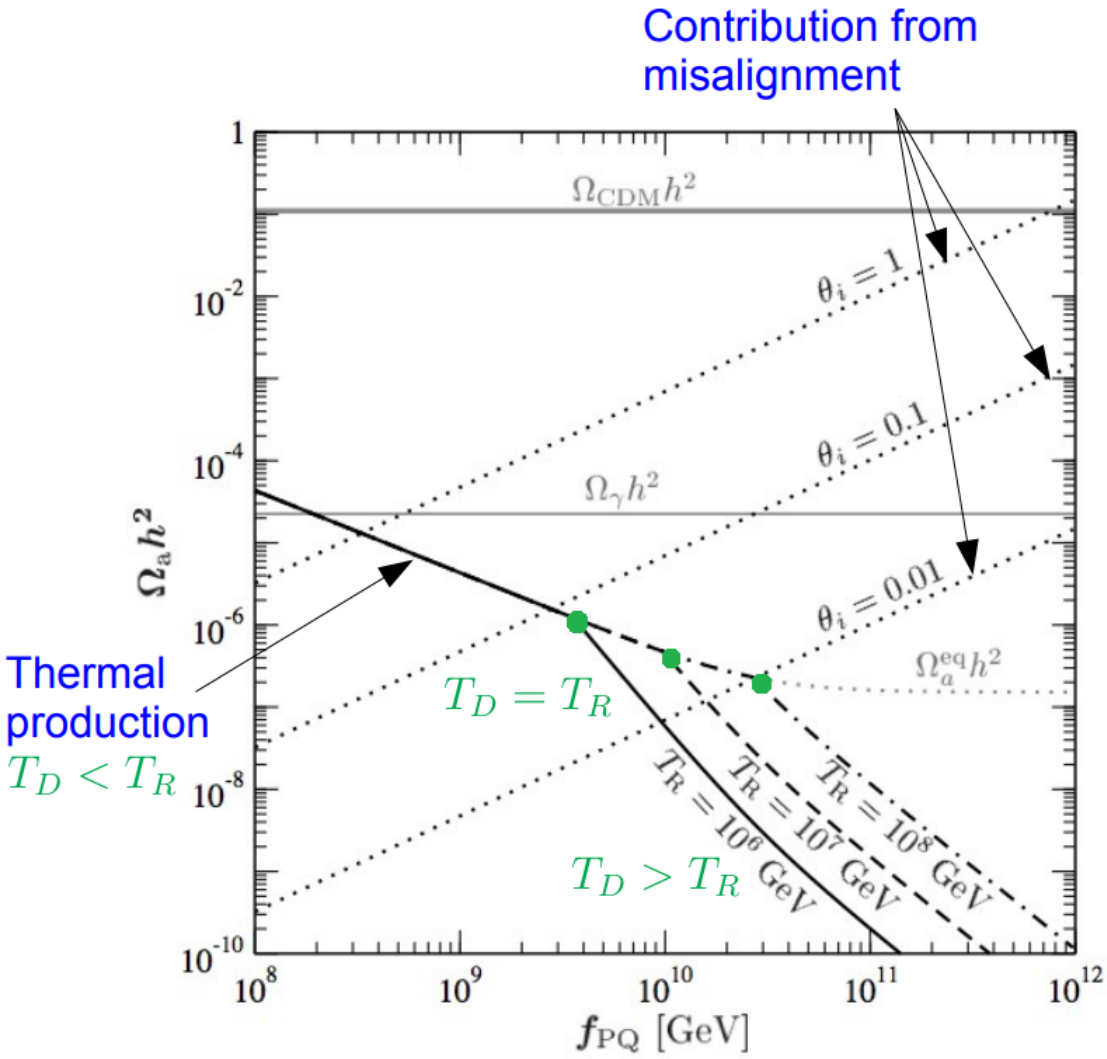

As we see, the Thermal production of axion is negligible, but it may not be the case if nonzero C_γ and C_i were considered (still an open question). In addition, the axion condensate from the misalignment mechanism is considered as well (the dotted lines), see

Eq.(1.177). Thus total density would be

$$\Omega_a h^2 = \Omega_a^{\rm MIS} h^2 + \Omega_a^{\rm TP} h^2, \tag{1.195}$$

where we set $\Omega_a^{\rm MIS} = \Omega_a^{\rm Eq.1.177}$.

1.5.4 Axion Strings and Domain Walls

The potential at Eq.(1.156) and Eq.(1.157) give a total potential at $T \to 0$ limit [10]

$$V(\phi) = \frac{\lambda}{4}\left(|\phi|^2 - \eta^2\right)^2 + \frac{m_a^2 \eta^2}{N_{DW}^2}\left[1 - \cos\left(N_{DW}\theta\right)\right], \quad \text{with} \quad \theta \equiv \frac{a}{\eta}. \tag{1.196}$$

At the G (see Eq.(1.107)) PQ-scalar symmetry breaking, the $\langle\phi\rangle = \eta$, the cosmic strings are formed. Then the phase part of ϕ became axion i.e. $\phi \to \eta e^{ia/\eta}$. Then the second term in Eq.(1.196) is from instanton vacuum which breaks the $U(1)_{PQ}$ into its subgroup $Z_{N_{DW}}$ (it is the symmetry only if the minima at the original point of the potential, see note.20). Furthermore, this term becomes non-negligible when the mass of the axion is lager then the friction of cosmic expansion, i.e. $m_a \gtrsim H$ from Friedmann equations, see details in Section.4 of [5].

The calculations are mainly following [80]. Since the $m_a(T)$ and $\eta(T)$ are temperature dependent, the second term in Eq.(1.196) can be write as

$$V(\phi, a) \to \frac{\lambda}{4}\left(|\phi|^2 - \eta^2\right)^2 + \chi(T)\left[1 - \cos(N_{DW}\theta)\right], \tag{1.197}$$

where $\chi(T) = m_a^2(T) f_a^2(T)$ with $f_a \equiv \eta / N_{DW}$ is a calculable temperature-dependent topological susceptibility of QCD, which is not determined at high-temperature [81, 2]. Form Figure.1 of [80]:

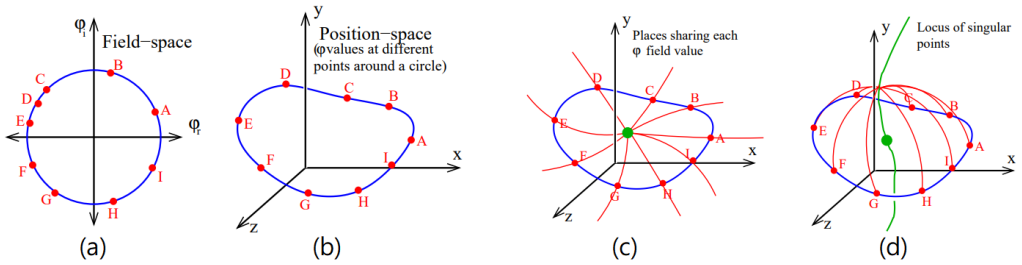

At $T > \Lambda_{QCD}$, before axion shift symmetry breaking, figure (a) shows a series of points along the minimum of the potential in field-space, they can be mapped onto a loop in position-space (b). Then at $T \simeq \Lambda_{QCD}$, the axion shift symmetry break to $Z_{N_{DW}}$ symmetry, i.e. from A to I, $N_{DW} = 9$ different phases show up. They should meet at a singularity in $\bar{\theta} = \langle a \rangle / f_a$ as (c), and the singular point forming a string as (d). Another point of view with $N_{DW} = 3$ is from Appendix.B2 of [10]:

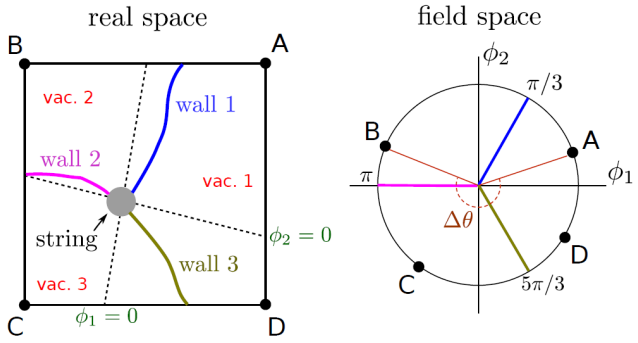

In this picture, the scalar field was written as $\phi = |\phi| e^{ia/\eta} \equiv \phi_1 + i\phi_2$, therefore the axion is already included in a linear combination of ϕ_1 and ϕ_2. As we see, for example, the real space between wall-1 and wall-2 is at vacuum-1.

- The string energy density can be wrote as [80],

$$\begin{aligned}\mu \equiv \frac{\text{Energy}}{\text{length}} &= \int r dr d\theta \left(\frac{1}{2}\nabla\phi^{\dagger}\nabla\phi + V(\phi)\right) \\ &\simeq \pi \int r dr \left(\frac{\partial_\theta \phi^{\dagger}}{r}\frac{\partial_\theta \phi}{r}\right) \\ &\simeq \pi \int_{1/m_s}^{1/H} r dr \frac{f_a^2}{r^2} = \pi f_a^2 \ln\left(m_s/H\right) \equiv \pi f_a^2 \kappa, \end{aligned} \tag{1.198}$$

where the integral over r is cut off at small r by the scale where $v(r) \neq 1$, namely, the radius of string core $r > 1/m_s$. On the other hand, using particle horizon as the upper limit of the radius of the string, see Eq.(1.159). The m_s is the mass of the real scalar field, i.e. from Eq.(1.196), $m_s^2 \equiv \lambda f_a^2$. Numerically, the $\kappa \sim 70$ with $\lambda \sim 1$, $f_a \sim 10^{11}$GeV, and $H \sim 1/(2t) \sim 10^{-18}$GeV at $T \sim 1$GeV, the reason for taking $T \sim 1$GeV is at Eq.(1.170), [80].

- Surface mass density of domain walls. Following Appendix. E of [10]. At Eq.(1.196), there have two kinds of domain walls: First, the domain wall from the first term of Eq.(1.196) i.e. PQ scalar ϕ at $T \sim f_a \gg T_0$ where T_0 is the temperature today, this domain walls density will be diluted very fast (see, Chapter 7.2 of [6] Table.7.1). Therefore its effects are negligible. Second, we only need to consider the domain walls from axion with broken axion shift symmetry $Z_{N_{DW}}$. Axion's Lagrangian,

$$\mathcal{L}_a = \frac{\eta^2}{2}(\partial_\mu \theta)^2 - \frac{m_a^2 \eta^2}{N_{DW}^2}\left(1 - \cos N_{DW}\theta\right), \tag{1.199}$$

again where $\theta \equiv a/\eta$. To solve equation of motion in Eq.(1.199) by using $\theta(x, y, z, t) = \theta(z)$,

we have

$$\theta(z) = \frac{2\pi k}{N_{DW}} + \frac{4}{N_{DW}} \tan^{-1} \exp(m_a z), \qquad k = 0, 1, \cdots, N_{DW} - 1. \tag{1.200}$$

Integrating our energy density, the surface energy density of the domain wall would be

$$\sigma_{wall} = \int_{-\infty}^{\infty} dz \eta^2 \left(\frac{d\theta}{dz}\right)^2 = \frac{8 m_a \eta^2}{N_{DW}^2}. \tag{1.201}$$

If we also include the effects by the neutral pion fields vary inside the wall i.e. using Eq.(1.123) as the potential, the Eq.(1.201) has an additional factor

$$\sigma_{wall} \to 4.32 f_\pi m_\pi \eta / N_{DW} = 9.23 \frac{m_a \eta^2}{N_{DW}^2}, \tag{1.202}$$

see Eq.(3.13) in [82].

• As we discussed T_1 at Eq.(1.170), the axion rolling down to its minimum only when $T \sim T_1$ i.e. $m_a(T_1) \simeq 3H(T_1)$ at this time, the domain walls are formed. In addition, at a later moment t_w, the axion domain walls are dominated in the space. One we can estimate (This plot is from Kawasaki's slide):

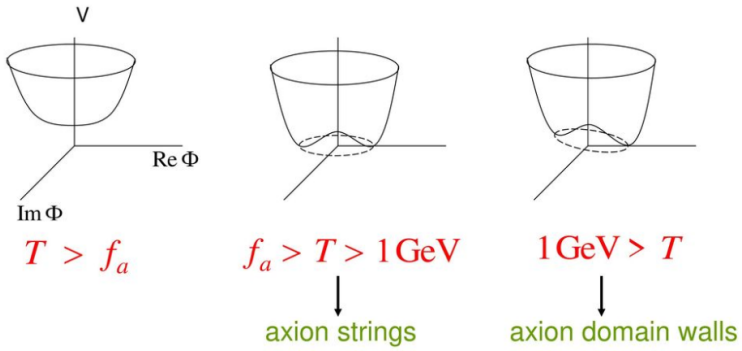

Axion strings formed at: time $= t_s$, temperature: $T_s \simeq f_a$,

Domain walls formed at: time $= t_1$, temperature: $T_1 \simeq 1\,\text{GeV}$, see Eq.1.170,

Domain walls dominated at: time $= t_w \simeq \dfrac{1}{m_a}$,

where "dominated" is compared only to string, and $t_s < t_1 < t_w$. This t_w can be found at Eq.(2.5) in [10] or by using Eq.(1.199) and Eq.(1.201) we have:

$$t_w \equiv \frac{\mu(t_w)}{\sigma_{wall}} = \frac{\pi}{9.23}\frac{\ln(m_s/H)}{m_a}, \tag{1.203}$$

• The **Axion Domain Wall Problem** or called Overclosure problem on axion domain walls, see Chapter.3 in [67] for more details or [10]. After the time t_w, the domain walls are straightened by their tension force up to horizon scale $d_H = H^{-1}$ such as the wall curvature radius and the distance of two neighboring walls. For example, considering a $N_{DW} = 2$ (i.e. two minima $\pm$) case, the domain walls structure is (from Cambridge website):

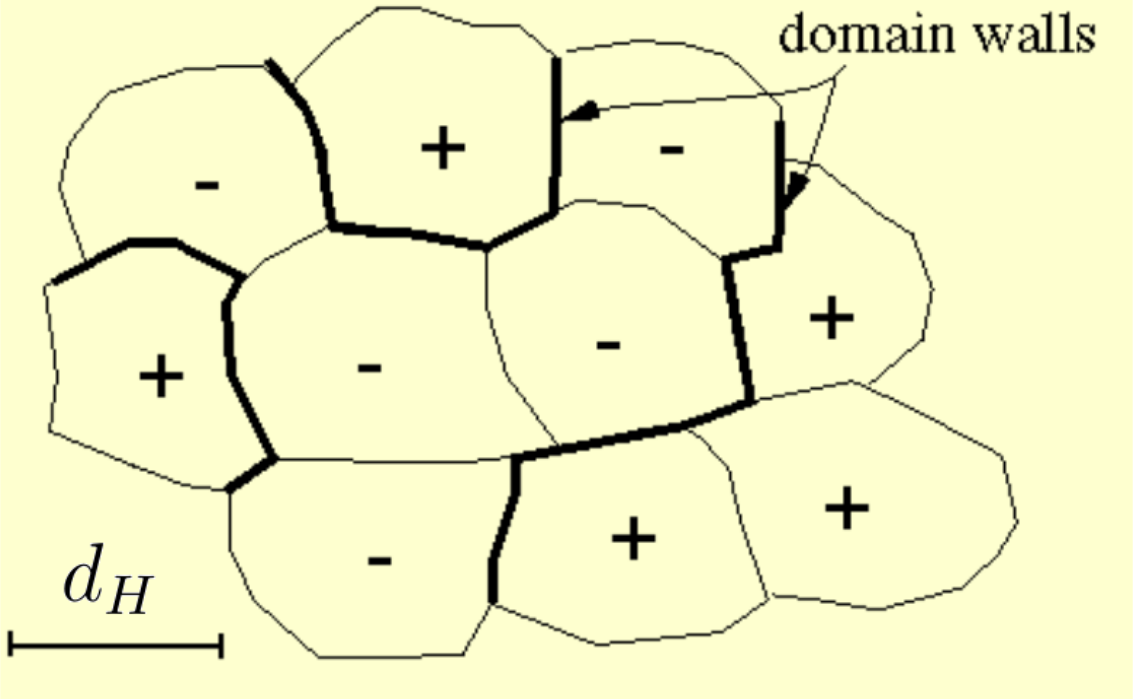

The Kibble mechanism for the formation of domain walls.

where only bold lines are domain walls. Form Kibble mechanism Eq.(1.159), we have $d_H \simeq \frac{1}{H}$. Therefore, the energy density of domain walls is diluting as[24]

$$\rho_{wall} \simeq \frac{\sigma_{wall}}{H^{-1}} \propto t^{-1} \tag{1.204}$$

where radiation dominated $H^{-1} = 2t$ is used, and $\sigma_{wall} \simeq$ constant by using Eq.(1.158) and Eq.(1.201) at $T < T_1 \simeq 1\,\text{GeV}$. Since this dilution of domain walls is slower than that of matters $\rho_m \sim R(t)^{-3} \sim t^{-3/2}$ and radiation $\rho \sim R(t)^{-4} \sim t^{-2}$ as well [73], its energy

[24]This is true for simulations, i.e. $\langle v^2 \rangle \simeq 0.577$ at RD or 0.16 at MD, see [83]. The theoretical calculation at [6].

density will eventually dominate in universe at the time (Eq(74) of [67] or see [73]):

$$H^2 \sim \frac{8\pi G}{3}\rho_{wall} \quad \rightarrow \quad t_{\rm WD} = \frac{3}{16\pi G\sigma_{wall}}, \tag{1.205}$$

where G is Newton's gravitational constant. Its temperature is $T \sim \mathcal{O}(10)$keV [9].

However, there have three solutions to solve the axion domain wall problem (details in Chpater.3 of [67]): First, if the PQ phase transitions earlier than inflation, i.e. all of the effects of axion would be homogenized by inflation, and there are no string s or domain walls. Second, If domain wall number $N_{DW} = 1$, ρ_{wall} will be decaying by gravitational radiation, heating and reflecting axion by against false vacuum region (DW do not radiate axion, but string does, so there still has axion contribution from Fig.1.8). In this case, the picture of the domain wall will be shown as Fig.1.8.

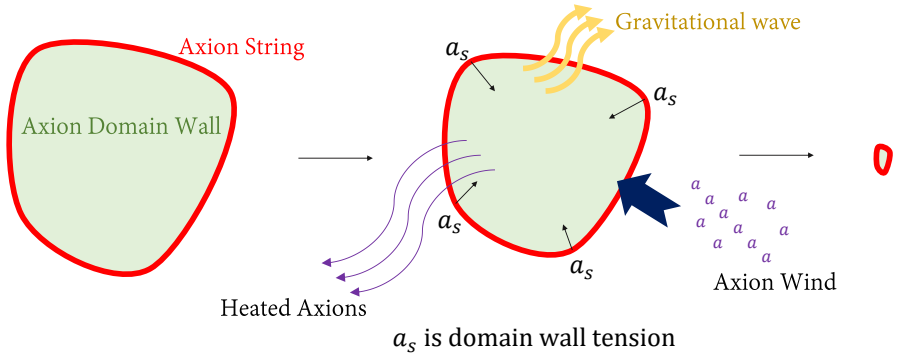

Figure 1.8: The Axion Domain Wall will eventually disappear, see Fig.2 in [8] and Fig.1.12 as well.

The tension $a_s = p_F + \mu\ell - p_T$, where $p_T = \sigma_{wall} \times A$ is the tension from domain wall surface density with area A.

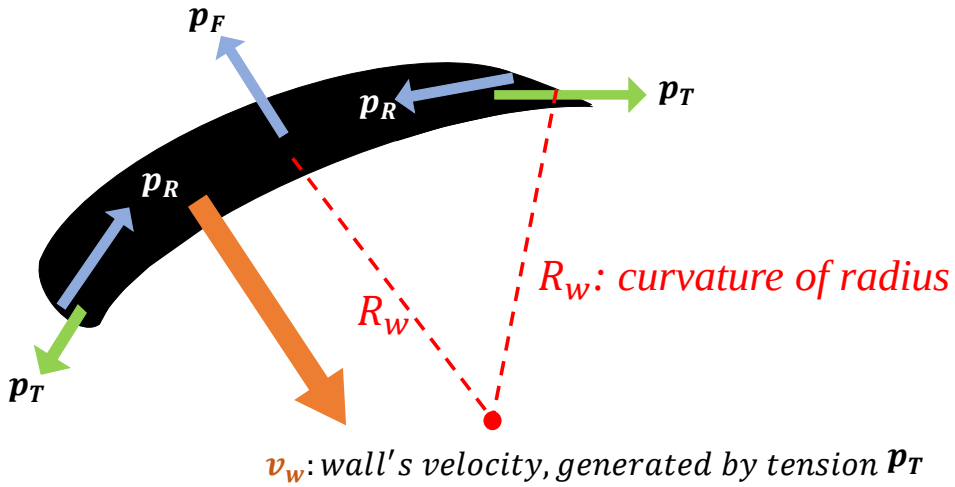

Figure 1.9: Domain wall tensions, where the black plane is the domain wall.

The p_F is from colliding between the domain wall and particles. The p_R is the summation of the reheating of particles (generated by the colliding), gravitational force, and energy-losing rate from particle radiation. We simply assume $p_R \sim p_F$ here for a simple calculation.

In Fig.1.8, the domain wall tension a_s is created by gravity, and a good video for this [**?**]. More details of the discussion are at Chapter 3.1 of [67], and the energy loss rate can be found in Chapter 4.3 in [67]. However, it would not be the case if we consider $N_{DW} > 1$. For example $N_{DW} = 2$, there should have two tension applying on the string by different domain walls but in opposite directions, i.e.

It consequently introduces an oscillation mode on the string and then creates the gravitational wave, see Eq.(85) and Eq.(86) in [67], but its energy density $\rho_{wall}(t)$ still decreases slower than matter and radiation. An example for $N_{DW} = 4$ on the intersecting surface of string (This figure is from Cambridge website):

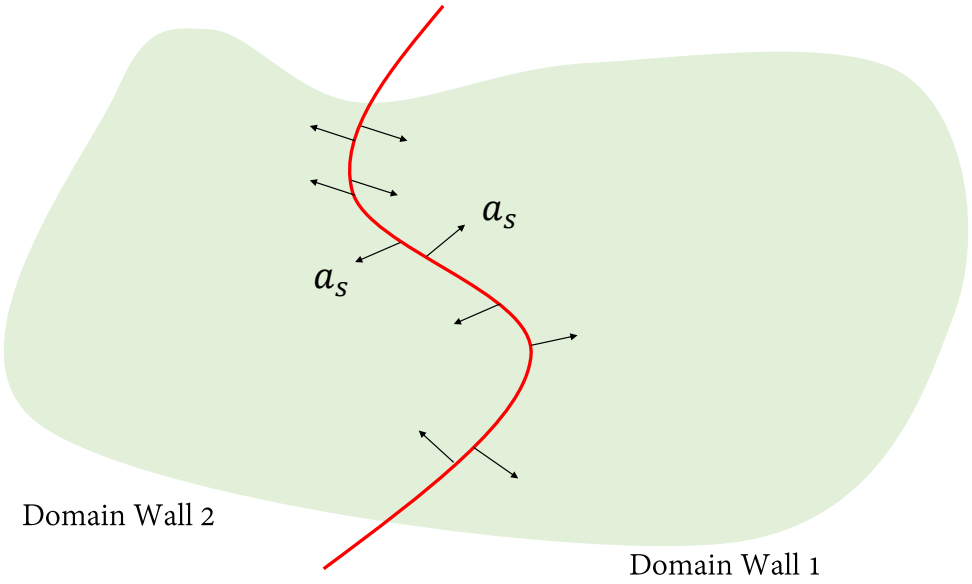

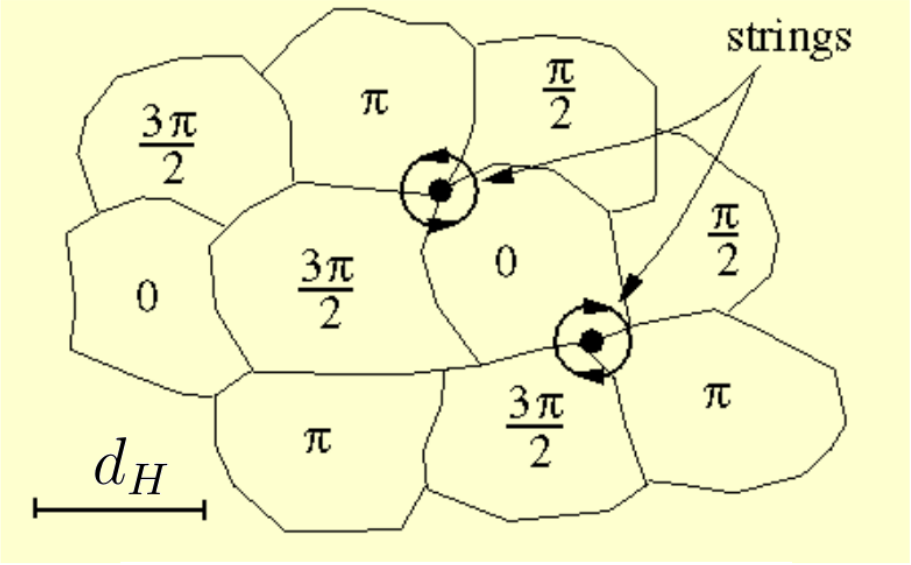

The Kibble mechanism for the formation of cosmic strings.

where is only two strings, other vertexes are not. However, even at $N_{DW} > 1$, there still have some events for two stings collision, it may make some loops then radiate axion and gravitational wave.

Third, considering a bias term that breaks the Z_{DW} symmetry, then the domain

Figure 1.10: Potential Eq.(1.207), from [8].

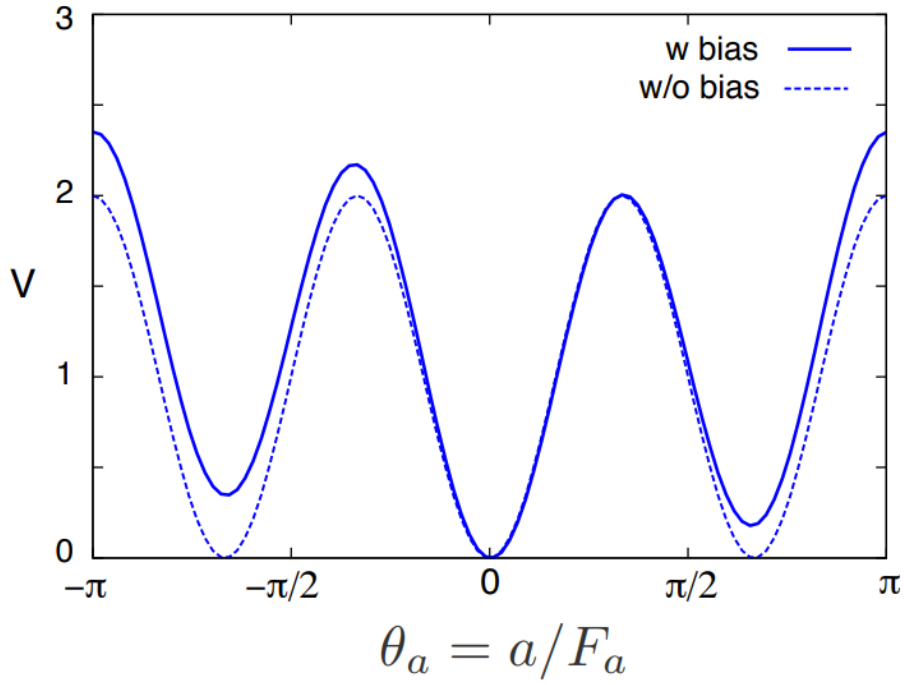

walls and strings would quickly decay to gravitational wave and axion [8]. The bias term is introduced by Sikivie [84], and a later study [85]. This term is added on potential Eq.(1.197):

$$\delta V = -\Xi\eta^3 \left(\Phi e^{-i\delta} + \text{h.c.}\right) \tag{1.206}$$

where Ξ is a dimensionless parameter that is assumed to be super smaller than unity. After PQ-SSB, the ground energy would be lifted by (Eq(88) at [67])

$$\delta V_a = -2\Xi\eta^4 \cos\left(\frac{a}{f_a} - \delta\right), \tag{1.207}$$

adding this term then draw Eq.(1.197), we have Fig.1.10, and result is at Fig.1.16.

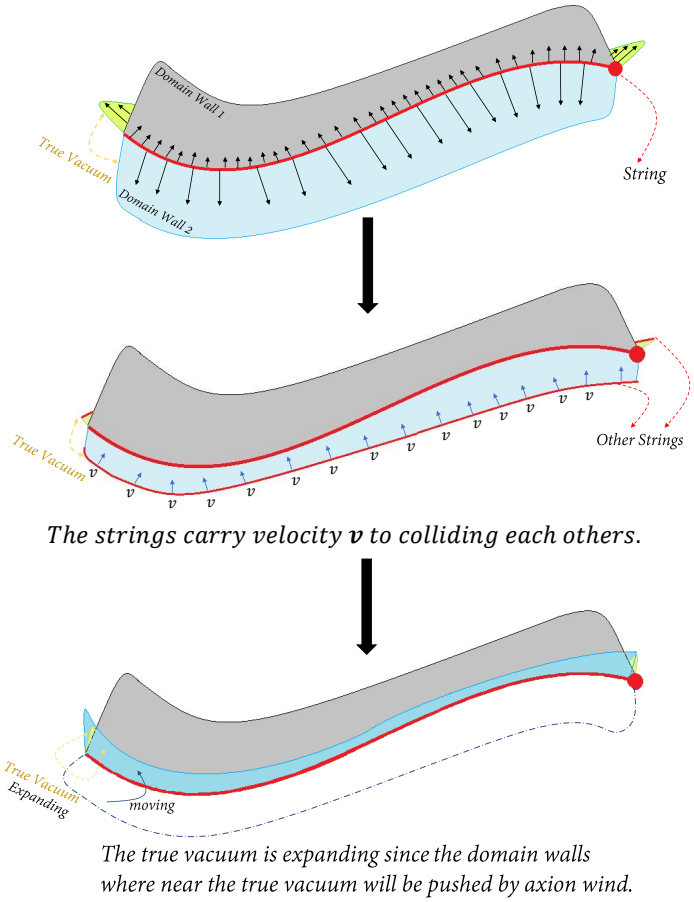

Figure 1.11: We pick up the wall at $\theta_a = \pi/3$ as blue, $\theta_a = -\pi/3$ as green, and $\theta_a = \pi$ as Black in Fig.1.10. The domain walls move like this show. The asymmetry of surface tension on domain walls will make the collision between strings more frequent. The axion wind will provide pressure on domain walls, then expand the true vacuum area.

Due to this term, domain walls become unstable, and the true vacuum on axion direction will be shifted to $|\theta| \to |\theta - \delta|$, and its energy density is lowered by an order $\Xi\eta^4$ to the original vacua. Consider the bias force $p_b \sim \delta V_a/N_{DW}$ balance to tension $p_T \sim \sigma/R_w$ at domain wall annihilation time t_{dec} , where R_w is curvature radius $R_w \sim t/\mathcal{A} \simeq t$, (see

[9, 8]):

$$t_{dec} \sim \frac{\sigma_{wall}}{\Xi \eta^4 / N_{DW}}. \tag{1.208}$$

After t_{dec} the bias force will dominate in the domain wall network. Requiring that the decay of walls occurs before the wall domination i.e. $t_{dec} < t_{\rm WD}$,

$$\Xi > 7.2 \times 10^{-60} \times N_{DW}^{-3} \left(\frac{m_a}{6 \times 10^{-4} \text{eV}} \right)^2. \tag{1.209}$$

To sum, the Misalignment Mechanism (oscillation), strings, and domain walls both contribute to matter-like relic density ([8]):

$$\Omega_{a,\rm Mis} \simeq 0.19 \langle \theta_1^2 \rangle \left(\frac{f_a}{10^{12}\,\text{GeV}} \right)^{1.19}, \tag{1.210}$$

$$\Omega_{a,\rm str} \simeq (4.0 \pm 2.0) \left(\frac{f_a}{10^{12}\,\text{GeV}} \right)^{1.19}, \tag{1.211}$$

$$\Omega_{a,\rm wall} \simeq (11.8 \pm 5.7) \left(\frac{f_a}{10^{12}\,\text{GeV}} \right)^{1.19}, \tag{1.212}$$

where $\langle \theta_1^2 \rangle = 6.85$ is at Eq.(1.183), and the Eq.(1.210) only works on Cold Axion, see Eq.(1.170). All of above provide a DM-like constraint i.e. $\sum \Omega_a \lesssim 0.11$:

$$f_a \lesssim (2.0 \sim 3.8) \times 10^{10}\,\text{GeV}. \tag{1.213}$$

1.5.5 Numerical Simulation of Axion String and Domain Walls

In this subsection, we provide a short review of the simulation studies [9, 8]. They considered a 3D simulation for stable domain walls, and a 2D simulation for unstable domain walls. They find the scaling solution and the spectrum of domain wall decay.

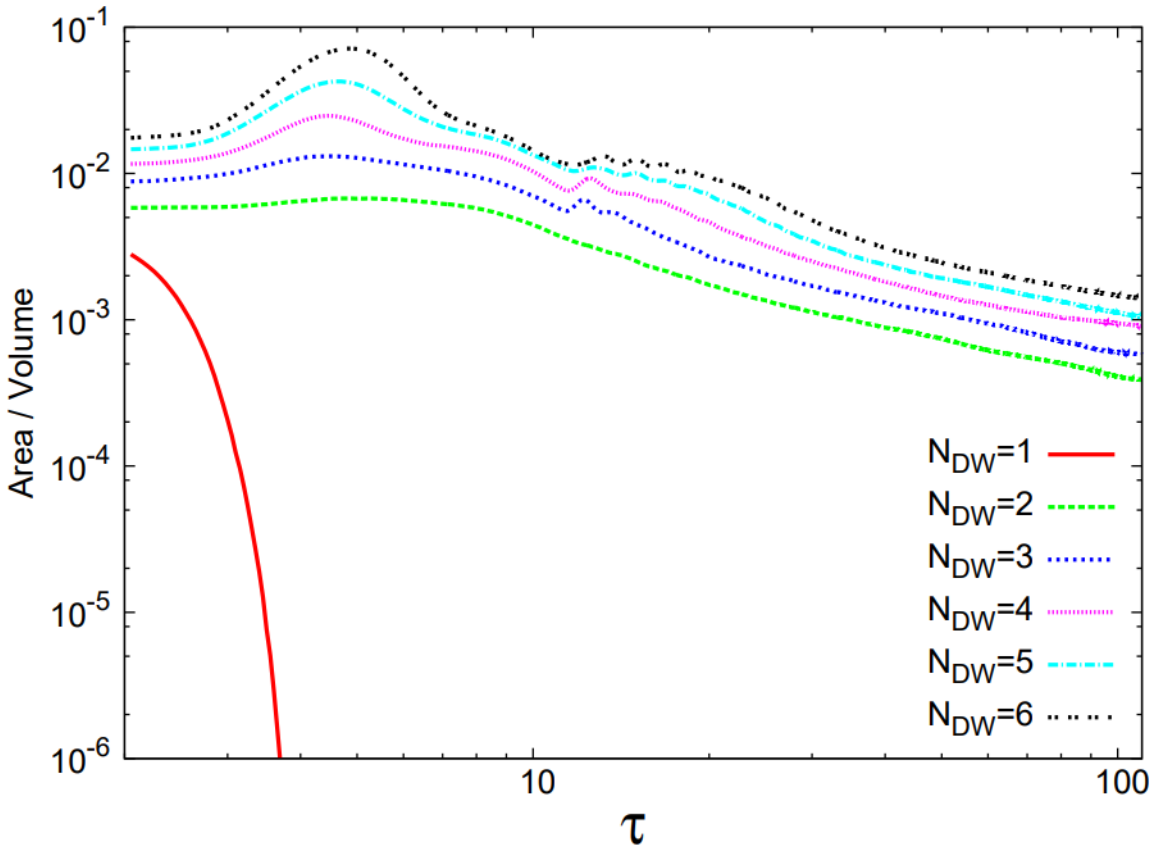

Figure 1.12: This graph is cited from [9] shows the area of domain walls with different domain wall numbers N_{DW}. The τ is conformal time. As we see in Fig.1.8, the domain wall will decay very fast at $N_{DW} = 1$ case. On the other hand, domain walls will decay very slowly with $N_{DW} > 1$, therefore, eventually, a non-neglectable domain wall density will dominate in the universe, the so-called Axion Domain Wall Problem.

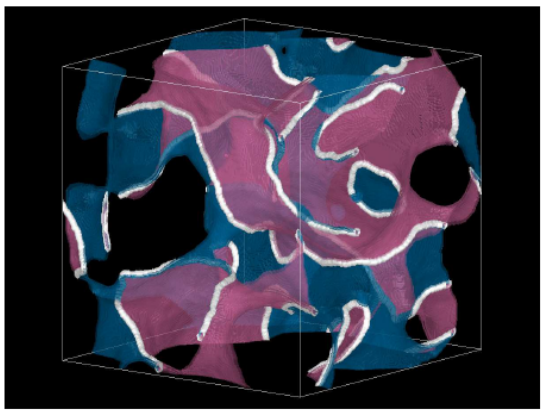

(a) $N_{\mathrm{DW}} = 2$

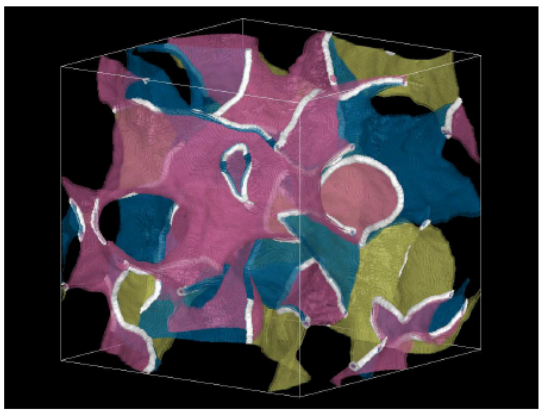

(b) $N_{\mathrm{DW}} = 3$

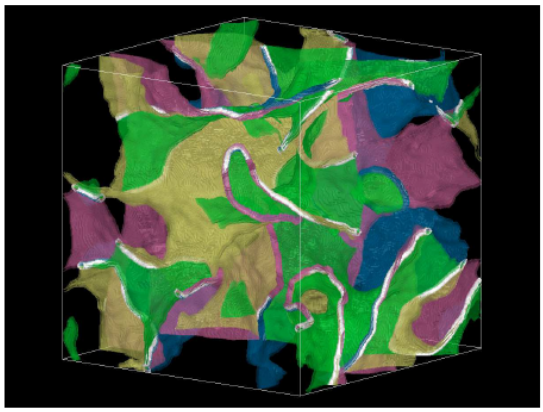

(c) $N_{\mathrm{DW}} = 4$

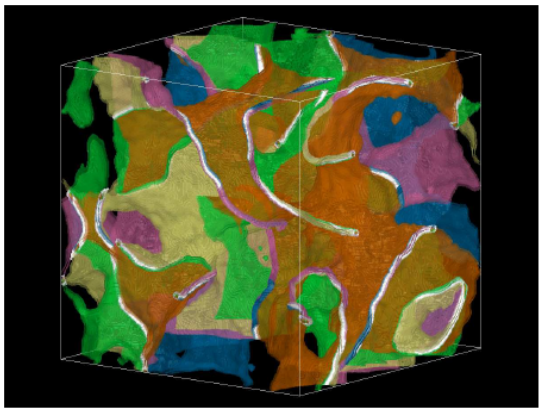

(d) $N_{\mathrm{DW}} = 5$

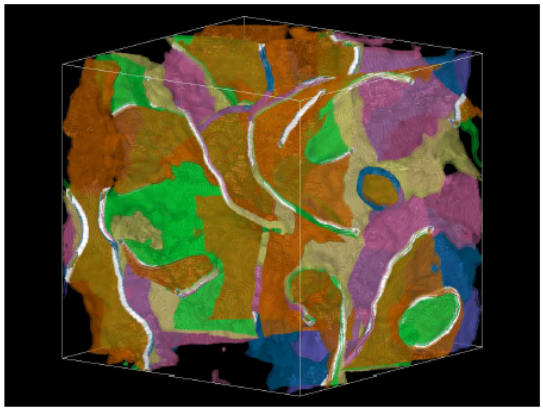

(e) $N_{\mathrm{DW}} = 6$

Figure 1.13: This graph is cited from [9]. The white lines correspond to the position of the core of strings, which is identified by using the method described in Appendix B.1 of [10]. N_{DW} domain walls are represented by surfaces with various colors, which are identified by using the method described in Appendix B.2 of [10].

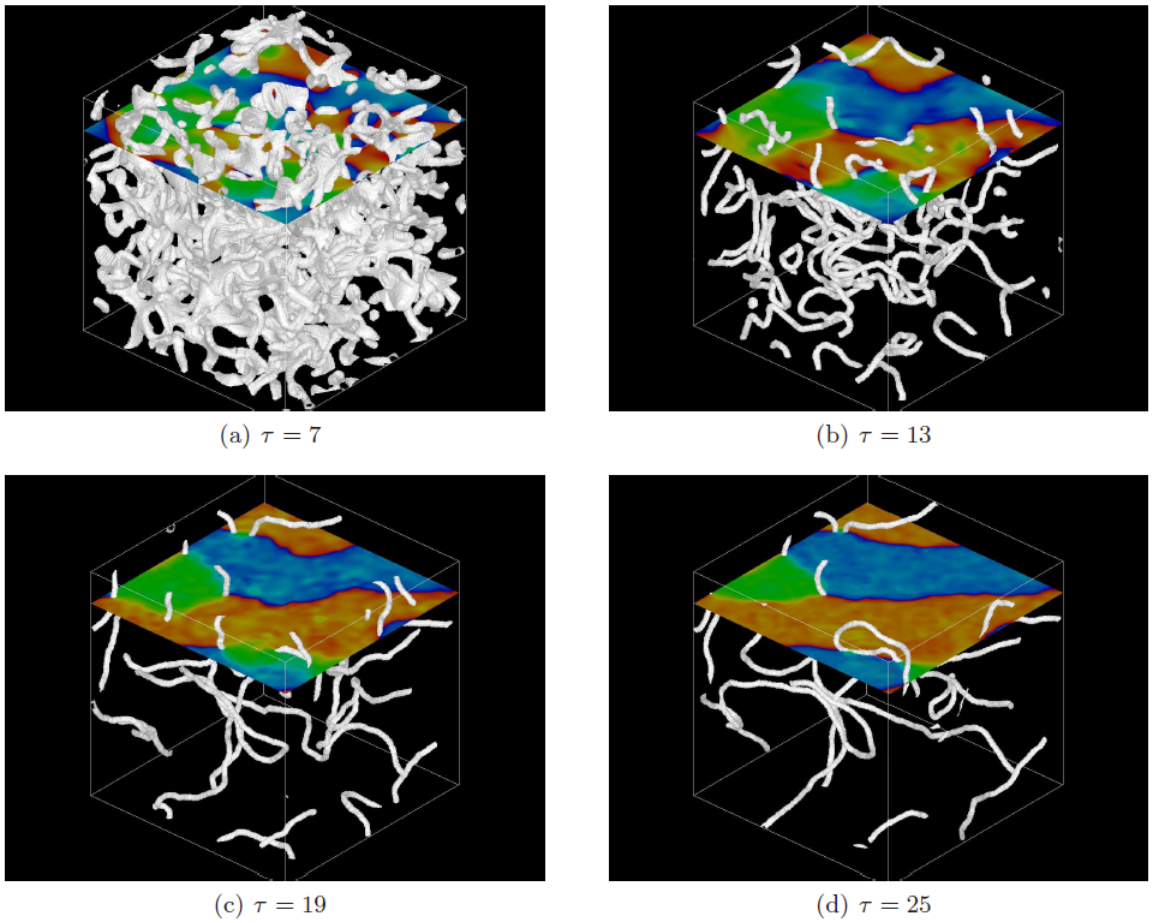

(a) $\tau = 7$ (b) $\tau = 13$

(c) $\tau = 19$ (d) $\tau = 25$

Figure 1.14: This graph is cited from [9]. The value of θ_a varies from $-\pi$ (blue) to π (red). At late times, the value of θ_a is separated into three domains represented by blue, red, and green regions. Domain walls are located around the boundary of these three regions, $\theta_a = \pi/3$, $\theta_a = -\pi/3$, and $\theta = \pm\pi$. Strings, which are represented by white lines, pass through the point where three regions meet each other.

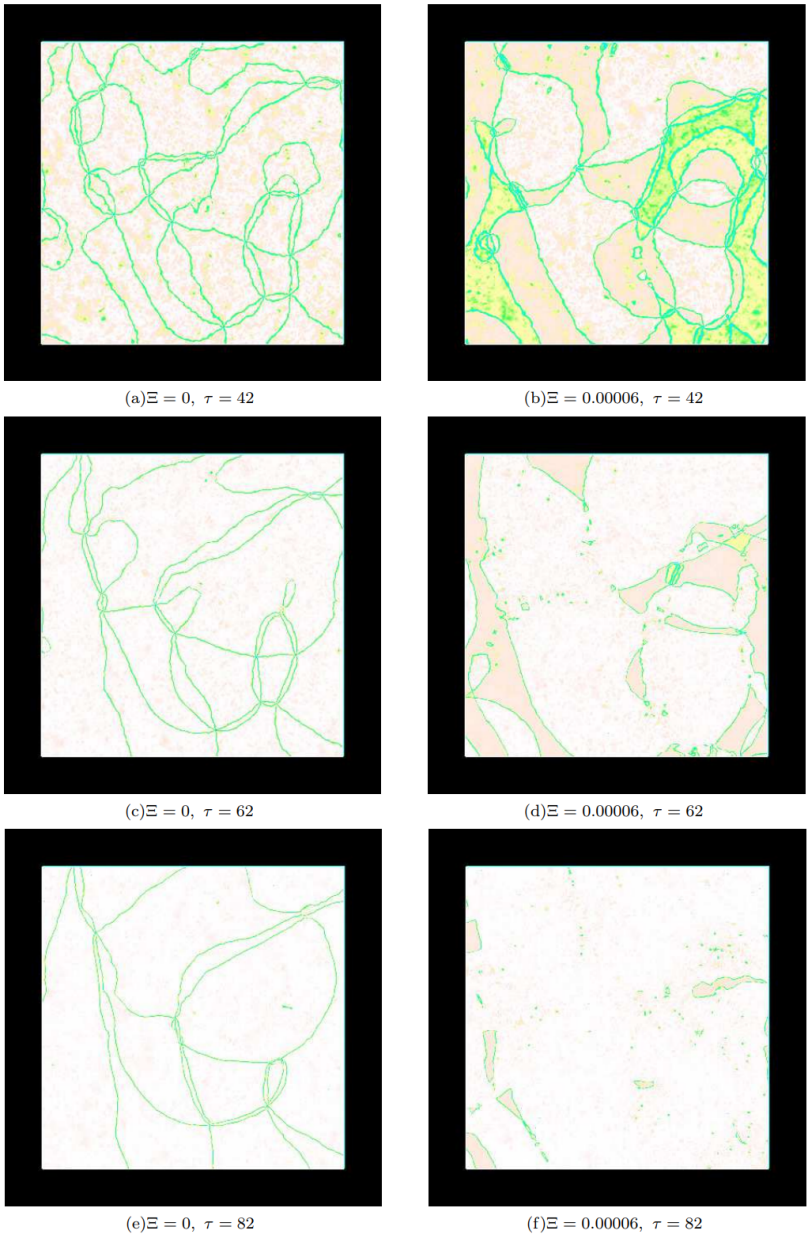

(a)$\Xi = 0,\ \tau = 42$ (b)$\Xi = 0.00006,\ \tau = 42$

(c)$\Xi = 0,\ \tau = 62$ (d)$\Xi = 0.00006,\ \tau = 62$

(e)$\Xi = 0,\ \tau = 82$ (f)$\Xi = 0.00006,\ \tau = 82$

Figure 1.15: This graph is cited from [8]. The green region corresponds to the core of domain walls $V(\Phi) = 2m_a^2\eta^2/N_{DW}^2$ and the white region corresponds to the vacuum $V(\Phi) = 0$. The Ξ is from the bias term Eq.(1.206), and the δ does not affect the dynamics.

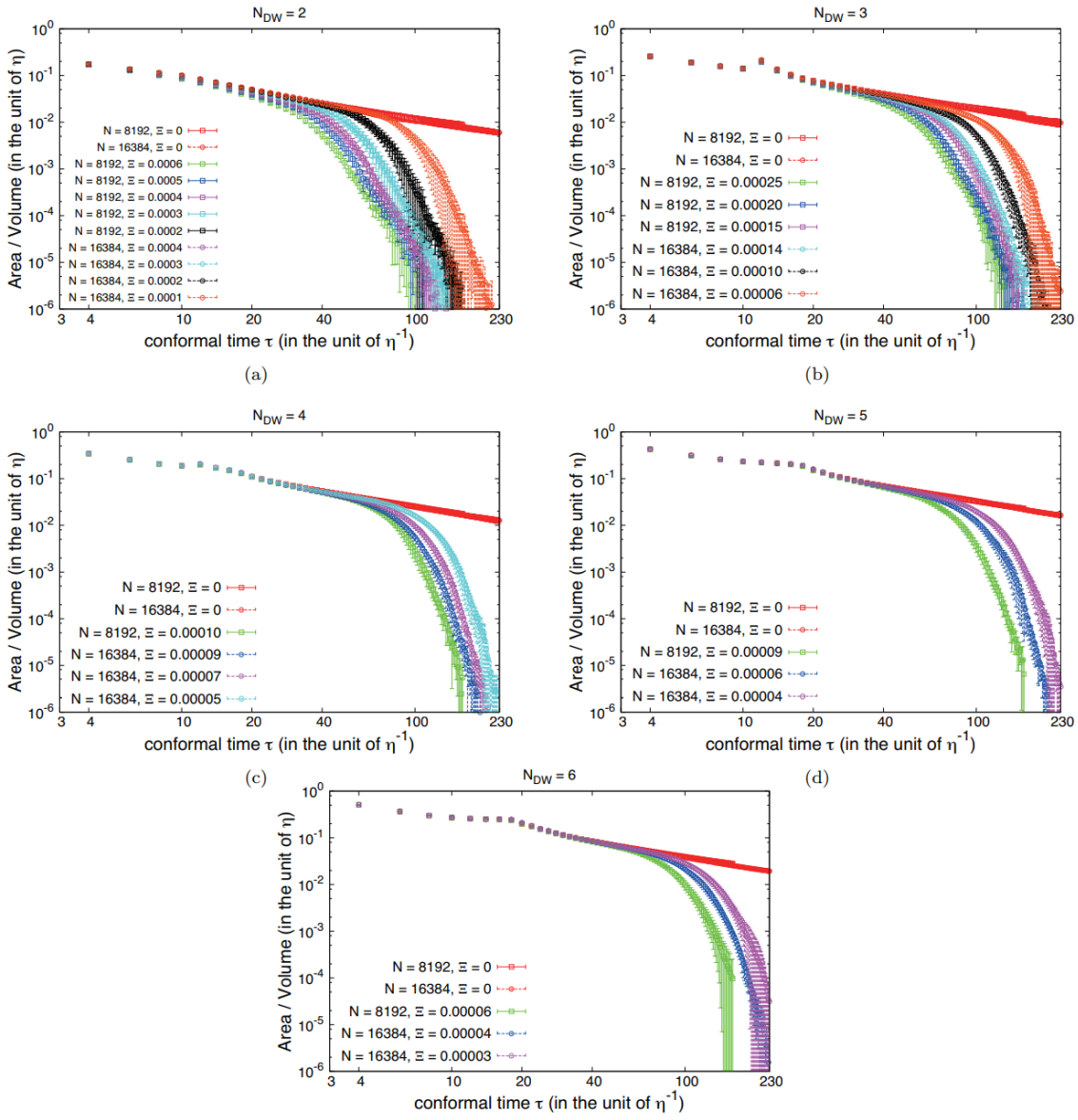

Figure 1.16: This graph is cited from [8]. As we can see in this graph, the domain wall energy density will quickly decrease with growing time. So, the Axion domain wall problem can be solved by adding a bias term in potential, i.e. Eq.(1.206).

Chapter 2

A Review for Topological Defects

2.1 Cosmic Strings

In the following, our discussion and calculation are based on [86, 87].

2.1.1 String Dynamics

If the radius of curvature of string R is much larger than its thickness δ, we can simply use the *Nambu-Olesen* action for gauge string or *Kalb-Ramond* action for global string,

$$S = \int \mathcal{L}\sqrt{-\gamma}d^2\zeta = \begin{cases} \mu \int \sqrt{-\gamma}d\zeta^2 & \text{Gauge} \\ \mu \int \sqrt{-\gamma}d\zeta^2 + \frac{1}{6}\int \sqrt{-g}H^2 d^4x + 2\pi\eta \int B_{\mu\nu}d\zeta^{\mu\nu} & \text{Global} \end{cases} \tag{2.1}$$

where η is string forming scale, $B_{\mu\nu}$ is the antisymmetric tensor field, $H_{\mu\nu\lambda}$ is its field strength and $d\zeta^{\mu\nu}$ is the worldsheet area element. It is described by a string worldsheet i.e. a two-dimensional surface. One is ζ^1 which corresponds to the length of the string.

Another is ζ^0, moving of string. These can be represented as

$$x^\mu = x^\mu(\zeta^a), \quad a = 0, 1. \tag{2.2}$$

So we can rewrite the Lorentz-invariant scalar

$$d^2s = g_{\mu\nu} x^\mu_{,a} x^\nu_{,b} d\zeta^a d\zeta^b = \gamma_{ab} d\zeta^a d\zeta^b, \tag{2.3}$$

where γ_{ab} is a 2D string worldsheet metrics. In following, we denote the $\{\mu, \nu, \rho, \sigma\}$ index are in 4D spacetime, $\{a, b\}$ are in 2D sting worldsheet. Varying the Nambu action Eq.(2.1) obtains the equation of motion

$$x^\nu_{,a}{}^{;a} + \Gamma^\nu_{\tau\lambda} \gamma^{ab} x^\tau_{,a} x^\lambda_{,b} = \begin{cases} 0 & \text{Gauge} \\ \dfrac{2\pi\eta}{\mu} H^\nu_{\tau\lambda} \epsilon^{ab} x^\tau_{,a} x^\lambda_{,b} & \text{Global} \end{cases} \tag{2.4}$$

If the string is moving in a background radiation fluid, there would has Aharonov-Bohm (gauge string) or Everett scattering (global string) between string and particles. that effects scattering provides a frictional force per unit length

$$\mathbf{F}_f = -\frac{\mu}{\ell_f} \frac{\mathbf{v}}{\sqrt{1 - v^2}}, \tag{2.5}$$

where $\mathbf{v}$ is the string velocity and ℓ_f is the friction length scale of string. For the both strings, its length scale are

$$\ell_f = \begin{cases} \dfrac{\mu}{\beta T^3} & \text{Gauge} \\ \dfrac{\mu}{\beta T^3} \ln^2 (T\delta) & \text{Global} \end{cases} \tag{2.6}$$

where T is the background temperature, and β us a numerical factor related to the number of particle species interacting with the string. The force can be included by adding a term

$$\left(u^\nu - x^\nu_{,a} x^{\sigma\,,a} u_\sigma\right) \frac{1}{\ell_f} \tag{2.7}$$

on right-hand side of Eq.(2.4). The $u^n u$ is the four-velocity of the background fluid. Furthermore, if the strings are within the FRW universe with Lorentz-invariant scalar

$$ds^2 = a^2(\tau)\left(d\tau^2 - \mathbf{dx}^2\right); \tag{2.8}$$

then $u^\nu = \left(a^{-1}(\tau), \mathbf{0}\right)$ and choosing the gauge conditions $\zeta^0 = \tau$ to identify conformal and worldsheet times, also require $\dot{\mathbf{x}} \cdot \mathbf{x}' = 0$ which means the string velocity is always orthogonal to the string direction. As above, the string equation of motion can be expressed as

$$\ddot{\mathbf{x}} + \left(2\frac{\dot{a}}{a} + \frac{a}{\ell_f}\right)\left(1 - \dot{\mathbf{x}}^2\right)\dot{\mathbf{x}} = \frac{1}{\epsilon}\left(\frac{\mathbf{x}'}{\epsilon}\right)', \tag{2.9}$$

$$\dot{\epsilon} + \left(2\frac{\dot{a}}{a} + \frac{a}{\ell_f}\right)\dot{\mathbf{x}}^2 \epsilon = 0, \tag{2.10}$$

where the coordinate energy per unit length ϵ is defined by

$$\epsilon^2 = \frac{\mathbf{x}'^2}{1-\dot{\mathbf{x}}^2}, \tag{2.11}$$

the dots and primes respectively denote derivatives with respect to τ and space $\zeta^1 \equiv \zeta$.

2.1.2 Lengthscale Evolution

The total string energy can be read as

$$E = \gamma\mu \times \ell = \mu a(\tau) \int \epsilon d\zeta, \tag{2.12}$$

where γ is relativity factor $\gamma = 1/\sqrt{1-v^2}$, which velocity was defined as averaged RMS i.e.

$$v^2 \equiv \langle \dot{\mathbf{x}}^2 \rangle = \frac{\int \dot{\mathbf{x}}^2 \epsilon d\sigma}{\int \epsilon d\sigma}. \tag{2.13}$$

We use these two variables to describe the large-scale evolution of the string network. Furthermore, the total string energy density $\rho \propto E/a^3$, so we have[1]

$$\frac{d\rho}{dt} = \frac{1}{a^3}\frac{dE}{dt} - 3\frac{E}{a^4}\frac{da}{dt} \tag{2.14}$$

$$\overset{2.12}{=} \frac{1}{a^3}\left(\frac{E}{\mu}\frac{d\mu}{dt} + \frac{E}{a}\frac{da}{dt} + \frac{E}{\epsilon}\frac{d\epsilon}{dt}\right) - 3\frac{\rho}{a}\frac{da}{dt} \tag{2.15}$$

$$\overset{2.10}{=} \begin{cases} \frac{1}{a^3}\left(\frac{E}{\mu}0 + EH - E\left(2H + \frac{a}{\ell_f}\right)v^2\right) - 3\rho H & \text{Gauge} \\ \frac{1}{a^3}\left(\frac{E}{\mu}\frac{d\mu}{dt} + EH - E\left(2H + \frac{a}{\ell_f}\right)v^2\right) - 3\rho H & \text{Global} \end{cases} \tag{2.16}$$

[1] For doing $\frac{dE}{dt}$, since t isn't function of ζ (no any form like $dt = [...]d\zeta$), we should do differential on μ, a and ϵ, respectively.

where Hubble parameter $H = \frac{\dot{a}}{a}$. In short, the averaged RMS equation of motion is

$$\frac{d\rho}{dt} = \begin{cases} -\left[2H(1+v^2) + a\dfrac{v^2}{\ell_f}\right]\rho & \text{Gauge} \\ -\left[2H(1+v^2) + a\dfrac{v^2}{\ell_f} + \dfrac{1}{\mu}\dfrac{d\mu}{dt}\right]\rho & \text{Global} \end{cases} \tag{2.17}$$

This equation only included the strings that do **Not** interact with other strings e.g. long strings and "small, short-lived" loops. Those strings usually have a low probability to interact with other strings before their demise.

• Usually, people assume that the long-string network evolution can be characterized by a single lengthscale L. This scale can be defined as correlation length or the distance between two strings.

• We define the strings longer than $\ell > L$ as long (or infinite) string, otherwise loops $\ell < L$. The long strings are moving as Brownian.

• The network density of long strings reads as

$$\rho_\infty \equiv \frac{\mu}{L^2}. \tag{2.18}$$

• The rate of loop production from long-string collisions can be written as

$$\left(\frac{d\rho_\infty}{dt}\right)_{\text{to loops}} = \rho_\infty \frac{v_\infty}{L} \int w\left(\frac{\ell}{L}\right) \frac{\ell}{L} \frac{d\ell}{L} \equiv \tilde{c} v_\infty \frac{\rho_\infty}{L}, \tag{2.19}$$

where we define a loop "chopping" efficiency factor $\tilde{c}$ and assume it is a constant (compare to Eq.(2.26) in [86], a factor g is absorbed in $\tilde{c}$). This $w(\ell/L)$ is the same as $f(\ell/L)$ in Eq.(9.3.25) in [87].

2.1.3 Scale-Invariant Solutions

Define two parameters in VOS-Model (the λ is defined by scaling factor $a(t) \equiv t^{\lambda}$ with λ=const., and $0 < \lambda < 1$.),

$$\gamma^2 \equiv \xi^{-1} \equiv \left(\frac{L}{t}\right)^2 \equiv \frac{k(k+\tilde{c})}{4\lambda(1-\lambda)}, \qquad v^2 = \frac{k(1-\lambda)}{\lambda(k+\tilde{c})}. \tag{2.20}$$

Use this two, replace k with taking $N \to \infty$, we have (see also eq.(17) of [Martins:1811.12678])

$$\tilde{c} = 2(1-\lambda v^2-\lambda)\frac{\gamma}{\sqrt{v^2}}, \tag{2.21}$$

where $v = v_\infty$. This agree to Eq.(9.3.17) of [87], we have to emphasize that the c in [87] is defined as $c \equiv \tilde{c}v$ in Eq.(2.22), and recently papers defined $c \to \tilde{c}$, i.e.

$$\left(\frac{d\rho_\infty}{dt}\right)_{\text{to loops}} \equiv cv_\infty \frac{\rho_\infty}{L}. \tag{2.22}$$

2.1.4 One-scale density

This part follows section 9.3.3 of [87]. From its Eq.(9.3.19)

$$\dot{\rho}_L = -3\left(\frac{\dot{a}}{a}\right)\rho_L(\ell,t) + g\frac{\mu}{L^4} f(\ell/L). \tag{2.23}$$

to solve this differential equation, first, consider the scaling term only

$$\dot{\rho}_L = -3\left(\frac{\dot{a}}{a}\right)\rho_L(\ell,t). \tag{2.24}$$

We have

$$\frac{d\rho_L}{\rho_L} = -3Hdt. \tag{2.25}$$

For example, in RD, $H = 1/2t$, so

$$\rho_L \propto t^{-3/2}. \tag{2.26}$$

Use this result (blank the scaling term) to Eq.(2.23),

$$\dot{\rho}_L = g\frac{\mu}{L^4} f\left(\ell/L\right) \quad \rightarrow \quad \rho_L = g\frac{\mu}{L^4} f\left(\ell/L\right) dt \propto t^{-3/2}. \tag{2.27}$$

Since the RHS should be proportional to $t^{-3/2}$, we can drop out the $t^{-3/2}$ then integrate others out like (use $L \equiv \gamma t = t/\sqrt{\xi}$)

$$\begin{aligned}
g\frac{\mu}{L^4} f\left(\ell/L\right) dt =& \frac{g\mu}{\gamma^4 t^4} f(\ell/L) dt \\
=& \frac{g\mu}{\gamma^4 t^{3/2}} \left[t^{-5/2} f(\ell/L) dt \right] \\
=& \frac{g\mu}{\gamma^4 t^{3/2}} \left[t^{-5/2} f(x) \frac{\gamma t^2}{\ell} dx \right] \\
=& \frac{g\mu}{\gamma^3 t^{3/2} \ell} \left[t^{-1/2} f(x) dx \right] \\
=& \frac{g\mu}{\gamma^3 t^{3/2} \ell} \left[\sqrt{\frac{x\gamma}{\ell}} f(x) dx \right] \\
=& \frac{g\mu}{\gamma^{5/2} t^{3/2} \ell^{3/2}} \left[\sqrt{x} f(x) \int_{\ell/\gamma t}^{\infty} dx \right],
\end{aligned} \tag{2.28}$$

where we define $x \equiv \frac{\ell}{L} = \frac{\ell}{\gamma t}$, so $dx = -\frac{\ell}{\gamma t^2} dt$. At late times, $t \to \infty$, we define a parameter as

$$\nu_r \equiv g\gamma^{-5/2} \int_0^\infty \sqrt{x} f(x) dx = gc\sqrt{\alpha}\gamma^{-3}, \tag{2.29}$$

where $f(x) = c\delta(x - \alpha/\gamma)$ is suggested by Eq.(9.3.25) of [87], and the chopping factor $c \equiv \tilde{c} v_\infty$ from Eq.(2.22). This result is the same as Eq.(9.3.27) of [87]. Another example, in MD, $H = 2/3t$, so Eq.(2.26) rewrite to

$$\rho \propto t^{-2}. \tag{2.30}$$

So we have

$$\begin{aligned} \rho_L = g\frac{\mu}{L^4} f\left(\ell/L\right) dt =& \frac{g\mu}{\gamma^4 t^2} \left[t^{-2} f(\ell/L) dt\right] \\ =& \frac{g\mu}{\gamma^3 t^2 \ell} \left[f(x) \int_{\ell/\gamma t}^\infty dx \right]. \end{aligned} \tag{2.31}$$

Another example, if $a \propto t^{2/6}$, $H = 1/3t$. We have

$$\rho_L \propto t^{-1}. \tag{2.32}$$

So we have

$$\rho_L = g\frac{\mu}{L^4} f\left(\ell/L\right) dt = \frac{g\mu}{\gamma^4 t}\left[t^{-3} f(\ell/L) dt\right] = \frac{g\mu}{\gamma^2 t \ell^2}\left[f(x)\int_{\ell/\gamma t}^{\infty} x dx\right]. \tag{2.33}$$

We can define

$$\nu_6 \equiv \frac{g}{\gamma^2}\int_0^{\infty} f(x) x dx = \frac{g}{\gamma^2} c\frac{\alpha}{\gamma} = \frac{g\alpha\tilde{c}v_{\infty}}{\gamma^3}. \tag{2.34}$$

Use Eq.(2.21), we have $\tilde{c}v_{\infty} = \frac{2}{3}(2 - v_{\infty}^2)\gamma$. Then use $\rho_L(\ell, t) = \mu\ell n(\ell, t)$ to simply get $n(\ell, t)$ the number density of loop per $a^3(t)$ per ℓ. The final step is that shift $\ell \to \ell + \Gamma G\mu t$ to add the radiation effect, so we obtain Eq.(9.3.26) of [87] from Eq.(2.28).

2.2 Domain Wall

2.2.1 Introduce VOS

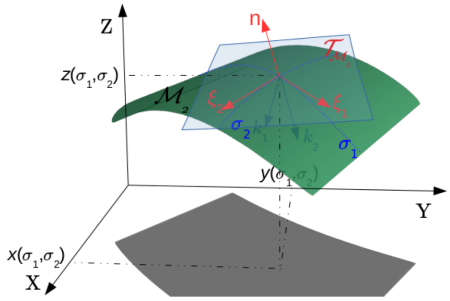

Figure 2.1: The wall surface $\mathcal{M}_2$ parameterized by two parameters, σ_1 and σ_2. The vectors on tangential surface are defined by $\xi_\alpha \equiv \frac{\partial x}{s^\alpha}$ where S_α is defined at Eq.(2.46), and $n^i \equiv \frac{\dot{x}^i}{|\dot{x}^i|}$.

Domain wall surface $\mathcal{M}_2$ can be described by the vector function $x^\mu(\sigma_1, \sigma_2, \tau)$, where $\tau \equiv \sigma_0$ is conformal time. The Domain wall shows as [88]. We expect that the function x^μ is smooth, so every two tangential vectors will be orthogonal

$$\partial_{\sigma_1} x^\mu \partial_{\sigma_2} x_\mu \equiv x^\mu_{,1} x_{\mu,2} = 0, \quad \text{and} \quad x^\mu_{,\tau} x_{\mu,1} = x^\mu_{,\tau} x_{\mu,2} = 0, \tag{2.35}$$

where $n^\mu \equiv x^\mu_{,\tau}/|x^\mu_{,\tau}|$ is normal vector on tangential surface. We also define $\partial_\tau x^\mu = x^\mu_{,\tau} \equiv \dot{x}^\mu$. The second normal relation is true only if the surface area of the domain wall is larger than Hubble's surface.

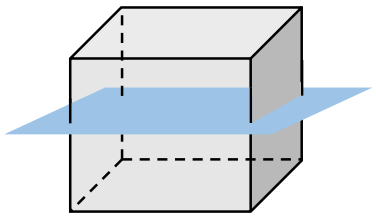

The wall-moving on σ_1 and σ_2 directions can be ignored. The domain wall action

is imitated from the Goto-Nambu string,

$$S = -\int \mathcal{L} d^3\sigma dz = -\sigma_w \int \sqrt{\gamma} d^3\sigma, \tag{2.36}$$

where σ_w is energy surface density, z is orthogonal to $\sigma_{1,2}$, and

$$\gamma_{ab} = g_{\mu\nu} x^{\mu}_{,a} x^{\nu}_{,b}, \quad \text{with} \quad \gamma \equiv \mathrm{Det}\left[\gamma_{ab}\right] = \frac{1}{3!}\epsilon^{ab}\epsilon^{cd}\gamma_{ac}\gamma_{bd} \overset{2.35}{=} \gamma_{00}\gamma_{11}\gamma_{22}, \tag{2.37}$$

where $x^{\mu}_{,a} = dx^{\mu}/d\sigma^a$, and the Eq.(2.35) gives $\gamma_{01} = \gamma_{02} = \gamma_{12} = 0$. The Lagrangian reads

$$\int d\mathcal{L} = \frac{1}{2}\int \sqrt{\gamma}\gamma^{ab} d\gamma_{ab} \; = \; \sqrt{\gamma}, \quad \text{with} \quad \int \mathcal{L} dz = \sigma_w, \tag{2.38}$$

where z is the direction that orthogonal to σ_1 and σ_2, see Eq.(13.2.7) of [87]. So the equation of motion reads

$$\frac{\partial \mathcal{L}}{\partial x^{\lambda}} - \partial_c\left(\frac{\partial \mathcal{L}}{\partial x^{\lambda}_{,c}}\right) = \frac{1}{2}\sqrt{\gamma}\gamma^{ab} g_{\mu\nu,\lambda} x^{\mu}_{,a} x^{\nu}_{,b} - \partial_c\left(\sqrt{\gamma}\gamma^{ab} g_{\mu\lambda} x^{\mu}_{,a}\delta^c_b\right) = 0, \tag{2.39}$$

and the energy-momentum tensor gives

$$T^{\mu\nu}\sqrt{-g} \equiv -2\frac{\delta S}{\delta g_{\mu\nu}} = \sigma_w \int \sqrt{\gamma}\gamma^{ab} x^{\mu}_{,a} x^{\nu}_{,b} \delta^4\left(x^{\rho} - x^{\rho}(\sigma^c)\right) d^2\sigma d\tau, \tag{2.40}$$

where $-g \equiv \mathrm{Det}|g_{\mu\nu}|$. So the energy is gave

$$
\begin{aligned}
E =& T^{00} dV \\
=& T^{00} a^3(\tau) dx dy dz \\
=& \sigma_w \int \sqrt{\gamma}\gamma^{ab} x^0_{,a} x^0_{,b} \delta^4 \left(x^\rho - x^\rho(\sigma^c)\right) d^2\sigma d\tau a^3(\tau) dx dy dz / \sqrt{-g} \\
=& \sigma_w \int \sqrt{\gamma}\gamma^{ab} \underbrace{x^0_{,a} x^0_{,b}}_{a^2(\tau) \text{ if a=b=0}} d^2\sigma \delta(t) \frac{dt}{a(\tau)} \\
=& \sigma_w a(\tau) \int \sqrt{\gamma}\gamma^{00} d^2\sigma \\
\equiv& \sigma_w \, a^2(\tau) \underbrace{\int \varepsilon d^2\sigma}_{\text{effective area}} , \quad \text{with} \quad \varepsilon \equiv \sqrt{\gamma}\gamma^{00}/a(\tau),
\end{aligned}
\tag{2.41}
$$

where $\sqrt{-g} = a^3(\tau)$ in FRW metric, $a(\tau)d\tau = dt$ and

$$
x^0_{,a} = \frac{d\tau}{d\sigma^a} = \{1, 0, 0\}, \quad \text{for} \quad a = \{0, 1, 2\}, \tag{2.42}
$$

since $\{\tau, \sigma_1, \sigma_2\}$ are independent to each other e.g. $d\sigma_i/d\tau = 0$. Since [2]

$$
g_{\mu\nu,\lambda} = \frac{dg_{\mu\nu}}{dx^\lambda} = \{2\frac{\dot{a}}{a} g_{\mu\nu}, 0, 0, 0\}, \quad \text{for} \quad \lambda = \{0, 1, 2, 3\}, \tag{2.43}
$$

[2] We should treat the time of wall $t = t(\tau)$ as our definition $x^\mu(\sigma_1, \sigma_2, \tau)$

where $i, j = \{1, 2, 3\}$, $\dot{a}(\tau) = da(\tau)/d\tau$, and

$$g_{\mu\nu} = \begin{pmatrix} a^2(\tau) & 0 & 0 & 0 \\ 0 & -a^2(\tau) & 0 & 0 \\ 0 & 0 & -a^2(\tau) & 0 \\ 0 & 0 & 0 & -a^2(\tau) \end{pmatrix}, \tag{2.44}$$

and $g^{\mu\nu} = 1/g_{\mu\nu}$. We can rewrite Eq.(2.39) in FRW metric as

$$\frac{\dot{a}}{a}\delta_{0\lambda}\sqrt{\gamma}\gamma^{ab}\gamma_{ab} - \partial_c\left(\sqrt{\gamma}\gamma^{ab}g_{\mu\lambda}x^{\mu}_{,a}\delta^c_b\right) = 0. \tag{2.45}$$

Let's redefine the coordinates σ_1 and σ_2 to s_1 and s_2 which makes the tangential vectors to be unit-vectors as

$$\frac{\partial x^i}{\partial s_\alpha} \equiv \frac{x^i_{,\alpha}}{|x^i_{,\alpha}|} \equiv \xi^i_\alpha, \qquad \text{i.e.} \qquad \left|\frac{\partial x^i}{\partial s_\alpha}\right|^2 = 1, \ \forall\, \alpha = \{1, 2\}, \tag{2.46}$$

where is no summation on i and α. Using this substitutes to Eq.(2.45) we have (for $\lambda = 0$)[3],

$$\begin{aligned}
\frac{\dot{a}}{a}\sqrt{\gamma}\gamma^{ab}\gamma_{ab} - \partial_b\left(\sqrt{\gamma}\gamma^{ab}g_{\mu 0}x^{\mu}_{,a}\right) &\overset{\mu=0}{=} \frac{\dot{a}}{a}\sqrt{\gamma}\gamma^{ab}\gamma_{ab} - \partial_b\left(\sqrt{\gamma}\gamma^{ab}g_{00}x^{0}_{,a}\right) \\
&\overset{2.42}{=} \frac{\dot{a}}{a}\sqrt{\gamma}\gamma^{ab}\gamma_{ab} - \partial_b\left(\sqrt{\gamma}\gamma^{0b}g_{00}x^{0}_{,0}\right) \\
&\overset{2.35}{=} \frac{\dot{a}}{a}\sqrt{\gamma}\gamma^{ab}\gamma_{ab} - \partial_0\left(\sqrt{\gamma}\gamma^{00}g_{00}x^{0}_{,0}\right) \\
&\overset{2.41}{=} \frac{\dot{a}}{a}\sqrt{\gamma}\gamma^{ab}\gamma_{ab} - \partial_0\left(\varepsilon a^3(\tau)\right) \\
&\overset{2.49}{=} \frac{\dot{a}}{a}\sqrt{\gamma}\times 3 - \partial_0\left(\varepsilon a^3(\tau)\right) \\
&\overset{2.41}{=} 3\dot{a}\varepsilon/\gamma^{00} - \partial_0\left(\varepsilon a^3(\tau)\right) \\
&\overset{2.50}{=} 3\dot{a}\varepsilon a^2\left(1-\dot{x}^i\dot{x}_i\right) - \partial_0\left(\varepsilon a^3(\tau)\right) \\
&= 3\dot{a}\varepsilon a^2\left(1-\dot{x}^i\dot{x}_i\right) - \dot{\varepsilon}a^3 - 3\varepsilon\dot{a}a^2 \\
&= -\dot{\varepsilon}a^3 - 3\varepsilon\dot{a}a^2\dot{x}^i\dot{x}_i = 0,
\end{aligned} \tag{2.47}$$

where $g_{00} = -a^2(\tau)$, γ_{ab} is diagonal since Eq.(2.35), again $\partial_\tau x^\mu = x^\mu_{,\tau} \equiv \dot{x}^\mu$, and $\partial_0 = \partial/\partial\sigma_0 = \partial/\partial\tau$, also $\dot{\varepsilon} = d\varepsilon/d\tau$. There also need

$$\gamma^{ab} \equiv \frac{1}{\gamma_{ab}} = \text{Inverse}\left[\gamma_{ab}\right] = \begin{pmatrix} \frac{1}{\gamma_{00}} & 0 & 0 \\ 0 & \frac{1}{\gamma_{11}} & 0 \\ 0 & 0 & \frac{1}{\gamma_{22}} \end{pmatrix}, \tag{2.48}$$

[3]This agrees to Eq.(3) in [88]

so we have

$$\gamma^{ab}\gamma_{ab} = \mathrm{Tr}\begin{pmatrix} 1 & 0 & 0 \\ 0 & 1 & 0 \\ 0 & 0 & 1 \end{pmatrix} = 3. \tag{2.49}$$

Using Eq.(2.48), we obtain

$$\gamma^{00} = \frac{1}{\gamma_{00}} = \frac{1}{a^2\left(1 - \dot{x}^i\dot{x}_i\right)}. \tag{2.50}$$

For $\lambda = i$,

$$\partial_c\left(\sqrt{\gamma}\gamma^{ab}g_{\mu i}x^{\mu}_{,a}\delta^c_b\right) = -\partial_b\left(\sqrt{\gamma}\gamma^{ab}a^2(\tau)x^i_{,a}\right), \tag{2.51}$$

for $b = 0$,

$$\partial_0\left(\sqrt{\gamma}\gamma^{00}a^2(\tau)x^i_{,0}\right) = \dot{\sqrt{\gamma}}\gamma^{00}a^2(\tau)x^i_{,0} + \sqrt{\gamma}\dot{\gamma}^{00}a^2(\tau)x^i_{,0} + \sqrt{\gamma}\gamma^{00}2\dot{a}ax^i_{,0} + \sqrt{\gamma}\gamma^{00}a^2(\tau)x^i_{,00},$$

where

$$\dot{\sqrt{\gamma}} = \frac{1}{2}\dot{\gamma}\gamma^{-1/2} = \frac{1}{2}\gamma^{-1/2}\frac{d}{d\tau}\left(\gamma_{00}\gamma_{11}\gamma_{22}\right),$$

and $\gamma_{00} = (a^2 - a^2\dot{x}^i\dot{x}^i)$, $\gamma_{11} = -a^2 x^i_{,1} x_{i,1}$, and $\dot{\gamma}^{aa} = -\dot{\gamma}_{aa}/\gamma^2_{aa}$,

$$\begin{aligned}
\dot{\gamma}_{00} &= 2\dot{a}a - 2\dot{a}a\dot{x}_i\dot{x}_i - 2a^2\ddot{x}_i\dot{x}_i, \\
\dot{\gamma}_{11} &= -2\dot{a}a x^i_{,1}x^i_{,1} - 2a^2\dot{x}^i_{,1}x^i_{,1}, \\
\dot{\gamma}_{22} &= -2\dot{a}a x^i_{,2}x^i_{,2} - 2a^2\dot{x}^i_{,2}x^i_{,2}.
\end{aligned}$$

for $b = \alpha = \{1, 2\}$,

$$\begin{aligned}
\partial_i\left(\sqrt{\gamma}\gamma^{\alpha\alpha}a^2(\tau)x^i_{,\alpha}\right) &= \frac{\partial}{\partial\sigma^\alpha}\left(\sqrt{\gamma}\gamma^{\alpha\alpha}a^2(\tau)x^i_{,\alpha}\right) \\
&= \frac{1}{2}\frac{d}{d\sigma^\alpha}\sqrt{\gamma}\gamma^{\alpha\alpha}a^2x^i_{,\alpha} + \sqrt{\gamma}\frac{d}{d\sigma^\alpha}\gamma^{\alpha\alpha}a^2x^i_{,\alpha} + \sqrt{\gamma}\gamma^{\alpha\alpha}a^2x^i_{,\alpha\alpha}
\end{aligned}$$

where $\gamma^{aa}_{,\alpha} = -\gamma_{aa,\alpha}/\gamma^2_{aa}$, so

$$\begin{aligned}
\frac{\partial}{\partial\sigma^\alpha}\gamma_{00} &= -2a^2\dot{x}^i_{,\alpha}\dot{x}^i, \\
\frac{\partial}{\partial\sigma^\alpha}\gamma_{11} &= -2a^2x^i_{,1\alpha}x^i_{,1}, \\
\frac{\partial}{\partial\sigma^\alpha}\gamma_{22} &= -2a^2x^i_{,2\alpha}x^i_{,2}.
\end{aligned}$$

Using above, our result exactly agrees to Eq.(11) in [88] as

$$\ddot{x}^i + 3\frac{\dot{a}}{a}\dot{x}^i\left(1 - \dot{x}^i\dot{x}_i\right) = \left(1 - \dot{x}^i\dot{x}_i\right)\left(k^i_1 + k^i_2\right), \tag{2.52}$$

where since the size of k^i_α is proportional to inverse of curvature radii, $|k^i_\alpha| \propto 1/R_\alpha$, hence $k^i_\alpha \equiv \frac{\partial\xi^i_\alpha}{\partial s_\alpha} \equiv \frac{a(\tau)}{R_\alpha}u^i_\alpha$, where $u^i_\alpha \equiv k^i_\alpha/|k^i_\alpha|$ are units vectors, and R_α are curvature radii of σ_1

or σ_2, respectively.

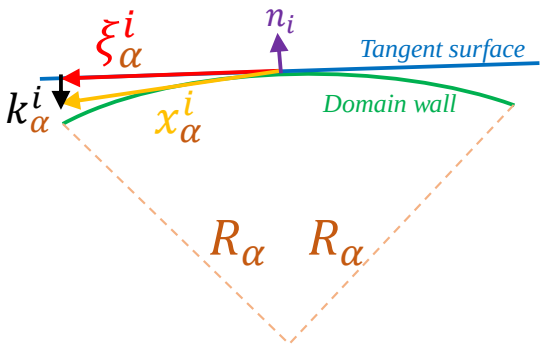

To average Eq.(2.47) and Eq.(2.52) with contracting n_i, we obtain

$$\frac{d\rho}{dt} = -H\rho\left(1+3v^2\right), \tag{2.53}$$

$$\frac{dv}{dt} = (1-v^2)\left(\frac{k_w}{L} - 3Hv\right), \tag{2.54}$$

where t is physical time, and $H = \frac{1}{a}\frac{da}{dt}$. We also used

$$\frac{E}{V} = \rho = \frac{\sigma_w a^2}{V}\int \varepsilon d^2\sigma, \tag{2.55}$$

and the root-mean-squared velocity

$$v^2 = \frac{\int \dot{x}^2 \varepsilon d^2\sigma}{\int \varepsilon d^2\sigma}. \tag{2.56}$$

We also assumed that the curvature radii are equal to correlation length $R_1 = R_2 = L$. The k_w is called *momentum parameter*, is defined by adding K_1 and K_2 as

$$k_w \equiv K_1 + K_2, \qquad \text{and} \qquad K_\alpha \equiv |u^i_\alpha n_i|, \tag{2.57}$$

theoretically, we expect $1 \geq K_\alpha \geq 0$ (hence $0 \leq k_w \leq 2$) and approximately to be a constant during cosmological physics time evolution. This momentum parameter is assumed in the from

$$k_w \equiv k(v) = k_0 \frac{1 - \left(qv^2\right)^\beta}{1 + \left(qv^2\right)^\beta}, \tag{2.58}$$

where β, k_0 and q are unknown parameters but can be determined in simulation. Not like helicoidal solution on string case, the domain wall has no nontrivial analytic solution. The parameter $1/q$ is an averaged maximal velocity for the wall network. It cannot be larger than the maximum velocity of walls $v^2_{\max}$,

$$0 < \frac{1}{q} \leq v^2_{\max} = \frac{n}{n+1} = \frac{2}{3}, \tag{2.59}$$

in n-dimensional topological defects ($n = 1$ for string, $n = 2$ for walls) [89].

2.2.2 Energy losing

Domain wall chopping

The domain wall network loses energy by the domain wall intersections and creation of sphere-like objects that eventually collapse (walls are repelled to each other),

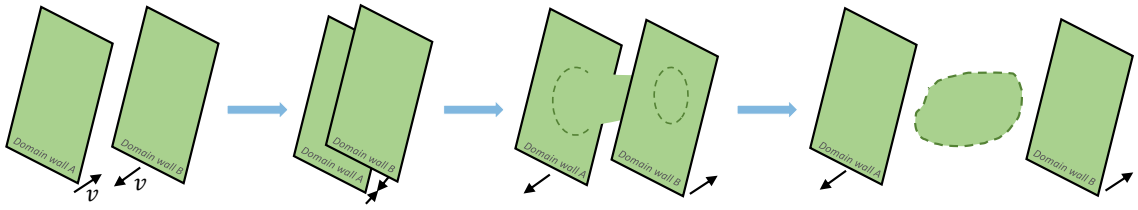

This effect can be concluded by a *chopping* parameter c_w that add in equation of motion Eqs.(2.53-2.54), and also replace the domain wall correlation length $L(\tau) = \sigma_w/\rho(\tau)$ as

$$\frac{dL}{dt} = \left(1 + 3v^2\right) HL + c_w v, \tag{2.60}$$

$$\frac{dv}{dt} = (1 - v^2)\left(\frac{k_w}{L} - 3Hv\right). \tag{2.61}$$

Gravitational behavior

We review the development of the topology theory with the following literature studies.

- Vilenkin1982 [90]

They only mentioned that the string-wall network are oscillating at a typical frequency $\omega \sim R^{-1}$ where $R \geq \mu/\sigma_w$ is the piece of domain wall size, μ is string tension, its energy

losing rate by gravitational radiation is

$$\frac{dM}{dt} \sim -GM^2R^4\omega^6 \sim -G\sigma M, \tag{2.62}$$

where M is string-wall mass. The lifetime of the piece is independent of its size,

$$\tau_w \sim (G\sigma)^{-1} \sim (m_p/\eta)^2 \, m_a^{-1}, \tag{2.63}$$

where $\eta = f_a$ is PQ-symmetry-SSB scale, and axion mass m_a. Worth to mention that when the piece becomes smaller than μ/σ, its mass is determined mostly by string, and the decay time is $\tau \leq (G\mu)\, R \leq (G\sigma_w)^{-1}$.

- Vilenkin1981 [91] and Vilenkin1983 [92]

The energy-momentum domain wall is described by a classical solution of

$$T^\nu_\mu(x) = \sum_i \frac{\partial \mathcal{L}}{\partial \phi^i_{,\nu}} \phi^i_{,\mu} - \delta^\nu_\mu \mathcal{L}, \tag{2.64}$$

where the i is summation over all possible fields, and we also assumed there is a static wall that parallel to y-z plane in a flat space-time. In thin-wall approximation

$$\tilde{T}^\nu_\mu(x) = \delta(x-a) \int T^\nu_\mu(x) dx, \tag{2.65}$$

where $x = a$ is position of the wall. Since $\phi(x)$ is only function of x (isotropic on y-z, and static), we conclude that

$$\tilde{T}^0_0 = \tilde{T}^2_2 = \tilde{T}^3_3. \tag{2.66}$$

From the conservation law

$$T^\nu_{\mu,\nu} = 0, \tag{2.67}$$

so

$$\frac{d}{dx} T^1_1 = 0, \quad \rightarrow \quad T^1_1 = \text{constant}. \tag{2.68}$$

Since the boundary condition of topological defects is $T^\nu_\mu = 0$ at $x = \pm\infty$, we conclude $T^1_1 = \tilde{T}^1_1 = 0$. Hence the energy-momentum tensor reads

$$\tilde{T}^\nu_\mu(x) = \sigma_w \delta(x-a) \times \text{diag}\,(1,0,1,1) = \delta(x-a) \times \text{diag}\,(\sigma_w, 0, -p, -p)\,, \tag{2.69}$$

where $p = -\sigma_w$ is the pressure that equals to surface tension. Note that this energy-momentum tensor is only Lorentz invariant on the parallel transformation of the wall i.e. the tangential motion of the wall is unobservable.

Weak Field approximation

The domain wall gravity can use the weak field approximation on the metric as

$$g_{\mu\nu} = \eta_{\mu\nu} + h_{\mu\nu}, \tag{2.70}$$

with $h_{\mu\nu} \ll 1$. The Einstein equation is

$$\left(\nabla^2 - \partial_t^2\right) g_{\mu\nu} = \left(\nabla^2 - \partial_t^2\right) h_{\mu\nu} = 16\pi G \left(T_{\mu\nu} - \frac{1}{2}\eta_{\mu\nu} T\right), \tag{2.71}$$

the harmonic coordinate condition

$$\partial_\nu \left(h^\nu_\mu - \frac{1}{2}\delta^\nu_\mu h\right) = 0, \tag{2.72}$$

which is useful on the weak field approximation. The remaining coordinate freedom is restricted to the transformations as

$$h'_{\mu\nu} = h_{\mu\nu} - \xi_{\mu,\nu} - \xi_{\nu,\mu}, \tag{2.73}$$

with

$$\left(\nabla^2 - \partial_t^2\right) \xi_{\mu\nu} = 0. \tag{2.74}$$

Btw, this is a usual solution on the harmonic-weak-field condition. Substituting Eq.(2.69)

to Eqs.(2.71-2.72), we obtain

$$h_{00} = 4\pi G\left(\sigma_w + 2p\right)|x| = -4\pi G\sigma_w|x|, \tag{2.75}$$

$$h_{11} = 4\pi G\left(\sigma_w - 2p\right)|x| = 12\pi G\sigma_w|x|, \tag{2.76}$$

$$h_{22} = h_{33} = 4\pi G\sigma_w|x|, \tag{2.77}$$

with

$$\xi_1 = 2\pi G\sigma_w x|x|, \quad \text{and} \quad \xi_0 = \xi_2 = \xi_3 = 0. \tag{2.78}$$

As we can see in this solution, the $h_{\mu\nu}$ will be larger than 1 at $|x| > 4\pi G\sigma_w$ i.e. the weak-field approximation is no longer valid. The energy-momentum tensor is given by

$$T^{00} = \sigma_w\delta(x - vt), \tag{2.79}$$

$$T^{22} = T^{33} = p\delta(x - vt), \tag{2.80}$$

$$T^{10} = T^{01} = \sigma_w v\delta(x - vt), \tag{2.81}$$

others are zero. From energy-momentum conservation, we have

$$T^{\nu}_{\mu,\nu} = 0 \quad \rightarrow \quad \partial_\nu\left(T^{\nu}_{\mu}\sqrt{-g}\right) = \frac{1}{2}\sqrt{-g}\frac{\partial g_{\sigma\tau}}{\partial x^\mu}T^{\sigma\tau}. \tag{2.82}$$

Consider $\mu = 1$ case, and integrating over x, we have

$$\frac{dv}{dt} = -\frac{1}{2}\frac{d}{dx}\left[h_{00} + \frac{p}{\sigma_w}\left(h_{22} + h_{33}\right)\right]. \tag{2.83}$$

If we take Eqs.(2.75-2.77) into Eq.(2.83), we will find

$$\frac{dv}{dt} = -\frac{1}{2}\frac{d}{dx}\left[-4\pi G\sigma_w|x| - 8\pi G\sigma_w|x|\right] = \begin{cases} 6\pi G\sigma_w, & x > 0 \\ -6\pi G\sigma_w, & x < 0 \end{cases} \tag{2.84}$$

It means the domain walls are repelled from each other [91].

Exact static solution of Domain wall gravity

Since as mentioned before, the weak field approximation is only work in the regime $|x| < 4\pi G\sigma_w$. We have to solve the exact solution on large distances. Again, consider the static solution with $T^{\nu}_{\mu} = 0$ everywhere except in y-z plane and using reflection symmetry $x \to |x|$, we have (The general solution with only depends on one spatial coordinate is call *Kasner* solution, if depends on (t, x) is *Rindler* solution [93])

$$ds^2 = e^{2u}\left(dt^2 - dx^2\right) - e^{2v}\left(dy^2 + dz^2\right), \tag{2.85}$$

where $u = u(t, x) = u(t, -x)$, $v = v(t, x) = v(t, -x)$ and they should be discontinuous at $x = 0$. The static solution is suggested by [92, 94],

$$ds^2 = (1 + A|x|)^{-1/2}\left(dt^2 - dx^2\right) - (1 + A|x|)\left(dy^2 + dz^2\right). \tag{2.86}$$

To find the constant A, we use weak field approximation regime $A|x| \ll 1$ to find the $h_{\mu\nu}$ metric as

$$h_{00} = -\, h_{11} = -\frac{1}{2}A|x|, \tag{2.87}$$

$$h_{22} = h_{33} = -A|x|. \tag{2.88}$$

This solution disagrees to Eqs.(2.75-2.77), since we do not consider the harmonic conditions Eq.(2.73) yet. We have to firstly using Eq.(2.73) as

$$h_{00} = -\,\frac{1}{2}A|x| - \xi_{0,0}, \qquad h_{11} = -\frac{1}{2}A|x| - \xi_{1,1}, \tag{2.89}$$

$$h_{22} = -\,A|x| - \xi_{2,2}, \qquad h_{33} = -A|x| - \xi_{3,3}. \tag{2.90}$$

Since the metric is function of x only, we expect $\xi_0 = \xi_2 = \xi_3 = 0$, therefore

$$\xi_1 = \frac{1}{2}Ax|x|. \tag{2.91}$$

Then compare to Eqs.(2.75-2.77),

$$A = -4\pi G\sigma_w, \qquad p = -\frac{1}{4}\sigma_w. \tag{2.92}$$

This solution does not match weak-field approximation. We should note that there is a singular at $1 + A|x| = 0$, since a negative A. To avoid this singular, we have to require $\sigma_w < 0$, which is a negative energy of the wall, is unphysical. So this solution is concluded in [91] that the static domain wall is gravitationally unstable and will eventually collapse

to singularities. However, this solution is wrong (the wrong metric was used Eq.(2.86)), the exact solution should be exactly matched to weak-filed approximation within $|x| < 4\pi G\sigma_w$. So the author redo the calculation, by using the metric as [92]

$$ds^2 = e^{-K|x|}\left[dt^2 - dx^2 - e^{Kt}\left(dy^2 + dz^2\right)\right], \tag{2.93}$$

they eventually found the constant $K = 4\pi G\sigma_w$, and at weak-field limit $K|x| \ll 1$, this result is matched to Eqs.(2.75-2.77). Furthermore, the proper distance from the wall ($x = 0$) to $x = \pm\infty$ is given

$$\int_0^\infty \exp\left(-Kx/2\right) dx = 2K^{-1} = \left(2\pi G\sigma_w\right)^{-1} = 2|x_{\max}|. \tag{2.94}$$

This gives an event horizon $d_H = \left(2\pi G\sigma_w\right)^{-1}$ that if an observer at $x = 0$ never sees particles or light cross the surfaces at $x = \pm\infty$ in his flat coordinate i.e. the $2K^{-1}$ in domain wall's non-flat coordinate.

An easier way to understand is that considering a sphere of domain wall with radius R. The mass of this sphere is $M = \pi R^2\sigma_w$. The event horizon is given

$$\frac{1}{2}mc^2 \leq \frac{GMm}{R} \quad \rightarrow \quad R \geq \left(2\pi G\sigma_w\right)^{-1} = d_H, \tag{2.95}$$

where the regime $R \geq d_H$ are all lied on light-cone $t = x$ line. For all the domain wall spheres within this condition, will they collapse? Answered in [95], only the spherical wall will collapse to the black hole, and Eq.(2.95) agrees to Eq.(3.9) in [95] but a factor 1/2. If

they do collapse, this also gives a collapsing time of the sphere domain wall as

$$t_c \sim (G\sigma)^{-1}\,. \tag{2.96}$$

After this time, the domain wall will collapse which may avoid the domain wall problem. Another question, can the domain wall's size be larger than d_H^2? By the way, the domain wall black hole is studied in [96].

Similar analysis can be used in the string case, the string loop has the mass as $M = 2\pi R\mu$, so similarly ($\mu = 2\pi\eta^2$)

$$\frac{1}{2}mc^2 \leq \frac{GMm}{R} \quad \rightarrow \quad \frac{1}{2}c^2 \leq \frac{G2\pi R\mu}{R} = 2\pi G\mu \quad \rightarrow \quad \eta \geq \frac{m_p}{2\sqrt{2}\pi}, \tag{2.97}$$

namely, the collapsing strings should enter to quantum gravity regime, that's why we don't need to worry about the string collapsing within current phenomenology. Furthermore, there has no constraint on string event horizon, so string loop is safely on its gravitational behavior. On the other hand, the string cannot help for forming BH, since the η should be much larger than inflation scale, the string will be diluted out by inflation.

- Kodama1994 [97]

They concluded that the domain wall does not emit gravitational waves spontaneously by its free oscillations. But the spherical symmetry may make the spacetime solutions describing the emission of gravitational waves

Chapter 3

Kinetic Misalignment Mechanism

3.1 Introduction

Axions are ultra-light pseudo-scalar particles that are generically predicted in the Peccei-Quinn (PQ) mechanism [98, 99, 100], a compelling solution for the Strong CP problem in particle physics. Recently QCD axions and axion-like particles (ALPs) have attracted substantial interest as a leading dark matter (DM) candidate alternative to WIMPs [101, 71, 72, 70].

Understanding the production mechanism of axions is critical for determining their potential as a viable DM candidate and related phenomenology [102, 5]. Despite extensive literature on this subject, our understanding is not yet complete. For instance, for post-inflationary PQ symmetry breaking, axion topological defects (cosmic strings, domain walls) necessarily form and through their subsequent decays may contribute to axion relic abundance (Ω_a) in significant ways [103, 104, 105, 106, 8, 107]. However, the prediction of such contributions is still challenging, while a growing effort has recently been made

[108, 109, 110, 31, 111, 112, 113, 114]. Meanwhile, our understanding of possible outcomes of the misalignment production may not be complete either. According to the conventional misalignment mechanism, axion field starts with an initial value, θ_i ($\theta \equiv a/Nf_a$), away from the true vacuum, then begins to oscillate around the minimum when its mass $m_a \sim 3H$ (H: Hubble expansion rate), and behaves like cold DM after that. In order to solve the equation of motion for axion evolution, the initial velocity $\dot{\theta}_i$ also needs to be specified, which is implicitly assumed to be zero in the conventional misalignment, and directly affects the Ω_a prediction. Meanwhile, nonzero $\dot{\theta}_i$ is possible and well-motivated. *Then how would a nonzero initial velocity of the axion field influence the axion relic abundance and phenomenology?*

In this work we propose and systematically investigate an alternative misalignment mechanism with an initial condition $\dot{\theta}_i \neq 0$. Based on classified benchmark examples in a UV model-independent approach, we demonstrate the conditions when axion relic density prediction can significantly differ from the conventional, with potentially dramatic enhancement or suppression depending on specifics with $\dot{\theta}_i$ and whether the PQ symmetry breaks before/during or after inflation. An example model realizing such an initial condition is illustrated in Appendix. B. Another recent work [115] also considered the possibility of $\dot{\theta}_i \neq 0$, focusing on the large $\dot{\theta} > 0$ region, demonstrating examples of interesting UV complete models leading to an enhanced Ω_a.

3.2 The Origin of a Nonzero Initial Velocity

Axion originates from the phase of a complex scalar Φ whose vacuum expectation value $f_a/\sqrt{2}$ leads to the spontaneous breaking of the $U(1)_{\rm PQ}$ symmetry (or a generic global $U(1)$ for ALPs) [1]:

$$\Phi \equiv \frac{1}{\sqrt{2}} (f_a + \phi)\, e^{ia/f_a} \tag{3.1}$$

where ϕ and a are the radial and angular (axion) modes, respectively. The conserved Noether charge associated with the PQ symmetry is $R^3 f_a^2 \dot{\theta}$ where R is the cosmic scale factor. $\dot{\theta}_i \neq 0$ thus corresponds to the rotation of the Φ field and an asymmetry of the global PQ charge. Such a charge asymmetry can result from higher dimensional operators that explicitly breaks $U(1)_{\rm PQ}$ in the early Universe, in analogy to the Affleck-Dine (AD) mechanism for baryogenesis [116, 117, 118, 119]. This effect in fact can be generic for an approximate global symmetry [119, 117, 118]. Alternatively $\dot{\theta}_i \neq 0$ may originate from axion models with a small dimensionful symmetry-breaking term which introduces a slope in axion potential [120]. Such PQ-breaking effects should be absent today in order not to undermine the solution to the Strong CP problem, which can be realized by tying its strength to the Hubble rate or a dynamical field that has a larger value in the early Universe. Although the specifics of $\dot{\theta}_i$ is model-dependent, important phenomenological insights can be obtained by studying the axion evolution with benchmark examples that we will demonstrate.

[1] Without loss of generality we focus on the simplest scenario where domain wall number $N = 1$.

3.3 Axion Misalignment Mechanism with a Nonzero Initial Velocity

We first present Fig. 4.1 as a cartoon illustration for two representative possibilities of $\dot{\theta}_i \neq 0$ initial condition (IC), with related technical details elaborated later. In conventional misalignment, axion field starts at rest with the rescaled field value θ_i, then roll down the periodic potential well, and start oscillating when $m_a \sim 3H$ (at $t_o^{con} \sim 1/m_a$). In both cases we show, the field starts with θ_i at time t_i. The lower panel demonstrates the possibility where the axion field has a negative moderate initial velocity to allow it to roll down further in the potential well so that the field value becomes smaller than θ_i when oscillation begins. This would lead to a suppression of the axion relic density. The upper panel shows the possibility with a high initial velocity, which may delay the onset of oscillation (at t_o) to be later than t_o^{con}, thus reduce the entropy $s(t_o)$ then and enhance the relic density of the axion ($\Omega_a \propto Y_a \equiv n_a/s$).

We now study the dynamics of axion evolution in details. The equation of motion (e.o.m) of axion field with rescaled $\theta(t) \equiv a(t)/f_a \pmod{2\pi}$ in FRW cosmology is [2]

$$\ddot{\theta} + 3H\dot{\theta} + m_a^2(T)\theta = 0. \tag{3.2}$$

In the conventional misalignment mechanism, $\dot{\theta}(t_i) \equiv \dot{\theta}_i = 0$, and the axion field freezes at a random initial field value θ_i from PQ breaking to QCD phase transition. For post-inflation PQ breaking, Ω_a is obtained by averaging over the randomly distributed θ_i over all causal

[2] We assume that by t_i of our consideration the radial mode has settled into its true vacuum, therefore does not influence axion evolution through coupled e.o.m's.

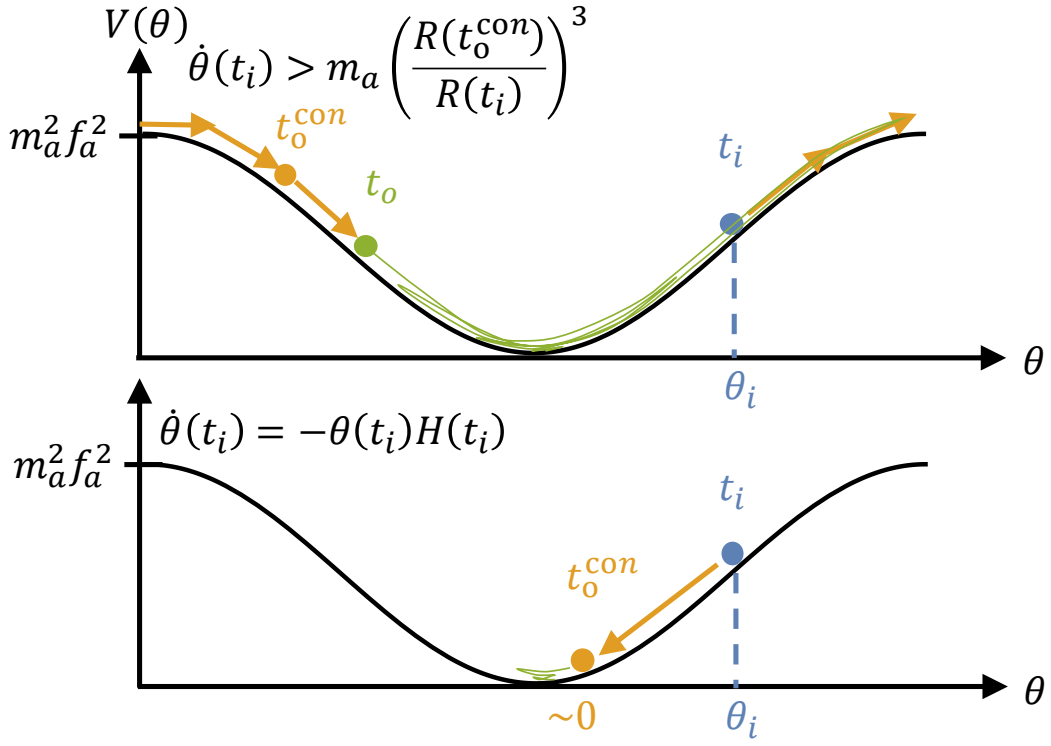

Figure 3.1: Cartoon illustration of the axion field evolution for the two representative possibilities with $\dot{\theta}_i \neq 0$, as explained in the text. The axion starts at θ_i as blue, then follows the orange arrows until it starts to oscillate at $t_o(t_o^{con})$. The green trajectory represents the sequence of motion. In the conventional misalignment, the field starts with $\dot{\theta}_i = 0$.

patches. For QCD axion, we will assume $m_a(T) \propto T^{-4}$ as found by instanton calculation [121, 122, 123, 124, 125], while a constant m_a may apply for general ALPs.

We start by investigating the axion evolution at early times well before oscillation starts. The starting time t_i is generally assumed to be at PQ breaking scale, but can be later times when the axion picks up a nonzero $\dot{\theta}_i$. Allowing $\dot{\theta}(t_i) \neq 0$, and dropping the potential term in Eq. 3.14 which is negligible for this early regime, we find the following

solution in general cosmology, with background energy density $\rho \propto R^{-n}$:

$$\theta(t) = \begin{cases} \theta_i + \dfrac{\dot{\theta}_i}{H_i}\left(\dfrac{2}{6-n}\right)\left[1 - \left(\dfrac{R(t)}{R(t_i)}\right)^{n/2-3}\right], & (n \neq 6) \\ \theta_i + \dfrac{\dot{\theta}_i}{3H_i}\ln\left[\dfrac{t}{t_i}\right], & (n = 6) \end{cases} \tag{3.3}$$

$$\dot{\theta}(t) = \dot{\theta}_i \left(\frac{R(t_i)}{R(t)}\right)^3. \tag{3.4}$$

We will assume standard cosmology (i.e. radiation domination (RD), $n = 4$, thus $\theta(t) \propto 1/\sqrt{t}$) except when considering inflationary effects. The energy density of the axion evolves as $\rho_a(t) = \frac{1}{2}\dot{\theta}^2(t) f_a^2 + \frac{1}{2} m_a(T)^2 \theta(t)^2 f_a^2$, and relic density can be estimated as:

$$\Omega_a = m_a(T_o) m_a(T=0) \theta_o^2 f_a^2 \frac{s_0}{s(t_o)\rho_c}, \tag{3.5}$$

where $\theta_o \equiv \theta(t_o)$, t_o implicitly depends on $\dot{\theta}_i$, s_0 and ρ_c are the current-day entropy and critical density, respectively.

We now specify two benchmark types of initial condition of $\dot{\theta}_i$ to find concrete form of solutions given by Eqs. 3.3.

Type-I IC: $\dot{\theta}_i = -\delta H_i$, where δ is a constant parameter independent of θ_i. To simplify discussion we choose the convention of $\delta \geq 0$ without loss of generality [3]. While the detailed UV physics leading to such initial conditions is not our focus here, they may arise from an AD-like scenario [126], which readily gives $|\dot{\theta}(t_i)| \sim H(t_i)$ upon PQ-breaking at $t_i \sim m_{\rm pl}/f_a^2$ (assuming PQ-breaking during radiation domination around $T \sim f_a$) [4]. Applying this IC

[3] The late time evolution of the field with $\delta < 0$ is nearly the same as their $\delta > 0$ counterpart.

[4] The specifics of initial velocity depends on the radial mode in the UV model. The AD mechanism can generate a initial velocity with a varying ratio to the Hubble rate, see e.g. [126, 127, 128].

to Eq. 3.3 in RD we find

$$\theta(t) = \theta_i - \delta + \delta \left(\frac{R(t_i)}{R(t)} \right), \quad \text{Mod}[2\pi]. \tag{3.6}$$

Provided a small/moderate $\dot{\theta}(t_i)$, the oscillation onset t_o in the new scenario is also close to t_o^{con}. However, with sufficiently large $\dot{\theta}_i$ the kinetic energy (KE) could be larger than the potential energy V at t_o^{con}, and oscillation can only start later when KE $\sim$ V. Such a delayed t_o may enhance Ω_a since $\Omega_a \sim \rho_a(t_o)/s(t_o)$. For high $|\dot{\theta}_i|$ we can estimate t_o as the earliest time when KE and V become equal ($\theta_o \approx 2\pi$):

$$\dot{\theta}_i \, (t_i/t_o)^{3/2} \approx 2\pi \, m_a(t_o). \tag{3.7}$$

Combining Eq. 3.7 and $m_a(t_o^{con}) \approx 3H(t_o^{con})$, we can find the critical δ_c: for $\delta > \delta_c$ a notable delay of t_o relative to t_o^{con} would occur:

$$\delta_c \approx 6\pi \, (t_o^{con}/t_i)^{1/2} \simeq 2 \times 10^{11} \left(\frac{f_a}{10^{11}\,\text{GeV}} \right)^{7/6}, \tag{3.8}$$

where we assumed t_i around the PQ-breaking time $\sim M_P/f_a^2$. Note that δ_c can be much smaller if t_i (when axion picks up a nonzero velocity) is much later than PQ-breaking time.

Next we will discuss the evolution patterns in different δ parameter regions based on Eqs. 3.3, 3.13. The two distinct scenarios of PQ breaking after and before/during inflation will be considered in order.

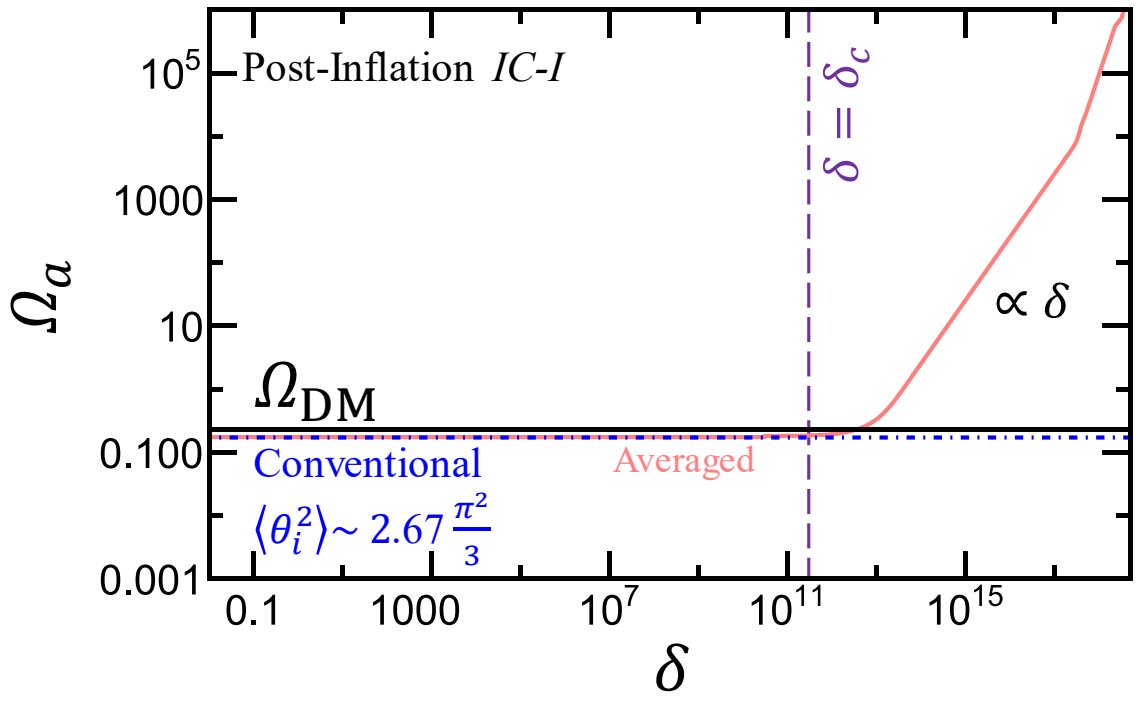

Figure 3.2: The dependence of axion relic abundance on initial velocity (δ) for Type-I IC, post-inflation PQ breaking ($f_a = 10^{11}$ GeV). The kink around $\delta \sim 10^{20}$ is due to the change in the number of relativistic degrees of freedom, g_*, which is accounted for in our numerical calculation.

IC-I: Post-inflationary $U(1)_{PQ}$ breaking.

In each of the following cases, we consider the field evolution with a random initial field value θ_i which upon considering Ω_a will be averaged over post-inflationary causal patches as $\langle\theta_o^2\rangle = \langle\theta_i^2\rangle \sim 2.67\pi^2/3$ [129, 130].

(i) $0 < \delta < \theta_i$, i.e., with generally small initial KE. For generic $\theta_i \sim 1$, although the $\frac{R(t)}{R(t_i)}$ term in Eq. 3.3 slightly reduces $\theta(t)$ over time, the effect is negligible relative to the constant term and $\theta_o \sim \theta_i$. Therefore the axion evolution and the prediction $\Omega_a \propto \theta_o^2$ is very similar to the conventional prediction Ω_a^{conv} and remains so after averaging over causal patches.

(ii) $\theta_i < \delta < \delta_c$, i.e., with moderate initial KE. In this case KE becomes important at early

stages of the field evolution, but is not yet sufficient to cause a notable delay of the t_o relative to t_o^{con}. In this regime as δ increases θ_o and thus Ω_a become more sensitive to δ (oscillatory dependence) due to the periodic nature of the field potential. In particular, Ω_a can be much suppressed for particular δ values that causes cancelation among the θ_i and δ-dependent terms in Eqs. 3.13, i.e., when

$$\theta_o = 2\pi k, \qquad k \in \mathbb{Z}. \tag{3.9}$$

However, with a constant δ such an accidental cancelation only occurs for certain θ_i's, and its effect is washed out after averaging. Consequently, the Ω_a prediction is comparable to Ω_a^{con}.

(iii) $\delta > \delta_c$, i.e., with high initial KE. This case is similar to the above (ii), yet the difference is that KE is reshifted to $\sim V$ after t_o^{con}, so the oscillation is delayed. Although $\rho(t_o)$ is the same as in case (ii) at the onset of axion oscillation, the entropy then is diluted as $s(t_o) \sim s(t_o^{con})\,(t_o^{con}/t_o)^{3/2} \propto \delta^{-1}$ (using Eqs. 3.13, 3.7). Like in (ii), accidental cancelation Eq. 3.9 can happen but becomes irrelevant after averaging. Therefore Ω_a is enhanced relative to Ω_a^{con} by a factor of $\sim \delta/\delta_c$.

(iv) $\delta = \theta_i$ or $\delta \approx \theta_i$, the special regime where δ is equal to or in the close vicinity of θ_i. This case is qualitatively different from the previous ones. Due to the (almost) cancelation between θ_i and δ, $\delta\left(\frac{R(t_i)}{R(t)}\right)$ term in Eq. 3.13 dominates the evolution which causes a potentially dramatic decrease in $\theta(t)$ until oscillation starts around $t_o \sim t_o^{con}$, with $\theta(t_o) = \theta_o \ll \theta_i$.

$\rho_a(t_o)$ would be expected to be suppressed by $\sim \theta_o^2/\theta_i^2$ relative to the conventional. However, he cancelation between δ and θ_i only occurs for patches with peculiar θ_i, and the effect disappears after averaging over post-inflationary patches.

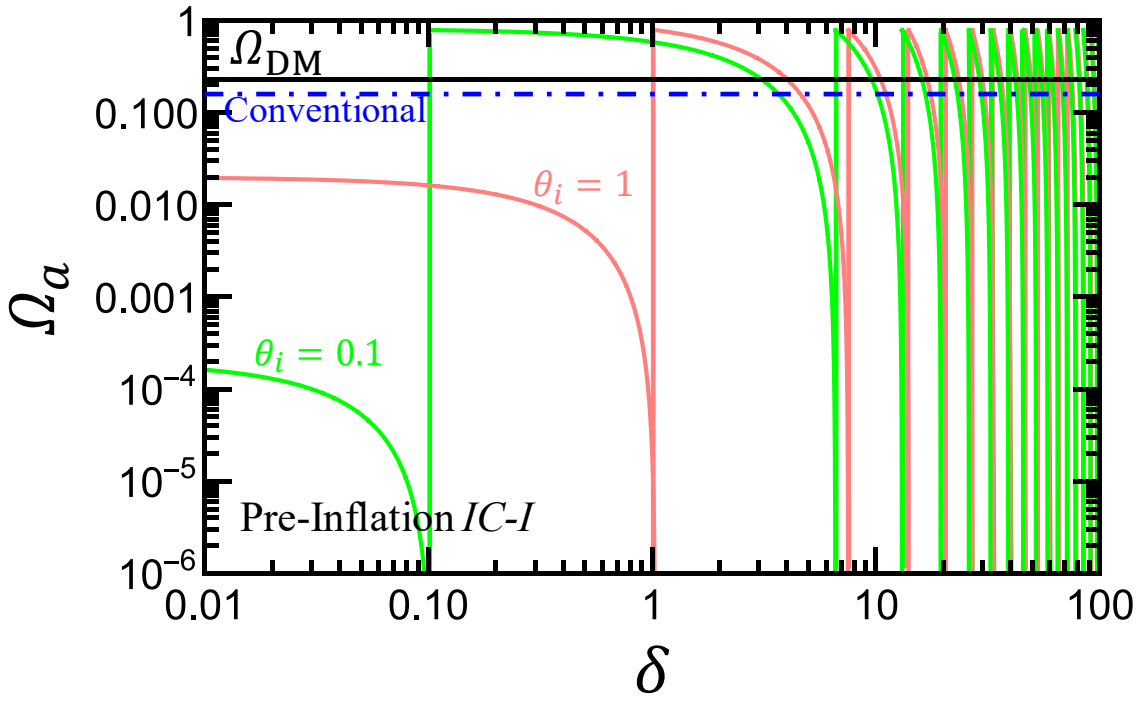

Figure 3.3: The dependence of axion relic abundance on initial velocity (δ) for Type-I IC, pre/during-inflation PQ breaking ($f_a = 10^{11}$ GeV, $t_I = 10^3 t_i$). The oscillatory dependence in large δ region is shown.

Detailed illustrations for the field evolution in each of these cases can be found in Fig. S1 in the Appendix. A. A representative example of Ω_a-δ relation is shown in Fig. 3.2 based on numerical results. The analytical estimate of Ω_a is summarized later in Eq. 3.10. *The upshot for the post-inflation scenario is: Ω_a can be similar to or enhanced relative to the conventional misalignment due to $\dot{\theta}(t_i) \neq 0$, while the potential suppression effect in specific patches is resolved after averaging over post-inflationary causal patches.*

IC-I: Before or during inflation $U(1)_{PQ}$ ***breaking.*** During inflation the KE in the axion field is rapidly diluted, while θ_i or the potential energy freezes in as its value at the onset of inflation (or at PQ breaking time if PQ breaks during inflation). Many of the discussions for the post-inflationary scenario apply here, but there are key differences due to inflationary effects. We briefly summarize the results for the same four cases as follows:

(i) $0 < \delta < \theta_i$: similar to the conventional pre-inflationary case.

(ii) $\theta_i < \delta < \delta_c$: in general similar to the conventional, but unlike in the post-inflationary scenario, the accidental cancelation/suppression on Ω_a (i.e. $\theta_o \approx 0$ in Eq.(3.9)) persists without the averaging.

(iii) $\delta > \delta_c$: the situation with ρ_a evolution is similar to the above (iii), but the enhancement due to the diluted $s(t_o)$ is absent due to the intervention of inflation which cuts short the KE domination time (unless inflation happens after QCD phase transition). Therefore the result is in general similar to the conventional, but accidental suppression is possible for certain δ.

(iv) $\delta = \theta_i$ or $\delta \approx \theta_i$. For PQ breaking during inflation, the situation is similar to the conventional, since the initial KE is quickly depleted by inflation before it can drive down θ_i value. However, if the PQ breaks before inflation with a moderate/large separation in their scales, the $\dot{\theta}(t_i) \neq 0$ initial condition can leave a trace despite inflation: the field value is already driven down to $\theta_I \equiv \theta(t_I) \approx \frac{R(t_i)}{R(t_I)}\theta_i$ for $\theta_i - \delta \to 0$, where t_I is when inflation starts. $\theta(t_I)$ then freezes in as the effective new initial condition for axion misalignment after inflation.

Detailed illustrations for the field evolution in each of these cases can be found in Fig. S2 in Appendix. A. A representative example of Ω_a-δ relation for this scenario is illustrated in Fig. 3.3 based on numerical results. *The upshot for this pre/during inflation scenario is: Ω_a is similar to or suppressed relative to the conventional due to $\dot{\theta}(t_i) \neq 0$, while the potential enhancement effective in post-inflationary case is wiped out by inflation.*

We now summarize the prediction for Ω_a with IC-I for post- and pre-inflation cases in order:

$$\Omega_a^{\text{post}-\text{I}} \simeq \begin{cases} \Omega_a^{con} = 0.02\,\langle\theta_o^2\rangle \left(\dfrac{f_a}{10^{11}\,\text{GeV}}\right)^{7/6}, & \delta < \delta_c \\ \Omega_a^{con}\dfrac{\delta}{\delta_c} \simeq 0.01\,\langle\theta_o^2\rangle \left(\dfrac{\delta}{10^{11}}\right), & \delta \geq \delta_c, \end{cases} \tag{3.10}$$

and

$$\Omega_a^{\text{pre}-\text{I}} = \Omega_a^{con}\frac{\theta_I^2}{\langle\theta_o^2\rangle}, \tag{3.11}$$

For the last equality in the 2nd line of Eq. 3.10, we used Eq. 3.8 which assumes t_i at PQ breaking scale $t_i \sim m_{pl}/f_a^2$. Other t_i choices would change the numerics. θ_I in Eq. 3.11 is obtained from Eq. 3.13 with $t = t_I$, which as discussed can lead to a suppression in $\Omega_a^{\text{pre}-\text{I}}$ when $\theta_i \approx \delta$.

Note that *case (iv) of this scenario provides a new possibility for Ω_a to account for Ω_{DM} with $f_a \gtrsim 10^{11}$ GeV* due to specific relations between θ_i and $\dot{\theta}_i$ even with a natural $\theta_i \sim 1$. On the other hand, one could argue that this is trading one type of fine-tuning for another type. Although challenging it is curious to see if it is possible to distinguish the

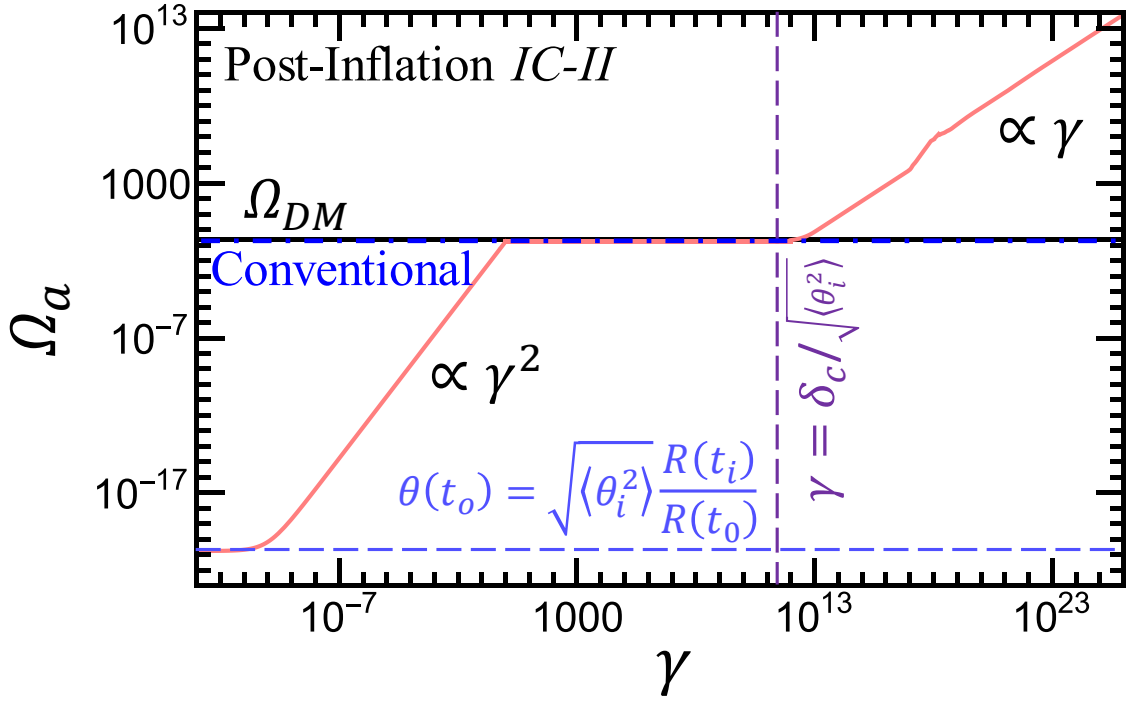

Figure 3.4: . The dependence of axion relic abundance on initial velocity (γ) for Type-II IC ($f_a = 10^{11}$ GeV), post-inflationary PQ-breaking.

two types of fine-tuning combining various avenues of observational data.

Type-II IC: $\dot{\theta}_i = -(1-\gamma)\theta_i H_i$, where $\gamma \geq 0$. This IC is inspired by case (iv) with Type-I IC. Most results in IC-I apply, with the replacement of $\delta \to (1-\gamma)\theta_i$ in Eq. 3.13. The key difference is that here the relation $\dot{\theta}_i \propto \theta_i$ is assumed to be valid for any θ_i, *therefore the aforementioned suppression effect in case (iv) (here $\gamma \to 0$) is robust and survives even after averaging patches for post-inflationary PQ breaking.* The realization of such an IC generally requires an explicit PQ breaking term in the axion potential effective in the early Universe, which is beyond the scope of this work but would be interesting to explore. *We highlight this possibility since it provides a novel dynamic way to accommodate*

large $f_a \gtrsim 10^{11}$ GeV QCD axion as a DM candidate for post-inflation PQ breaking. Despite requiring a special relation between θ_i and $\dot{\theta}_i$, this solution is intriguing considering that for post-inflationary PQ breaking in the conventional misalignment there is no way to even fine-tune to accommodate $f_a \gtrsim 10^{11}$ GeV, since θ_i is averaged to $O(1)$. We show the Ω_a-γ relation for IC-II in Figs. 3.4 and 3.5, for post- and pre-inflation PQ-breaking, respectively.

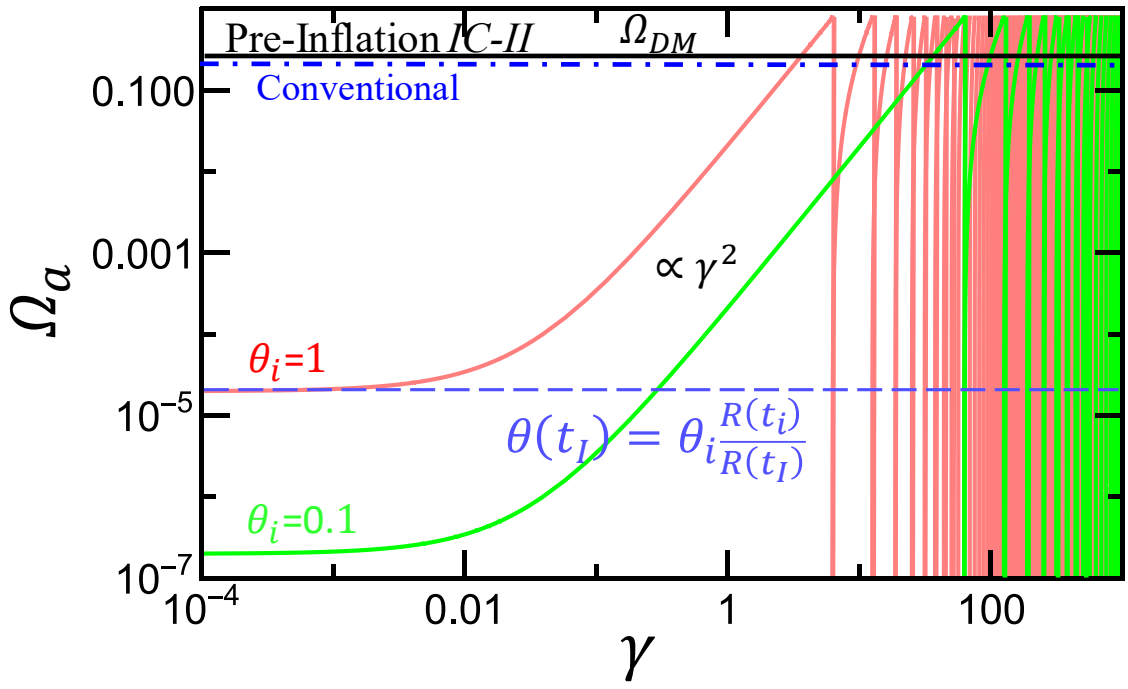

Figure 3.5: . The dependence of axion relic abundance on initial velocity (γ) for Type-II IC ($f_a = 10^{11}$ GeV and $t_I = 10^3 t_i$), pre/during-inflationary PQ-breaking.

The main difference from IC-I in the Ω_a prediction, i.e., for case (iv) (small γ) in the post-inflation scenario, is demonstrated with the following formula:

$$\Omega_a^{\rm post-I} \simeq \begin{cases} \Omega_a^{con}\gamma^2, & 1.3cm\frac{R(t_i)}{R(t_o)} \le \gamma \le 1 \\ \Omega_a^{con}\left(\frac{R(t_i)}{R(t_o)}\right)^2, & 0.45cm0 \le \gamma \le \frac{R(t_i)}{R(t_o)}, \end{cases} \tag{3.12}$$

where we can clearly see the suppression relative to the conventional by a factor of γ^2 or $\left(\frac{R(t_i)}{R(t_o)}\right)^2$. This result shows that the relic abundance of axion can be either very large or being suppressed to be very small. All the parameter space that is constrained by dark matter relic abundance turns out free.

3.4 The dynamics of Axion Evolution with An Initial Velocity

In this section, we illustrate the time evolution of $\theta(t), |\dot{\theta}(t)|, \rho_a(t)$ for the different scenarios of non-zero $\dot{\theta}_i$ in the main text. We will refer to Type-I IC to be specific, while each of the cases may apply to Type-II IC by the substitution of $\delta \to (1-\gamma)\theta_i$ in $\theta(t)$ solution as

$$\theta(t) = \theta_i \left[\gamma + (1-\gamma)\left(\frac{R(t_i)}{R(t)}\right)\right], \quad \text{Mod}[2\pi]. \tag{3.13}$$

The difference between IC-I and IC-II in predicting Ω_a is explained in the main text. The results shown in Figs. 3.6, 3.7 are obtained by solving the equation of motion

$$\ddot{\theta} + 3H\dot{\theta} + m_a^2(T)\theta = 0. \tag{3.14}$$

By solving the above E.O.M, we can also obtain the averaged background energy density $\bar{\rho}_a$ and pressure $\bar{P}_a$ of the axion field are:

$$\bar{\rho}_a = \frac{1}{2}\dot{a}^2 + \frac{1}{2}m_a^2 a^2, \qquad \bar{P}_a = \frac{1}{2}\dot{a}^2 - \frac{1}{2}m_a^2 a^2. \tag{3.15}$$

The equation of state can then be found by applying

$$w(t) \equiv \frac{\bar{P}_a}{\bar{\rho}_a}. \tag{3.16}$$

IC-I Post-inflationary $U(1)_{PQ}$ ***breaking:*** the representative solutions for this scenario in the following four cases are illustrated in Fig. 3.6. θ_i takes a random initial value which will be averaged over post-inflationary patches for Ω_a calculation

(i) $0 < \delta < \theta_i$, i.e., with generally small initial KE. This is illustrated with green dashed lines ($\delta \sim 0$, overlapping with conventional case) in Fig. 3.6 for constant m_a, while for QCD axion the evolution before t_o^{con} follows the orange line (overlapping with green for $w(t)$ and $\theta(t)$).

(ii) $\theta_i < \delta < \delta_c$, i.e., with moderate initial KE. The evolution for this case is illustrated with blue lines in Fig. 3.6 (for θ_i away from the cancelation region $\theta_o = 2\pi k, \quad k \in \mathbb{Z}$). Due to the dominance of KE over V in early times, both the constant m_a and the QCD cases essentially follow same evolution (this also applies to the case (iii) and (iv) below). We can see that due to the large θ_i the field's equation of state in early stage is kination-like.

(iii) $\delta > \delta_c$, i.e., with high initial KE. This case is illustrated with black lines in Fig. 3.6.

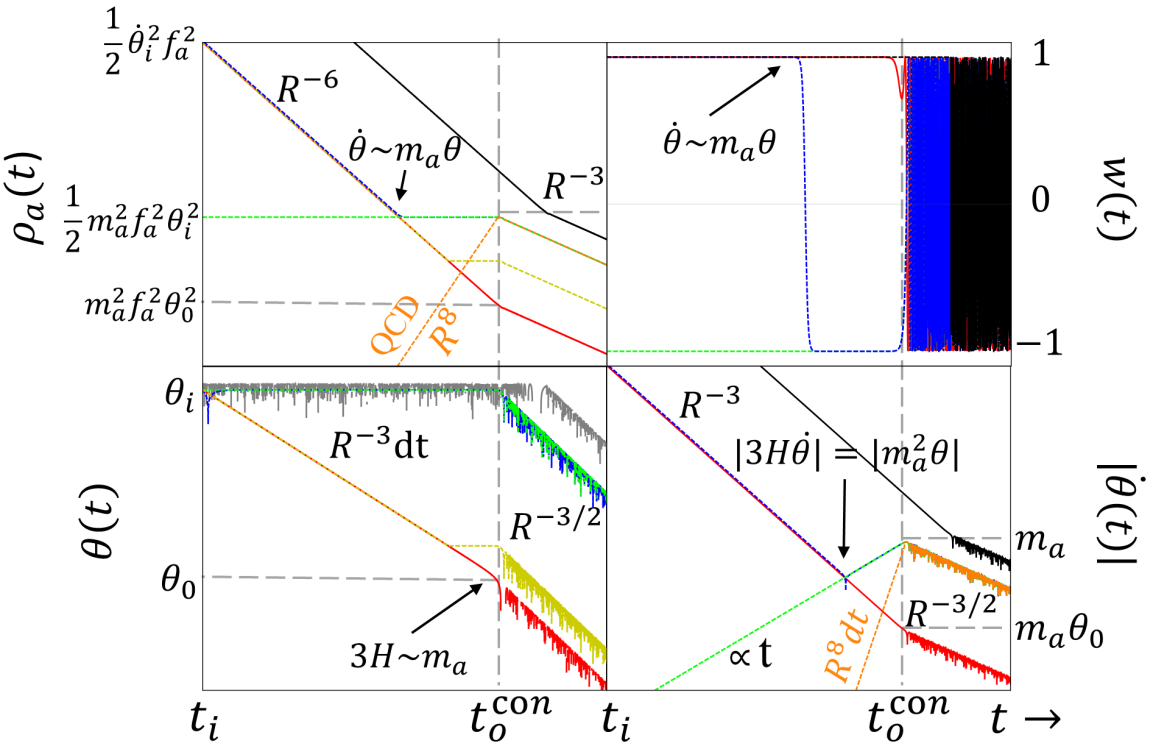

Figure 3.6: The time evolution of the axion field with Type-I IC in post-inflation PQ-breaking scenario (for an individual θ_i, before averaging). Green/orange: case (i), blue: case (ii), black: case (iii), red: case (iv). In addition, we assume the axion mass $m_a^2 \propto R^8$ as QCD axion in orange curve, others are assumed as constant. Details are also given in the text.

(iv) $\delta = \theta_i$ or $\delta \approx \theta_i$, the special regime where δ is equal to or in the close vicinity of θ_i. This case is demonstrated in red in Fig. 3.6 for $\delta = \theta_i$, in yellow for $\delta \approx \theta_i$. ***IC-I Pre-inflationary*** $U(1)_{PQ}$ ***breaking:*** the representative solutions for this scenario in the following four cases are illustrated in Fig. 3.6, with the same color codes as in their post-inflationary counterparts.

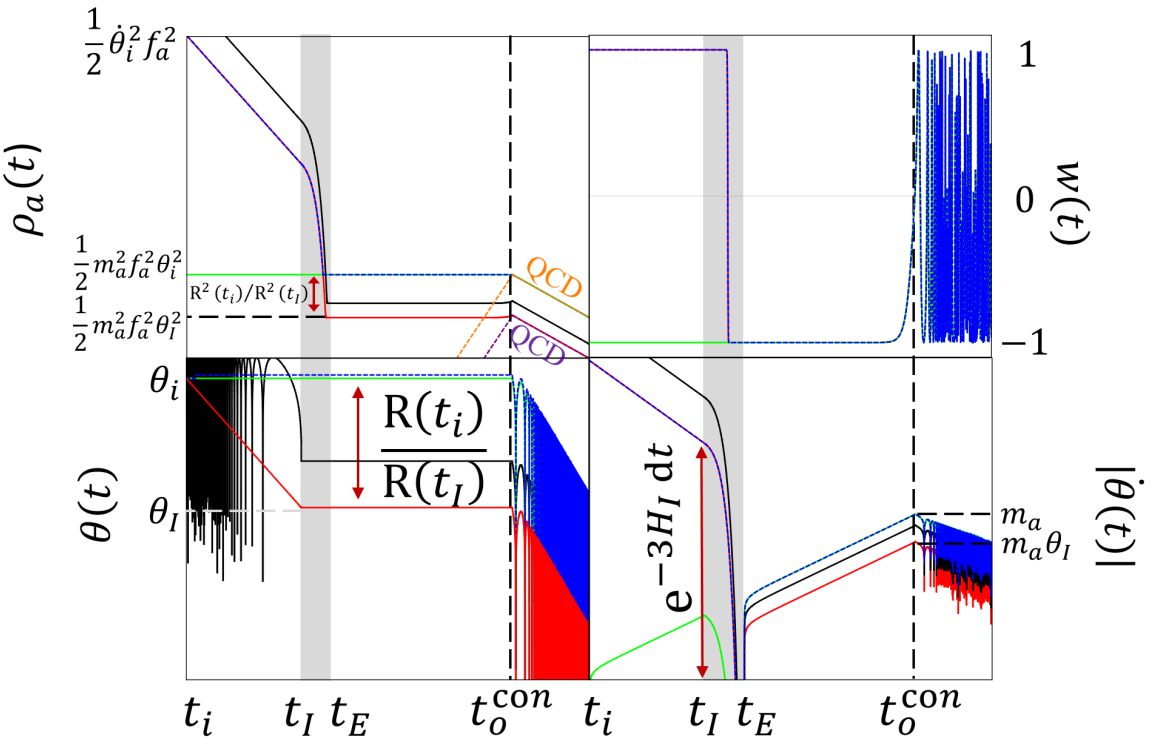

Figure 3.7: The time evolution of the axion field with Type-I IC, in the pre-inflationary PQ-breaking scenario. Color codes are the same as in Fig. 3.6. In addition, we assume the axion mass $m_a^2 \propto R^8$ as QCD axion in orange and purple curves, others are assumed as constant. Details are given in the text.

3.5 An Example Model Generating An Axion Initial Velocity

In this section, we demonstrate a simple example of generating a nonzero initial velocity of axion starting from $\dot{\theta}(t \to 0) = 0$, as a result of the breaking of axion shift symmetry in the early Universe. Such a symmetry breaking is analogous to that realized at late times by the QCD instanton effect. This is consistent with the expectation that PQ symmetry, as a global symmetry, is generally considered approximate/accidental. In particular, we consider the following effective action involving higher dimension operators

(dimension $\lambda+1$, $\lambda>0$):

$$S \supset -\int dx^4\sqrt{-g}\Bigg[\partial^\mu\Phi_i^\dagger\partial_\mu\Phi_i+\lambda_1\left(\Phi_1^\dagger\Phi_1-\frac{f_a^2}{2}\right)^2 + g_f\left(\frac{\Phi_2}{\Lambda_2}\right)^\lambda\Phi_1+h.c.\Bigg],$$

with

$$\Phi_1=\frac{1}{\sqrt{2}}\left(f_a+\phi\right)e^{ia/f_a}, \tag{3.17}$$

where $i=\{1,2\}$, and Φ_2,ϕ are CP-even scalar. The angular mode of Φ_1 is identified as the axion, while there is no spontaneous symmetry breaking occurring through Φ_2 (at least in the early universe). For simplicity, we assume the effective coupling g_f is real, and this term explicitly breaks the axion shift symmetry. Λ_2 is the cutoff scale of this effective action, and $\Lambda_2\gg f_a$. The effective potential can be rewritten by the form

$$\mathcal{L}\supset-\sqrt{2}g_f f_a\left(\frac{\Phi_2}{\Lambda_2}\right)^\lambda\cos\left(\frac{a}{f_a}+\alpha_0\right). \tag{3.18}$$

Considering the motivated possibility that Φ_2 may be displaced from its true vacuum at the end of inflation, the dynamics of the field Φ_2 in Eq.(3.18) provides a variety of possibilities to generate a nontrivial axion velocity at $t_{\rm osc}$ (the onset of axion oscillation). For instance, we consider that $V(\Phi_2)$ takes the following power-law form, which can occur in e.g. quintessence

models [131, 132, 133, 134]:

$$V(\Phi_2) = g_N \Phi_2^N, \tag{3.19}$$

where g_N is a constant parameter. We simply assume that this term dominates the potential in early universe. With the dominant background energy density generically parametrized as $\rho \propto R^{-m}$, we find $\rho_{\Phi_2} \propto R^{-n}$, where $n = \left(\frac{N}{N-2}\right) m$. By solving the time evolution of Φ_2 in this potential, we find

$$\Phi_2(t) \propto t^{1-N/(N-2)}, \quad \forall\, N > 2., \;\; n \neq m, \;\; \frac{6-n}{m} > 0, \tag{3.20}$$

Plugging this solution to Eq.(3.18), we obtain the axion potential at early times:

$$V_\Lambda(a) = \Lambda^4 \left(\frac{t_2}{t}\right)^p \cos\left(\frac{a}{f_a} + \alpha_0\right), \tag{3.21}$$

where $\Lambda^4 \equiv \sqrt{2} g_f f_a (M_2/\Lambda_2)^\lambda$ with initial field value of $\Phi_2(t_2) = M_2$, $p \equiv -\lambda(1 - N/(N-2)) > 0$. With the $V_\Lambda(a)$ given above, we can write down the parametrized equation of motion for the axion field:

$$\begin{aligned} \ddot{a} + \frac{6}{m}\frac{1}{t}\dot{a} \; - \frac{\Lambda^4}{f_a}\left(\frac{t_2}{t}\right)^p \sin\left(\frac{a}{f_a} + \alpha_0\right) \\ + m_a^2(T) f_a \sin\left(\frac{a}{f_a}\right) = 0. \end{aligned} \tag{3.22}$$

A key feature of this model with positive p is that the effect of the potential $V_\Lambda(a)$ is suppressed/negligible after $t \sim 1/m_a$. Consequently, the conventional axion dynamics is

restored after QCD phase transition. Therefore the axion has enough time to enter into QCD vacuum and behaves just like the standard QCD axion at late times. We also find that the constraint of solving strong CP problem is weaker than the DM relic density constraint. To see this, we know the following constraint from neutron EDM measurements:

$$\theta(t_0) < \theta_{QCD} \simeq 10^{-10}. \tag{3.23}$$

We also know that axion energy density today is

$$\rho_a(t_0) = m_a^2 f_a^2 \langle \theta^2(t_0) \rangle = 3.49 \times 10^{-5}\,\mathrm{GeV}^2 \langle \theta^2(t_0) \rangle,$$

where we substituted $m_a f_a = 5.7 \times 10^{-3}\,\mathrm{GeV}^2$ [121]. Therefore Eq. 3.23 implies an upper bound on axion relic abundance today. Putting all numerics together, we find $\Omega_a \lesssim 10^{22}$, which is a much more forgiving bound than the DM over-closure bound. Therefore the strong CP constraint can be satisfied as long as $\Omega_a \leq \Omega_{\mathrm{DM}}$, and the implied constraints on model parameters can be found in Eqs. 10-12 in the main text.

The example we demonstrated provides a class of models parametrized by p, λ and m, that can generate diverse possibilities of initial conditions for the axion field including a sizable initial velocity. In the following, we will show a choice of parameters that can generate our IC-I (iv) and IC-II.

Example: $p = 2$**,** $\lambda = 10$**,** $m = 4$

Here we consider $p = 2$, $\lambda = 10$, $m = 4$, consequently $N = 12$ and $n = 4.8$. In this case, the equation of motion of axion in the very early Universe can be approximately as the following (the choice of $\alpha_0 = \pi$ leads to $c > 0$, while $\alpha_0 = 0$ leads to $c < 0$, and QCD axion potential is negligible during this early era of interest):

$$\ddot{a} + \frac{3}{t}\dot{a} + \frac{c}{t^2}a = 0. \tag{3.24}$$

where define $|c| \equiv \Lambda^4 t_2^2 / f_a^2$. The solution is

$$a(t) = c_1 t^{n_+} + c_2 t^{n_-}, \tag{3.25}$$

where

$$n_\pm = \frac{1}{2}\left(-2 \pm \sqrt{4 - 4c}\right). \tag{3.26}$$

In general, c is suppressed by PQ-scale f_a and high energy physics scale Λ_2. Therefore, we expect $-1 \leq c \leq 1$ and consequently $-1 \leq n_+ \lesssim 0.414$. Assuming that initially at t_2, $a(t_2) \sim \pi f_a$ and $\dot{a}(t_2) = 0$, we find that n_+ term will dominate at late times, and the axion follows the relation

$$\frac{\dot{a}(t)}{a(t)} \simeq n_+ \frac{1}{t} = n_+ \frac{m}{2} H(t). \tag{3.27}$$

To give a numerical benchmark example, we consider

$$M_2 \sim 10^5 \mathrm{GeV}, \quad g_N \sim 1\,\mathrm{GeV}^{-8},$$

$$\Lambda \sim 10\sqrt{m_a f_a}, \quad m_a \sim 10^{-15}\,\mathrm{GeV},$$

$$t_2 \sim 10^{-2} t_o^{con}, \quad \alpha_0 = \pi.$$

This implies

$$c = \Lambda^4 \frac{t_2^2}{f_a^2} \sim 1 \quad \rightarrow \quad n_+ \sim -1, \tag{3.28}$$

therefore

$$\frac{\dot{a}(t_o^{con})}{a(t_o^{con})} = \frac{\dot{\theta}(t_o^{con})}{\theta(t_o^{con})} \sim n_+ \frac{m}{2} H(t_o^{con}) \sim -H(t_o^{con}). \tag{3.29}$$

This gives our IC-I-(iv) and IC-II.

Chapter 4

Global String Gravitational Waves and Archaeologies

4.1 Introduction

The detection of gravitational waves (GW) by the LIGO/Virgo collaboration [135, 136, 137] opens up a new observational window into the cosmos, and offers unprecedented opportunities to probe fundamental physics beyond the Standard Model (SM). The presence of a cosmologically generated stochastic GW background (SGWB) is highly motivated and has been actively searched for/studied by the LIGO and LISA collaborations [138, 139, 140, 141]. Although still being investigated, the intriguing stochastic signal recently reported by the NANOGrav collaboration [142, 143, 144] has been shown to be possibly explained by a SGWB of cosmic origin [145, 146, 147, 148, 149, 150, 151, 152]. Furthermore, the detection of a cosmogenic SGWB can potentially address many long-standing questions in particle

physics and cosmology (e.g. [153, 154, 14, 13, 155, 156, 157, 158, 159, 160, 161, 162, 163]), and allows us to probe very early stages of the Universe.

Among the known cosmological sources of SGWB (see review [164]), cosmic strings stand out as one that can yield strong signals over a wide frequency range due to continuous emission over a long period of time. Cosmic strings are one-dimensional, topologically stable objects that are generically predicted by many theoretical extensions of the Standard Model of particle physics, e.g., field theories with a spontaneously broken $U(1)$ symmetry (gauge or global) [165, 166, 167, 168, 169, 170, 171], and the fundamental and/or composite strings in superstring theory [172, 173, 174, 175, 176]. After formation, the strings quickly evolve towards a scaling regime where the string network consists of a few Hubble-length long strings per horizon volume, along with more copious loops formed by long string intersections. The loops then oscillate and radiate energy in the form of GWs and/or other particles until they decay away. Most literature on GW signatures from cosmic strings have been focused on those sourced by local strings or superstrings which typically can be described by Nambu-Goto (NG) action. In contrast, a global string network as a potential source of GWs has been largely ignored since by naive estimate GW radiation would be overwhelmed by Goldstone emission which occurs with a much larger rate. Very recently, inspired by its intimate connections to axion dark matter physics, significant progress has been made in simulating global topological defects and on the GW signals originated from it [109, 111, 177, 178, 15]. With a semi-analytical approach based on the Velocity-dependent One-Scale (VOS) model, our earlier work [156] demonstrated that the GW signal from global strings, albeit notably smaller than that from its NG string counterpart, can be within reach

of future GW experiments such as LISA [140, 141], AEDGE [179], DECIGO and BBO [180]. Such a positive prospect of detection has been confirmed by simulation-based work [15, 178], although details differ which will be addressed in this work.

The frequency spectrum of the SGWB from a cosmic string network can also serve as a powerful tool to probe the very early cosmic history that is not accessible by existing means. The ΛCDM cosmology was established based on precise measurements of electromagnetic radiation over different frequency ranges with a variety of experiments. A simple extrapolation of ΛCDM cosmology back in time suggests that the Universe is radiation dominated from the recent matter-radiation equality all the way back to the end of inflation. This paradigm is supported by observing cosmic microwave background (CMB), the relic photons that started free traveling when the radiation temperature was about 0.3 eV. The success of BBN theory in predicting primordial abundances of light elements also provides evidence for a radiation dominated era up to $T \sim 5$ MeV. However, the hypothesis of radiation domination (RD) for epochs prior to BBN or at radiation temperature higher than ~ 5 MeV is yet to be experimentally tested. On the other hand, possibilities of non-standard pre-BBN cosmologies are well motivated by many grounds, such as dark matter [181, 182], axion physics [183, 5], baryogenesis [184, 185], non-minimal inflation/reheating [186, 187], and string compactification [188, 189]. In particular, recently there has been an increased interest in the impact of non-standard cosmology on dark matter physics [190, 191, 192]. The discovery of GWs leads to unprecedented opportunities to shed light on this mysterious pre-BBN primordial dark age [193, 194, 195]. GWs are the only cosmic messengers that can travel freely throughout space-time since the Big Bang. They carry

unique information about the earliest phases of the Universe's evolution, beyond what can be assessed by observing EM radiations. Due to the continuous, potentially strong GW emissions from a string network throughout a long era of cosmic history, the SGWB frequency spectrum from cosmic strings is particularly appealing as a tool for looking back in time or *cosmic archaeology* [14, 13, 155]. The application of this idea in the context of NG strings was recently proposed and studied in [14, 13], based on a frequency-time (temperature) correspondence. Cosmic archaeology with global string induced GWs was only briefly discussed in [156], which we will explore in great detail in this update.

In this work, we aim at an extensive study of SGWB signals originated from a global string network, and a comprehensive investigation into the potential new physics imprints in the pre-BBN Universe that can be detected with such a GW spectrum. Greater technical details are given, which may serve as a handy reference for future studies. Our primary approach is to use the analytic VOS model calibrated with simulation results (directly obtained for early times). Due to technical difficulties of simultaneously capturing physics at hierarchical scales, current simulations can only cover the evolution history of a global string network up to a few e-folds of Hubble expansion after the formation time. Thus, whether it is reliable to make a direct extrapolation of simulation results to late times (most relevant for observations today) requires further investigation. On the other hand, while VOS model for global strings are still being tested and needs to be calibrated with simulation data, the prediction for late times by the VOS model is obtained by solving the evolution equation incorporating the known physics effects instead of simple extrapolation. Therefore, such a semi-analytical approach is highly complementary to the simulation efforts

and the two approaches can lead to insights to help improve each other. We significantly updated and expanded the related studies initiated in our earlier paper [156], taking into consideration the very recent developments since then. For instance, [162, 158] show that the inclusion of the very high oscillation modes can drastically change the shape of the GW spectrum from NG strings in (early-)matter dominated era, which was neglected in earlier literature. We included the contribution from these high modes in this updated study, which leads to substantial modifications to the GW spectrum at low f for standard thermal history as well as at high f with the presence of an early matter domination epoch. We also discuss the consequence for the prediction of SGWB if the non-scaling behavior found in some simulation results for early evolution sustains in the late-time evolution of a global string network, compare with the results found in [15, 196], and suggest potential modifications to the VOS model to accommodate such a feature. We will dive into the time-frequency correspondence for global strings, which is the guiding principle for testing standard cosmology. We conduct an extensive study on probing a potentially existing non-standard equation of state of the pre-BBN Universe such as early matter domination (EMD) or kination, where we also include a concrete example for a finite duration of a kination epoch. In addition, we study the effects on the GW spectrum with the presence of new massive degrees of freedom. Furthermore, a detailed discussion is given to address uncertainties such as loop size distribution, radiation parameters, and distinguishing from other SGWB sources. Our results directly apply to pure global strings associated with massless Goldstone. The application to the axion case where the Goldstone acquires a mass at a QCD(-like) phase transition is more complex and requires treatments of the axion

domain walls in addition to the strings, see for example [197]. We reserve a dedicated study on the axion case for future work. We also comment on the prospect of addressing the recent NANOGrav result with global strings.

The rest of this article is organized as follows. In Section 4.2.1 we will present our methodology based on the analytical Velocity-dependent One-Scale (VOS) model for global strings calibrated with recent simulation results. In Section 4.2.2 we derive the GW frequency spectrum from a global string network in the context of standard thermal history. In Section 4.3 we illustrate the relation between the frequency of a GW signal observed today and its emission time in the early Universe. With several benchmark examples, we show how this relation can be used to test standard cosmology and detect potential new physics. Related experimental constraints and sensitivities are also demonstrated in Section 4.3 and 4.4. In Section 4.5 we will address various uncertainty factors that may affect the results, as well as how to distinguish global string induced SGWB from other potential SGWB sources. We make our conclusions in Section 8.

4.2 Evolution of a Global Cosmic String Network

4.2.1 Velocity-dependent One-Scale (VOS) model for global strings

Recent years have seen rapid developments in simulating a global/axion string network [177, 109, 198, 199, 200, 112, 201, 196, 111, 202]. Nevertheless, a technical challenge persists for pure numerical simulation to track the network's evolution over the entire relevant cosmic history. Two characteristic scales need to both be captured by simulation: the string width which is about the inverse of the related symmetry breaking scale $r_{\rm core} \sim 1/\eta$,

the time-dependent horizon size of the Universe which is of the Hubble scale H^{-1}. There is generally a large hierarchy between the two scales, which can be up to $\eta/H \sim 10^{57}$ in the late-time universe. However, current simulations can only cover very early stage of the evolution up to $\eta/H \sim 10^3$, therefore extrapolation, potentially unreliable for late times, has to be made to make prediction for observations today. Our approach here is to adopt an analytical VOS model that captures the essential physics, and use it to study and predict the evolution of the string network over a long range of time, while calibrating the input model parameters with data points for early time evolution that have been made available by simulations.

In this section, we review the VOS model of a global string network and compare its predictions with that from simulations. The VOS model was originally introduced in the context of NG strings [203, 204, 205], and recently extended/updated including the application to axion strings [206, 207, 31]. The VOS model has been widely supported by simulation results in the case of NG strings [208, 209, 210], yet for global strings it is still being tested by simulations. According to the VOS model, starting with an arbitrary initial condition, the cosmic string network would eventually enter a scaling regime [196, 109], where the correlation length L (or the mean of the inter-string separation scale) of the strings remains constant relative to the horizon size, and the energy density of the network tracks the total background energy density with a coefficient $\sim G\mu$. The network typically consists of a few horizons sized long strings along with copious sub-horizon sized string loops. In this regime, the energy density of the string network relative to the background energy density does not grow with the scale factor a due to the energy loss from the decay of the

loops. While GWs constitute the leading radiation by the NG strings, they are irreducible but subdominant mode for global strings for which the emission of Goldstone particles is more important[1]. The energy density of the global string network (mainly stored in long strings) is

$$\rho_\infty = \frac{\mu(t)}{L^2(t)} = \xi(t)\frac{\mu(t)}{t^2}, \tag{4.1}$$

where the dimensionless parameter $\xi(t)$ is defined as the number of long strings per horizon volume. $\mu(t)$ is the time-dependent tension (i.e. energy per unit length) of the global strings (μ is a constant for NG or local strings),

$$\mu(t) = 2\pi\eta^2 \ln\frac{L}{\delta} \equiv 2\pi\eta^2 N, \tag{4.2}$$

with

$$\delta \sim (\sqrt{\lambda} m_\phi)^{-1} \quad \text{and} \quad m_\phi^2 = \lambda \left| \left(\frac{T^2}{3} - \eta^2 \right) \right| \sim \lambda\eta^2, \tag{4.3}$$

where δ is the width of the string core, λ is the coupling in ϕ^4 theory and m_ϕ sets the mass of the Higgs-like complex ϕ whose VEV breaks the global $U(1)$, and we have defined the time-dependent parameter N which will be used in later discussions. The temperature T dependent thermal mass contribution is negligible well after the symmetry breaking phase transition ($T \ll \eta$), and thus we ignore it in our analysis. We consider $\lambda \sim 1$ such that m_ϕ

[1]We neglect the emission of radial mode which is shown to decouple soon after the network formation [15, 177] and may be generally suppressed when the loop size is larger than $\sim 1/\eta$ [199].

and η are comparable. The evolution equation for the correlation length L is [168, 31, 203, 204]

$$\left(2-\frac{1}{N}\right)\frac{dL}{dt}=2HL\left(1+\bar{v}_{\infty}^{2}\right)+\frac{L\bar{v}_{\infty}^{2}}{\ell_f}+\bar{c}\bar{v}_{\infty}+s\frac{\bar{v}_{\infty}^{6}}{N}, \tag{4.4}$$

which couples to the evolution equation for the average long string velocity $\bar{v}_{\infty}$:

$$\frac{d\bar{v}_{\infty}}{dt}=\left(1-\bar{v}_{\infty}^{2}\right)\left[\frac{k_v}{L}-2H\bar{v}_{\infty}\right], \tag{4.5}$$

where k_v is the momentum parameter. While we will investigate the detectability of GW signal, we left out the GW radiation term in these evolution equations because its contribution here is sufficiently suppressed [168]. The terms on the RHS of Eq. 4.4 represent, in order, the dilution effect from the expansion of the Universe, thermal friction effect with characteristic scale $\ell_f \propto \mu T^{-3}$, loop chopping rate parameter $\bar{c}$, and the back-reaction due to Goldstone boson emission [31, 204]. The thermal friction is negligible as the Universe cools down such that $T \ll \eta$.

In the following analysis we consider various possibilities of background cosmology parametrized by n, defined as

$$\rho \propto a^{-n}, \qquad a(t) \propto t^{2/n} \tag{4.6}$$

where $a(t)$ is the expansion parameter as a function of time t, ρ is the background cosmic energy density. $n = 3, 4$ correspond to the cases of matter (MD) and radiation (RD)

domination, respectively. We focus on the range of $2 < n \leq 6$ ($n = 6$ corresponds to kination epoch which we will discuss more in Sec. 4.4).

In the scaling regime, the parameters ξ and $\bar{v}_\infty$ are approximately time-independent. For a specific n, the solution to the evolution equations in the VOS model can be expressed as [31]

$$\xi = \left(\frac{L}{t}\right)^{-2} = \frac{8\left(1 - \frac{2}{n} - \frac{1}{2N}\right)}{nk_v(k_v + \bar{c})(1 + \Delta)}, \qquad \bar{v}_\infty^2 \equiv v_0^2(1 - \Delta) = \frac{n - 2 - \frac{n}{2N}}{2}\frac{k_v}{k_v + \bar{c}}\left(1 - \Delta\right), \tag{4.7}$$

with

$$\Delta \equiv \frac{\sigma}{N(k_v + \bar{c})}, \qquad \sigma \equiv s v_0^5. \tag{4.8}$$

The Goldstone particle radiation term $s\bar{v}_\infty^6/N$ is treated as a perturbation (valid when $\Delta \ll 1$), and v_0 is the solution to $\bar{v}_\infty$ in the limit where the Goldstone emission term is set to 0. The model parameters $\{\bar{c}, k_v, \sigma\}$ can be extracted by calibrating with current simulation results, as we will discuss.

Although the presence of a scaling regime with a constant ξ as in the VOS model has been confirmed by simulations for NG or gauge strings [211, 212, 213, 214, 215, 216], the situation is not yet clear for global strings. Some of the recent simulation studies such as

[177] suggest a time-dependent $\xi(t)$ that grows linearly with N in small $4 \lesssim N \lesssim 7$ region,

$$\xi(t) \simeq 0.24(2) \times N + \beta, \tag{4.9}$$

where β is a constant bearing large uncertainty related to initial condition. The linear increase of ξ in N is also found in some other simulation studies [202, 196, 108, 110, 111, 198], but is in conflict with other groups' simulation results, which predict a nearly constant ξ [178, 112, 200, 215, 205, 217, 218, 219, 220, 8]. This discrepancy is an intriguing puzzle, and requires further investigation with higher resolution simulations. Given the uncertainty, while we mainly focus on the application of the VOS model, here and in Sec. 4.5.3 we also carefully considered the effect of potential deviation from scaling and suggest modification/extension to the current VOS model.

In order to calibrate the parameters $\{\bar{c}, k_v, \sigma\}$ for the VOS model, we fit data extracted from simulation results in [108, 109, 112], as summarized in Table. 4.1. The error bars are visually estimated from the plots in [108, 109, 112], as we are doing a simplified statistical analysis as in [31]. Our best fitting result for the VOS model parameters are as follows:

$$\{\bar{c}, k_v, \sigma\} \simeq \{0.497, 0.284, 5.827\}, \tag{4.10}$$

and the fitting quality is about 3.3-σ significance (p-value < 0.001). Such a fitting quality reflects moderate tensions among simulation data listed in Table. 4.1, possibly due to the different simulation methods as well as the different ways of counting the number of strings

that are employed in the literature. We will assume that these same parameters apply for different scenarios of cosmological background, e.g. radiation domination (RD) or matter domination (MD) [2]. As an example, for $N = 70$, we obtain the number of strings per Hubble volume $\xi \sim 4.0$ and $\bar{v}_\infty \sim 0.57$ in RD, and $\xi \sim 3.55$ with $\bar{v}_\infty \sim 0.40$ in MD.

In Fig. 4.1 we show the evolution of ξ and $\bar{v}_\infty$ as functions of N using the VOS model with the fitting model parameters listed above. Given the recent findings suggesting deviation from scaling (Eq.(4.9)), in the sub-figure of Fig. 4.1 where the small N region is zoomed in, we also show the 1-σ area of Eq.(4.9) as the yellow band (the error bar is given in [177]), in comparison with the VOS model prediction (sold curve). We found that in the region of small $N \lesssim 7$ the VOS model prediction is consistent with a linear growth of ξ in N, provided that β is not too small, e.g. $\beta \sim 0.20$ is taken as an example in our analysis. The late-time evolution in the scaling regime is insensitive to the exact value of β which depends on initial conditions. Nevertheless, as can be seen in Fig. 4.1, at large N VOS model prediction approaches scaling, i.e. a nearly constant ξ. For our later analysis of the GW signals, the late-time evolution in the region of $N \gtrsim 50$ region is most relevant, yet is beyond the reach of most of current simulations. In contrast, VOS model provides a reasonable prediction for the entire time range of interest, after calibrating with low N simulation data.

The data points we used and listed in Table.4.1 were also applied in [31]. We initially considered using a larger data set for the fitting by including more simulation results,

[2] While this assumption has been confirmed for NG/local strings, a recent simulation work for global strings [196] suggests that $\bar{c}$ may differ with different background cosmologies. The deviation mostly originates from the difference in the predicted averaged velocity $\bar{v}_\infty$, while ξ is about the same in different cases.

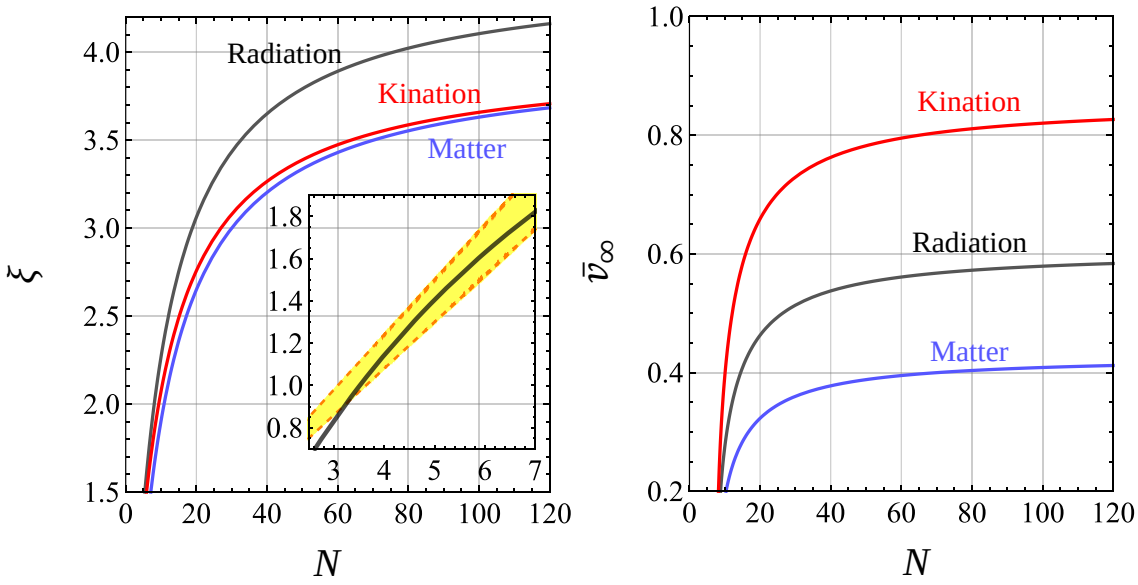

Figure 4.1: The number of global string per Hubble volume ξ and the average long string velocity $\bar{v}_\infty$ as functions of $N \equiv \ln\frac{L}{\delta}$, as predicted by the VOS model, for different background cosmologies. The subfigure in the left panel is the zoom-in of ξ evolution in the low N range during radiation domination, where the yellow band shows the 1-σ uncertainty region based on the finding by simulation (as shown in Eq.(4.9) with $\beta \sim 0.20$).

but they are in some way in conflict with the data in Table.4.1. In order to have meaningful results, we decided to leave out the data sets that fit VOS model poorly. The discrepancies among different simulation results could be in part because these simulations are done with very different methods, covering different ranges of N, and the number of strings and the velocities are counted by different numerical algorithms [31]. Further investigations and developments are certainly required to reach a convergence among different simulation results. To fairly consider these other data sets, in the following, we further discuss their implications and why we left them out of our analysis.

First, note that the VOS model is only valid once the string network enters the scaling region $N \sim 6$ (e.g. see Fig. 3 of [109]). The evolution in the very early stage of $N \lesssim 5$ is sensitive to the initial condition. Therefore, for our fitting, we exclude simulation

data points with very low N's such as in [110] ($N = 2 - 4$). The result from [200] is not included because we found that its large velocity $\bar{v} = 0.609 \pm 0.014$ leads to a poor χ^2 fit with other simulation data[3]. Ref. [196] simulated the global string network with cosmological background parameter $n \leq 3$, without a data point simulated with a radiation-dominated background, thus cannot be analyzed with the results included in Table. 4.1. Another reason we did not include data from [196] is that their results suggest a time-dependent loop chopping rate, which does not match the VOS model. [111] suggests another pattern of deviation from scaling that is inconsistent with Eq.(4.9). While these suggested non-scaling behaviors only directly apply to low N range and do not converge among literature, it is intriguing to consider their potential effects on GW signals (if the non-scaling persist till large N) and how VOS model would need to be revised accordingly. We leave more discussion on this topic in Sec. 4.5.3.

In this study, we simply keep the velocity parameter k_v as a constant as in the conventional VOS model. Nevertheless, some studies suggested the possibility of velocity-dependent momentum parameter $k_v = k_v(v)$ [205, 221, 206, 222]

$$k_v(v) = k_0 \frac{1 - (qv^2)^\beta}{1 + (qv^2)^\beta}, \tag{4.11}$$

where $q \simeq 2.3$, $\beta \simeq 1.5$, and $k_0 \simeq 1.37$ [206, 222]. We found that in RD background Eq.(4.11) gives a numerical value of velocity parameter $k_v(v = \bar{v}_\infty) \sim 0.3$ at high $N \gtrsim 10$ which is consistent with our fitting result Eq.(4.10). In addition, there is a debate about

[3]With the large velocity, the χ^2 prediects $\{\bar{c}, k_v, \sigma\} \simeq \{0.588, 0.395, 0.314\}$ with p value $\ll 0.01\%$. It consequently decreases the ξ by a factor of 2, and no significant change on $\bar{v}_\infty$. Those parameters would reduce the GW production rate to about 44%.

Reference	N	ξ	$\bar{v}$
Klaer et al. [108]	55	4.4 ± 0.4	0.50 ± 0.04
	31	4.0 ± 0.4	0.50 ± 0.04
	15	2.9 ± 0.3	0.51 ± 0.04
Gorghetto et al. [109]	$6-7$	1.0 ± 0.30	
Hindmarsh et al. [112]	6	1.19 ± 0.20	

Table 4.1: Results from recent global string network simulations (in a radiation dominated background) for the number of strings per Hubble volume ξ and the average velocity of long strings $\bar{v}$ in radiation dominated background. These data points were also applied in [31]. In the main text, we explain why some other recent simulation results were left out of this table (thus our analysis) and their implications.

whether the chopping parameter $\bar{c}$ is time-independent: e.g. [196] suggests that $\bar{c}$ decreases with N, while [200] fits a constant value $\bar{c} = 0.843 \pm 0.039$ in radiation background. We will not elaborate on these two particular types of uncertainty.

4.2.2 Dynamics of global string loops: formation and radiation into GWs and Goldstones

A global cosmic string network forms during the phase transition around $T \sim \eta$. The dynamics of the very early stage of evolution is sensitive to initial conditions. However, the string network would soon evolve towards an initial condition independent scaling regime [202, 177, 109, 196, 108], namely, $\xi \sim$constant (or with potential deviation from scaling suggested by some recent work, see earlier discussion and later in Sec. 4.5.3). The horizon-sized long strings randomly intersect each other and lose energy via forming sub-horizon sized loops, which subsequently oscillate and radiate energy until they decay away. The loop size distribution at formation time can be parameterized by: a distribution function $\mathcal{F}_\alpha$ and the fraction of energy stored in loops that can be released as radiation (GWs or

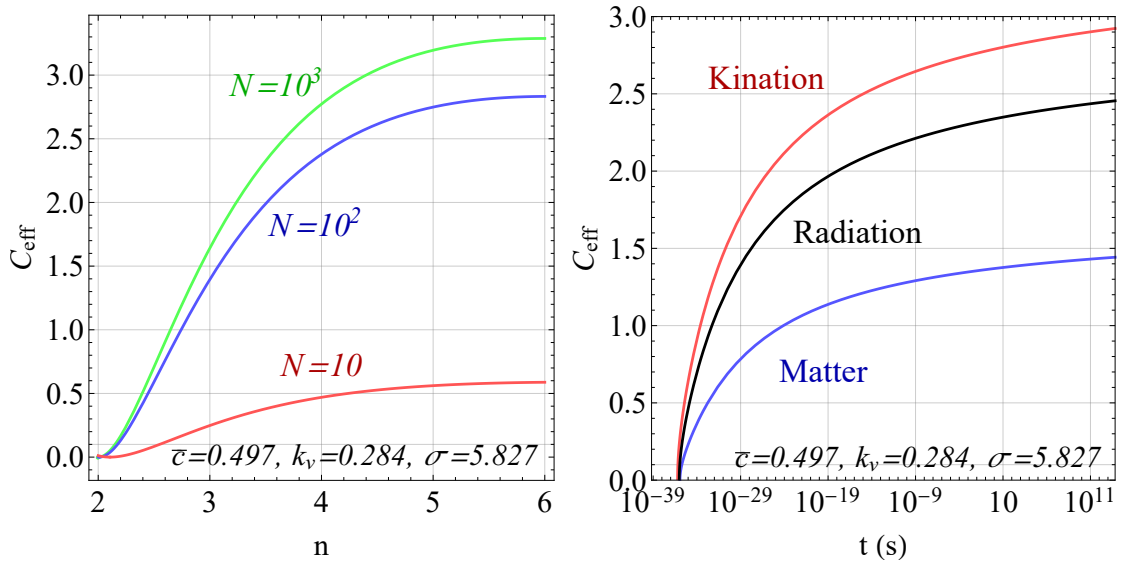

Figure 4.2: The dependence of loop emission factor $C_{\rm eff}$ on the background cosmology as derived from the VOS model, as well as its evolution in time (characterized by $N \equiv \ln\frac{L(t)}{\delta}$ or t). In the example shown, the symmetry breaking scale is taken as $\eta = 10^{15}$ GeV.

Goldstones), F_α. In this work, we consider two representative scenarios in detail, both inspired by simulation results: (1) a nearly monochromatic loop size at formation $\ell_i \sim \alpha t_i$ with $\alpha \sim 0.1$, such that $\mathcal{F}_{\alpha\sim0.1} \sim 1$, while $\sim 90\%$ fraction of loop's energy is in the form of kinetic energy which would eventually redshift away without contributing to GWs, thus $F_\alpha \sim 0.1$, as inspired by [209, 208]; and (2) a flatter, log-uniform distribution of loop size as suggested in [109]. In this section we focus on the simpler first case, and the second scenario will be discussed in Sec. 4.5.1. In Sec. 4.5.1 we also comment on other loop distribution possibilities to account for the related uncertainties [223].

By energy conservation, for a specific α the formation rate of string loops in a scaling string network is given by

$$\frac{d\rho_o}{dt} \times \mathcal{F}_\alpha = -\left(\frac{d\rho_\infty}{dt}\right) \times F_\alpha \times \mathcal{F}_\alpha = \bar{c}\bar{v}_\infty \frac{\mu}{L^3} F_\alpha \mathcal{F}_\alpha, \tag{4.12}$$

where the chopping rate parameter $\bar{c}$ is given in Eq.(4.10), and ρ_o denotes the energy density of string loops. The number density of loops with length $\ell = \alpha t$ is then

$$dn_o = \frac{\bar{c}\bar{v}_\infty \mathcal{F}_\alpha F_\alpha}{\alpha t L^3} dt \equiv \mathcal{F}_a C_{\rm eff} \frac{F_\alpha}{\alpha} \frac{dt}{t^4}, \tag{4.13}$$

where we define the loop emission parameter $C_{\rm eff}$

$$C_{\rm eff} \equiv \bar{c}\bar{v}_\infty \xi^{3/2}. \tag{4.14}$$

We obtain $C_{\rm eff}$ for different background cosmologies (i.e. equations of state) based on the solutions given in Eq.(4.10) and Eq.(4.7). Fig. 4.2 illustrates the solution and evolution of $C_{\rm eff}$. Numerically, we found $C_{\rm eff} \simeq \{1.32, 2.26, 2.62, 2.70\}$ for $n = \{3, 4, 5, 6\}$ (n parameterizes cosmology as defined in Eq.(4.6), respectively. Note that $C_{\rm eff}$ falls down to zero when the $\bar{v}_\infty \to 0$, which corresponds to the time t_η when the Goldstone radiation becomes important in the equation of motion Eq.(4.4), i.e. $\Delta(t = t_\eta) = 1$ in the string network evolution (see Eq.(4.7)):

$$t_\eta \simeq \frac{\sqrt{\xi(t_\eta)}}{\eta} \exp\left(\frac{\sigma}{k + \bar{c}}\right). \tag{4.15}$$

The right panel of Fig. 4.2 illustrates this point with numerical results. With our calibrated parameters, t_η as defined corresponds to $N \sim 6-7$, which implies that the perturbative VOS model [31] has large uncertainties in such a low N range.

After formation, a global string loop would rapidly oscillate and emit energy in the form of GWs and Goldstones by the following energy loss rates until the loop disappears completely [107]:

$$\frac{dE}{dt} = -\Gamma G\mu^2 - \Gamma_a \eta^2. \tag{4.16}$$

Note that the parameter $\Gamma_{(a)}$ only depends on the loop trajectory [168, 224], thus we expect that the Goldstone radiation constant Γ_a should be close to the value of the GW radiation constant $\Gamma \sim \Gamma_a$ [224] which is also determined by the loop shape. In the following, we assume benchmark values $\Gamma \sim 50$ [225, 226, 208, 209], and $\Gamma_a \sim 65$ [224, 168]. We will discuss the effect of varying Γ_a, Γ in Sec. 4.5.2 to account for the potential uncertainty on the radiation parameters.

The size of a loop with initial length $\ell_i = \alpha t_i$ therefore decreases as

$$\ell(t) \simeq \alpha t_i - \Gamma G\mu(t-t_i) - \frac{\Gamma_a}{2\pi}\frac{1}{\ln(L/\delta)}(t-t_i), \tag{4.17}$$

where t_i is the loop formation time. The radiation of GW and Goldstone from a loop can be decomposed into a set of normal-mode oscillations with frequencies $\tilde{f}_k = 2k/\tilde{\ell}$, where mode numbers $k = 1, 2, 3\cdots$, and $\tilde{\ell} \equiv \ell(\tilde{t})$ is the instantaneous size of the loop when it

radiates at $\tilde{t}$. We can rewrite the radiation parameters in a decomposed form

$$\Gamma^{(k)} = \frac{\Gamma k^{-\frac{4}{3}}}{\sum_{m=1}^{\infty} m^{-\frac{4}{3}}}, \quad \text{and} \quad \Gamma_a^{(k)} = \frac{\Gamma_a k^{-\frac{4}{3}}}{\sum_{m=1}^{\infty} m^{-\frac{4}{3}}}, \tag{4.18}$$

where $\sum_{m=1}^{\infty} m^{-\frac{4}{3}} \simeq 3.60$, $\sum_k \Gamma^{(k)} = \Gamma$, and $\sum_k \Gamma_a^{(k)} = \Gamma_a$. We have assumed that the cusps are the dominating source of GW and Goldstone emissions as found in NG string simulations [227, 228, 229]. The contributions from kinks and kink-kink collisions follow different power laws: $\Gamma^{(k)} \propto k^{-5/3}$ and k^{-2} for kinks and kink-kink collisions, respectively [230, 231, 232]. As shown in Eq.(4.16), relative to Goldstone emission, GW radiation is suppressed by a factor of $\sim \eta^2/m_p^2$, where m_p is Planck scale. Nevertheless, the suppression factor becomes less severe as the symmetry breaking scale η gets closer to m_p.

Our main analysis results shown in Sec. 4.3 are obtained by focusing on the simple, motivated assumptions made in this section. Nevertheless, we acknowledge other possibilities of C_{eff} and $\Gamma_{(a)}$ that were suggested in literature. We further discuss the effects on phenomenology in light of possible deviations from our assumptions on these factors in Sec. 4.5.2 and Sec. 4.5.3.

4.3 SGWB Spectrum from Global Strings

In this section we will first show the derivation and numerical results of SGWB frequency spectrum from a global cosmic string network assuming a standard cosmic history (Sec. 4.3.1, 4.3.2). Then in order to give more physics explanation and insights, in Sec. 4.3.3 we provide parametric estimates for the relic densities of Goldstones and GWs emitted from global strings, and compare them with GW signals from NG strings.

4.3.1 Derivation of GW spectrum from global strings

The generic form of the relic energy density of a SGWB is given by

$$\Omega_{\rm GW} = \frac{f}{\rho_c}\frac{d\rho_{\rm GW}}{df}, \tag{4.19}$$

where $\rho_{\rm GW}$ is the energy density of GWs, and $\rho_c = 3H_0^2/8\pi G$ is the critical density. String loops emit GWs from normal mode oscillations with frequencies $\tilde{f}_k = \frac{2k}{\tilde{\ell}}$, where $k \in \mathbb{Z}^+$, $\tilde{\ell}$ is the loop size at emission time $\tilde{t}$ [233, 177]. Taking into account of redshift effects, the observed frequencies today are then

$$f_k = \frac{a(\tilde{t})}{a(t_0)}\tilde{f}_k = \frac{2k}{\tilde{\ell}}\frac{a(\tilde{t})}{a(t_0)}. \tag{4.20}$$

The relic GW background is obtained by summing over all harmonic modes

$$\Omega_{\rm GW}(f) = \sum_k \Omega^{(k)}_{\rm GW}(f) = \sum_k \frac{f_k}{\rho_c}\frac{d\rho_{\rm GW}}{df_k}. \tag{4.21}$$

Using Eq.(4.13) and Eq.(4.17) that we derived earlier and integrating over emission time $\tilde{t}$, we can derive the contribution $\Omega^{(k)}_{\rm GW}(f)$ from an individual k mode as

$$\Omega^{(k)}_{\rm GW}(f) = \frac{\mathcal{F}_\alpha}{\rho_c}\frac{2k}{f}\frac{F_\alpha}{\alpha}\int_{t_F}^{t_0} d\tilde{t}\frac{\Gamma^{(k)}G\mu^2}{\left(\alpha + \Gamma G\mu + \frac{\Gamma_a}{2\pi N}\right)}\frac{C_{\rm eff}\left(t_i^{(k)}\right)}{t_i^{(k)4}}\Theta(t_i,\tilde{t})\left(\frac{a(\tilde{t})}{a(t_0)}\right)^5\left(\frac{a(t_i^{(k)})}{a(\tilde{t})}\right)^3 \tag{4.22}$$

where t_F is the formation time of the global string network, t_0 is the current time, and the

causality and energy conversation conditions are imposed by

$$\Theta(t_i, \tilde{t}) = \theta(\tilde{\ell})\,\theta(\tilde{t} - t_i). \tag{4.23}$$

With Eq.(4.17) we can derive that a loop that emits GW at time $\tilde{t}$ leading to an observed frequency f was formed at the time

$$t_i^{(k)}(\tilde{t}, f) = \left(\frac{1}{\alpha + \Gamma G\mu + \frac{\Gamma_a}{2\pi N}}\right)\left[\tilde{\ell}(\tilde{t}, f, k) + \Gamma G\mu\tilde{t} + \frac{\Gamma_a}{2\pi N}\tilde{t}\right], \tag{4.24}$$

Note that to consider the radiation of Goldstones, we may define $\Omega_{\rm Gold}(f)$ in analogy to Eq.(4.22) with the simple replacements: $\Gamma \to \Gamma_a$, and $\Gamma G\mu^2 \to \Gamma_a \eta^2$. We will apply this prescription in later discussions involving Goldstone radiation (e.g. Sec. 4.3.3).

Earlier studies based on radiation dominated background [224, 234, 235] found that the first few k-modes dominate the GW radiation from loops. However, recent work (in the context of NG strings) showed that a large value of $k \gtrsim 10^5$ may be needed to converge, depending on the background cosmology [162, 158, 236]. For instance, including higher k modes changes the power-law index of $\Omega_{\rm GW}(f)$ from -1 to $-1/3$ in a MD epoch. In this work we investigated the importance of high k modes in the context of global strings and found similar results. We found that to reach a converging result for $\Omega_{\rm GW}(f)$ up to ~ 100 Hz, i.e. within the frequency range relevant for current and near-future GW detections, up to $k \sim 10^8$ modes need to be included. Higher f range requires more k modes to converge. To draw the full spectrum shown in Fig. 4.3 we took into account of up to $k \sim 10^{15}$ modes in our analysis.

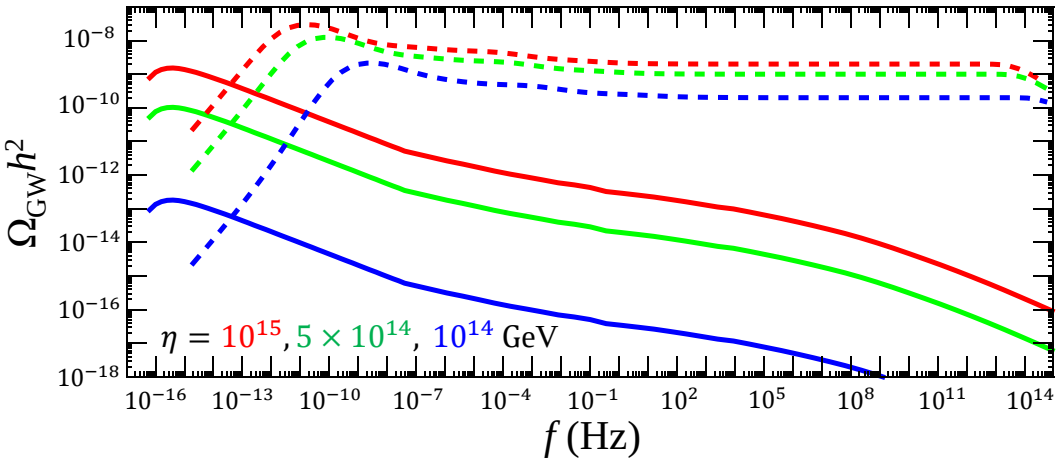

Figure 4.3: Gravitational wave spectra from a global (solid) and NG (dashed) string network with $\alpha = 0.1$, $F_\alpha = 0.1$, for $\eta = 5\times10^{15}$ (red), 10^{15} (orange), 5×10^{14} (green), $and 10^{14}$ GeV (blue). Up to $k = 10^{15}$ harmonic modes are included in the summation.

Fig. 4.3 demonstrates the SGWB spectrum calculated numerically with the method we outlined. The corresponding results for NG strings are also shown in comparison, with more explanation given in Sec. 4.3.3. While the very high f range $f \gg 100$ Hz is well beyond the reach of any foreseeable experiment, we keep it in Fig. 4.3 for theoretical completeness by capturing physics at times as early as the formation time of the string network. As can be seen, towards high f the spectrum falls most significantly starting around the frequency $f_\eta \sim \frac{2}{\alpha t_\eta}[a(t_\eta)/a(t_0)] \sim 10^{10}$ Hz [237], as a result of the string network formation time and the validity cutoff of the perturbative VOS model (Eq.(4.15)). The exact shape of the falling spectrum at frequencies $f > f_\eta$ has uncertainties and is sensitive to the initial condition and the very early stage of string network evolution, which is not captured by the VOS model. Then over a wide range of f the spectrum gradually declines towards higher f ($\sim \ln^3(1/f)$, see Eq.(4.25) below), corresponding to the emissions during the RD era. Note that this feature of the SGWB spectrum from global strings is in contrast to a nearly flat plateau as

in its NG string counterpart. Starting at $f_0 \simeq \frac{2}{\alpha t_0} \sim 3.6 \times 10^{-16}\,\mathrm{Hz}$, the spectrum behaves as $f^{-1/3}$ until $f_{\rm eq} \sim 1.8 \times 10^{-7}\,\mathrm{Hz}$, which is due to the transition to the late MD era. $f_{\rm eq}$ indicates the frequency corresponding to the emission around the matter-radiation equality time. We will elaborate the f-T or f-t correspondence later in Sec. 4.4.1. Note that the $f^{-1/3}$ behavior was obtained by summing up to high oscillation modes $k \gg 10^5$ which was shown to be important for a MD background [162, 158]. By only summing up to low k modes ($k \ll 10^5$) it would be f^{-1}. The low end of the frequency spectrum has a cutoff corresponding to emission at the present time t_0, with a maximum point shortly before the ending of the spectrum at f_0.

By combining Eq.(4.31) and Eq.(4.42) we derive the following analytical approximation for global string SGWB spectrum in different f regions, which shows the parametric dependence:

$$\Omega_{\rm GW}(f)h^2 \simeq \tag{4.25}$$
$$\begin{cases} 5.1\times10^{-15}\left(\dfrac{\eta}{10^{15}\,\mathrm{GeV}}\right)^4\left(\dfrac{f}{f_\eta}\right)^{-1/3}, & \text{for } f > f_\eta \\ 8.8\times10^{-18}\left(\dfrac{\eta}{10^{15}\,\mathrm{GeV}}\right)^4 \ln^3\left[\left(\dfrac{2}{\alpha f}\right)^2 \dfrac{\eta}{t_{\rm eq}}\dfrac{1}{z_{\rm eq}^2\sqrt{\xi}}\Delta_R^{1/2}(f)\right]\Delta_R(f), & \text{for } f_\eta > f > f_{\rm eq} \\ 2.9\times10^{-12}\left(\dfrac{\eta}{10^{15}\,\mathrm{GeV}}\right)^4\left(\dfrac{f}{f_{\rm eq}}\right)^{-1/3}, & \text{for } f_0 < f < f_{\rm eq} \\ 0, & \text{for } f < f_0 \end{cases}$$

where $t_{\rm eq}$ and $z_{\rm eq}$ denote the time and redshift at the matter-radiation equality, respectively. $\Delta_R(f)$ accounts for the effect of varying the number of relativistic degrees of freedom, g_*

and g_{*S}, over time:

$$\Delta_R(f) = \frac{g_*(f)}{g_*^0}\left(\frac{g_{*S}^0}{g_{*S}(f)}\right)^{4/3}, \tag{4.26}$$

where $g_*(f)$ and $g_{*S}(f)$, are obtained by applying the f-T relation which will be introduced later in Eq.(4.32), and the superscript 0 indicates the values today. Note that here we focus on global strings associated with massless Goldstones, thus they are stable until the current time. In the case of axion strings with massive Goldstones, the string network would turn to domain walls and finally disintegrate around the transition time when Goldstones acquire masses. In that case, the GW spectrum would beget a cut with potentially distinct structure around a characteristic $f_{\rm cut}$ that is larger than f_0.

4.3.2 GW frequency spectrum and experimental sensitivities

Fig. 4.4 illustrates the SGWB signal originated from global strings based on our numerical results. We also include related experimental sensitivities: current constraints (solid lines) from LIGO [238, 239, 138, 137] and European Pulsar Timing Array (EPTA) [240], Parkes Pulsar Timing Array (PPTA) [241, 242, 210]; the projected future sensitivities (dashed lines) with LIGO A+ [243], LISA [141], DECIGO/BBO [180], AEDGE/AION [179, 244], Einstein Telescope (ET) [245, 246], Cosmic Explorer (CE) [135], and Square Kilometer Array (SKA) [247]; as well as the region corresponding to the recent NANOGrav excess [143, 144]. We can see that as expected from Eq.(4.31) the global string GW spectrum is sensitive to the symmetry breaking scale η. Experiments such as LISA, BBO and SKA can probe $\eta \gtrsim 10^{14}$ GeV. Among the existing searches, PPTA gives the strongest constraint

of $\eta \lesssim 2 \times 10^{15}\,\text{GeV}$. These sensitivities/constraints on η may be improved/relieved with non-standard cosmology and alternative modelings, see discussions in Sec. 4.4 and Sec. 4.5. Various intriguing interpretations of the recent NANOGrav excess as a SGWB signal have been considered [145, 146, 248, 147, 148, 149, 150, 151, 152]. In particular, [15] and [151] investigated the possibility of fitting the NANOGrav signal with GWs from QCD axion strings or general ALP strings. The former [15] found that the GW amplitude hinted by the NANOGrav data requires $f_a \gtrsim 10^{15}\,\text{GeV}$ which is in conflict with bound on ΔN_{eff} from BBN and CMB data, given that the axions are emitted as radiation from the strings. Nevertheless, the latter suggests that a non-standard cosmological history may improve the fit [151]. In our independent check by including high k modes in the summation, we find that the GW frequency spectrum follows a power-law $f^{-1/3}$ in the range of $f \leq f_{\text{eq}}$ (defined before Eq.(4.25)), and with $4.3 \times 10^{15}\,\text{GeV} \leq \eta \leq 6.1 \times 10^{15}\,\text{GeV}$, global strings can lead to a good 1-σ fit to the NANOGrav 12.5-year data [143]. However, as also discussed in [143, 145], such a spectrum with a gentle slope is in tension with previous bounds from PPTA [242, 241], EPTA [240], and NANOGrav 11-year data [142]. Such a tension may be eased by re-analyzing the data sets using different choices of the red noise model [249] which is being investigated. Variations to the standard theoretical assumptions may allow a viable interpretation of the NANOGrav signal as originated from a global/axion string network, consistent with PPTA data and ΔN_{eff} constraints, which we will explore in future study. In Sec. 4.3.3, we will discuss the ΔN_{eff} bound on Goldstone and GW emissions in detail. Other relevant constraints on the global $U(1)$ breaking scale η include inflation scale and CMB anisotropy bound, which were discussed in [156], also pointing to $\eta \lesssim O(10^{15})$ GeV.

CMB polarization data potentially yields stronger bound on GW in the frequency range of $10^{-17} - 10^{-14}$ Hz [241, 250, 251]. Nevertheless, in Sec. 4.4.1 we will demonstrate that this latter constraint does not apply to our case following the introduction of the f-T relation.

Comparison with literature:

GW signals from a global string network have also been recently investigated by simulation approaches based on a Nambu-Goto effective theory [15] or field theory for global defects [178]. Our results agree with others' on some general features such as $\Omega_{\rm GW} \propto \eta^4$, but differ in details. [15] simulated the global string network in a radiation background during a very early stage of evolution, i.e. $N \lesssim$ 7-8, and extrapolated the linear growth of $\xi \propto N$ to high N when computing the GW spectrum. They agree with our finding that the global strings can lead to detectable GW signals, but found that the GW spectrum scales as $\Omega_{\rm GW} \propto \eta^4 N^4$, instead of $\eta^4 N^3$ as found in our analysis (see Eq.(4.31) in Sec. 4.3.3). The N^3 dependence we found results from the prediction of the conventional scaling VOS model. The difference may be resolved if the loop emission factor $C_{\rm eff}$ in the VOS model is not (nearly) a constant but evolves as $C_{\rm eff} \propto N$ (see Eq.(4.14). We further discuss the effect of such a non-scaling behavior or deviation from the conventional VOS in Sec. 4.5.3. On the other hand, [178] found that the GW spectrum asymptotes to an exact scale invariant form, and the amplitude of the signal is below the prediction by both our method and by [15]. The possible explanations for this discrepancy was suggested in [156, 15], while further investigation is certainly needed to fully resolve this issue.

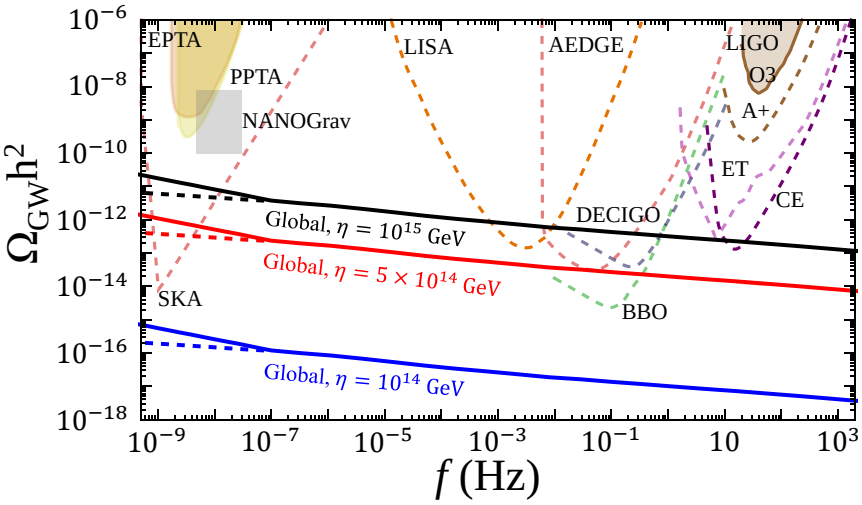

Figure 4.4: Gravitational wave spectrum from a global cosmic string network with $\alpha = 0.1$, $F_\alpha = 0.1$ for $\eta = 10^{14}$, 5×10^{14}, 10^{15} GeV. The solid curves shown are the full results with standard cosmology, dashed lines show the contribution from emission during radiation domination. Exclusion limits or projected sensitivities with various GW experiments are also shown.

4.3.3 Comparison with GWs from NG strings, relic densities of GWs and (massless) Goldstones

In this subsection, we give a simple estimate for the relic density of GWs from global strings which captures key parametric dependence, and compare it with that for NG strings. This can help us gain insights into the detectability of the GW signal from global strings. For example, the energy density of the emitted GWs contributes to the amplitude of primordial tensor power spectrum that should be constrained by CMB data [251], we will discuss this constraint in detail in Sec. 4.4.1. In addition, while in this work we focus on GW radiation from global strings, it is important to better understand Goldstone emission which is the dominant radiation mode in this case. We thus also present a parametric estimate for the relic density of the emitted Goldstone and compare it with GW emission.

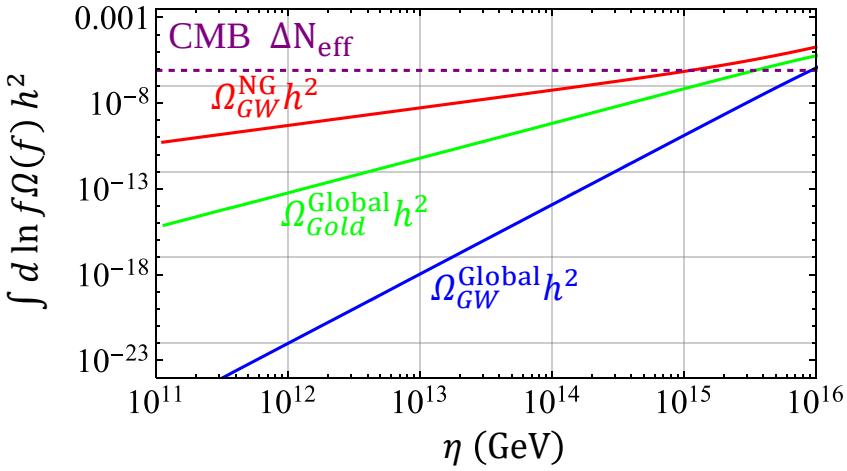

Figure 4.5: The total relic densities (integrated over f) of GWs from a NG string network (red), of GWs from a global string network (blue), and of massless radiation-like Goldstone bosons from a global string network (green), as functions of the symmetry breaking scale η (related to the string tension μ). The purple dashed line shows the constraint on extra radiation energy density by CMB data: $\Delta N_{\rm eff} \lesssim 0.2$ [11] or $\int d(\ln f) \Delta\Omega_{\rm rad} h^2 \lesssim 8.1 \times 10^{-7}$ [11, 12], which requires $\eta \lesssim 3.5 \times 10^{15}$ GeV.

As shown in Fig. 4.5, with these analyses we can find the constraint on η considering the upper limit on extra radiation energy density $\Delta N_{\rm eff}$ from BBN/CMB data. As mentioned earlier, in this work we focus on the simple case with massless Goldstones and our discussion about Goldstone emission is illustrative and concise. Nevertheless, some key insights can be applied to axion strings where the Goldstones are massive as potential dark matter candidates. We leave a detailed discussion on Goldstone radiation and its impact on axion DM physics for future work.

A key difference between the dynamics of a global and a NG string network is that the global string loops are rather short-lived due to the strong Goldstone emission rate. We consider a loop formed at time t_i which decays away at time $t_r \equiv \gamma_r(t_i) t_i$, where

we have adopted a unified notation for the cases of NG and global string loops for an easy comparison: $r = \{\text{NG, global}\}$. Using Eq.(4.17) we find the following expression for estimating the lifetime parameter $\gamma(t_i)$ for the two cases:

$$\gamma_r(t) \equiv \frac{\alpha + \Gamma G\mu + \kappa}{\Gamma G\mu + \kappa} \simeq \begin{cases} \dfrac{\alpha}{\Gamma G\mu} \simeq 5 \times 10^{10} \left(\dfrac{\eta}{10^{12}\text{GeV}}\right)^{-2} & \text{NG String } (\kappa = 0) \\ \dfrac{\alpha + \kappa}{\kappa} \simeq 2 & \text{Global String} \end{cases} \tag{4.27}$$

where

$$\kappa \equiv \frac{\Gamma_a}{2\pi N}. \tag{4.28}$$

Our ansatz of $\alpha \sim 0.1 \gg \Gamma G\mu$ is applied to derive the final results. The lifetime of a loop formed at time t_i with an initial length of αt_i can then be estimated as $\tau_r = (\gamma_r(t_i) - 1)t_i$. Recent simulations support our estimates of global string loop's lifetime [199, 177]. Due to the time dependence of global string tension (i.e. the N-dependence), κ varies in the range of $0.6 \lesssim 1/\kappa \lesssim 10$ throughout the expansion history of universe. Therefore, the global strings are short-lived and are expected to decay in about one Hubble time after its formation (but the lifetime is still sufficient to yield detectable GWs with large η). In contrast, as can be seen from Eq.(4.27), the NG string loops generally survive a much longer time after formation. Due to this drastic difference in loop lifetime, with the same parameters such as η and loop distribution function, GWs from a global string network on average experience a larger redshift effect after emission, which contributes to a suppressed GW amplitude (along with the suppression effect due to the Goldstone dominance) and shifts the spectrum towards lower frequencies. We show the result in in Fig. 4.3.

We now estimate the relic densities of GW and Goldstone emitted from global strings. As mentioned in Sec. 4.3.1 the formulation for GW calculation given in Eq.(4.22) and Eq.(4.23) can be applied to the Goldstone case with the replacements of $\Gamma \to \Gamma_a$, and $\Gamma G\mu^2 \to \Gamma_a \eta^2$. (based on Eq.(4.16)). We can then express the total relic densities (integrated over f) of GWs and Goldstones from global string radiation in the following unified form:

$$\Omega_\beta = \int d\,(\ln f)\,\Omega_\beta(f), \qquad \text{with } \beta = \{\text{GW, Gold}\}. \tag{4.29}$$

Our numerical results of the relic energy densities are illustrated in Fig. 4.5 as functions of symmetry breaking scale η, along with $\Omega_{\rm GW}$ from NG strings for comparison. The upper limit on the total relic radiation energy density from the CMB data is also shown [252, 12, 11]. One can see that the constraint is dominantly driven by the emission of radiation-like Goldstones, which requires $\eta \lesssim 3.5 \times 10^{15}$ GeV, while for GWs alone the constraint is relaxed to $\eta \lesssim 9 \times 10^{15}$ GeV. In comparison, with a non-scaling solution as suggested in Eq.(4.9) this CMB constraint on η would be tighter: $\eta \lesssim 9 \times 10^{14}\,$GeV [15], as the total energy of the string network would increase relative to the scaling scenario (see Sec. 4.5.3 for more related discussion).

Next we further discuss the parametric dependence of $\Omega_{\rm GW}$ and $\Omega_{\rm Gold}$ for global strings and compare with $\Omega_{\rm GW}$ for NG string. For a fair comparison, we assume that the symmetry breaking scale η and the string network evolution parameters such as the long string number density ξ and loop size α are the same for the NG and global string network under consideration. Then we consider $\Omega_{\rm GW}^{\rm Global}$, $\Omega_{\rm Gold}^{\rm Global}$ and $\Omega_{\rm GW}^{\rm NG}$ as observed at a time

parametrized by $N \equiv \ln(L\eta)$. Based on simple analytic estimates checked with numerical fitting, we find the following relations:

$$\Omega_{\rm GW}^{\rm NG} : \Omega_{\rm Gold}^{\rm Global} : \Omega_{\rm GW}^{\rm Global} \simeq 1 : N\sqrt{\frac{\Gamma G\mu}{\alpha}} : N\sqrt{\frac{\Gamma G\mu}{\alpha}}\frac{\Gamma G\mu}{\Gamma_a/(2\pi N)}, \tag{4.30}$$

where $\frac{\alpha}{\Gamma G\mu}$ is the lifetime parameter for NG string, $\gamma_r^{\rm NG}$, as defined in Eq.(4.27), which accounts for the aforementioned difference in redshift effects between global and NG case, and the square-root of $\frac{\Gamma G\mu}{\alpha}$ is due to the redshift of the GW energy $\propto a(t) \propto t^{1/2}$; the N factors account for the log enhanced string tension for global strings; $\frac{\Gamma G\mu}{\Gamma_a/(2\pi N)}$ represents the different energy loss rates to GWs vs. to Goldstones. We also find the following key parametric dependencies (focusing on η and N) for each of these Ω's:

$$\Omega_{\rm GW}^{\rm NG} \propto \eta, \qquad \Omega_{\rm Gold}^{\rm Global} \propto \eta^2 N, \qquad \Omega_{\rm GW}^{\rm Global} \propto \eta^4 N^3, \tag{4.31}$$

The η dependence of GWs from NG strings that we found agrees with earlier literature [168, 13, 14, 225, 230, 253, 254, 210, 209, 255], and $\Omega_{\rm GW}^{\rm Global} \propto \eta^4$ agrees with two most recent independent simulations [15] and [178]. Nevertheless, the N-dependence of the scaling solution of long string number density ξ in the VOS model (see Eq.(4.7)) disagrees with some of the simulation results which suggest a logarithmic increase in ξ based on low N data [15]. The effect of a non-scaling ξ persisting till late times, e.g. $N > 70$, will be discussed in Sec. 4.5.3, including a comparison with the result in [15].

4.4 Probing the Early Universe

In this section we investigate how the SGWB spectrum from a global string network would alter if the cosmic history and particle content of the early Universe differ from the standard scenario which we assumed in Sec. 4.3. This in turn allows us to use such GW signals to test the standard paradigms and probe the dynamics of the early Universe well before BBN. Such an idea of using GWs for *cosmic archaeology* was proposed and developed in the context of NG strings [14, 13]. The situation with global strings bear similarities with that of NG strings, yet with significant differences. In the following, we will demonstrate our findings and make comparison with NG string results.

4.4.1 The connection between the observed GW frequencies and emission times

In the context of NG strings, the frequency-temperature (f-T) correspondence during a RD era was derived in [13], and serves as the foundation of cosmic archaeology with the f spectrum of GWs from strings. The analogous relation for global strings can be derived following the same method. Nevertheless, the derivation can be greatly simplified in this case. As explained in Sec. 4.3.3 (Eq.(4.31)), a key difference between NG and global string loop dynamics is that, global string loops decay away within ~ 1 Hubble time after formation due to the strong Goldstone emission rate. Therefore, the timescale when the GW emission from a loop occurs is approximately the same as the loop's formation time, i.e. $\tilde{t} \sim t_i$ (Eq. (4.17)). For an estimate, it suffices to focus on the $k = 1$ mode which we find to be the dominant one in the cases of interest. With this understanding and following

the calculation in Sec. 4.3.1, we find that a specific f_Δ band observed today relates to a particular emission temperature T_Δ in the following way:

$$f_\Delta \simeq \frac{2}{\ell(\tilde{t})}\frac{a(t_\Delta)}{a(t_0)} = \frac{2}{\alpha z_{\rm eq} t_{\rm eq} T_{\rm eq}}\left[\frac{g_*(T_\Delta)}{g_*(T_{\rm eq})}\right]^{1/4} T_\Delta$$
$$\simeq (3.02\times 10^{-6}\,{\rm Hz})\left(\frac{T_\Delta}{1\,{\rm GeV}}\right)\left(\frac{\alpha}{0.1}\right)^{-1}\left[\frac{g_*(T_\Delta)}{g_*(T_{\rm eq})}\right]^{1/4}, \tag{4.32}$$

where the loop size at the emission time $\ell(\tilde{t}) \simeq \alpha t_i \equiv \alpha t_\Delta$ (see Eq.(4.17)), $z_{\rm eq} \simeq 3387$ is the redshift at the matter-radiation equality, and $t_{\rm eq}$, $T_{\rm eq}$ are the corresponding time and temperature, respectively. Note that f_Δ linearly depends on T_Δ, but is insensitive to the symmetry breaking scale η, unlike in the case of local strings. Eq. (4.32) applies to RD era, while f-T relation varies with background cosmology, which we will discuss in Sec. 4.4.2. A departure from the standard cosmology at T_Δ would thus imprint itself in the GW spectrum around the corresponding f_Δ.

In Fig. 4.6 we illustrate the f-T relation derived for SGWB spectrum from global strings, in comparison with the recent results for NG strings [13, 14]. There are two major differences between the two cases: f-T correspondence for NG strings has η-dependence while for global strings it is almost independent of η which makes it more robust in a way; for the same f the corresponding emission T is much earlier for global strings than for NG strings. Both these differences originate from the aforementioned fact that global string loops decay shortly after formation and their resultant GW signal observed in a certain f band has undergone longer period of redshift after emission (relative to its NG counterpart). Note that due to the current bounds from LIGO and PPTA, η for NG strings

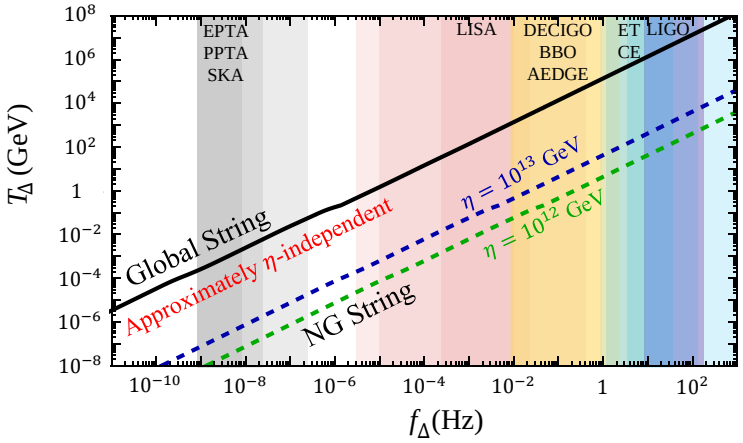

Figure 4.6: Frequency f_Δ where the GW spectrum from cosmic strings would be altered due to a transition to a non-standard cosmology at T_Δ (Eq.(4.32)): the comparison between the results for global strings (the upper-left black line) and NG strings [13, 14] (the lower-right dashed lines). The relevant experimental sensitivities are also shown in different colors, where the darkest bands indicate peak sensitivities. This illustrated the $f_\Delta - T_\Delta$ relation given in the main text.

is constrained as $\eta \lesssim 1.89 \times 10^{13}\,\text{GeV}$ [13, 210]. If the recent NANOGrav excess indeed originates from NG cosmic strings, it favors $\eta \simeq 3 - 5 \times 10^{13}\,\text{GeV}$ [145, 146]. According to Fig. 4.6 these constraints/potential signal implies that GW spectrum from NG strings can reach up to $T \sim 10^4$ GeV (with ET and CE). In contrast, as shown in Fig. 4.6 global strings can probe much earlier cosmic history, up to $T \sim 10^8$ GeV. As discussed in Sec. 4.3.2, $\eta \gtrsim 10^{14}\,\text{GeV}$ is needed to be within experimental sensitivity reach in terms of Ω_{GW}, while other constraints require $\eta \lesssim O(10^{15})\,\text{GeV}$. Fig. 4.7 illustrates the f-T relation for global strings in a different manner where the sensitivity to η is explicitly shown. As demonstrated in Fig. 4.7, global string GWs can trace the cosmic history over a rather wide range in time: up to $T \sim 10^8$ GeV (with ET and CE) and down to $T \sim 10^{-4}\,\text{GeV}$ (with PPTA and SKA) which intriguingly corresponds to the beginning of the BBN era.

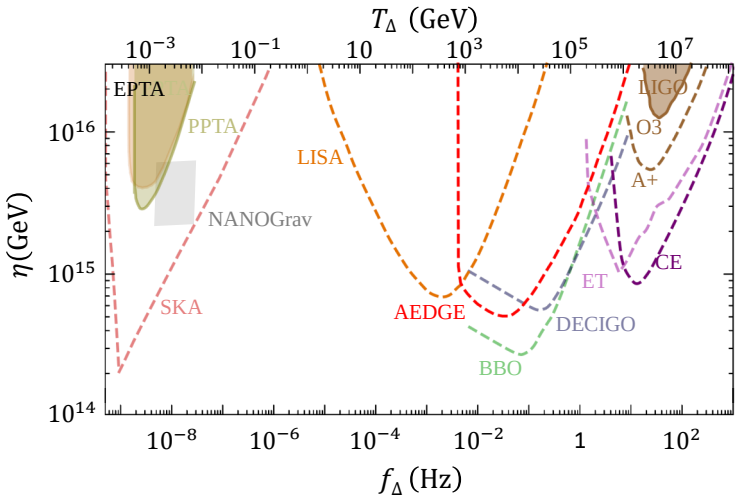

Figure 4.7: Another illustration for f_Δ-T_Δ relation for GW frequency spectrum from global strings, where the experimental sensitivities to η are shown.

The f-T relation as we have elaborated can also help us understand why the global string scenario safely evades the potentially strong bound on $\Omega_{\rm GW}$ in the range of $f \sim 10^{-17} - 10^{-14}$ Hz by the CMB polarization data [241, 250, 251]. The f-T relation in Eq.(4.32), together with the observation that global string loops decay in one Hubble time, indicate that the SGWB signal below a certain f range could not be generated until after a certain time or below a certain T. In Fig. 4.8 we illustrate the constraints from CMB polarization data, and the decomposed contributions to a SGWB induced by global strings: the signal in the low f range of $f \sim 10^{-17} - 10^{-14}$ Hz in fact is not populated until after the photon decoupling, thus is not present at the CMB epoch to be subject to the constraint. One can also simply estimate f corresponding to the photon decoupling $T_\gamma \sim 0.3\,\text{eV}$ using Eq.(4.32), and confirm that GWs with $f \lesssim 10^{-15}$ Hz is emitted afterwards.

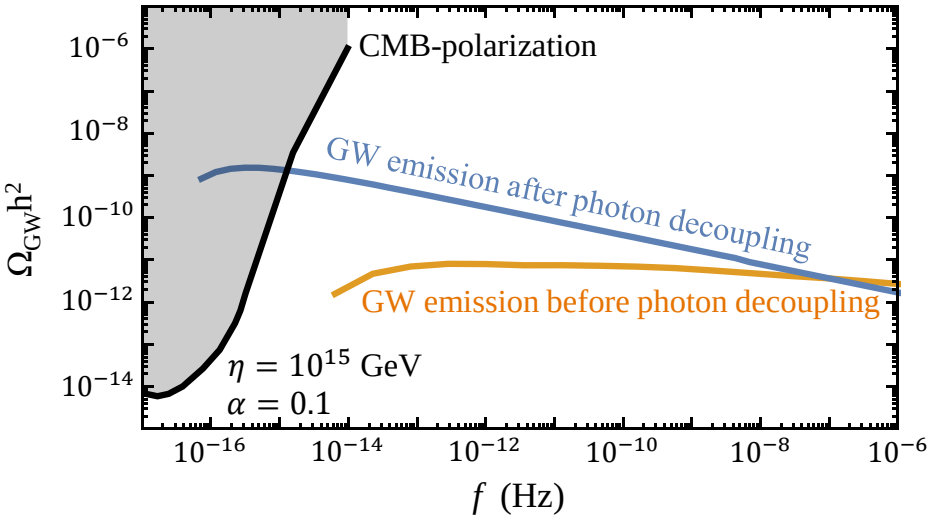

Figure 4.8: GW spectrum from a global string network decomposed into contributions from before and after photon decoupling, which demonstrates how CMB polarization constraint is safely evaded (see main text for details). In the example shown, $\eta = 10^{15}$ GeV ($G\mu = 10^{-11}$) .

4.4.2 Probing new phases of cosmological evolution

According to the standard thermal history, the Universe is radiation dominated starting from the end of inflation all the way down to the matter-radiation equality at $z_{\rm eq} \sim 3000$. Nevertheless, so far there is no data evidence to support this assumption for the epoch prior to the BBN time, i.e. the primordial dark age. On the other hand, recently there has been substantial interest to consider well-motivated non-standard cosmology scenarios, where the standard RD era transits to a different phase at some point in the early Universe, such as EMD or kination. An EMD era can be due to the temporary domination of a long-lived massive particle or oscillations of a scalar moduli field [256]. More generic possibilities arise in models where a scalar field ϕ oscillates in a polynomial potential $V(\phi) \propto \phi^N$, characterized by an averaged equation of state $w = (N-2)/(N+2)$. In the limit $N \to \infty$,

we have $n = 6$ in Eq.(4.6) which is called kination phase, as the kinetic energy of the scalar dominates. Kination can generally arise in inflation [131], quintessence, dark energy [133], and axion-like particle (ALP) models with varying power of sin-Gordon potential [134] or with a non-zero initial field velocity [257, 115]. In order to retain the successful predictions of BBN theory, for all these scenarios the Universe needs to settle to RD before the BBN time $T_\Delta \sim 5\,\mathrm{MeV}$.

It is thus intriguing to see how the SGWB from global strings would alter in a non-standard cosmology and the related implication for detections. From another perspective, similar to the finding in the context of NG strings, SGWB from global strings thus opens up the possibility of probing the early Universe during the primordial dark age that may not be directly accessible otherwise. This allows us to test the standard assumption about cosmology while uncovering potential deviations. The base of this method lies in the f-T relation during RD (Eq.(4.32)) which allows us to relate a deviation from the standard prediction for the SGWB frequency spectrum to a time point in history where RD transits to a new (earlier) phase. To calculate $\Omega_{\mathrm{GW}}(f)$ with a non-standard cosmology background, we follow the method given in [156, 13]: we assume that the Universe transits from RD to a new equation state parametrized by n (Eq.(4.6): $\rho \propto a^{-n}$) at T_Δ, and match the energy density at T_Δ for a smooth transition. $\Omega_{\mathrm{GW}}(f)$ can then be calculated using Eq.(4.22) with the input of a non-standard evolution of $a(t)$.

We therefore expect that a non-standard cosmology leads to a modified GW spectrum in the high frequency region starting round f_Δ corresponding to the transition in cosmic history occurring around T_Δ (see Eq.(4.32)). Numerically, we found that $\Omega_{\mathrm{GW}}(f)$ can

be parametrized in the following way in large f region for general cosmologies (parametrized by n):

$$\Omega_{\rm GW}(f) \propto \begin{cases} f^{\frac{8-2n}{2-n}} \log^3\left\{ \frac{\eta}{\sqrt{\xi}} \left[\left(\frac{20}{f}\right)^2 \frac{1}{t_{eq}} \frac{t_\Delta^{1-4/n}}{z_{eq}^2} \Delta_R^{1/2}(f) \right]^{1/(2-4/n)} \right\}, & \text{for } n \geq \frac{26}{7}, \\ f^{-\frac{1}{3}}, & \text{for } n < \frac{26}{7}, \end{cases} \tag{4.33}$$

where t_Δ is the time corresponding to the temperature T_Δ, and we have assumed $\alpha = 0.1$. Eq. (4.33) shows that $\Omega_{\rm GW}(f \gg f_\Delta) \propto f^{+1}$ for kination ($n = 6$) and $\propto f^{-1/3}$ for MD ($n = 3$). Note that the validity of the VOS model approach requires $n > 2$, otherwise both ξ and $\bar{v}_\infty$ would me imaginary valued according to Eq. 4.7. Another caveat is that, at sufficiently large $f \gtrsim f_\eta$ such that $\log(...) \sim 1$ or $N \sim O(1)$ (corresponding to the very early stage after the string network formation), $\Omega_{\rm GW}$ would universally fall as $\Omega_{\rm GW} \propto f^{-1/3}$, for different background cosmologies.

In Fig. 4.9 we show our numerical results for benchmark examples of GW spectrum from a scaling global cosmic string network with a non-standard cosmology background such as kination or EMD, contrasted by the standard prediction shown in solid black line. We can see that compared to standard cosmology, with the presence of an EMD phase $\Omega_{\rm GW}(f)$ falls faster towards higher f, making it harder to observe in that f range. On the other hand, the spectrum rises above the standard prediction at high f in case of an early kination phase, leading to a stronger signal. The kination case thus is more subject to existing constraint

from LIGO. In general, the LIGO O3 constraint on T_Δ can be expressed as

$$\left(\frac{T_\Delta}{100\,\mathrm{GeV}}\right)^{-1}\left(\frac{\eta}{10^{15}\,\mathrm{GeV}}\right)^{4}\lesssim 1, \tag{4.34}$$

where we have dropped the logarithmic dependence from Eq.(4.33) for a simple estimate. The LIGO constraint can be relaxed if the duration of kination is short enough so that it transits to other phases (e.g. RD, EMD or vacuum energy domination) at a time corresponding to an f band below LIGO reach. In fact a sufficiently short span of kination epoch is also required to satisfy CMB/BBN bound on extra radiation density as we reviewed earlier in Sec. 4.3.3. With these motivations, in the following we further consider a concrete example with two stages of transitions where kination is preceded by an earlier RD era and investigate the constraints on the model due to the CMB/BBN bound on ΔN_{eff} (both Goldstone and GW).

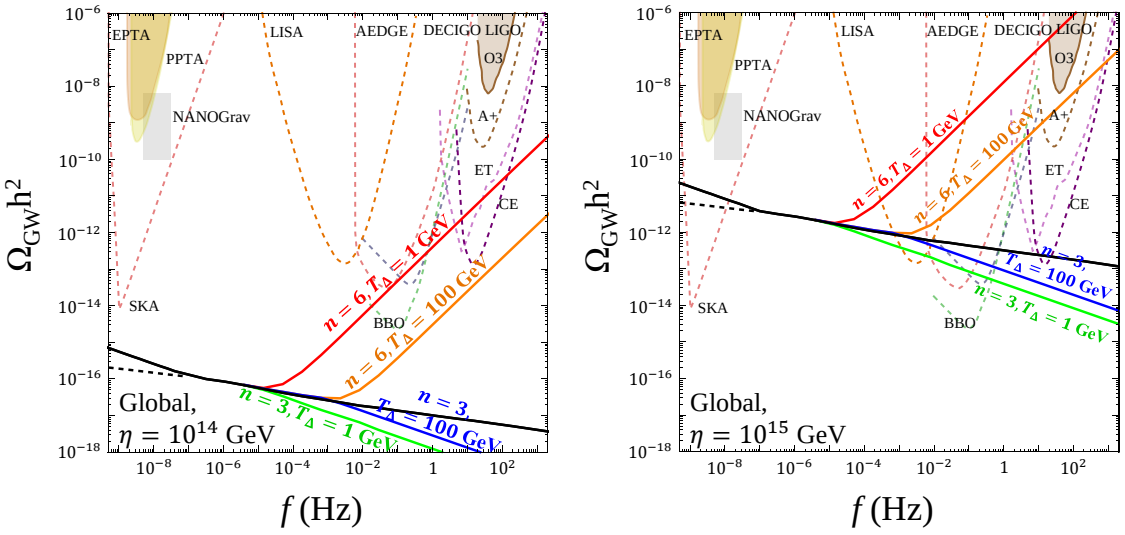

Figure 4.9: Gravitational wave spectrum from a global cosmic string network with $\alpha = 0.1$, $F_\alpha = 0.1$ for $\eta = 10^{14}$ (left) and 10^{15} GeV (right). The solid black lines show the GW spectrum with the standard cosmological evolution. The colored lines show the results with an EMD ($n = 3$) or kination ($n = 6$) that ends and restores the late RD era at the temperature $T_\Delta = 10$ GeV or 10^2 GeV. The sensitivities of related GW experiments are also shown.

A two-stage transition scenario with kination:

We assume that at $T = T_{\Delta 2} > T_{\Delta 1}$ kination transits to an early RD era (note: not the later standard RD era). Such a scenario can be realized if, for instance, a dominating radiation species decays to kination particles around $T_{\Delta 2}$. Other possibilities of exiting kination at high T exist, e.g. by a vacuum energy dominated phase such as inflation. However, a long period of vacuum energy domination would dilute the overall GW signal significantly [258, 158]. An alternative is to have a short duration of vacuum energy domination (mini-inflation) which then transits to an early RD. Kination can also be preceded by a dominating matter-like species that decay to kination particles. Here we choose to consider the simple scenario of RD-kination-RD for illustration.

Examples of GW spectrum of such a two-stage transition scenario are shown in the left-panel of Fig. 4.10: $\Omega_{\rm GW}$ linearly rises with f in a finite frequency range of $f_{\Delta 2} > f > f_{\Delta 1}$ due to kination, then restores the logarithmically decreasing behavior in the range of $f > f_{\Delta 2}$ (Eq.(4.33)) during the early RD. The three benchmark cases shown satisfy both LIGO O3 bound and the CMB $\Delta N_{\rm eff}$ bound that we will discuss next. The characteristic frequency $f_{\Delta 1}$ corresponding to the later stage of transition at $T_{\Delta 1}$ can be estimated by Eq.(4.32). Similarly, based on Eq.(4.20), the frequency corresponding to the earlier transition at $T_{\Delta 2}$ can be estimated as (applying $\rho \propto a^{-6}$ for kination)

$$f_{\Delta 2} = \left(\frac{T_{\Delta 2}}{T_{\Delta 1}}\right)^2 f_{\Delta 1}. \tag{4.35}$$

Now we consider the implication of the CMB $\Delta N_{\rm eff}$ bound on additional relic radiation for this kination example. We assume the equation of state of the Goldstones emitted from global strings is radiation-like. As suggested by the sharp rising of GW spectrum shown in Fig. 4.10 in the presence of a kination phase, the relic radiation energy densities of Goldstone and GW from the string network are dominated by the emission during the kination epoch, $T_{\Delta 1} < T < T_{\Delta 2}$, which can be roughly estimated as

$$\Omega_{\rm Gold}h^2 \sim \left\{8.0\times 10^{-9}\left(\frac{T_{\Delta 1}}{\rm GeV}\right)^{-1.6}\left(\frac{T_{\Delta 2}}{\rm GeV}\right)^{1.5} + \Omega^{15}_{\rm Gold}h^2\right\}\left(\frac{\eta}{10^{15}\,\rm GeV}\right)^2, \tag{4.36}$$

$$\Omega_{\rm GW}h^2 \sim \left\{1.3\times 10^{-11}\left(\frac{T_{\Delta 1}}{\rm GeV}\right)^{-1.37}\left(\frac{T_{\Delta 2}}{\rm GeV}\right)^{1.2} + \Omega^{15}_{\rm GW}h^2\right\}\left(\frac{\eta}{10^{15}\,\rm GeV}\right)^4, \tag{4.37}$$

where $\Omega_{\{\rm GW,Gold\}}$ are defined in Eq.(4.29), and numerically computed/fitted based on Eq.(4.22). We also defined the reference values with $\eta = 10^{15}\,$GeV assuming the standard

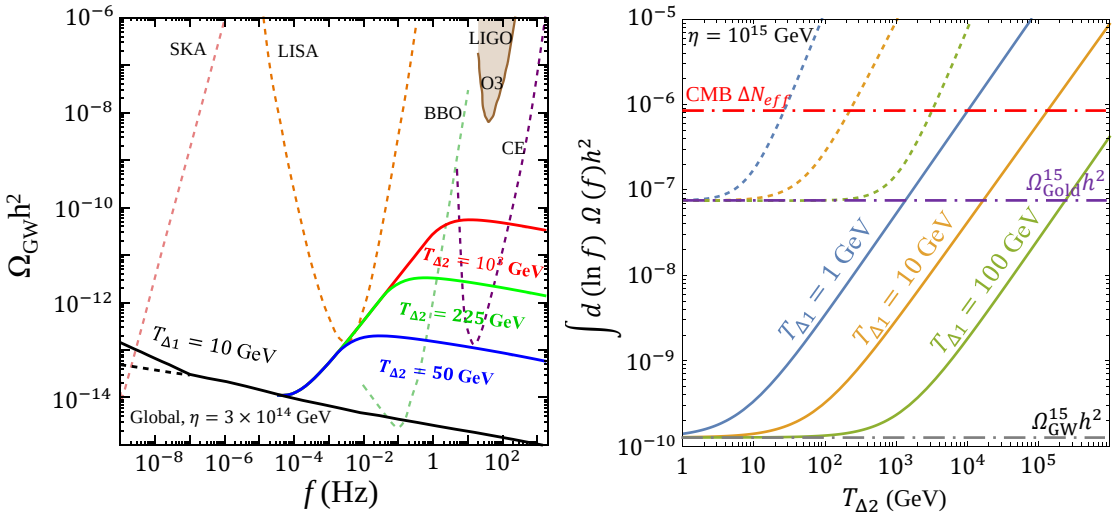

Figure 4.10: Left panel: examples of GW spectra from global strings with two-stage phase transitions including kination: from an early RD era to kination at $T_{\Delta 2}$, and from kination to standard cosmology at $T_{\Delta 1}$. Right panel: the relic energy densities of GWs (solid) and Goldstones (dashed) from global strings with varying phase transition temperatures ($T_{\Delta 1}$, $T_{\Delta 2}$). The red dotted-dashed line shows the CMB bound on extra radiation energy density [12, 11].

cosmology:

$$\Omega^{15}_{\rm Gold}h^2 \simeq 7.5 \times 10^{-8}, \qquad \Omega^{15}_{\rm GW}h^2 \simeq 1.3 \times 10^{-10}. \tag{4.38}$$

As discussed in Sec. 4.3.3, the emission of radiation-like Goldstone dominates the bound. The right panel of Fig. 4.10 illustrates three viable benchmark scenarios assuming $\eta = 10^{15}\,\text{GeV}$, parametrized by $T_{\Delta 1}$, $T_{\Delta 2}$: with $T_{\Delta 2} = 25\,\text{GeV}$, $180\,\text{GeV}$, and $3150\,\text{GeV}$, the CMB $\Delta N_{\rm eff}$ bound requires $T_{\Delta 1} \gtrsim 1\,\text{GeV}$, $10\,\text{GeV}$, and $100\,\text{GeV}$, respectively.

4.4.3 Probing new degrees of freedom

Many BSM theories involve new particles that are relativistic and in thermal equilibrium in the early Universe, e.g. in many potential solutions to the electroweak hierarchy problem [259, 260, 261, 120], and theories of dark sectors [262, 263, 264, 265, 266, 267, 268, 269, 270, 271, 272]. These particles would contribute to the effective number of relativistic degrees of freedom (DOFs) in energy, g_*, and in entropy, g_{*S}, in the high T Universe, but can generally be out of reach of available probes such as by the LHC or CMB experiments due to heavy masses or feeble interactions with the SM. The methodology for calculating the effect of new DOFs on the SGWB spectrum of NG strings was introduced in [13]. In this work, we briefly review the method and apply it to obtain results in the case of global strings.

We illustrate the effect of new massive DOFs on the string GW spectrum without referring to the details of the underlying theory. We model the change in the number of DOF with the following assumption where g_* rapidly decreases as T drops below a mass threshold $T_{\Delta g}$ [13]:

$$g_*(T) = g_*^{\rm SM}(T) + \frac{\Delta g_*}{2}\left[1 + \tanh\left(10\frac{T - T_{\Delta g}}{T_{\Delta g}}\right)\right] \simeq \begin{cases} g_*^{\rm SM}(T) & ; T < T_{\Delta g} \\ g_*^{\rm SM}(T) + \Delta g_* & ; T > T_{\Delta g} \end{cases} \tag{4.39}$$

To numerically demonstrate the effect, we choose the well-motivated scenario, where $T_{\Delta g}$ is of weak scale, which may be motivated from solutions to the Hierarchy Problem. In particular, in Fig. 4.11 we choose the benchmark values of $T_{\Delta g} = 200\,\text{GeV}$, $\Delta g_* = 0, 10^2, 10^3$, and assume $g_* \simeq g_{*S}$. As can be seen, relative to the prediction with SM DOFs only, the

spectrum falls towards higher f starting from a frequency $f_{\Delta g}$ that agrees with the prediction by the f-T relation in the RD era (see Eq.(4.32)).

Such an effect can be understood by analytical estimates following [13]. Deep in the RD regime, the Hubble rate and the corresponding time depend on g_* in the following way:

$$H \simeq \sqrt{\Delta_R \Omega_R} H_0 a^{-2}, \qquad t \simeq \frac{a^2}{2\sqrt{\Delta_R \Omega_R}}, \tag{4.40}$$

with

$$\Delta_R(a) = \frac{g_*(a)}{g_*^0} \left(\frac{g_{*S}^0}{g_{*S}(a)} \right)^{4/3}, \tag{4.41}$$

where H_0 is the current Hubble constant, and Ω_R is the radiation energy relic density observed today. Note that $\Delta_R(a)$ is simply a variational form of $\Delta_R(f)$ as defined in Eq. (4.26). Applying this simplification in Eq.(4.22), we have

$$\Omega_{\rm GW}\left(f \gg f_{\Delta g}\right) \simeq \Omega_{\rm GW}^{\rm SM}(f) \left(\frac{g_*^{\rm SM}}{g_*^{\rm SM} + \Delta g_*} \right)^{1/3}, \tag{4.42}$$

where $\Omega_{\rm GW}^{\rm SM}(f)$ indicates the amplitude with SM DOFs only. Eq.(4.42) clearly shows that the overall amplitude of the high f tail ($f > f_{\Delta g}$) of $\Omega_{\rm GW}$ decreases with the presence of additional DOFs, agreeing with numerical findings.

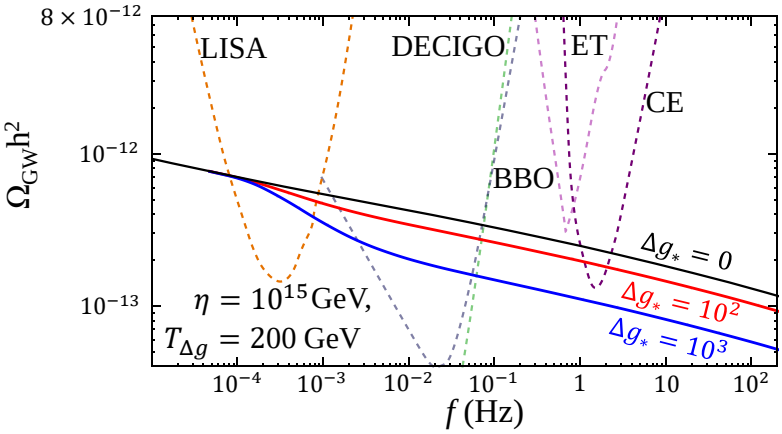

Figure 4.11: Modification to the GW spectrum from a global string network due to an increase in the number of relativistic degrees of freedom above $T_{\Delta g} = 200\,\text{GeV}$. In the example shown, $\eta = 10^{15}\,\text{GeV}$, $\alpha = 0.1$, and $\Delta g_* = 0, 10^2, 10^3$ (shown in black, red, and blue, respectively). The relevant experimental sensitivities are also shown.

4.5 Discussion

4.5.1 Sensitivity to the loop size parameter α and its distribution

Throughout our work we have used $\alpha \simeq 0.1$ as the peak value of loop sizes at their formation time, which is inspired by results from NG string simulations [209, 208]. However, there are still uncertainties about loop distribution for global strings. To investigate how such uncertainties may impact the predicted GW spectrum, in this subsection we consider two alternative scenarios of loop distribution: 1. varying α for the peak value, and 2. a log uniform distribution of loops as suggested in [109].

Alternative-1: varying α for the peak value.

The analysis with different α values is straightforward with our formulations in Sec. 4.3. In the left panel of Fig. 4.12 we show the α dependence of $\Omega_{\rm GW}(f)$ for specific f's normalized by the prediction with $\alpha = 0.1$ (the benchmark choice used in earlier sections)

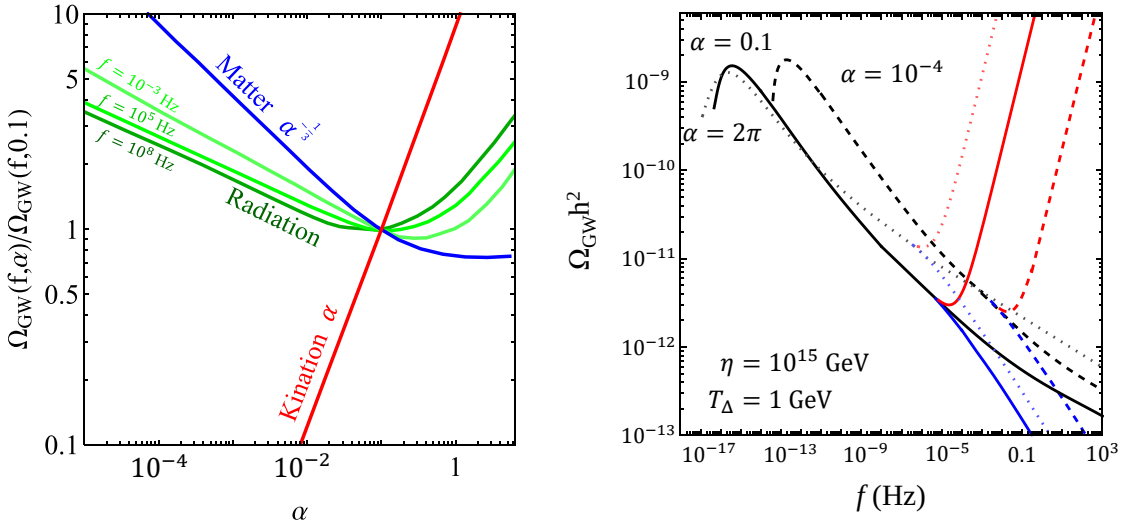

Figure 4.12: Left panel: $\Omega_{\rm GW}(f,\alpha)$ normalized by the prediction with $\alpha = 0.1$, varying α in the range of $10^{-5} \leq \alpha \leq 10$, $\eta = 10^{15}\,\text{GeV}$ for different background cosmologies (for MD and kination, the departure from standard cosmology is assumed to occur at $T_\Delta = 1\,\text{GeV}$). The green lines show the results with radiation dominated epoch with varying $f = 10^{-2},\ 10^{-5},\ 10^{-8}\,\text{Hz}$, and the red (blue) line shows the results for kination (matter) domination which are insensitive to f. Right panel: GW frequency spectra with varying loop size α (dotted: $\alpha = 2\pi$, solid: $\alpha = 0.1$, dashed: $\alpha = 10^{-4}$) with various background cosmologies: standard cosmology (black), kination (red) and EMD (blue)–another way of illustration with the same choices of η, T_Δ as in the left panel.

with different background cosmologies, assuming $\eta = 10^{15}\,\text{GeV}$. As shown, RD, MD, and kination-dominated eras have different dependencies on α, which are insensitive to f for the cases of MD and kination. The α dependence can be discussed in two distinct regions. Firstly, in the range of $\alpha < \kappa \sim 0.11$, the loop lifetime is shorter than a Hubble time, and thus the analysis and discussion in the previous sections can apply: the 2nd line in Eq.(4.25) explains the result for RD; the redshift effect on GWs is the same since the loop would decay off immediately, and smaller α corresponds to higher N for fixed frequency i.e. larger string energy density. The GW spectrum consequently increases. In addition, we find that in a kination epoch, the spectrum linearly increases with α, while in matter

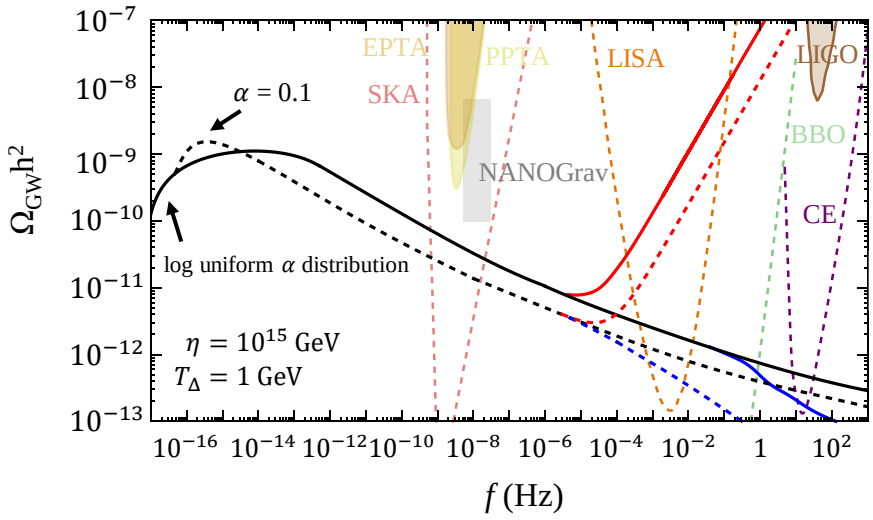

Figure 4.13: Solid lines: GW spectrum with a logarithmic uniform loop size distribution (Eq.(4.39)) for different cosmology backgrounds; dashed lines: results with a monotonous $\alpha = 0.1$ as applied in previous sections (for comparison). For the cases with kination or EMD, the departure from standard cosmology is assumed to occur at $T_\Delta = 1\,\mathrm{GeV}$.

domination $\Omega_{\rm GW}(f) \propto \alpha^{-1/3}$. In the other region of $\alpha > \kappa$, the loops are long-lived, and thus the spectrum in RD agrees with the NG string case, which gives $\Omega_{\rm GW}(f) \propto \alpha^{1/2}$ [13]. In this large α region, $\Omega_{\rm GW}(f)$ still linearly increases with α in kination, while becoming approximately α independent in MD.

Alternative-2: A log uniform distribution.

Fig. 5 of the recent global string simulation [109] suggests a logarithmic uniform distribution of the size of string loops at formation time, which is very different from the nearly monotonous α that we have assumed inspired by NG string simulation. While this hint of log uniform distribution is yet to be further tested, we consider how this variation can impact the prediction for GW signals. A log uniform distribution indicates that at formation time the loop number density $dn(\ell)/d\ell$ at size ℓ follows $dn(\ell)/d(\log \ell) \sim$ const, or

$dn(\ell)/d\ell \propto 1/\ell$. Our method of calculating SGWB signal with a monotonous loop formation size α as shown in Eq.(4.22) can be adapted to this alternative distribution by replacing $\mathcal{F}_\alpha/\alpha...$ in Eq.(4.22) (the "..." part represent other parts in the formula for computing GWs) with a sum over thinly sliced loop sizes in the range of $\pi/\eta < \ell < \pi/H$:

$$\sum_\alpha \frac{\mathcal{F}_\alpha}{\alpha}... = \lim_{n\to\infty} \sum_{x=0}^{n} \frac{1}{n} \left(\frac{1}{e^{-\frac{x}{n}\delta+y}} \right) ... = \frac{1}{\delta} \int_y^{\delta-y} e^x dx... = \frac{1}{\delta} \int_{\alpha_1}^{\alpha_0} \frac{1}{\alpha^2} d\alpha..., \tag{4.43}$$

where we have applied $\mathcal{F}_\alpha = \frac{1}{n}$ and $\alpha = e^{-x}$ to implement the log uniform distribution, and taken the continuous limit to get the second equality. The parameters $y,\ \delta,\ \alpha_0,\ \alpha_1$ are introduced to rewrite the integration limits in more convenient forms: $\ell_{\rm max} \sim \pi/H \equiv \alpha_0 t \equiv e^y t$, and $\ell_{\rm min} \sim \pi/\eta \equiv \alpha_1 t \equiv e^{-\delta+y} t$. However, in our numerical calculation we found that including small loops down to the scale of π/η leads to very large $\Omega_{\rm GW}(f) \gg 1$ in certain f range as a consequence of energy conservation. Therefore, we assume a lower cutoff of α at $\alpha \sim 10^{-4}$. The exact value of small scale cutoff on α is not essential for our study here, as our purpose is to simply show an example of how a log uniform distribution can alter the GW spectrum.

In Fig. 4.13 we show the GW spectrum predicted with the assumed log uniform distribution for different cosmology scenarios. We find that by summing over the loop sizes in the range of $10^{-4} \leq \alpha \leq 2\pi$, the GW amplitude is generally increased over many decades in the frequency range except around the cutoff around $f_0 \sim 10^{-16}\,$Hz. Due to the inclusion of larger loops up to $\alpha = 2\pi$ in the distribution, the low frequency cutoff extends to $\sim 2/(2\pi t_0)$.

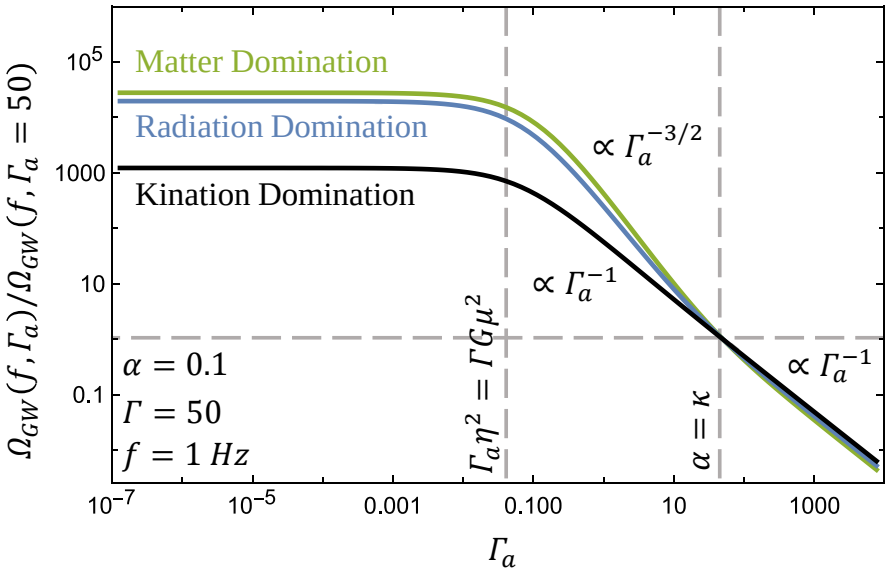

Figure 4.14: An illustration of $\Omega_{\rm GW}(f)$ for varying Γ_a (the Goldstone radiation parameter), normalized to the results with $\Gamma_a = 50$ (the benchmark value used in earlier sections). We fix other parameters as: $\Gamma = 50$, $\eta = 10^{15}$ GeV, $f = 1$ Hz. The results for different background cosmologies are shown in different colors. The three regions as discussed in the text are divided by the vertical dashed lines.

4.5.2 Sensitivity to the loop radiation parameter Γ and Γ_a

While we chose motivated benchmark values of loop radiation parameters Γ and Γ_a in our main studies, we acknowledge that there are still uncertainties around these values. Here we investigate how the GW signal would change by varying Γ and Γ_a. Considering energy conservation law and energy loss rates in Eq.(4.16), naively, we expect the GW density to depend on Γ, Γ_a simply as $\Omega_{\rm GW} \propto \frac{\Gamma G\mu^2}{\Gamma_a \eta^2}$. However, such dependencies can be more complex as the redshift-related factors $a(\tilde{t})$ and $t_i^{(k)}$ in Eq.(4.22) also depend on Γ_a, Γ. In Fig. 4.14 we illustrate the possibilities for the Γ_a dependence of $\Omega_{\rm GW}(f)$ based on numerical results (fixing $f = 1$ Hz and $\eta = 10^{15}$ GeV and $\Gamma = 50$ for example). Γ dependence is simpler, linear as naively expected, unless GW becomes the dominant radiation mode

($\Gamma_a \ll \Gamma$). We will show the Γ dependence explicitly in the following formulae/discussion. As can be seen in Fig. 4.14 there are three distinct regions in the $\Omega_{\rm GW}(f) - \Gamma_a$ relation, which we can understand analytically as follows:

• Large Γ_a, such that loops decay within a Hubble time after formation, driven by strong Goldstone emission. In this region $\alpha < \kappa$, where $\kappa \equiv \Gamma_a/(2\pi N)$ (Eq.(4.24)), and we can estimate with $N \sim 70$ for relevant observations. The Γ_a term thus dominates both numerator and denominator of Eq.(4.24), which implies that both $a(\tilde{t})$ and $t_i^{(k)}$ in Eq.(4.22) are insensitive to Γ_a. Therefore, $\Omega_{\rm GW}(f)$ in Eq.(4.22) depends on Γ, Γ_a as

$$\Omega_{\rm GW}(f) \propto \frac{\Gamma}{\Gamma_a}. \tag{4.44}$$

• Medium size Γ_a, such that loops survive beyond a Hubble time after formation, while Goldstone radiation still dominates over GWs. In this region, $\alpha > \kappa > \Gamma G\mu$, and thus redshift factors $a(\tilde{t})$ and $t_i^{(k)}$ in Eq.(4.22) depend on Γ_a. By fitting numerical results we find the following relations which depend on background cosmologies:

$$\Omega_{\rm GW}(f) \propto \begin{cases} \dfrac{\Gamma}{\Gamma_a^{3/2}}, & \text{for RD and EMD,} \\ \dfrac{\Gamma}{\Gamma_a}, & \text{for Kination.} \end{cases} \tag{4.45}$$

As discussed in Sec. 4.4.2, the GW frequency spectrum with an EMD is dominated by loop radiation during the later radiation domination era. Consequently, the $\Omega_{\rm GW}(f)$-Γ_a relation is approximately the same as RD for the benchmark frequency $f = 1\,\text{Hz}$.

• Small Γ_a, such that $\Gamma_a \lesssim \Gamma G\mu^2/\eta^2$ (i.e. $\kappa < \Gamma G\mu$, and the Goldstone emission term in Eq.(4.16) becomes negligible relative to the GW radiation). Given the hierarchy between the Planck mass and the viable η value considering the relevant constraints, this scenario is only possible for very small $\Gamma_a \ll \Gamma$. In this case, GW radiation would become the dominant energy loss mechanism and $\Omega_{\rm GW}(f)$ would increase as, $\Gamma^{-1/2}$ which agrees with the related result for NG strings [13].

4.5.3 Non-scaling solution

In this subsection, we consider the impact of possible non-scaling solutions on the GW signals. The violation of the scaling properties in the case of global strings were found in some of the recent simulation studies [202, 196, 108, 110, 111, 198, 109, 177]. This suggests that the attractor solution of the average number of strings per Hubble patch, ξ, logarithmic growing with N. Note that in most of these studies the non-scaling behavior is found in the low N regime which is within direct reach of current simulations, and whether such a behavior can apply to large N still needs to be investigated. As earlier shown in Fig. 4.1, the VOS model can be consistent with the non-scaling solution Eq.(4.9) (or Eq.(4.46) below) within the range of low N, $3 \lesssim N \lesssim 7$, then predicts $\xi \sim$ const for larger N. Nevertheless, it is intriguing to see how the GW spectrum would change if such a behavior does sustain throughout the evolution history of the string network, and whether/how a variation to the original analytical VOS model may match this behavior. We will focus on the following two examples and then comment on other possibilities, and in both cases we adopt the

non-scaling solution as suggested in simulations [196, 15, 177]

$$\xi = 0.24(2)N + 0.2, \tag{4.46}$$

where $N \equiv \ln(\eta/H(t))$. We consider ξ taking the above non-scaling form in both examples that we will discuss next, and adopt the relevant parameters from the VOS model for the GW calculations (Eqs.(4.12,4.13,4.14)).

In the first possibility we consider, in addition to Eq. 4.46, we apply the following benchmark parameters: a constant average velocity of long strings $\bar{v}_\infty \simeq 0.50 \pm 0.04$, and a loop chopping parameter $\bar{c} = 0.497$, which we obtained in Sec. 4.2.1 based on fitting simulation results (Table. 4.1). With Eq.(4.13), primarily derived based on energy conservation, we find the prediction for effective loop formation parameter $C_{\rm eff} \propto N^{3/2}$. With this $C_{\rm eff}$ as an input for Eq.(4.22) we computed the GW spectrum, and found that the amplitude is larger than the prediction in [15] by a factor of $\mathcal{O}(10-100)$, depending on frequencies. This discrepancy motivated us to introduce the second scenario which is found to lead to a good agreement with [177]: while still assuming Eq. (4.46), this example involves a time-dependent $\bar{c}\bar{v}_\infty$, and consequently a different form of $C_{\rm eff}$:

$$\bar{c}\bar{v}_\infty = 0.15(1)N^{-1/2} \quad \rightarrow \quad C_{\rm eff} \simeq 0.018(3)N. \tag{4.47}$$

Based on the analysis method given in Sec. 4.3.3, the GW spectrum with the non-scaling solution Eq.(4.47) in a RD background (the spectrum would be cut off at lower frequencies

by a QCD-like phase transition as shown in [15]) can be estimated as

$$\Omega_{\rm GW}h^2 \simeq 2.6\times10^{-17}\left(\frac{\eta}{10^{15}\,{\rm GeV}}\right)^4 \log^4\left[\left(\frac{2}{\alpha f}\right)^2 \frac{\eta}{t_{eq}}\frac{1}{2z_{eq}^2}\Delta_R^{1/2}(f)\right]\Delta_R(f). \tag{4.48}$$

The notable difference between this result and that based on the scaling VOS model solution (Eq.(4.25)) is the power law index of the log term (i.e. $\log^4$ vs. $\log^3$), which enhances the GW amplitude by $\mathcal{O}(10)$ for this non-scaling example. The enhancement is due to the increase in loop number density (Eq. 4.13). Fig. 4.15 illustrates the GW spectrum predicted with a non-scaling solution where $\xi \propto N$, including a comparison between our results based on a variation to the VOS model (Eq. (4.47)) and the result in [15] based on extrapolating simulation results to large N. A good agreement between our second scenario (Eq.(4.47)) and that in [15] can be seen in Fig. 4.15. In particular ,our analytic fit for the GW spectrum (Eq.(4.48)) captures the key $\log^4$ dependence that agrees with [15]. This agreement suggests that the extrapolation of the non-scaling solution to large N may be reproduced in a variation to the original VOS model, where the relations $\bar{c}\bar{v}_\infty \propto N^{-1/2}$ and $\xi \propto N$ are realized. This hint may be helpful for future investigations.

As a supplemental discussion, in Fig. 4.16 we illustrate and compare the different predictions of GW spectrum based on the two aforementioned non-scaling scenarios, with various background cosmologies. As shown, in the second scenario (Eq.(4.47)) the GW spectrum amplitude is lowered by $\mathcal{O}(10)$ relative to the first scenario (Eq.(4.46)), which is due to the different predictions for loop number density ($C_{\rm eff} \propto N$ v.s. $C_{\rm eff} \propto N^{3/2}$). In the frequency range of our interest, the result is insensitive to the initial condition dependent

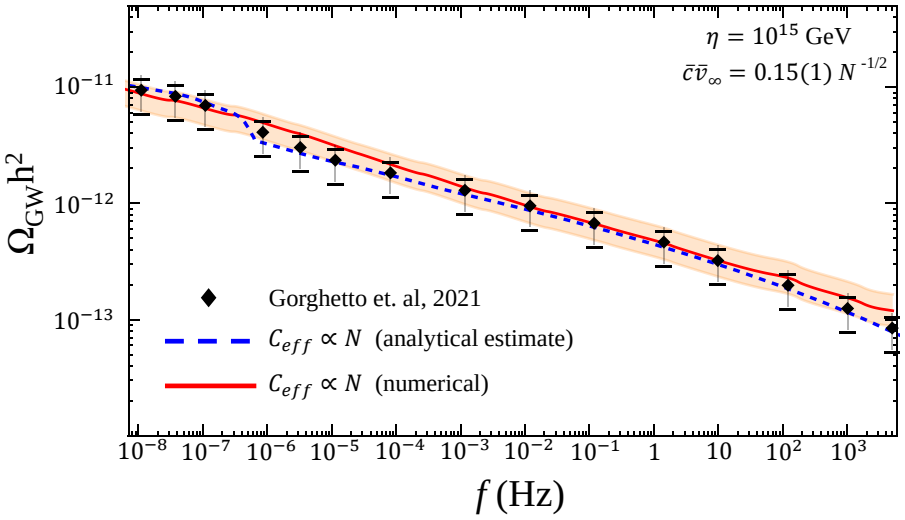

Figure 4.15: GW spectrum in the radiation dominated epoch assuming a non-scaling solution ($\xi = 0.24(2)N+0.2$): a comparison between the result with our assumption/method and that obtained in the recent simulation work [15]. The data points with error bars are taken from [15]. The blue dashed curve is based on our analytical estimate Eq.(4.48). The red curves with shadowed uncertainty band is based on our numerical calculation of Eq.(4.22) with linear growth of $C_{\rm eff} \propto N$. Further details are given in the main text.

parameter β: as discussed in [109, 177], the linearly growing term in Eq.(4.46) would quickly dominate the string network evolution. Then the energy loss will be linearly afterward as we have seen in earlier sections.

A very different form of non-scaling solution was suggested in another simulation work [111]:

$$\xi = 2.60 \times \log\left(\frac{T_{\rm PQ}}{T}\right) + 1.27, \tag{4.49}$$

where $T_{\rm PQ} \sim \eta$ is the temperature when the PQ symmetry breaking occurs. The prediction for ξ as in Eq.(4.49) is significantly larger than non-scaling results from other groups' simulations [196, 108, 110, 109, 177]. As suggested by the authors of [111], the predic-

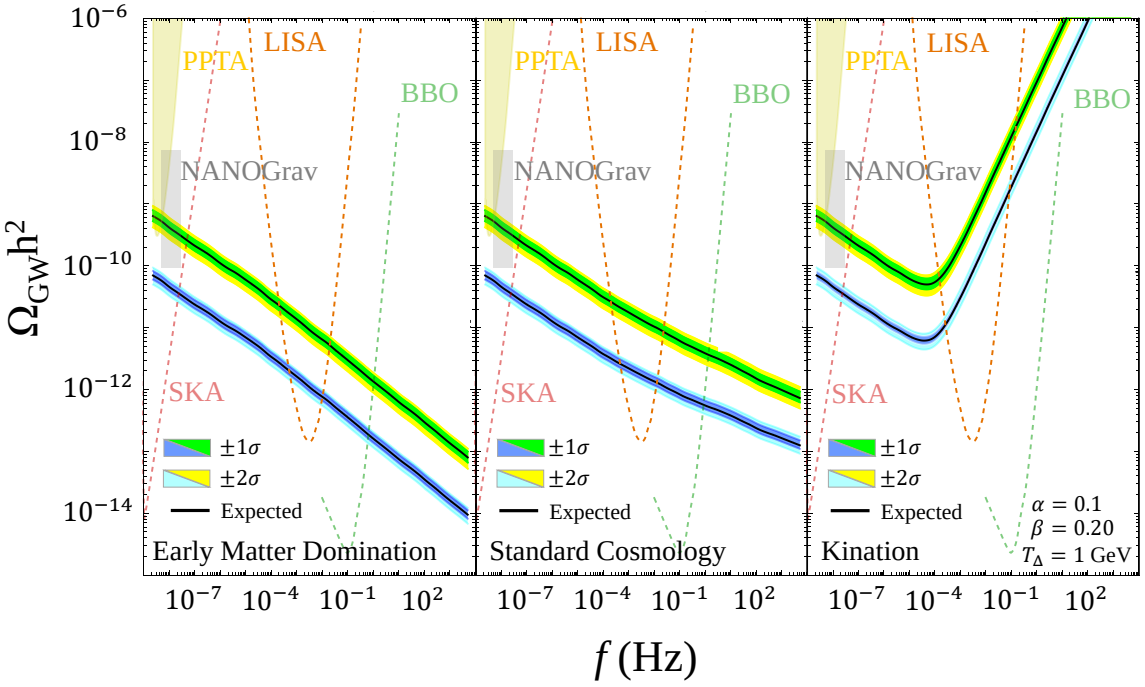

Figure 4.16: An example of GW spectra from a global string network with a non-scaling solution Eq.(4.9) in various cosmological backgrounds. Upper lines show the results with $C_{\text{eff}} \propto N$, lower lines show the results with $C_{\text{eff}} \propto N^{3/2}$. Details about the two scenarios of C_{eff} can be found in the main text. The black lines show the central values, while the yellow(Green) and cyan(Blue) areas represent the 2(1) sigma uncertainty range for the linear growth $\xi = 0.24(2)N + 0.2$. A set of related experimental sensitivities are also shown.

tion of Eq.(4.49) only provides a rough counting for cosmic strings, which may address the discrepancy, while further investigations are needed. We attempted to fit Eq.(4.49) with a variation of VOS model, but found a rather poor VOS model fit for the 13 data points provided in [111] due to the large value ξ given in Eq.(4.49), which is inconsistent with other simulation results. Assuming the non-scaling behavior as in form of Eq.(4.49) sustains till late times, we expect the GW amplitude to be amplified by a factor of $\mathcal{O}(10-100)$ relative to the scaling case due to the larger loop density implied (similar to the case inspired by [109]).

4.5.4 Distinguish from other SGWB sources

In this subsection, we discuss potential challenges for detecting a SGWB signal from global strings in practice, including astrophysical background and a comparison with other cosmological sources of SGWB.

SGWB from global strings, like other cosmogenic SGWBs, may be contaminated by astrophysical sources of SGWB, e.g. from unresolved binary black hole mergers [138, 273, 274, 275, 276, 277, 278]. Progress has been made in recent years to address this important issue of distinguishing a cosmological SGWB from its astrophysical counterpart. The potential solutions include: identify and subtract astrophysical sources using information from future GW detectors with improved resolutions [279, 280, 281]; optimized statistical analysis beyond the conventional cross-correlation method [282, 283, 284]; utilize spectral information over a wide frequency band [239, 285, 286, 287, 288, 278, 289, 290, 291]. Detailed discussions on this subject can be found in e.g. [13, 278, 287].

Upon detection of a cosmogenic SGWB signal, it is important to analyze and identify the nature of the underlying physics. Global cosmic string is among many motivated new physics sources that can give rise to a SGWB [164, 292, 293], for example, primordial inflation [294, 295] and black hole [296], preheating [297, 298, 299, 300], first-order phase transitions [301, 302, 303, 304, 305], and other types of topological defects [306, 254] including local/NG strings [225, 167, 307, 308, 309, 310]. A key to distinguishing the various cosmological sources lies in the GW spectral information. For instance, SGWB from a first-order phase transition features a peaky spectrum in frequency associated with specific split power laws, which results from the fact that the GWs were emitted during a specific

epoch in the early Universe. In contrast, SGWBs from cosmic strings (both global and NG) feature a rather long (nearly) flat plateau towards high frequencies, due to the continuous emission throughout the cosmic history. We refer to [13] for more detail regarding the general comparison of SGWB originated from cosmic strings with other cosmological sources. Here we highlight the prospect of distinguishing SGWB from global strings vs. that from NG strings. As seen in Sec. 4.3.1 and Fig. 4.3 the GW spectrum from global strings has a long tail which logarithmically declines towards high frequencies, whereas the spectrum from NG strings is very close to simple flatness (except for the mild steps due to the change in g_*). A main cause of such a difference is the logarithmic time-dependence of the global string tension, Eq.(4.46). The difference would be further amplified if the non-scaling behavior as discussed in Sec. 4.5.3 is confirmed to last till late times. In practice, we therefore expect that for global strings, GW searches at lower frequencies such as SKA in general have a better prospect of detection than those at higher frequencies such as LIGO (the prospect also depends on the experimental sensitivities).

In summary, while challenges for experimentally detecting a global string sourced SGWB are present, potentially promising solutions exist and will be further developed in coming years. Using frequency band information is a common potential solution for disentangling a global string signal from both astrophysical background and other cosmological sources, which will be strengthened with a multi-band GW experimental program [241, 287, 290, 278].

Chapter 5

Determine early dark energy in gravitational wave data

5.1 Introduction

Gravitational waves (GWs) search technologies [311, 312, 275, 274, 313] have strong ongoing research interest. Implications from these developments focus not only on discovering new astrophysical objects [273, 314], but also probing gravitation physics [315, 316, 317, 318, 319, 320] and non-standard cosmologies [321, 156, 155, 17, 322, 323, 162, 157]; and GW observations has been used to measure the current Hubble rate H_0 [279, 324, 325, 326]. Although not yet sufficiently precise to resolve the Hubble tension, estimates will be continuously improved.

Increasingly attention is focusing on possible solutions of Hubble tension, a Hubble rate discrepancy between local observations, such as supernovae signals [327, 328, 329, 330,

331, 332], lensing time delays [333, 334, 335, 336, 337, 338, 339] and non-local searches, e.g. the cosmic microwave background (CMB) [11, 340, 341, 342]. Local measurements confirm H_0 is approximately five sigma statistical significance above observation in the CMB with assuming standard cosmological model (ΛCDM). This strong disagreement has been closely examined using many statistical [343, 344, 345, 346] and measurement methods [347, 348, 337, 349, 332, 350], and re-examining potential technical issues [351, 352, 353, 354, 355, 356] in both local and CMB measurements (see reviews [357, 358, 348, 359]). Various evidence suggests the discrepancy arises due to a currently unknown physical phenomenon outside conventional ΛCDM predictions.

V. Poulin *et al.* [16, 134, 360] showed that early dark energy (EDE) behaves as a cosmological constant when comoving scaling factor $a(t)$ is smaller than critical $a_c \sim 10^{-4}$, and is then diluted faster or equal to radiation-like component to relieve the Hubble tension. EDE contributes up to 20% energy density of the universe (model-dependent) at a_c, consequently accelerating the universe expansion and hence slightly delaying the universe entering the matter-domination era. This framework brings H_0 in estimated CMB to be consistent with local measurements and also with measured high and low redshifts [361, 362, 363, 364].

We adopted the simplest EDE model, i.e., slow-rolling potential $V(\phi) \propto \phi^{2n}$ with scalar field ϕ [365, 366, 257]. Effective mass for ϕ is lighter than the Hubble rate on the early universe, and hence Hubble friction overdamps scalar field motion and freezes it. Consequently, the scalar field behaves as a subdominant cosmological constant until the Hubble rate decreases to approximately scalar effective mass, namely, the driving force overcomes the Hubble friction. Subsequently, the field starts oscillating as a fluid with equation of state $w_\phi = (n-1)/(n+1)$.

Cosmic strings, one dimension long-lived topological defects, are stable and predictable sources for stochastic GW background (SGWB) and hence ideal creator sources for GW as a messenger that carries new signal from the early universe [104, 367, 188]. Such stable objects arise from beyond standard model theories, such as spontaneously broken $U(1)$ [165, 166, 167, 168] or superstring theories [172, 173, 174, 175]. The GW frequency spectrum formed by the cosmic string network is an approximate plateau over a broad frequency range with parameter $G\mu$ dependence, where G is the Newtonian gravitational constant and μ is string tension. GW experiments EPTA [368] and PPTA [242] provide strong bounds on $G\mu \lesssim 2 \times 10^{-11}$ [17], but this remains in tension with the NANOGrav 12.5yr result [369] $G\mu \in (2, 30) \times 10^{-11}$ in 95% C.L. [145, 146]. The tension may be due to the different noise analysis methods [249].

This paper shows that EDE imprints a GW signal in the SGWB formed from the cosmic string network that is distinguishable from other astrophysical and cosmological signals in the GW frequency spectrum. Such a unique spectrum could be detected in future GW experiments LISA [370, 141, 286] and SKA [247]. We also contour the SKA and LISA sensitivities on EDE parameter space.

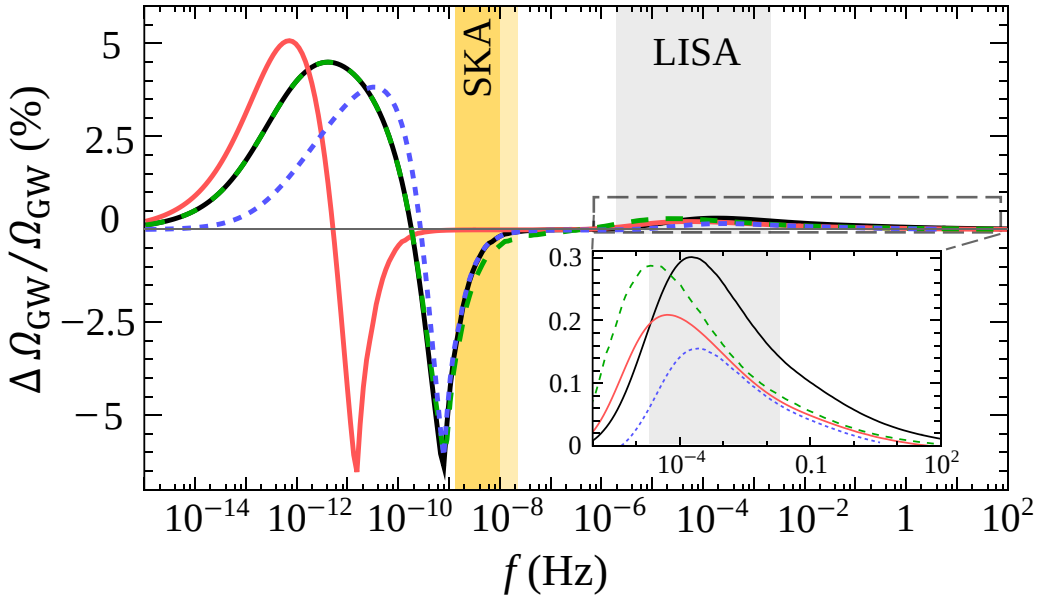

Figure 5.1: Signal difference ratio versus GW frequencies as defined in Eq.(5.6). The black solid curve: $G\mu = 10^{-12}$, $a_c = 10^{-4.48}$, $n = 2$ and $f_{\rm EDE} = 4\%$. According to black curve, others are changing one parameter on each, e.g. red: change $a_c \to 10^{-3.57}$, green: $G\mu \to 10^{-11}$, and blue: $n \to 3$. The a_c correspond to highest and lowest values in 68%C.L. CMB analysis [16]. LISA and SKA sensitivities targeting $G\mu = 10^{-12}$ cosmic string GW spectrum (see Fig. 2 in [17]) show as gray and yellow area, respectively. The lighter yellow is for $G\mu = 10^{-11}$.

5.2 Framework

Nambu-Goto string action is an effective model that describes cosmic string network evolution [223]. These strings formed at time t_F when the temperature cools to symmetry breaking scale of theory. Shortly after, the defects behave as a scaling invariant network that includes a few long (super-horizon length) strings and a collection of closed loops chopped from long strings. GW loop emission dominates the network energy loss, and loop number density $n_o(t_i, t)$ is characterized by [168]

$$dn_o(t_i, t) = \frac{0.1}{\alpha} \int_{t_F}^{t} C_{\text{eff}}(t_i) \frac{dt_i}{t_i^4} \left(\frac{a(t_i)}{a(t)} \right)^3, \tag{5.1}$$

where loops form at t_i and subsequently continuously diluted until time t, factor 0.1 represents 90% string energy release to loop kinetic energy and subsequent diluted off, and parameter $\alpha = 0.1$ [208, 209] characterize initial loop size $\ell(t_i) = \alpha t_i$. The appendix reviews the simulation calibration parameter C_{eff} [322, 17], which controls loop production. Created loops are shortened by radiating GWs

$$\ell(t) = \alpha t_i - \Gamma G\mu(t - t_i), \qquad \text{with} \quad t \geq t_i, \tag{5.2}$$

where GW emission parameter $\Gamma = 50$ [208, 209, 225, 371, 372]. Loop emission characterizes in normal modes $k \in \mathbb{Z}^+$ oscillation with emitted GW frequency,

$$f = \frac{2k}{\ell} = \frac{a(t)}{a(t_0)} \frac{2k}{\alpha t_i - \Gamma G\mu(t - t_i)}, \tag{5.3}$$

where emitted GWs redshift to today (t_0). Thus, the SGWB frequency spectrum can be computed by summing all normal modes,

$$\Omega_{GW}(f) = \frac{f}{\rho_c}\frac{d\rho_{GW}}{df} = \sum_k \Omega_{\rm GW}^{(k)}(f), \tag{5.4}$$

with

$$\begin{aligned}\Omega_{GW}^{(k)}(f) &= \frac{1}{\rho_c}\frac{2k}{f}\frac{F_\alpha \Gamma^{(k)} G\mu^2}{\alpha(\alpha+\Gamma G\mu)} \\ &\times \int_{t_F}^{t_0} dt \frac{C_{\rm eff}(t_i)}{t_i^4}\left(\frac{a(t)}{a(t_0)}\right)^5\left(\frac{a(t_i)}{a(t)}\right)^3 \theta(t_i - t_F)\theta(\ell(t)),\end{aligned} \tag{5.5}$$

where critical density $\rho_c = 3H_0^2/8\pi G$, cusp dominates GW emission $\Gamma^{(k)} = \Gamma/(3.6\,k^{4/3})$ [17], and we sum over k modes up to $k \leq 10^5$.

To visualize EDE influence on SGWB, we define signal difference to SGWB spectrum ratio as,

$$\frac{\Delta\Omega_{\rm GW}}{\Omega_{\rm GW}}(f) \equiv \frac{\Delta\Omega_{\rm GW}(f)}{\Omega_{\rm GW}^{\Lambda\rm CDM}(f)} \equiv \frac{\Omega_{\rm GW}^{\rm EDE}(f) - \Omega_{\rm GW}^{\Lambda\rm CDM}(f)}{\Omega_{\rm GW}^{\Lambda\rm CDM}(f)}, \tag{5.6}$$

where superscripts imply GW frequency spectra on different cosmologies. Fig. 5.1 shows that EDE modifies the spectrum in two frequency regions: firstly, in contrast to ΛCDM, diluting EDE delays entering of matter domination, which slows down the redshift on GWs that emitted by the loops with loop formation time $t_i \lesssim \Gamma G\mu t_c/\alpha$ where t_c is the universe age at a_c. This mechanism *peaks* the GW spectrum at frequency $f \sim 10^{-4}$ Hz. The resulting spectrum typically increases at characterized frequency f_p, which can be estimated from

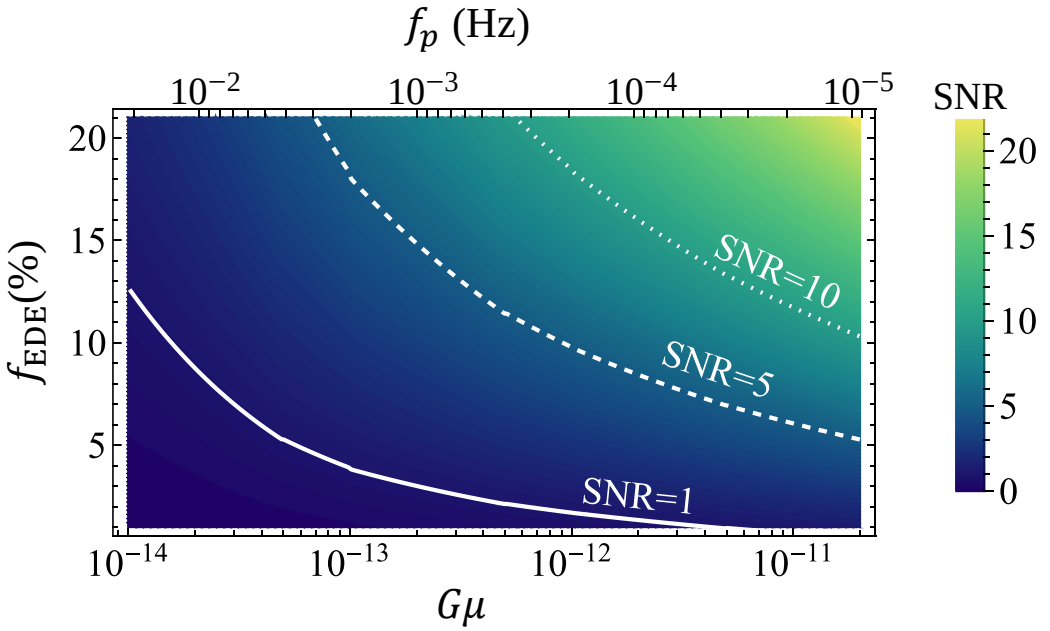

Figure 5.2: Energy density fraction of early dark energy f_{EDE} versus string tension parameter $G\mu$ with peak frequency f_p on upper x-axis, and fixing early dark energy potential exponent parameter $n = 2$ and critical redshift $a_c = 10^{-4.48}$. The colored region shows influenced cosmic string GW background Signal-to-Noise Ratio (SNR) with LISA 4 years nominal mission operating period, see Eq.(5.22).

Eq.(5.3) as,

$$f_p \sim \frac{2\epsilon}{\Gamma G\mu t_c}\frac{a_c}{a(t_0)}, \tag{5.7}$$

where $\epsilon \sim \mathcal{O}(1)$ is a numerical parameter. The shape of this peak approximately estimate to

$$\frac{\Delta\Omega_{\rm GW}}{\Omega_{\rm GW}}(f) \propto \begin{cases} \left(\frac{f}{f_p}\right)^{-0.23}, & \text{for } f \geq f_p, \\ \left(\frac{f}{f_p}\right)^{3}, & \text{for } f < f_p, \end{cases} \tag{5.8}$$

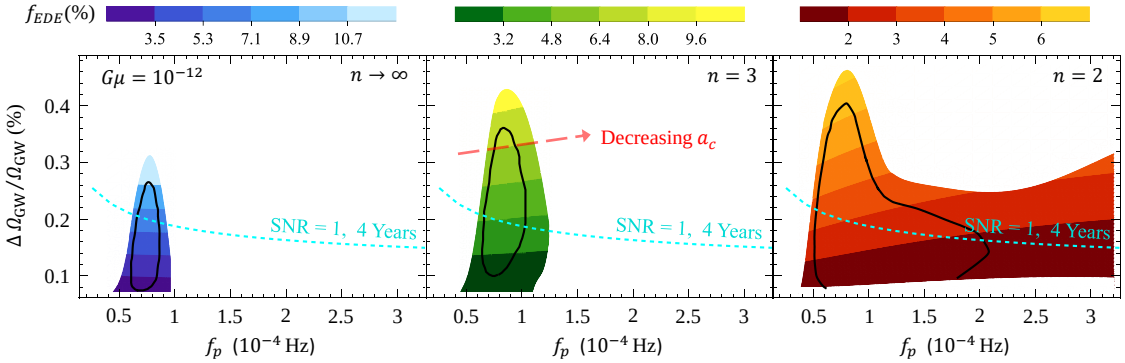

Figure 5.3: GW spectrum difference ratio $\Delta\Omega_{\rm GW}/\Omega_{\rm GW}$ at peak frequency f_p with fixed $G\mu = 10^{-12}$. The colored areas and the black circled areas represent the 95% C.L. and 68% C.L. in CMB numerical analysis, respectively. The CMB analysis is directly quoted from [16], they scan early dark energy (EDE) total energy fraction $1\% \leq f_{\rm EDE} \leq 13\%$ and critical scaling factor $10^{-4.8} \leq a_c \leq 10^{-3.4}$ in different EDE potential ϕ^{2n} exponents $n = \{2, 3, \infty\}$. The dashed curves show the signal-noise-ratio SNR = 1 with LISA 4 years collection. The curves on the boundaries between each color (e.g. between lighter green and green) are a_c variations with fixed $f_{\rm EDE}$ as the red dashed line.

and the slower diluting EDE (lower n) more significantly delays the universe entering the matter domination epoch while GWs experience a longer and slower dilution period, hence increasing the signal difference.

Second, faster universe expansion at t_c reduces loop chopping efficiency i.e., reduces $C_{\rm eff}(t_i = t_c)$ in Eq.(5.1), due to less frequent intercommutation between strings. Such a mechanism implies a signal difference *dip* at characteristic frequency $f_d \sim 10^{-9}$ to 10^{-11} Hz as shown in Fig. 5.1, which can be computed from Eq.(5.3) with GWs emission today,

$$f_d \sim \frac{2}{\alpha t_c}. \tag{5.9}$$

Shortly after t_c, more long strings have entered the horizon, loop chopping efficiency turns back to about that for ΛCDM, and again, the delayed entering of matter domination era. Therefore, loop number density increases slightly, and redshift effects on GW slow. This

mechanism increases signal difference at frequencies below but close to f_d.

Universal fitting on a wide frequency spectrum not only determines string tension parameter $G\mu$, but also addresses EDE parameters. $f_{\rm EDE}$ proportionally controls both signal difference peak and dip amplitudes, whereas peak amplitude is sensitive to n but dip amplitude is independent. Therefore, we expect peak and dip amplitudes pin down $f_{\rm EDE}$ and n, and f_d and f_p can be used to address a_c (as shown in Fig. 5.1).

Modified GW frequency spectra present in LISA [370, 141, 286] and SKA [247] frequency sensitivities (Fig. 5.1) and hence we focus on analyzing signal-to-noise ratio (SNR) for the remainder of this paper.

5.2.1 Application of VOS Model

In this subsection, we review the velocity-dependent one-scale (VOS) model that used to predict the string network evolution [373, 203, 204], and most of the content can also be found in Refs. [17, 322, 374, 375, 236]. The VOS model is used to describe the evolution of long Nambu-Goto string network in terms of a mean string velocity [373, 203, 204]

$$\bar{v} = \sqrt{\frac{m}{2}\frac{k(\bar{v})}{[k(\bar{v})+\bar{c}]}\left(1-\frac{2}{m}\right)}, \tag{5.10}$$

and a characteristic length,

$$\xi = \frac{m}{2}\sqrt{\frac{k(\bar{v})\,[k(\bar{v})+\bar{c}]}{2(m-2)}}, \tag{5.11}$$

as a fraction of the horizon, where the m is exponent of scaling factor in universe energy density $\rho \propto a^{-m}$, the chopping parameter $\bar{c} = 0.23$ [204], and the ansatz function [204]

$$k(\bar{v}) = \frac{2\sqrt{2}}{\pi}(1-\bar{v}^2)\left(1+2\sqrt{2}\bar{v}^3\right)\frac{1-8\bar{v}^6}{1+8\bar{v}^6}. \tag{5.12}$$

The long string energy density express

$$\rho_L = \frac{\mu}{(\xi t)^2}, \tag{5.13}$$

and the intercommutation between strings chops them to loops as energy losing as

$$\frac{d\rho_L}{dt} = \bar{c}\bar{v}\frac{\rho_L}{\xi t} = \bar{c}\bar{v}\frac{\mu}{(\xi t)^3}. \tag{5.14}$$

Consequently, the loops number density at evolution time t with particular loop size $\ell(t_i) = \alpha t_i$ that formed at time t_i reads

$$dn_o(t_i, t) = \frac{0.1}{\alpha}\int_{t_F}^{t} C_{\text{eff}}(t_i)\frac{dt_i}{t_i^4}\left(\frac{a(t_i)}{a(t)}\right)^3, \tag{5.15}$$

with

$$C_{\text{eff}}(t_i) = \frac{\bar{c}}{\gamma}\bar{v}\xi^{-3} \tag{5.16}$$

where C_{eff} implies that the energy gain from string network, and a^3 is due to number density dilution. The $\gamma = \sqrt{2}$ is loop Lorentz boost [208, 209]. EDE locally influences the universe expansion rate around $a(t) \sim a_c$, and therefore it would influence the C_{eff} on such a period. A smaller C_{eff} implies a faster universe expansion rate, i.e. smaller m. It is because of a less frequently intercommuation rate in a faster expanding universe.

We present C_{eff} versus scaling factor a in Fig. 5.4, the bumps on the black curve are caused by the changing relativistic degree of freedom in early universe. EDE locally influences C_{eff} around a_c as the colored ranges. Before a_c, EDE behaves as a cosmological constant that accelerates the universe expansion rate, and therefore C_{eff} is smaller than the one in ΛCDM around the a_c. Shortly after, EDE starts diluting with a dilution rate that is faster or equals to radiation-like components, then the universe expansion rate m turns to slightly larger than the m in ΛCDM. Consequently, C_{eff} increases to slightly higher than in ΛCDM. All curves converge when EDE energy density isn't comparable to other components.

5.2.2 Numerical Details

Parameters

The cosmological parameters we used in numerical is as following: the scale factor for Hubble expansion rate $h = 0.71$ [16], pressureless matter density of the universe $\Omega_m = 0.31$, dark energy density of the ΛCDM universe $\Omega_\Lambda = 0.69$, today temperature $T_0 = 2.726\,\text{K}$, and relativistic degrees of freedom $g_*(T)$ is quoted from [376].

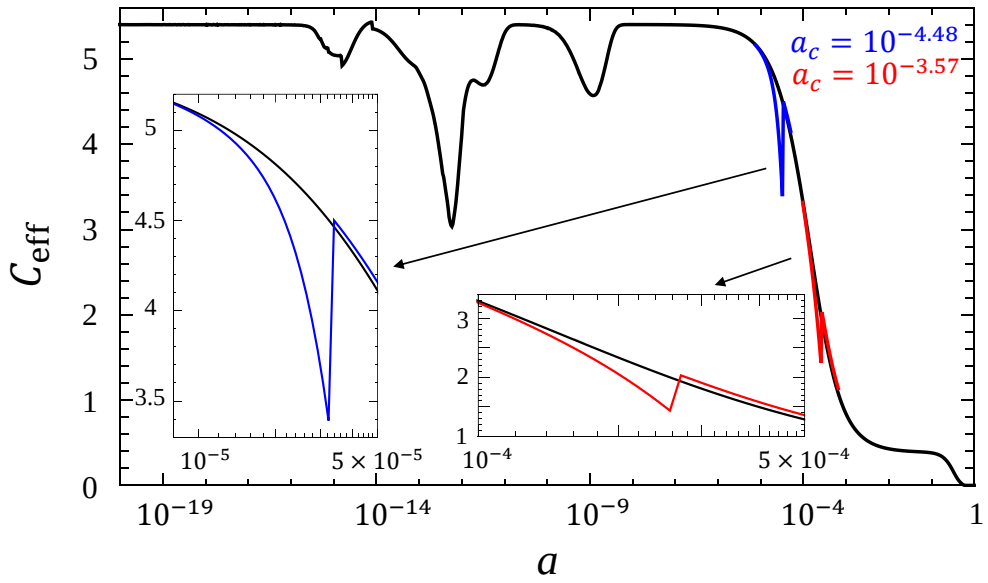

Figure 5.4: $C_{\rm eff}$ versus scaling factor a. The black curve is in ΛCDM. The modified universes with the EDE are shown as $a_c = 10^{-4.48}$ and $a_c = 10^{-3.57}$ as blue and red, respectively.

LISA noise background

To estimate the noise background in the LISA to a stochastic gravitational wave background, we express the result that concluded in [287]. The signal-to-noise ratio is defined as $\{i = \text{SKA}, \text{LISA}\}$

$$\text{SNR} = \sqrt{T_i \int_{f_{\rm min}}^{f_{\rm max}} df \left(\frac{\Omega_{\rm GW}(f)}{\Omega_n^i(f)} \right)^2}, \tag{5.17}$$

where $\Omega_{\rm GW}(f)$ represents the GW signal spectrum, T_i is experiment operating period, and the integration range is the experiment sensitive region that is $20\mu\,\text{Hz} \leq f \leq 1\,\text{Hz}$ in LISA.

The effective strain noise spectral spectrum is expressed as

$$\Omega_n^i(f) = S_n^i(f)\frac{2\pi^2 f^3}{3H_0^2}, \tag{5.18}$$

with the effective noise power spectrum,

$$S_n^{\rm LISA}(f) \simeq 2\sqrt{2}\frac{20}{3}\left[\frac{S_I(f)}{(2\pi f)^4} + S_{II}\right]\left[1 + \left(\frac{3f}{4f_*}\right)^2\right] \tag{5.19}$$

where $f_* = c/(2\pi L)$ with light speed c and $L = 2.5 \times 10^6$ km, and $S_{II} = 3.6 \times 10^{-41}\,{\rm Hz}^{-1}$ is an optical path-length fluctuation. The acceleration noise $S_I(f)$ reads

$$S_I(f) = 5.76 \times 10^{-48}\left[1 + \left(\frac{f_1}{f}\right)^2\right]{\rm s}^{-4}{\rm Hz}^{-1}, \tag{5.20}$$

where $f_1 = 0.4\,{\rm mHz}$. As discussed in [287], the SNR in Eq.(5.17) is an idealization, we ignore foreground contamination, non-Gaussianity, data interruption, and other systematic issues.

SKA noise background

The noise background of interferometer and pulsar timing experiments have been nicely reviewed in the appendix of [290]. As the result, the effective strain noise spectral spectrum is defined as Eq.(5.18), and the effective noise power spectrum is given [377, 378, 379]

$$S_n^{\rm SKA}(f) = 12\pi^2 f^2\left[\frac{2}{N_{\rm SKA}(N_{\rm SKA}-1)}\right]^{1/2}\frac{D_n^{\rm SKA}}{\zeta_{\rm rms}}, \tag{5.21}$$

where $\zeta_{\rm rms} \simeq 0.147$, number of pulsars $N_{\rm SKA} = 50$ [247, 380], operating time $T_{\rm SKA} = 20$yrs [290, 381], and the 20 years timing noise spectra $D_n^{\rm SKA} \simeq 1.1 \times 10^{-9}\,{\rm Hz}^{-3}$ [290, 239]. The sensitive frequency range is from the operating period $f_{\rm min} = 1/T_{\rm SKA}$ to the cadence of the timing observation, $f_{\rm max} = 1/T_c$ where $T_c = 1\,{\rm week}$ [247, 380].

5.3 Signal-to-Noise Ratio

Early dark energy has relatively small energy contribution in the early universe, hence its influence GW variation is small compared to string SGWB, but could still be larger than noise background if string tension is sufficiently large. For comparing signal difference and noise background, we define SNR as $\{i = {\rm SKA}, {\rm LISA}\}$

$$\mathrm{SNR} = \sqrt{T_i \int_{f_{\rm min}}^{f_{\rm max}} df \left(\frac{\Delta\Omega_{\rm GW}(f)}{\Omega_n^i(f)} \right)^2}, \tag{5.22}$$

where the SKA and LISA are calculated separately, frequency is integrated on the experimental sensitivity region, T_i is the observation period, and $\Omega_{\rm n}^i(f)$ is an effective strain noise spectral spectrum for LISA and SKA, respectively. SNR analysis has been widely studied [290, 287, 239, 291] and numerical details are provided in the appendix.

The peak frequency f_p is within the LISA goal sensitivities $20\mu\,{\rm Hz} \leq f \leq 1\,{\rm Hz}$ [370] for $G\mu \leq 2 \times 10^{-11}$ as presented in Fig. 5.2, and the peaky signal is more significant than noise background for most of interesting parameter space. More string energy causes stronger cosmic string SGWB, and hence the signal is more significant for larger $G\mu$.

Fig. 5.3 shows signal difference ratio $\Delta\Omega_{\rm GW}/\Omega_{\rm GW}$ at peak frequency f_p. The colored areas were studied in CMB analysis [16] for relieving the Hubble tension. We

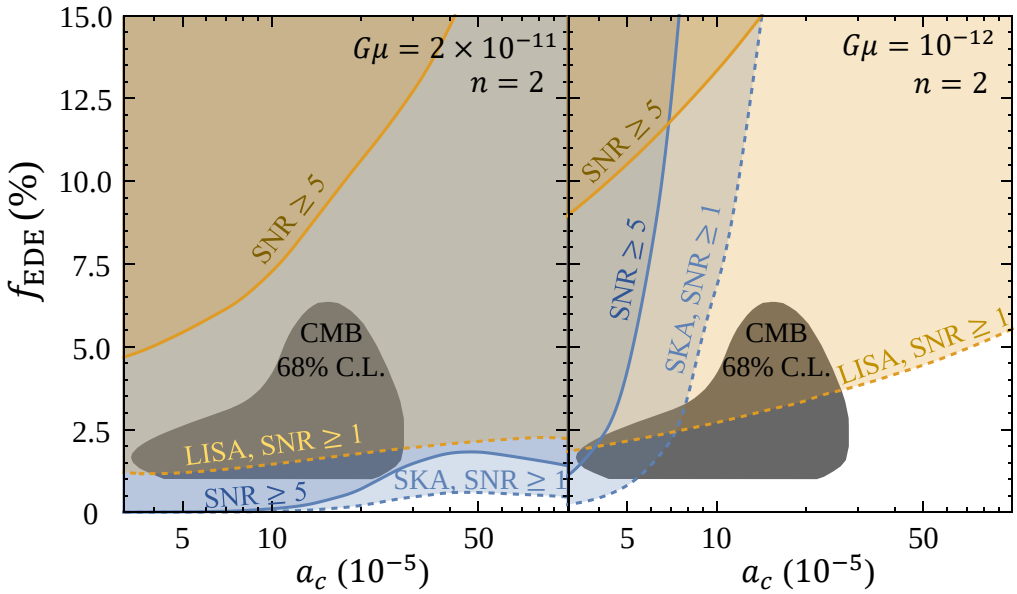

Figure 5.5: Energy density fraction of early dark energy $f_{\rm EDE}$ versus critical scaling factor a_c with marking SNR for LISA 4 years operating and SKA 20 years observation period, respectively. The black areas present the CMB analysis with 68% C.L. from [16].

explicitly show that the signal difference could exceed the noise background (SNR$>$ 1) in the 4 years LISA collection, and therefore the EDE signal is detectable. As discussed, lower n has a larger signal difference due to the later universe transition to matter-domination era.

Fig. 5.5 shows LISA and SKA detection sensitivities to EDE parameter space. Signal difference can be larger than noise background over few frequency decades, including most sensitive LISA regions, see the gentle slope $f^{-0.23}$ over frequencies $f > f_p$ in Eq.(5.8). Thus, LISA can capture the EDE signal even though f_p is outside LISA sensitivities. Higher a_c corresponds to lower SNR because f_p moves away from LISA sensitivities with increasing a_c.

The pulsar timing detector SKA can capture (SNR>1) the signal difference dip, as presented in Fig. 5.5. There are two falls on the SKA curves on the left-panel: the fall on lower a_c is caused by the dip in signal difference; whereas the fall on higher a_c is due to the signal difference peak. If the NANOGrav signal is due to cosmic string i.e. $G\mu \geq 2 \times 10^{-11}$ [145, 146], then SKA and LISA should detect EDE signals in future observations. Scanning the 1σ regions, detectable EDE signal with $n = \{2, 3, \infty\}$ requires approximately at least $G\mu \gtrsim \{4.4, 6.7, 31\} \times 10^{-14}$ and $G\mu \gtrsim \{4.2, 20, 29\} \times 10^{-13}$ for LISA and SKA, respectively.

5.4 Distinguish signal from other sources

The EDE signal in cosmic string SGWB is distinguishable from other possible influences, such as string parameter variations, or sub-dominated SGWB from astrophysical or cosmological objects. For example, kinks or kink-kink collision modes [223], or string parameters α and Γ variations [17] would universally influence GW amplitude. Therefore, they cannot cause local amplitude modification as does EDE. We numerically checked that EDE influenced SGWB difference is much flatter than cosmic string SGWB with influence from astrophysical objects, such as binary black hole merger [382, 383] and inspiral [384, 385, 386]. On the other hand, a sub-dominated GWs from cosmological phenomena, e.g. flat frequency spectrum from inflation [387, 194, 164]; peaky spectrum from domain wall [388, 389]; or first order phase transition dynamics [390, 304, 290]: sound wave [391], bubble wall collision [392, 393] and magnetohydrodynamic turbulence [394, 292], frequency spectra are distinguishable to EDE as well. In particular, the dip structure signal difference at f_d cannot be caused by any other physical phenomena.

Chapter 6

Enhanced Early Galaxy Formation in JWST from Axion Dark Matter

6.1 Review for recent developments

The standard ΛCDM cosmology makes firm predictions for the abundance of dark matter halos as a function of time. However, recent James Webb Space Telescope (JWST) observations have revealed what may be an unexpectedly large population of luminous galaxies at redshifts 10 and above [395, 396, 397, 23, 398, 399, 400, 395]. In particular, Ref. [399] reported 25 spectroscopically confirmed galaxies at $z_{\rm spec} = 8.61 - 13.20$, two of which have $M_{\rm UV} < -19.8$ mag at $z > 11$. The reported number exceeds most predictions based on the ΛCDM cosmology, and may be the harbinger of new fundamental physics and/or lead to a new understanding of structure formation [401, 402, 403, 404, 405, 406, 407, 408].

These surprising JWST results have inspired many dedicated studies [409, 407, 408, 410, 411, 412]. Proposed explanations for the JWST excess include enhanced star formation, accelerated mass assembly, early or clustering dark energies, large scale-dependent non-Gaussianities, cosmic string loops, etc. [413, 414, 415, 416, 417, 418, 419, 420, 421, 422]. Among them, a population of high z heavy compact objects has emerged as a compelling solution [423, 419, 417, 418]. The presence of these objects in the radiation dominated era introduces isocurvature perturbations which enhance the matter power spectrum (MPS) with a shot-noise-like contribution up to a certain truncation scale [424]. This shot noise enhancement could then trigger higher star formation efficiency, particularly in the most massive halos and at earlier epochs [423, 413, 21]. To fully address the excess, however, these objects must be extremely massive and contribute a substantial fraction to the total matter content in the universe (Ω_m) [419, 417, 418].

A well-motivated source of such heavy compact objects is axion DM, which is the focus of this work. Large amplitude axion density fluctuations can collapse into massive clusters by $z \sim 10$ [425, 426, 427, 428, 429, 430, 431], with masses ranging from 10^{-12} $M_\odot$ to 10^4 $M_\odot$ [423, 432]. The mass of these clusters anti-correlates with the axion mass m_a, and the m_a range favored by the JWST excess is 10^{-19} eV $< m_a < 10^{-16}$ eV in the Standard Misalignment Mechanism (SMM) [419]. This mass range is excluded by black hole superradiance (BHSR) [24, 419, 25, 26, 27], and in addition requires a larger star formation efficiency f_* than expected from low redshift astrophysics.

In this work, we show that models with delayed axion oscillation, in particular the recently proposed kinetic misalignment mechanism (KMM) [115, 257], enable efficient formation of field fragments at sub-horizon scales [433, 434], opening up a parameter space safe from the BHSR constraint with astrophysically plausible f_*. In particular, we reveal a large viable parameter region with 10^{-22} eV $< m_a < 10^{-19}$eV that can explain the JWST excess, while being consistent with relevant constraints such as from BHSR, Lyman-α forest, and stellar dynamics [18, 435, 436, 25, 26, 27]. Furthermore, we demonstrate that the same ALP models that address the JWST excess may yield complementary signals in a variety of current/future axion search experiments [437, 438, 439], and intriguingly have the potential to alleviate puzzling features found in the small-scale structure of DM halos [440, 441, 442]. In addition, we identify a parameter range that is consistent with existing ΛCDM predictions, which is worth exploration even if the current JWST excess resolves upon further investigations.

6.2 Axion clusters from kinetic misalignment

We first review some essential aspects of axion physics that are relevant to this study. Axions are pseudo-Nambu-Goldstone bosons arising from spontaneous breaking of global Peccei-Quinn (PQ) symmetries, originally proposed to solve the strong CP problem in QCD [98, 99, 100]. Later on, they were found to be attractive dark matter candidates, and more general non-QCD ALPs are also well motivated from theoretical frameworks such as string theory and supersymmetry [101, 71, 72, 70]. The very light m_a needed to affect high redshift structure growth as we found is incompatible with the QCD axion.

Axions can be produced from both misalignment mechanisms (MM) and the decay of axion topological defects. The axion energy density resulting from the latter mechanism is contingent upon model specifics and still under development, with uncertainties in part due to technical challenges in simulations (see e.g. [443, 321, 156, 444, 445, 446, 111, 447], and the refs therein). In particular, the effect of topological defects can be absent in certain cosmological scenarios. For example, if PQ symmetry breaking occurs before inflation, axion cosmic strings would be sufficiently diluted; on the other hand, the contribution from axion domain walls can be inconsequential when compared to that from the MM mechanism, if the lifetime of domain walls is sufficiently short. For these reasons, here we choose to focus on the formation of axion clusters (ACs) via the misalignment mechanism.

In the SMM, the axion field value is initially displaced from its true potential minimum, with a zero initial velocity, then starts to oscillate when it obtains a mass m_a similar to the Hubble rate, $H_* \sim m_a$. The oscillations of the axion field then result in its relic abundance today (Ω_a) as a condensate of CDM. In contrast, in the recently proposed KMM [115, 257], a non-zero initial axion velocity is considered, which can arise from models with asymmetries in the PQ charges or some dimensional symmetry-breaking operators. This results in a larger kinetic energy for the axion, with the possibility of $H_* \ll m_a$, which delays the onset of axion field oscillation and thus alters the prediction for Ω_a. It was later shown in [434, 433] that such a delayed oscillation in the KMM also generically leads to a phenomenon called axion field fragmentation, which is the exponential growth of axion quanta via parametric resonances. The enhanced fluctuation due to the fragmentation triggers the formation of axion clusters, in a way distinct from that resulting from SMM.

Here we focus on the KMM scenario described in [434, 433], in the context of pre-inflationary PQ breaking, and follow the approach outlined there for analyzing axion cluster formation. We introduce a parameter $\eta \equiv m_a/H_*$ to characterize the degree of the oscillation delay due to KMM, which plays a key role in determining the scale of fragmentation, and consequently the mass function of the ACs. A delayed oscillation corresponds to a larger value of η, compared to approximately 3 in SMM. The parameter space can be divided into regions of incomplete fragmentation ($\eta \lesssim 40$), complete fragmentation ($40 \lesssim \eta \lesssim \mathcal{O}(10^3)$), and non-perturbative ($\eta \gtrsim \mathcal{O}(10^3)$) [434, 433].

The fraction of the field which is fragmented saturates quickly with increasing η, and we focus on the case of complete fragmentation which spans the bulk of the parameter space of interest. While η and f_a are in principle independent model parameters, for a given m_a and a specified Ω_a output, they have a 1-1 relation. As an example, for a simple, temperature-independent axion potential as used in most ALP models, f_a relates to η in the following way [434]:

$$f_a \approx 10^{15}\ \text{GeV} \left(\frac{10^{-20}\text{eV}}{m_a}\right)^{\frac{1}{4}} \left(\frac{90}{\eta}\right)^{\frac{3}{4}} \left(\frac{g_*}{4}\frac{\Omega_a h^2}{0.12}\right)^{\frac{1}{2}}, \tag{6.1}$$

where g_* is the effective degrees of freedom in the entropy evaluated at the onset of fragmentation. Throughout our paper, we will assume that all the DM is comprised of the ACs, i.e. $\Omega_a = \Omega_{\text{DM}}$, to fix η, which then fixes the 1-1 correspondence between f_a and η for a given m_a.

We assume complete fragmentation, in which case the dark matter is comprised of ACs with typical masses determined by the comoving scale around $k_{\rm osc} \approx m_a a_* \kappa_p$, where a_* is the expansion parameter at the oscillation onset [433]. $\kappa_p \sim O(1)$ is a correction factor that contains a mild η dependence, as we will discuss later in Eq. (6.8). The typical mass of the AC can be estimated as

$$\begin{aligned} M_0 &\approx \bar{\rho}_a \frac{4\pi}{3} \left(\frac{\pi}{m_a a_* \kappa_p} \right)^3 \\ &\approx 10^4 \ {\rm M}_\odot \left(\frac{70}{\eta} \right)^{\frac{3}{2}+0.66 \ \theta(\eta-80)} \left(\frac{4 \times 10^{-20} \ {\rm eV}}{m_a} \right)^{\frac{3}{2}}, \end{aligned} \tag{6.2}$$

where θ is the Heaviside Function, $\bar{\rho}_a$ is the average axion energy density and is taken to be the average DM energy density today. Both η and m_a anti-correlate with M_0, i.e. M_0 decreases as η, m_a increases. For a fixed M_0, increasing η can accommodate a smaller m_a, which can help alleviate the BHSR constraints. These axion clusters are produced from the collapse of the axion fields that fragmented at subhorizon scales.

The substantial mass of ACs naturally induces significant velocity-dependent gravitational scatterings [448]. In terms of the cluster mass, we have

$$\frac{\sigma}{M_0} \approx 10 \ {\rm cm}^2/{\rm g} \left(\frac{M_0}{10^4 {\rm M}_\odot} \right) \left(\frac{10 \ {\rm km/s}}{v} \right)^4, \tag{6.3}$$

where v is the relative velocity between the two ACs and anomalies in DM small scale structure observations may be addressed by values of $O(1)$ cm^2/g [440, 441, 442, 449, 450, 451, 452, 453, 454, 455, 456, 457, 458, 459, 460, 461]. The wave nature of ALPs in our considered mass range gives rise to pc to kpc scale solitonic cores in ACs and ALP halos,

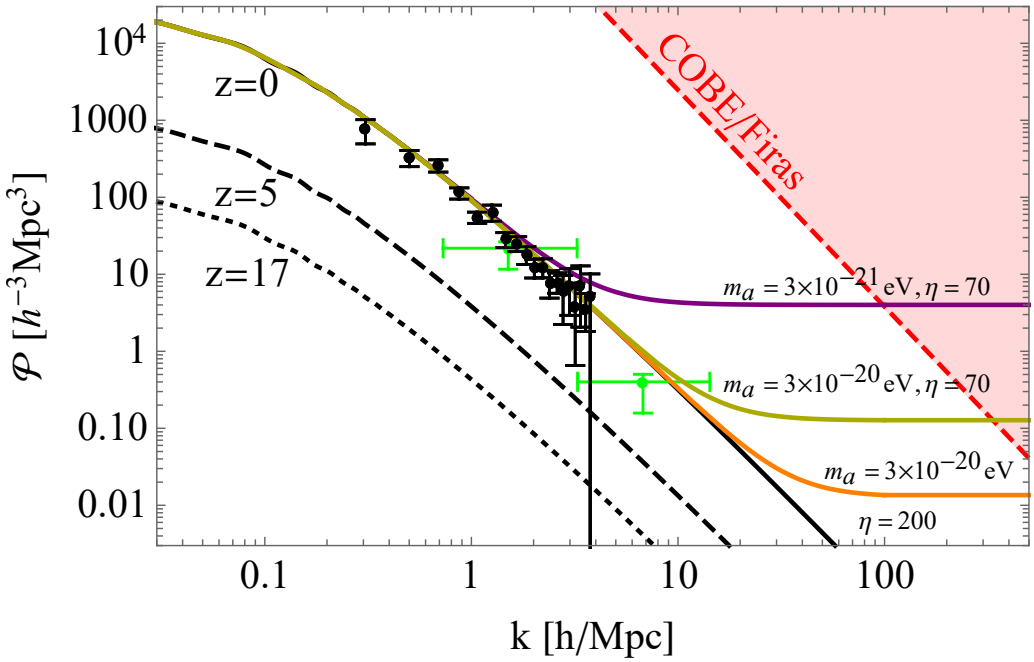

Figure 6.1: Example MPSs in KMM axion DM models (colored curves) compared to the MPS from a standard ΛCDM model. Data points with error bars represent Lyman-α measurements (black) from Ref.[18] and HST UV luminosity function measurements (green) from Ref.[19]. The red dashed curve denotes the maximal cut-off scale for k^4 growth in the adiabatic curvature power spectrum based on the COBE/FIRAS bound from Ref.[20]. Higher resolution Lyman-α surveys can extend the scales on which the power spectrum is measured to $k \sim 10$ h/Mpc, similar to the UV luminosity data [21, 22].

which may also help alleviate small scale challenges in ΛCDM [462, 5, 429]. Given a large cross-section, e.g., 10 cm^2/g, close encounters between ACs can merge them into larger, more diffuse structures within the ALP halos, enriching the small-scale features of our model. The diffuse nature of the ACs also alleviates the existing stringent constraints from stellar dynamical, microlensing, and small-scale structures that apply to massive compact halo objects such as primordial black holes [435, 436, 463, 464, 465, 466, 467]. Depending on the shapes of the ALP potential, ACs could further evolve into oscillons, which decay into axion stars [5, 468, 469, 470, 471, 472].

6.3 Matter power spectrum.

We decomposed the density perturbation into linear and quadratic components following the methodology outlined in Ref. [434]. The linear component approximately corresponds to the adiabatic perturbation in ΛCDM cosmology, denoted as $\mathcal{P}_{\rm CDM}(k)$. On the other hand, the quadratic component introduces a shot noise-like contribution referred to as $\mathcal{P}_{\rm AC}(k)$ which can be estimated as [418, 473, 474, 475]

$$P_{\rm AC}(k) \approx (D_{\rm iso}(0)-1)^2 \frac{f_{\rm AC} M_0}{\rho_c \Omega_a} \propto M_0, \quad \text{for } k < k_{\rm osc}. \tag{6.4}$$

Here ρ_c is the critical energy density today, $f_{\rm AC}$ is the fraction of dark matter comprised by ACs which we fix to be 1, $f_{\rm AC}\rho_c\Omega_a/M_0$ is the number density of the ACs, and $D_{\rm iso}(z)$ is the growth factor of isocurvature perturbations which can be parameterized as [474, 473, 475]

$$D_{\rm iso}(z) \quad = \quad \left(1 + \frac{\Omega_a}{\Omega_m a_-}\frac{3a}{2a_{\rm eq}}\right)^{a_-}, \tag{6.5}$$

where

$$a_- \quad = \quad (\sqrt{1+24\Omega_a/\Omega_m}-1)/4. \tag{6.6}$$

The $D_{\rm iso}$ does not evolve at $a \ll a_{\rm eq}$ and grow as $3a/(2a_{\rm eq})$ (identical to the adiabatic one) for $\Omega_a = \Omega_m$ at $a \gg a_{\rm eq}$. If ACs comprise only a fraction of dark matter, then $f_{\rm AC} < 1$, resulting in a smaller $P_{\rm AC}(k)$. Note that the AC number density is independent of Ω_a

because $M_0 \propto \Omega_a$. However, $P_{\rm AC}$ decreases as Ω_a decreases through the $D_{\rm iso}$ in Eq. 6.5 and Eq. 6.4, resulting in fewer high-z massive galaxies.

We numerically calculate the leading order $P_{\rm AC}(k)$, including backreaction, following Eq. 4.11 in Ref. [434], and parameterize the obtained results as [1]:

$$\mathcal{P}_{\rm AC}(k) = \frac{2\pi^2}{k^3} \frac{f(\eta)(D_{\rm iso}(0)-1)^2}{(D_{\rm iso}(z_{\rm eq})-1)^2} \left(\frac{\kappa}{\kappa_p(\eta)}\right)^3 \theta(\kappa_p - \kappa), \tag{6.7}$$

where $\kappa \equiv \frac{k}{m_a a_*}$, $\kappa_p(\eta)$ and $f(\eta)$ are numerical factors parameterized as

$$\kappa_p(\eta) \simeq \begin{cases} 0.9, & 40 \leq \eta \leq 80, \\ 0.9 \left(\frac{\eta}{80}\right)^{0.22}, & 80 < \eta \leq 10^3, \end{cases} \tag{6.8}$$

and

$$f(\eta) \simeq 1.19 \left(\frac{\eta}{80}\right)^{-0.1}, \qquad 40 < \eta \leq 10^3. \tag{6.9}$$

The spectrum $\mathcal{P}_{\rm AC}(k)$ becomes dominant at scales larger than $k_* \approx a_* H_*$ and is truncated at $k_{\rm osc}$. For $k > k_{\rm osc}$, the spectrum becomes negligibly small and decreases as $1/k^2$ [434, 433].

In Fig. 6.1, we show the MPS for three benchmark examples. The M_0 is 1.6×10^3, 1.5×10^4 $M_\odot$, and 4.9×10^5 for the orange, golden, and magenta cases, respectively. We will show in Fig. 6.3 that the case in gold color is favored in order to explain the JWST excess, the orange case is consistent with ΛCDM, while the magenta case overproduces

[1] We solved for the relic abundance neglecting the effect of fragmentation which could induce a sub-O(1) uncertainty [433]. A more accurate determination of the relic abundance requires dedicated study which is beyond the scope of this work.

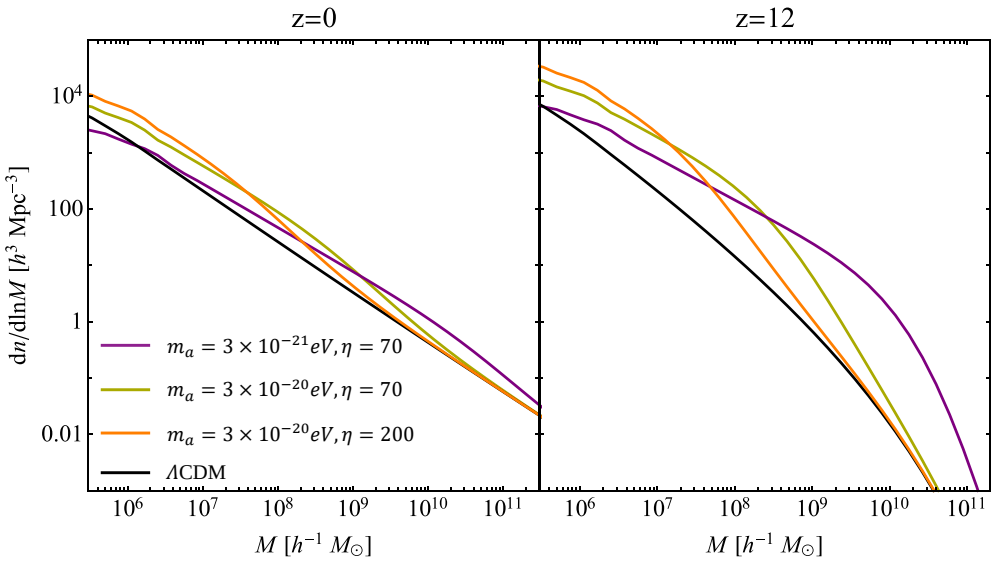

Figure 6.2: The halo mass function for the benchmark cases of Fig. 6.1 at redshifts $z = 0$ and $z = 12$.

structures and is excluded by measurements of the UV luminosity function. In all cases, $P_{\rm AC}(k) \gg P_{\rm CDM}(k)$ for $k > k_*$, where the spectrum plateaus, before being truncated at $k \sim k_{\rm osc}$ (beyond the range of Fig. 6.1). The case in gold color, specifically, has a transition around $k_* \sim 10$ h/Mpc, which is close to the scale associated with the JWST excess.

6.4 Halo Mass Function

The clustering of ACs in the matter era leads to the formation of halos. We use the Press-Schechter formalism to estimate the halo mass function (HMF) from the MPS [476]. Given an MPS $P(k, z)$ at redshift z, we compute the mass variance using a top-hat window function as

$$\sigma_M^2(R) = \frac{1}{2\pi^2}\int dk P(k,z)\left(3\frac{\sin(kR) - kR\cos(kR)}{kR}\right)^2 k^2,$$

where M and R are halo mass and radius and are related through $M = 4\pi\bar{\rho}_m R^3/3$, with ρ_m being the mean matter density today. The HMF is computed in terms of $\nu \equiv \delta_c^2(z)/\sigma_M^2$ as

$$\frac{dn}{dM} = \frac{\bar{\rho}_m}{M}\nu f_{\rm EPS}(\nu)\frac{d\ln\nu}{d\ln M}, \tag{6.10}$$

where $\nu f_{\rm EPS}(\nu)$ is a shape function including the effect of ellipsoidal collapse from Ref. [477]. This approach has been widely applied in the literature because of its simplicity. Ref. [417] demonstrated that this technique can produce reliable approximations of the N-body reconstructed HMFs, even in the presence of massive primordial black holes.

In Fig. 6.2, we show the obtained HMFs for the ΛCDM and the three benchmarks in Fig. 6.1 at $z = 0$ (left) and $z = 12$ (right). We see that the HMFs at $z = 0$ are relatively similar across all cases; however, at $z = 12$, the KMM cases exhibit significant enhancements towards larger halo masses, increasing the likelihood of finding halos hosting the very massive galaxies. Once small halos virialize, they almost decouple from the background evolution. Hence the abundance of massive halos is largely unaffected at low redshifts. As a result, the effect of our model becomes less significant today, which alleviates constraints from low redshift measurements [475, 467].

6.5 Phenomenology with JWST excess

The enhanced massive halo population as we see in Fig. 6.2 can trigger earlier galaxy formation and enhance the formation efficiency [423, 413]. To convert the model

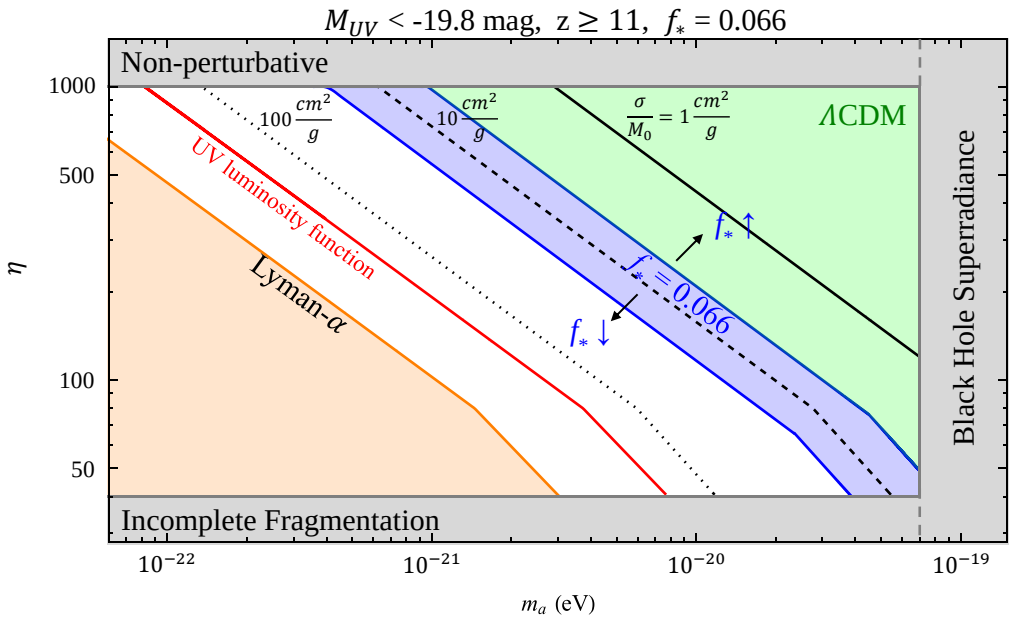

Figure 6.3: The viable model parameter space given the observations in Ref. [23], considering galaxies with $M_{\rm UV} < -19.8$ mag at $z \geq 11$. The 68% CL preferred region shaded in blue corresponds to a prediction of $0.74 < N_{\rm exp} < 4.3$. It is obtained for a star formation efficiency $f_* = 0.066$ and would shift up (down) if f_* increases (decreases). Black lines represent contours of the gravitational scattering cross section per mass for values of 1, 10, and 100cm^2/g, evaluated at a velocity of $v = 10$ km/s. At larger velocities, the cross section quickly reduces due to the v^{-4} dependence. Constraints from various sources exclude certain regions: the Lyman-α forest data [18] disfavors the orange area; the region to the left of the red curve is inconsistent with measured UV luminosity functions [19]; and the grey area to the right is excluded by BHSR constraints [24, 25, 26, 27].

prediction for HMF into the number of observed galaxies, we consider a simplified approach assuming a constant star formation efficiency f_*. We compute the expected number of observed galaxies with $M_{\rm UV} < -19.8$ mag at $z > 11$ as considered in Fig. 13 of Ref. [399], where the number of observed galaxies $N_{\rm obs} = 2$ is systematically higher than theoretical predictions from the literature [401, 402, 403, 404, 405, 406], e.g., 0.3 from Ref. [478] as a recent estimate. We convert the requirement of $M_{\rm UV} < -19.8$ mag into a minimum halo mass by using the $M_* - M_{\rm UV}$ relation of Ref. [478]. Assuming a constant star formation efficiency f_*, we set the minimum halo mass $M_{\rm min} = 1.8 \times 10^9 e^{-0.12 z_{\rm min}}/(f_* f_b)$ M$_\odot$, where

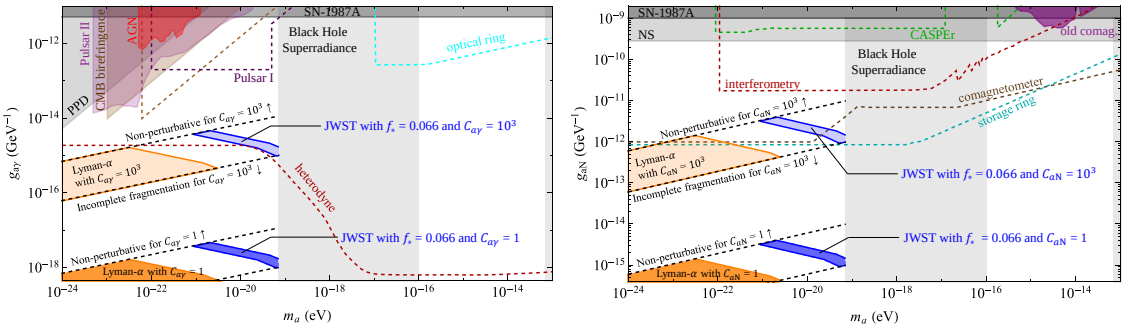

Figure 6.4: Axion-photon (left) and axion-nucleon (right) couplings versus axion DM mass m_a (assuming $\Omega_a = \Omega_{\rm DM}$ in Eq. 6.1). The blue and the lighter-blue regions correspond to the regions favoured by matching the JWST excess, with $C_{a\gamma,N} = 1$ and $C_{a\gamma,N} = 10^3$, respectively. The blue regions are bounded by two dashed black lines, corresponding to the requirement of perturbative η with complete fragmentation. Constraints from various existing searches (solid shaded regions) and forecasts (colored dashed lines) are also illustrated. See text for further details.

$z_{\rm min} = 11$, $f_b \approx 0.16$ is the baryon fraction in the matter energy density, and we set $f_* = 0.066$ so that the ΛCDM prediction is for an expected 0.3 galaxies at $z > 11$ [478]. The value of $f_* = 0.066$ is within expectations for a 10^{12} $M_\odot$ halo at z=0, but small compared to some theoretical models proposed to explain the JWST excess solely by extra star formation [413, 408, 407, 406, 479]. It has been noted that an excessively high f_* could introduce new tensions with the cosmic reionization history [480], making our obtained value a more desirable option. The number of expected galaxies count is calculated as

$$N_{\rm exp} = \frac{A_{\rm eff}}{4\pi} \int_{11}^{z_{\rm max}} dz \frac{dV_c}{dz} \int_{M_{\rm min}}^{M_{\rm max}} dM \frac{dn}{dM}, \tag{6.11}$$

where $A_{\rm eff} = 45$ arcmin^2 is the effective area of the observation following Ref. [399] and V_c is the comoving Hubble volume at z. dn/dM is the HMF in Eq. 6.10. Our result is not sensitive to $z_{\rm max}$, $M_{\rm max}$, provided that they are sufficiently large.

Fig. 6.3 presents the preferred 68% CL parameter regions for a constant $f_* = 0.066$ as a blue band in the $m_a - \eta$ plane. We obtain the blue band considering $0.74 < N_{\rm exp} < 4.3$ which arises from a Feldman-Cousins analysis for two observations and zero background [481], and the lower limit happens to coincide with that from Ref. [399]. For a higher (lower) value of f_*, the band would shift upward (downward). The upper-right corner corresponds to lower prediction for $N_{\rm exp}$ values that are consistent with ΛCDM predictions within the uncertainties [401, 402, 403, 404, 405, 406]. The lower-left region has higher $N_{\rm exp}$ and is constrained by Lyman-α and UV luminosity measurements [18, 19]. We also plot the contours of the gravitational scattering cross section of Eq. (6.3) evaluated at $v = 10$ km/s in Fig. 6.3. In the viable region, we see that the gravitational cross section takes values in $(1 - 100)$ cm^2/g, which could lead to novel signal predictions that can address the small-scale observations, e.g., the core-cusp problem and the too-big-to-fail problem [440, 441, 442, 449, 450, 451, 452, 453, 454, 455, 456, 457, 458, 459, 460, 461].

6.6 Implications for Axion Models

As shown in the last section, axion models with KMM can address the JWST excess, with a preferred parameter space spanning 4×10^{-22} eV $< m_a < 10^{-19}$ eV and $40 < \eta < 1000$. Existing ALP searches may provide valuable complementary probes for such ALPs, albeit in a model-dependent way. While the impact of ALP on structure formation is largely independent of the non-gravitational axion coupling to the Standard Model (SM) particles, most other ALP searches do depend on the specific coupling patterns.

Here we focus on axion interactions with photons and nucleons (N), as described by

$$\mathcal{L} \in \frac{g_{a\gamma}}{4} a F_{\mu\nu} \tilde{F}^{\mu\nu} + g_{aN} \partial_\mu a \bar{N} \gamma^\mu \gamma^5 N, \tag{6.12}$$

with effective couplings

$$g_{a\gamma} = C_{a\gamma} \alpha / (2\pi f_a), \qquad g_{aN} = C_{aN} / f_a, \tag{6.13}$$

where $F_{\mu\nu}$ represents the electromagnetic field strength, and $C_{a\gamma}$, C_{aN} are model-dependent parameters. In standard QCD axion inspired models such as KSVZ or DFSZ [482, 483, 484, 485], $C_{a\gamma}$, $C_{aN} \sim O(1)$. Meanwhile, other recently proposed well-motivated axion theories such as those with multiple PQ fermions, vector kinetic mixing, and axion clockworks, can generically predict significantly larger coupling C's, up to $\mathcal{O}(10^2 - 10^3)$ [486, 487, 488]. According to Eqs. 6.1 and 6.13, with our assumption of $\Omega_a = \Omega_{\rm DM}$, f_a and the corresponding η are fixed for given $g_{a\gamma}$ (g_{aN}) and $C_{a\gamma}$ (C_{aN}). Thus we may map the parameter regions in Fig. 6.3 onto the $m_a - g_{a\gamma,N}$ space as in Fig. 6.4. In light of the aforementioned theoretically motivated range for $C_{a\gamma}$, C_{aN}, in Fig. 6.4, the JWST excess favored regions are illustrated for two benchmark values: $C_{a\gamma}$, $C_{aN} = 1$ (blue band) and $C_{a\gamma}$, $C_{aN} = 1000$ (light blue band). The viable regions for other values of $1 \lesssim C_{a\gamma}$, $C_{aN} \lesssim 1000$ are expected to lie between these two bands. These bands are truncated from above and below (denoted by dashed black lines) by requiring that the corresponding η are within the perturbative regime with complete fragmentation, $40 \lesssim \eta \lesssim 1000$ (see discussion above Eq. 6.1), which we have chosen to focus on in our analysis. As $C_{a\gamma}$ or C_{aN} increases, the blue and orange

bands, along with the black dashed lines, would linearly shift upwards. We also show the current constraints (solid shaded regions) and future sensitivity forecast (bounded above by colored dashed lines) for a variety of experiments/observations, including Lyman-α [18], BHSR [25, 26, 27], Supernova-1987A [489], neutron star cooling (NS) [490, 491, 492, 493], protoplanetary disk polarimetry (PPD) [494], active galactic nuclei (AGN) [495], and old comagnetometer [439].

As can be seen from Fig. 6.4, upcoming experiments can offer complementary probes for KMM axion parameter range that could address the JWST excess. For example, for the benchmark of $C_{a\gamma} = 1000$ the reach of future heterodyne experiments [437] overlaps with the JWST excess favored region of ($g_{a\gamma}$, m_a). Similarly, future storage ring and co-magnetometer experiments would be able to explore the (g_{aN}, m_a) range motivated by the JWST excess [438, 439]. It is also worth noting that the experiments covering the further upper regions in Fig. 6.4, such as interferometry [496] and linearly polarized pulsar light (Pulsar I in Fig.6.4 left) [497], can potentially probe KMM axions with $\eta > 10^3$ and $C_{a\gamma}$ (or C_{aN}) $> 10^3$. However, these regions require a non-perturbative analysis of fragmentation ($\eta \gtrsim 10^3$), which is beyond the scope of this study.

Chapter 7

Dynamics of Long-lived Axion DWs and its Cosmological Implications

7.1 Introduction

Axions are ultra-light particles that are originally invoked as a compelling solution for the Strong CP problem in quantum chromodynamics (QCD) [98, 99, 100]. Recent years have seen a significant increase in interest in QCD axions and more general axion-like particles (ALPs), as dark matter (DM) candidates alternative to WIMPs [101, 71, 72, 70]. While most existing studies on axion phenomenology and detection focused on the axion particle per se, the impact of the accompanying axion topological defects, i.e. axion strings and domain walls (DWs), can be substantial, yet still not well understood. Such axion

topological defects are indispensable companions of axion particles for post-inflationary PQ symmetry breaking, with potentially significant contribution to axion relic abundance [103, 104, 105, 106, 8, 107], and may provide complementary search avenues for axion models [5, 498, 499, 500, 156, 321, 443, 501, 502, 503, 504, 505, 506]. A growing effort has been made in the past few years along this direction. However, there are still debates to be resolved and clarifications to be made, in part due to the technical challenges with simulating axion topological defects [108, 110, 31, 112, 114, 30, 177, 202, 109, 111, 219, 507, 220].

Axion cosmic strings form as the PQ breaking phase transition (PT) occurs at a high energy scale f_a, and prevail till the pseudo-goldstone boson (axion) later acquires a nonzero mass m_a and DWs enter the horizon. The structure of the DWs depends on the model specifics of the axion potential and is characterized by the axion mass and the DW number $N_{\rm DW}$. The case with $N_{\rm DW} = 1$ is most studied in recent years, where the DWs are short-lived and strings dominate the dynamics of the axion topological defects [111, 30, 202]. On the other hand, more generally for the $N_{\rm DW} > 1$ models e.g. Dine-Fischler-Srednicki-Zhitnitsky model [485, 484], the DWs are stable and problematic as they would over-close the Universe. Nevertheless, the $N_{\rm DW} > 1$ cases can be innocuous with the presence of a small symmetry-breaking bias in the axion potential, which yields the DWs that are long-lived but collapse before the BBN [508, 388]. Upon collapsing, long-lived DWs can leave observable imprints in the form of axion dark matter relic density, gravitational waves (GWs), as well as the impact on cosmic structure formation [8, 389]. A clear understanding of the evolution and dynamics of the DW network is crucial for predicting and probing such potentially rich phenomenology. However, the literature on

the dynamics of metastable DWs (axion associated or more general) is still relatively scarce [509, 510, 221, 511, 512, 8, 389], and further investigation is required to advance and clarify our understanding.

In this work, we conduct an updated analysis for the long-lived axion DWs and predict axion relic abundance produced from the axion DWs (with $N_{\rm DW}$=2 as a benchmark). We perform a 3D field theory lattice simulation for the axion field with grid size $N^3 = 1536^3$ in a radiation-dominated background, including the bias term in the axion potential, and solve the axion field equation of motion exactly. This differs from earlier simulation work, with the promise of potential improvement: e.g. the estimation of the decay time of metastable DWs in [8] and [507] is based on a 2D simulation, while the 3D simulation in [221, 511] employs Higgs DWs with Press-Ryden-Spergel (PRS) [513] approximation. In order to elucidate the physics of the dynamics of DW evolution, we investigated the DW radiation mechanisms by capturing through analyzing the axion spectrum and zoom-in the snapshots of animations from our simulation. In addition to obtaining results based on numerical simulation, through analytical fitting, we also present the velocity-dependent one-scale (VOS) model applicable to the metastable DW evolution. This is a notable extension of the framework of the VOS model which previously has been widely used to describe the evolution of other types of topological defects such as cosmic strings [203, 204] and, only recently a few attempts on stable DWs [221, 514, 511, 515, 516, 517]. By combining numerical and analytical approaches, our analysis leads to an updated prediction for the spectrum and relic abundance of axions radiated from DWs, as well as new insights into the evolution of DW substructures. This study may shed new light on the cosmological

implication of axion topological defects and their role in axion physics at large. In the following, we will first introduce the axion model and simulation setup that we adopted. Then we will present the essential results on the dynamics of axion DWs derived from the simulation, and demonstrate how these can be used to calibrate the analytical VOS model. Cosmological implications related to axion DM will be discussed before the conclusion.

7.2 Axion model

We first introduce the benchmark axion model that we consider and the essentials in our simulation. As a pseudo-Nambu-Goldstone boson, axion is associated with the angular mode of a complex scalar field whose VEV spontaneously breaks a global U(1) symmetry. The symmetry breaking occurs at a relatively high scale $f_a \gg \Lambda \simeq \sqrt{m_a f_a}$, where $\sim \Lambda$ is the energy scale of DW formation (i.e.$\Lambda_{\rm QCD}$ for QCD axion) when the radial mode acquires a mass $m_R \sim f_a$. Furthermore, the shift symmetry possessed by the angular mode is broken at the time when $3H = m_a$ (where H is Hubble rate), which is when DW enters into the horizon, much later than the global U(1) breaking. At later times when $H \ll f_a$, the effective Lagrangian for axion field $a = a(\mathbf{x}, t)$ with the radial mode integrated out reads

$$\mathcal{L} = |\partial_\mu a|^2 - V(a). \tag{7.1}$$

We consider a biased potential

$$V(a) = \frac{m_a^2 f_a^2}{N_{\rm DW}^2}\left[1 - \cos\left(N_{\rm DW}\frac{a}{f_a}\right) + \epsilon\left(1 + \cos\frac{a}{f_a}\right)\right], \tag{7.2}$$

where $\epsilon \ll 1$ is the bias parameter that causes DW to collapse, m_a and f_a are the axion mass and decay constant respectively. We consider $N_{\rm DW} = 2$, which implies one true vacuum and one false vacuum in the model [1]. This is a representative choice that involves a simple DW structure which eases the simulation analysis and also allows us to extrapolate our results to the string-wall scenario, which we will discuss in more detail later.

We estimate the DW surface tension based on the axion potential in Eq.(7.2):

$$\sigma_{\rm DW} \simeq \eta_{\rm DW}\,\frac{m_a f_a^2}{N_{\rm DW}^2}, \tag{7.3}$$

where $\eta_{\rm DW} = 8$ for the potential in Eq.(7.2), and $\eta_{\rm DW} = 8.97(5)$ for QCD axion with including pion contribution [518], we used the former in this study. The DWs are dynamical at cosmic time $t \sim 1/m_a$ when the horizon is comparable to the DW thickness $\delta \sim 1/m_a$.

[1] It is worth mentioning that the bias term in Eq.(7.2) doesn't shift the true vacuum in the axion potential, which is for avoiding the axion quality problem, see a review in [114].

7.3 Setup

7.3.1 Simulation Setup

The equation of motion (EoM) of the axion field in a flat homogeneous and isotropic Friedmann-Lemaitre-Robertson-Walker (FLRW) universe is

$$\frac{\partial^2 a}{\partial \tau^2} + 2\left(\frac{d\ln R}{d\ln \tau}\right)\frac{1}{\tau}\frac{\partial a}{\partial \tau} - \frac{\partial^2 a}{\partial x_i^2} = -R^2\frac{\partial V}{\partial a}, \tag{7.4}$$

where $R(t)$ is the scale factor, x_i is comoving space, τ is comoving time, and ∇ is the Laplacian in physical coordinates. We start our simulations at a time that is slightly earlier than the DW formation time.

For the initial condition (IC) of the field of our simulation, a random and uniform distribution of the axion field agrees with the consequence of stochastic inflation with an assumption that the axion potential scale $\sqrt{m_a f_a}$ is far below the inflation scale H_I (see [519] and a review the stochastic method [520]). We consider a simpler scenario in that we randomly assign field value $a = 0$ or π (the two vacuums in the potential) to realize an unbiased IC that half of the points on the lattice are in a true vacuum and assume zero initial field velocity $\dot{a}(t_i) \to 0$. As we will see that once the DW network enters the attractive solution, the so-called scaling regime, the DW network evolution will no longer be sensitive to IC. This statement has been observed in earlier simulations [521, 110, 500, 515, 389], and see [511] for a discussion of the effect of a biased IC on PRS DW evolution (and earlier references [512, 522, 523]).

Other simulation setups are as follows. We utilized all parameters with $f_a \to 1$. The lattice size is $N^3 = 1536^3$, and the simulation period starts from $1/H(t_i) = R(t_i)\Delta x_i$, and ends at $1/H(t_f) = (N/2)\Delta x_f$, where $\Delta x_i = 1$ is initial lattice spacing, $R(t_i) = 1$ is initial scaling factor, $\Delta x_f = R(t_f)\Delta x_i$ is comoving spacing at the end of simulation end, and assuming a radiation background $R(t) \propto t^{1/2}$. We fix the time interval $\Delta\tau = 0.1$ and test convergence by re-running with smaller time intervals, where τ is comoving time. Moreover, we fix the physical DW thickness as

$$\delta \sim \frac{1}{m_a} = \frac{1}{(N/2)R(t_i)\Delta x_i}. \tag{7.5}$$

These choices imply that the simulation starts at the time that the horizon size equals lattice spacing Δx_i, and ends when the horizon expands to half of the simulation size. On the other hand, the DW thickness δ occupies $N/2$ lattice grids at t_i, then as the coordinate expands, the simulation ends when two grids occupy δ. We chose such simulation setups for the following reasons:

(1) δ can not be smaller than the size of two grids for enough resolution of the DW. Lower resolution leads to incorrect and insensible simulation results such as a frozen DW in lattice because the gradient $\nabla^2 a$ in the equation of motion Eq.(7.4) would be incorrectly calculated in simulation. Also, a lower resolution would incorrectly induce a wrong tail in the axion kinetic spectrum at axion momentum $k \sim 2\pi/\Delta x_f$.

(2) We simulated with two types of boundary conditions (b.c.'s), periodic and symmetric, and investigated the results' robustness against the choice of b.c. As the simulation results are expected to be inevitably subject to b.c. (albeit not significantly as we found), in order

to mitigate the effect we conservatively collect simulation data from the middle 1/8 of the simulation box and discard the rest. This data collection range equals the Hubble box size at the end of the simulation.

In order to present a free axion spectrum by filtering out the DW contribution, we employ a mask function on the axion field as in previous studies [219, 8] (firstly applied in CMB analysis [524]). The method is to mask $\dot{a}(x)$ by a window function

$$\dot{a}(x) \to \theta(x-d)\dot{a}(x), \tag{7.6}$$

where x is the coordinate that origin at the DW center where $V(a(x=0)) = V_{\rm max}$, d is a mask function parameter, and $\theta(x)$ is the Heaviside step function. We fix $d = \delta/2$ in our simulation for excluding the DWs contribution to the power spectrum. But due to the influences on the DWs exerted by the background axion field, δ would not be perfectly a constant. Thus we cannot fully erase the DW contribution to the free axion spectrum, but our approach should provide a good estimation. A more effective algorithm to erase such a contribution may be developed with dedicated future work. The kinetic power spectrum is found to be insensitive to the choice of d that is not too far from δ, i.e. $\delta/4 \lesssim d \lesssim 2\delta$. We found that applying the mask function on the axion field $a(x) \to \theta(x-d)a(x)$ causes an insensible result on the gradient energy and potential, which is a sensitive variation on the blue tail of spectrum ($k \sim 1/m_a$) with a variation of d. This may be caused by the twinkling. The oscillons are flashing/twinkling in the simulation sub-horizon compact DW or oscillons (see the red points at the end of simulation at Fig. 7.1) that cannot be fully removed by the mask function. We thus only apply the mask function on the axion kinetic

energy and assume that the free axions are all in harmonic mode i.e. its kinetic energy takes half of its total energy for estimating the total free energy of the radiated axions.

Our DW simulation is run with various simulation conditions and ALP model benchmarks. We conducted 5 simulations for each benchmark with $\epsilon \sim 10^{-3}$ (to ensure convergence) while keeping the aforementioned parameters constant as described in the earlier paragraphs. Subsequently, we extrapolated our findings to lower ϵ values and a distinct range of m_a by analyzing the axion spectrum and monitoring the DW and axion background fields on the snapshot of simulation.

Besides the main simulation runs, we also conducted testing runs under various conditions and ALP model benchmarks. We assessed the impact of altering simulation parameters (with 5 testing runs for each benchmark as well) such as axion mass m_a, spanning a range from 0.5 to 2, initial scaling rate $R(t_i)$ with values of 0.5, 1, and 2, and x_i with values of 0.1, 1, and 10. Additionally, we considered different lattice sizes N (512, 1024, and 1536) and the mask function parameter d as previously mentioned. Remarkably, the variation in these parameters did not affect our analysis results for the axion kinetic spectrum, and consequently, our conclusions remained unaffected.

7.3.2 Application of our simulation to other models

Although we simulated a network with only a simple DW, our results can be applied to many more complex models if the model satisfy the following conditions:

(1) The DW network has enough time to enter the scaling regime.

(2) The DW properties such as its thinkness δ and DW number N should be the same as in this study.

The first condition erases the DW initial distribution effect from different models. The second ensures the DW dynamics agree with our found. As an example, we explain how our simulation can fit the QCD axion model. Firstly, considering the absence of cosmic string in the QCD axion models such that a pre-inflationary PQ symmetry breaking or PQ scalars have a non-simply connected topological structure. The differences between our study and a QCD axion model with $N = 2$ are the nonzero bias parameter ϵ in the potential Eq.(7.2) which should be small enough $\epsilon \lesssim 5 \times 10^{-3}$ to ensure that the DW network can enter the scaling regime. This refers to, as we will see in Sec.7.4, the stable DW network entering to scaling regime within a short period $\Delta t \lesssim 10/m_a$. Another difference is the DW thickness as

$$\frac{1}{\delta_{\rm QCD}} \simeq m_a(T) \simeq \begin{cases} m_a \left(\dfrac{\Lambda_{\rm QCD}}{T}\right)^4 & \text{for } T > \Lambda_{\rm QCD}, \\ m_a & \text{for } T \leq \Lambda_{\rm QCD}, \end{cases} \tag{7.7}$$

where QCD scale $\Lambda_{\rm QCD} = 400\,{\rm MeV}$, T is cosmic temperature, and the term is from a diluting instanton gas approximation [124, 123, 122, 125] (also see the results from lattice simulation [525, 518]). The QCD axion DW thickness $\delta_{\rm QCD}$ turns to a constant at time t_a, and afterward, the QCD axion DW evolution as in our simulation. In which, we should consider a small ϵ that the DW can live long enough to enter the rescaling regime after t_a. We will discuss this condition in the parameter space in Sec.7.8.

We did not simulate the QCD axion DW due to the limitations imposed by the lattice. The DW thickness, which rapidly shrinks as $\delta_{\rm QCD} \propto R(t)^{-4}$ in Eq.(7.7), imposes a significant constraint on the evolution period in our simulation. Because the thickness should be at least larger than the lattice spacing for accurate resolution. Consequently, we treated δ as a constant in our simulation, ensuring that the DW decays before the simulation concludes.

On the other hand, QCD axion models with existing cosmic strings, such as the PQ scalar with post-inflationary $U(1)$ symmetry breaking, maintain QCD axion strings until DW formation. Subsequently, two DWs attach to a single cosmic string, forming a string-wall network that differs significantly from what we considered in our study. However, we find that the influence of cosmic strings is negligible when the DW tension dominates the network [224], specifically when the condition

$$\sigma_{\rm DW} t/\mu > 1 \tag{7.8}$$

is satisfied, where $\mu \simeq 2\pi^2 f_a^2 \ln(t f_a)$ is the cosmic string tension. Under this condition, the string-wall structure approximates our simulation. However, for higher values of $N_{\rm DW} > 2$, where multiple DWs attach to a single string, a more complex scenario arises with the attachment of multi-DWs. We have chosen to leave the investigation of such complex scenarios with $N_{\rm DW} > 2$ for future work. In Section 7.8, we will present the parameter space availability under the constraint given in Eq.(7.8).

Furthermore, our decision to focus on the simplified case without string contributions is also influenced by technical considerations. Due to limitations in our simulation resources, the lattice size imposes constraints on extending the simulation period sufficiently to observe DW decay if cosmic strings are included. The scale gap between the width of the string ($\sim 1/f_a$) and the Hubble scale at the DW decay prevents us from adequately observing the network in our simulation with the current lattice size.

Our simulation result can not only apply to the QCD axion models but also to other axion-like particle models that satisfy the two conditions that we have discussed above.

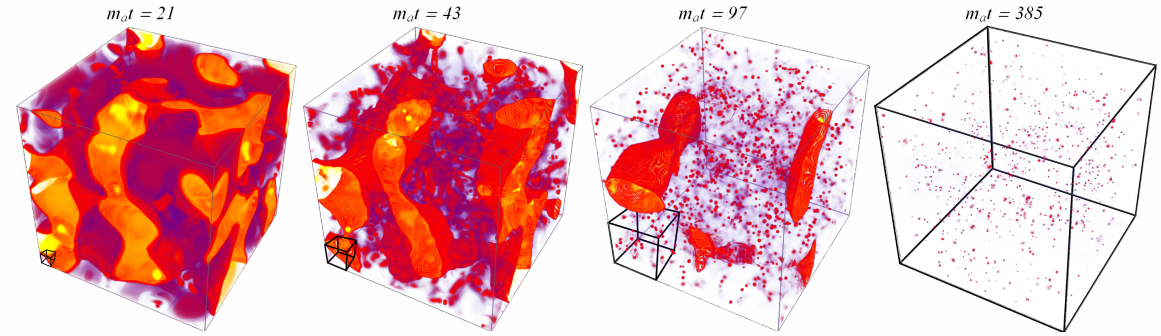

Figure 7.1: Visualization of lattice simulation with bias parameter $\epsilon = 0.0013$: snapshots in a time series (left to right: $m_a t = 21, 43, 97, 385$). The yellow (blue) region indicates a false (true) vacuum, and the red region represents DWs. The Hubble volume is shown as a black cube in the bottom-left corner of each snapshot (see animation for $\epsilon = 0.0012$). The small red points are defined as sub-horizon compact DW or oscillon, they are twinkling in the simulation.

7.4 Domain wall dynamics

7.4.1 Scaling behavior

In our simulation, we track the evolution of DWs and the pattern of energy loss from the DW network. A snapshot of the evolution is shown in Fig. 7.1, and its counterpart with non-biased potential is shown in Fig. 7.11 in the appendix[]. The left-most snapshot is taken as the network enters the scaling regime when the DWs flatten while expanding. Shortly after its formation ($\Delta t \lesssim 10/m_a$), the network approaches an attractive solution called the scaling regime while releasing energy through the following two mechanisms: (1) DW flattening motion that not only radiates the axion but also heats the axion background field and (2) the collapse of contraction compact DWs as shown in the second snapshot in Fig. 7.1 where the DWs flatten while collapse to compact DWs and oscillons. The former dominates the radiation for stable DW, and the latter is important for decaying DW.

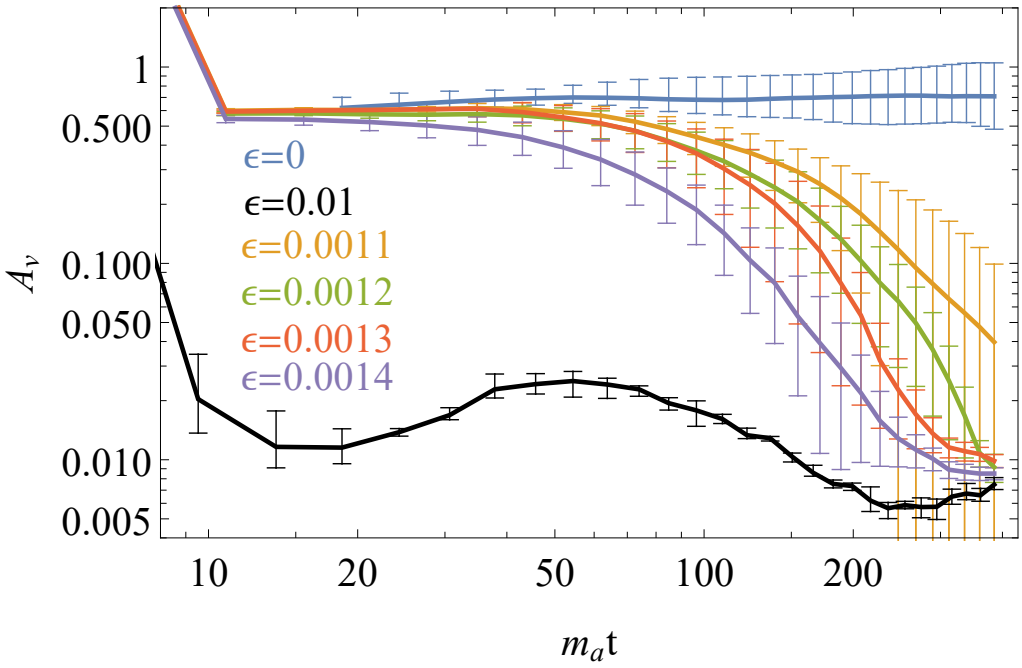

Figure 7.2: DW area parameter (defined in Eq.(7.10)) as a function of the cosmic time in our simulation, with varying bias parameter ϵ (defined in Eq.(7.2)).

Meanwhile, the out-of-horizon DWs enter into the horizon continuously, which consequently compensates for the energy loss due to the decay, such that the DW area per horizon volume A_v remains constant. This constant solution is the feature of the scaling region. Such a feature has been measured in literature [515, 514, 500, 8, 389], and also agrees with our findings as shown in Fig. 7.2. While the DWs turn to decay and collapse at about $t_{\rm decay}$ and the rescaling solution break. In the scaling regime, the DW energy density takes the following form:

$$\rho_{\rm DW} = \gamma^2 \frac{\sigma_{\rm DW} A_v}{t}, \tag{7.9}$$

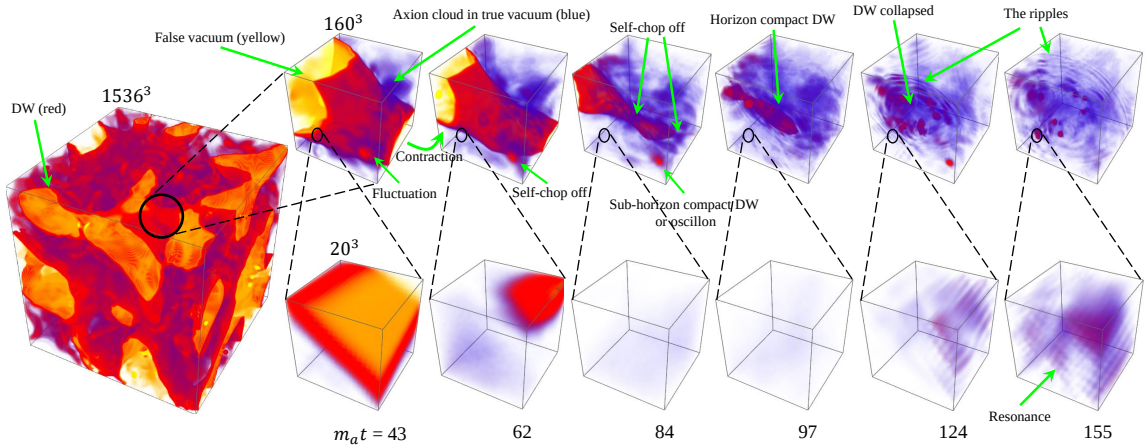

Figure 7.3: Visualization of the lattice simulation with the bias parameter $\epsilon = 0.0012$. The leftmost figure displays a snapshot of the entire simulation scale, where the domain wall (DW) is highlighted in red color. The upper-row showcases a zoomed-in region of our simulation with a 160^3 lattice, accompanied by a time series depicted at the bottom. The lower-row comprises smaller lattice sizes. Both sets of sub-figures encompass a range of features discovered in this study, and a detailed discussion of these features is provided in Section 7.4.2.

where $\gamma \simeq 1$ is the Lorentz factor that implies the contribution of the kinetic energy of the DW, and the area parameter is given by

$$A_v \equiv \frac{A_w t}{R(t)V} = 0.67^{+0.04}_{-0.04}, \qquad \text{for } \epsilon = 0, \tag{7.10}$$

where A_w is the DW comoving area, and V is the comoving volume. The result agrees with the simulation study [8, 389, 507, 389], but it is about 30% less than the prediction with PRS DW network [221]. On the other hand, in the metastable scenario, we find

$$A_v = c_1 + c_2 \,\mathrm{Exp}\left[-c_3 \left(\epsilon\sqrt{m_a t}\right)^{c_4}\right], \quad \text{for } \epsilon > 0, \tag{7.11}$$

with

$$c_1 = 0.0088^{+0.0009}_{-0.0009}, \quad c_2 = 0.62^{+0.06}_{-0.05},$$
$$c_3 = 3.98^{+0.40}_{-0.40} \times 10^6, \quad c_4 = 3.57^{+0.08}_{-0.11},$$

where the parameter c_1 term represents the residual compact DWs and oscillons at the end of the simulation. We cannot distinguish whether these are exactly small compact DWs or oscillons due to the limitation of the simulation period and resolution. The fitting model Eq.(7.11) is inspired by field theory analysis [509] that employs mean-field approximation method and Gaussian ansatz on the field probability distribution in the limit of small bias term $\epsilon \ll 1$. Moreover, the parameter $c_4 \sim 3$ is about the spatial dimension as predicted in [509], non-Gaussian field distribution may cause this discrepancy. The fitting model in Eq.(7.11) also fits the data in other DW simulation studies [523, 512, 511]. As the axion kinetic energy cools down, the true vacuum pressure force gradually overcomes the DW tension, which causes the decay and collapse of the DW network. We define the characteristic decay time of the DW, $t_{\rm decay}$, as when the DW area A_v becomes $\sim 10\%$ of the pre-collapsing value i.e. $0.1A_v(t \to 0) = A_v(t_{\rm decay})$. $t_{\rm decay}$ can be estimated by Eq.(7.11) as

$$\begin{aligned} t_{\rm decay} &\simeq \frac{\epsilon^{-2}}{m_a}\left(\frac{c_\mu}{c_3}\right)^{2/c_4} \\ &\simeq \frac{\epsilon^{-2}}{m_a}(3.22 \pm 0.94) \times 10^{-4}, \end{aligned} \tag{7.12}$$

where the factor

$$c_\mu = 2.32^{+0.61}_{-0.60}. \tag{7.13}$$

We further define the decaying period: start from the exponential component in Eq.(7.11) as lower than -1 until DW all decayed. Note that other semi-analytical estimation studies [8, 388] compare the pressure gap between vacua and use a power-law model to fit their data, and predict $t_{\rm decay} \propto 1/\epsilon$. This causes a notable difference from our results in the prediction for the axion relic abundance as shown in later sections.

7.4.2 Features in Simulation

In this subsection, we will discuss the simulated features that we discovered in our simulation snapshots, and further discuss their energy contribution and dynamic behavior later in Sec. 7.6 and Sec. 7.7.

As depicted in Fig. 7.3, the observed features are described as follows:

(1) DWs, represented as red walls in Fig. 7.3, primarily exist within super-horizon to horizon sizes, i.e. $k \lesssim H$. The process of these DWs' movements is analogous to the act of laying out a piece of paper flat, and we refer to this motion as "flattening". As a result of this flattening process, the energy of fluctuation radiate to a free axion field and is stored in the axion clouds.

(2) Axion clouds are regions of denser energy in the background axion field. They are illustrated by blue in the true vacuum and yellow in the false vacuum in Fig. 7.3.

(3) Self-chopping is a crucial mechanism in which DWs release energy to both the horizon

and subhorizon-sized compact DWs. The upper-row subfigures in Fig. 7.3 depicts the self-chopping processes.

(4) Contraction refers to the progressive reduction in the size of a compact DW over time. This phenomenon leads to the formation of a horizon compact DW from a super-horizon DW.

(5) Horizon compact DW refers to compact DW with a size approximately equal to the horizon scale. This compact structure is primarily formed through the self-chopping of a horizon-sized DW, which subsequently collapses shortly after its formation. As indicated by the upper-row subfigures in Fig. 7.3, the collapsed compact DW generates ripples and heats the background axion fields.

(6) Sub-horizon compact DWs are compact DWs with sizes ($\sim 1/m_a$) much smaller than the horizon scale. These structures are mainly formed through the self-chopping of fluctuations on the DW surface. Distinguishing between sub-horizon compact DWs and oscillons is challenging due to limited lattice resolution, as both structures occupy only a few lattice points. Note that at the initial stages of the simulation, the horizon and sub-horizon compact DWs are indistinguishable as they share (or approximately share) the same size scale.

(7) Ripples refer to axion waves propagating outward from the collapsing DWs. They retain energy and possess horizon scales ($k \lesssim m_a$) in our simulation.

(8) A resonance phenomenon is observed in which the axion clouds are divided into piles with scales of approximately $k \gtrsim 1/m_a$.

We will discuss these DW evolution features in the following content.

Through the monitoring of the simulation snapshots, the DW energy-releasing mechanism can be divided into two categories:

(1) Ripples: the process involves a DW self-chopping into a horizon-sized compact DW, which subsequently collapses while radiating a free axion field in the form of ripples and heating the background axion field. Similarly, a horizon compact DW, which is formed by the contraction of a super-horizon DW, falls into this category.

(2) Axion clouds: DW energy is released into axion clouds through the flattening motion.

Additional contributions from processes such as sub-horizon compact DW chopping exist, but they have a relatively minor impact compared to the aforementioned factors. The collapse of the horizon compact DWs also contributes to the formation of axion clouds. However, explicit evidence demonstrating its significant contribution is currently lacking. As we will see in Sec. 7.7, these two energy contributions will be discussed in a mathematical form with details.

Compared to the VOS model of cosmic strings, where the majority of energy is released through the formation of loops primarily generated by the interaction of two long strings [526]. Unlike cosmic string chopping, the chopping from two DWs is unlikely to happen, and the majority of energy loss is due to the two mechanisms discussed in the last paragraph. The energy contribution from sub-horizon compact DW self-chopping is negligible when compared to horizon-scale compact DW self-chopping. Moreover, it is frequently observed that super-horizon and horizon scale DWs tend to reduce in size by contraction or self-chopping into sub-horizon compact DWs as shown in the upper-row of

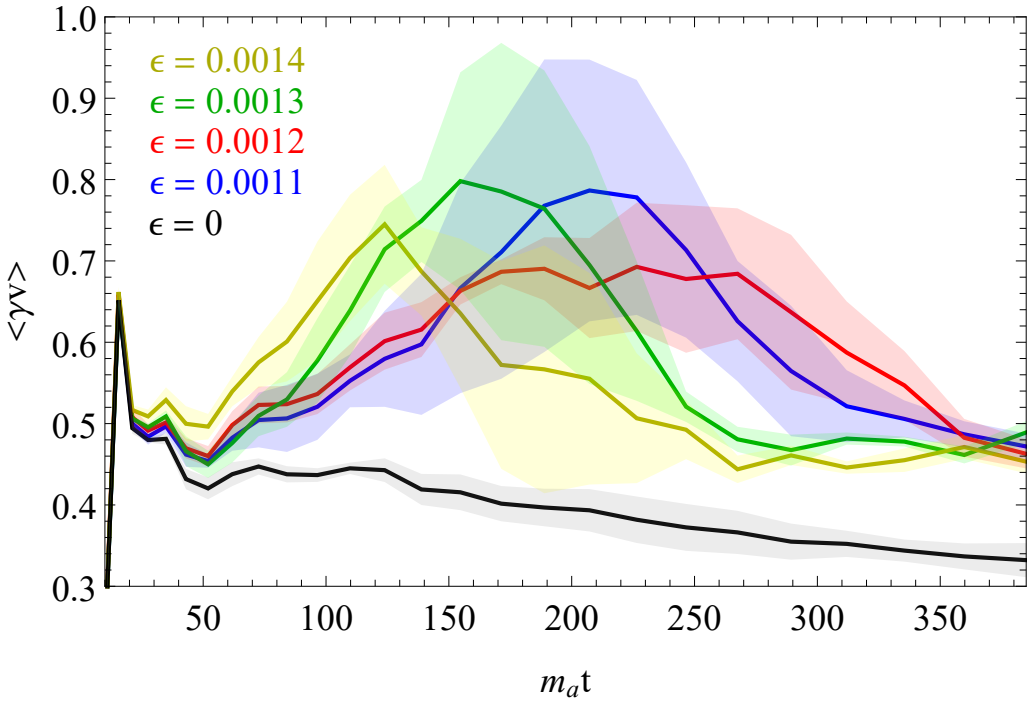

Figure 7.4: The average γv versus $m_a t$ with varying bias parameter ϵ. The uncertainties are shown as shadow areas.

Fig. 7.3, as opposed to arising from the collision or chopping of two horizon DWs.

7.5 Domain Wall Velocity

In DW dynamics, its velocity plays an important role in its equation of motion. We measure the velocity by tracking the movement of the maximum of the axion potential $V(a(x,t)) = V_{\max}$ in the simulation. The observed DW velocity is shown in Fig. 7.4 with varying ϵ. The network is first accelerated due to the pressure difference between the true and false vacua, then decelerated when the network decays. The peak of each curve thus locates at about $t_{\rm decay}$, see Fig. 7.5, where we show that the comparison of decay time $t_{\rm decay}$

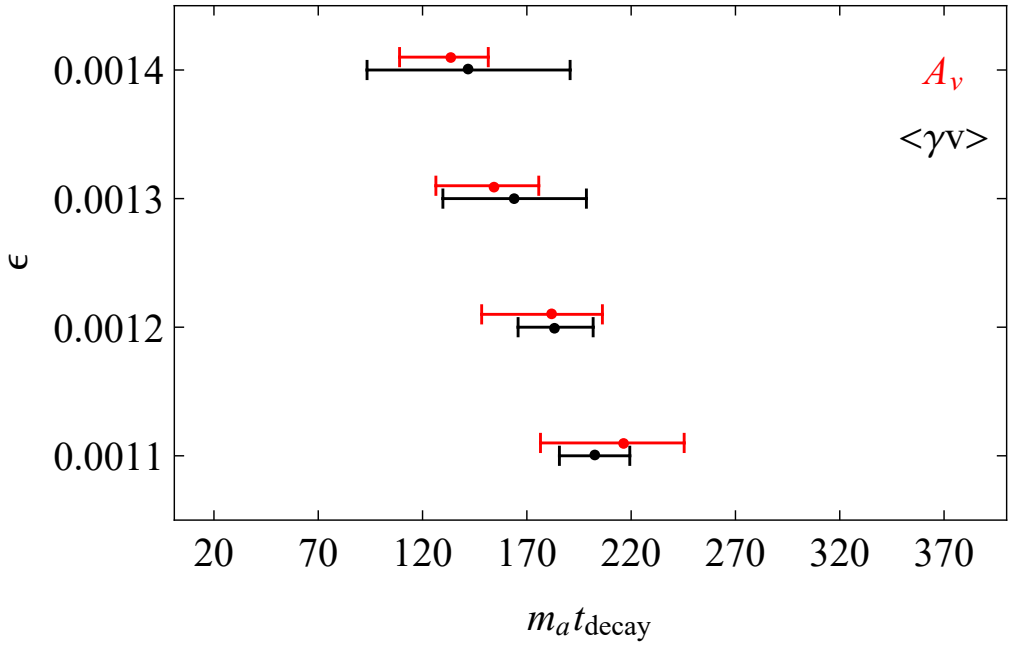

Figure 7.5: Bias parameter ϵ versus axion mass times decaying time $m_a t_{\rm decay}$. The red bars are the decay time calculated by Eq.(7.12) using the fitting result at Eq.(7.11). The black bars are the peaks in Fig. 7.4.

as defined in Eq.(7.12) and the peak of observed velocity.

To fit the DW velocity function, we consider the following model:

$$\gamma v = \frac{0.923 \pm 0.136}{(m_a t)^{0.614 \pm 0.031}} + \alpha_v e^{-(t-t_{\rm decay})^2/(2\sigma_v^2)}, \tag{7.14}$$

with

$$\alpha_v = (0.241 \pm 0.039), \quad \text{and} \quad \sigma_v = (52 \pm 20)\frac{1}{m_a}.$$

The Hubble friction, the interaction with the background axion field, and the flattening motion of the DW cause the deceleration of the DW as shown as the first term in Eq.(7.14).

This term indicates the velocity decrease during the scaling regime. The second term in Eq.(7.14) indicates the effect of the pressure difference between the true and false vacua in the decay phase, α_v represents the magnitude of the acceleration, σ_v is the uncertainty in our observation and the exponential presents that the acceleration stops at about $t \simeq t_{\rm decay}$.

The preceding section has centered on scrutinizing the domain wall's velocity. This groundwork paves the way for the subsequent sections, dedicated to exploring the repercussions of domain wall decay, particularly in relation to the emergence of a free axion spectrum.

7.6 Free Axion Spectral Analysis

We discuss the detail of the spectral analysis for free axion energy density in this section, which would be the key input for estimating axion dark matter relic density. As discussed in Sec. 7.3, we estimate the total free axion energy as twice of the masked axion kinetic energy. We then compute the free axion spectrum according to [109, 507] as

$$\rho_a = \int dk \partial\rho_a/\partial k, \quad \text{with} \quad \rho_a = \langle \dot{a}^2 \rangle, \tag{7.15}$$

where the axion spectrum $\partial\rho_a/\partial k$ is given by

$$\frac{\partial\rho_a}{\partial k} = \frac{k^2}{(2\pi L)^3} \int d\Omega_k |\tilde{\dot{a}}(k)|^2, \tag{7.16}$$

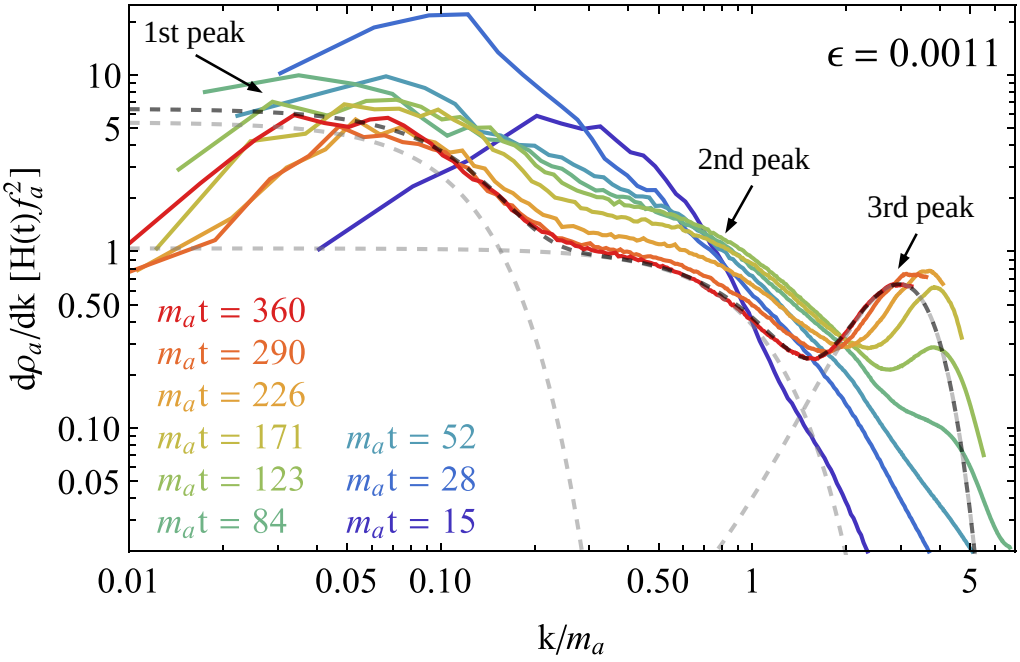

Figure 7.6: Free axion energy density spectrum $\partial\rho_a/\partial k$ as a function of physical momentum k, assuming the bias parameter $\epsilon = 0.0011$. The early to later spectrum is shown as blue to red. The spectrum can be split into three Gaussian distributions as shown as dashed gray curves corresponding to the 3 contributing terms in Eq.(7.17). From low k to higher k, these three Gaussian distributions present the energy density from misalignment ($k/m_a \lesssim 0.2$), free axions radiated by compact DW self-chopping, and collapsing ($k/m_a \lesssim 1$), and the small structure axion field such as the axion clouds with the resonance at ($k \sim \mathcal{O}(m_a)$), respectively. The smaller $k < 0.01m_a$ region is lacking data because of the simulation lattice size, and higher k has been cut at Nyqvist frequency as discussed in Sec.7.6.

where $\tilde{\dot{a}}(k)$ is the Fourier transform of $\dot{a}(x)$, $L = (N/2)R(t)\Delta x_i$ is the collected data range, and the momentum $\vec{k} \equiv \frac{2\pi\vec{n}}{L}$. In addition, we cut off the momentum that is higher than the Nyqvist frequency $k_{\rm Ny} = \pi/(R(t)\Delta x_i)$ to prevent corrupted data caused by insufficient resolution.

In Fig. 7.6 we show the free axion energy spectrum with snapshots for the cosmic time evolution, using different colors. The dark blue curve ($m_a t = 15$) represents the spectrum when the network just enters the scaling regime, and the red curve ($m_a t = 360$) presents the spectrum near the end of the simulation. We find that the spectrum can be fitted as a sum of three Gaussian distributions corresponding to distinct physics origins (to be explained later):

$$\frac{\partial \rho_a}{\partial k} = \sum_{i=1}^{3} \frac{\partial \rho_i(A_i, k_i, \sigma_i)}{\partial k}, \tag{7.17}$$

where the labels $i = \{1, 2, 3\}$ denote the 3 gray-dashed curves from low k to higher in Fig. 7.6, associated with the first, second, and third peak, as indicated respectively. These curves are parameterized by

$$\frac{\partial \rho_i(A_i, k_i, \sigma_i)}{\partial k} \equiv A_i \exp^{-(k-k_i)^2/\sigma_i^2}, \tag{7.18}$$

where we set $k_1 \simeq 0$ due to the lack of data within $k \leq 0.02$, $k_2 \simeq 0$ because the 1st peak overshadows the relevant data range, and

$$k_3 = (3.68 \pm 0.03) m_a, \tag{7.19}$$

which decreases as $1/R(t)$ after DW decay. We fit the parameters in Eq.(7.17) for each cosmic time snapshot in Fig. 7.6, then analyze their time dependence in the next section. The fitting results for the parameters and energy densities in Eq.(7.17) are given in Appendix.7.10. We have verified the peak by conducting additional tests involving variations

in the value of m_a and lattice spacing, as outlined in the simulation setup section, but the observation in Eq.(7.19) closely approaches the Nyquist frequency during the later stages of the simulation, indicating a potential influence of inherent resolution limitations on the magnitude of the peak.

We observe that ρ_1 is in reasonable agreement with the energy density of axions produced through the misalignment mechanism, specifically, $\rho_1 \sim m_a^2 f_a^2 / 2N_{\rm DW}^2$ [2], at the early stage of simulation, then redshifts like matter. As a result of this redshift, the spectral line associated with this contribution progressively shifts towards the lower frequencies over time.

The free axion energy density ρ_2 in Eq.(7.15) carries the energy contribution with the scale $k \lesssim m_a$. We attribute this energy to the horizon compact DW chopping, and there are two reasons for this designation: (1) The energy spectrum of ρ_2 coincides with the scale size of the ripples. (2) ρ_2 aligns well with the production process of the compact DW, as predicted by the DW VOS model (as referred to in DW chopping [515]). It is important to emphasize that while we observe the self-chopping phenomenon (as discussed in Sec.7.4.2), it differs from the definition of two DWs chopping in the VOS model. Nonetheless, they share a similar energy loss form in the equation of motion, as we will see in Sec.7.7.

[2]Note that the initial condition that sets the axion fields on vacuums seems to exclude the axion energy from the misalignment mechanism. However, it just stores the energy on the gradient energy budget at the onset of simulation.

Additionally, the energy density ρ_3 can be interpreted as the contribution from axion clouds with a resonance at k_3. This energy arises from various processes, as discussed in Sec.7.4.2. We anticipate that the primary contribution to this energy comes from the annihilation of fluctuations on the DW surface because the estimation of the energy released from these fluctuations aligns well with the energy density ρ_3 as demonstrated in Sec.7.7.

The energy release mechanisms discussed in Sec.7.4.2 occur in both the scaling regime and decaying period, and the compact DW collapse is more likely to occur in the decaying period. In other words, the biased potential significantly accelerates the DW flattening, contraction, and self-chopping. During the decaying phase, we find that the production of axion clouds (ρ_3) increases by about $\sim 70\%$, and the radiation for larger wavelength axion ripples (ρ_2) is enhanced by about $\sim 30\%$, compared to the scaling regime. The percentage is estimated at time $t_{\rm decay}(\epsilon \to 0.0012)$, and by comparing $\epsilon = 0.0012$ and $\epsilon = 0$ scenarios.

7.7 Model for Domain Wall Evolution

In this section, we present the coupled evolution equations for the energy densities of the DW network and of the free axions emitted from the DWs. The two components of axion energy densities sourced by different DW dynamics, ρ_2 and ρ_3, as identified via spectral analysis and monitoring simulation evolution in Sec.7.4.2 and Sec.7.6, are key inputs in this section. Here we will quantitatively model these contributions by numerically fitting simulation data. We have found the time-dependence of energy densities ρ_2 and ρ_3 in Sec.7.6, we further fit them into the DW evolution equations in this section.

We first generalize the DW evolution equation in the VOS model for a stable DW network [515, 514] as follows:

$$\frac{d\rho_{\rm DW}}{dt} = -(1+3v^2)H\rho_{\rm DW} - \left.\frac{d\rho_{\rm DW}}{dt}\right|_{\rm to2} - \left.\frac{d\rho_{\rm DW}}{dt}\right|_{\rm to3}, \tag{7.20}$$

where the right-hand side of the equation represents, in order, the redshift effect, the DW energy loss to ρ_2 and ρ_3, respectively. Here we have reasonably assumed that the final form of DW energy release is axions, as gravitational wave radiation albeit inevitable, is expected to be subleading.

By energy conservation, the latter two terms in Eq. 7.20 also enter the evolution equations of the free axions, which is essential for solving axion relic abundance. As revealed via the spectral analysis based on simulation results, free axion production from DWs can be roughly divided into two kinetic regions associated with distinct DW dynamics, corresponding to ρ_2, ρ_3. It is thus reasonable to consider the evolution of ρ_2 and ρ_3 components separately, then sum up their solution for the total axion abundance. We first write down the evolution equation for ρ_2, which originated from the collapse of compact DWs:

$$\frac{d\rho_2}{dt} = -3H\rho_2 + \left.\frac{d\rho_{\rm DW}}{dt}\right|_{\rm to2}, \tag{7.21}$$

where the $3H$ reflects the finding that this spectral component of axions generally has a longer wavelength and behaves like cold matter. The second term on the right-hand side reflects energy conservation and the aforementioned reasonable assumption that the DW energy release 100% goes to axions. As the second term descends from the formation of

compact DWs through DW self-chopping, we can explicitly model its evolution as follows:

$$\left.\frac{d\rho_{\rm DW}}{dt}\right|_{\rm to2} = \tilde{c}_v v \frac{\rho_{\rm DW}}{L_{\rm DW}}, \tag{7.22}$$

where the self-chopping efficiency parameter, $\tilde{c}_v$, can be modeled as

$$\tilde{c}_v \equiv c_v \gamma^{c_\gamma} \mathcal{A}_F^{-3/2}, \tag{7.23}$$

with

$$c_v = 0.36^{+0.07}_{-0.03}, \quad c_\gamma = 1.36^{+0.13}_{-0.18}, \tag{7.24}$$

where $L_{\rm DW} = \sigma_{\rm DW}/\rho_{\rm DW}$ is the DW correlation length. The value of the parameters c_v, c_γ and the power of $-3/2$ in $\mathcal{A}_F$ are calibrated by the simulation data as shown in Fig. 7.6. $\mathcal{A}_F$ is the area fraction parameter:

$$\mathcal{A}_F \equiv \frac{A_v(\epsilon)}{A_v(\epsilon \to 0)}. \tag{7.25}$$

where A_v is defined in Eq.(7.11). In the non-relativistic and stable DW limit, $\gamma \to 1$ and $\epsilon \to 0$, the Eq.(7.22) approaches the expression $c_v v \frac{\rho_{\rm DW}}{L_{\rm DW}}$ which was used to describe the energy loss resulting from the intersection of DWs, which leads to the creation of compact DWs that eventually collapse. This term is originally introduced by Kibble in the context of the cosmic string network [526], and later applied to the DW VOS model [515] for two DWs chopping. We slightly modify its physical interpretation to self-chopping and utilize

it to explain our data (see Fig. 7.7). The factor $\mathcal{A}_F^{-3/2}$ captures the simulation finding that compact DW production is more efficient during the decay phase, $v\rho_{\rm DW}/L_{\rm DW}$ represents the likelihood of DW self-chopping, and γ^{c_γ} indicates that an accelerated DW velocity increases the rate of self-chopping.

We further roughly estimate the solution of ρ_2 by solving the axion radiation equation Eq.(7.21) numerically as

$$\rho_2 R^3(t) \simeq 2\tilde{c}_v v \rho_{\rm DW}\Big|_{\epsilon\to 0,\ t\to t_{\rm decay}}, \tag{7.26}$$

where the DW network stops supplying the energy to ρ_2 at $t_{\rm decay}$, and substitutes $\epsilon \to 0$ into $\rho_{\rm DW}$ in Eq.(7.9), then the free axions redshift like matter afterwards. This estimation can be understood as energy conservation.

Next, we consider the evolution equation for the component of ρ_3, mostly due to the axion clouds production from the DWs. By analogy of Eq. 7.21 for ρ_2, we have:

$$\frac{d\rho_3}{dt} = -\lambda_3 H \rho_3 + \frac{d\rho_{\rm DW}}{dt}\bigg|_{\rm to3}, \tag{7.27}$$

where λ_3 represents the time-dependent redshift of this component of axion energy density. As shown in the spectral analysis, at production these axions are on average (semi-)relativistic with a shorter wavelength, thus radiation-like and $\lambda_3 \simeq 4$; then the axions cool down and become matter-like with $\lambda_3 = 3$ [3]. For simplicity, we use the following function

[3]The radiated axions can be understood as hot axions whose kinetic and gradient terms dominate their total energy. We have confirmed through simulations that for an axion field with initial conditions where the time derivative ($\dot{\theta}$), the spatial gradient ($\nabla_x\theta$), and the wavenumber (k) are all greater than m_a, (where $\theta = a(x)/f_a$), and ignorable potential energy, i.e., the kinetic and gradient components dominate. In this scenario, the total energy density redshifts like radiation, and the energy oscillates harmonically between

for λ_3 to fit the spectrum,

$$\lambda_3 = \begin{cases} 4 & \text{for} \quad t < t_{\rm decay}, \\ 3 & \text{for} \quad t \geq t_{\rm decay}. \end{cases} \tag{7.28}$$

Note that the $\lambda = 3$ period dominates the energy contribution due to the definition of $t_{\rm decay}$ at Eq.(7.12). The evolution of DW energy loss that leads to this component of axion production can be modeled as (to be explained later):

$$\begin{aligned} \left.\frac{d\rho_{\rm DW}}{dt}\right|_{\rm to3} &= \frac{1}{2}\frac{d}{dt}\left[\rho_{\rm DW}(1-v^2)^{c_{f2}}\left(\frac{m_a}{H}\right)^{c_{f1}(1-\mathcal{A}_F)}\right], \\ &\equiv \frac{1}{2}\frac{d}{dt}\mathcal{F}_A(t), \end{aligned} \tag{7.29}$$

where the parameters are calibrated by simulation data as:

$$c_{f1} = 0.44^{+0.20}_{-0.20}, \quad c_{f2} = 3.61^{+0.90}_{-0.98}. \tag{7.30}$$

Similar to the case of ρ_2, the numerical solution of Eq. (7.27) can be roughly estimated as

$$\rho_3 R^3(t) \simeq \mathcal{F}_A\Big|_{\epsilon\to 0,\ t\to t_{\rm decay}}. \tag{7.31}$$

We have chosen the model fitting form given by Eq. (7.29) for the following reasons. Firstly, the energy of the perturbation per unit area of the DW increases with the scalar (axion) mass m_a as estimated in [527]. Additionally, the total area of the horizon-sized DWs

the kinetic and gradient components. As the potential energy becomes comparable to the total energy, it starts diluting as matter-like (freezing at $V(a) \sim m_a^2 f_a^2$ when it becomes sub-dominant).

within a horizon decreases as H increases, and it is expected that the energy loss of DWs is greater for higher overall DW energy density $\rho_{\rm DW}$. These considerations are captured by the variables $1/H$, and $\rho_{\rm DW}$, respectively, along with their functional form in Eq. (7.29). In addition, the power of $c_{f1}(1-\mathcal{A}_F)$ renders the dimensionless parameter m_a/H negligible in the scaling regime, which captures the fact that the DW fluctuations release energy becomes more significant during the decay period. We also introduced a simple velocity dependence into Eq. (7.29), which implies a significant contribution to ρ_3 occurs at the deceleration period in Fig. 7.4 i.e. the decay period of DW.

It is important to highlight that the term described in [221], representing the axion radiation resulting from surface fluctuations of the DWs, does not align well with the axion spectrum depicted in Fig. 7.6 of our simulation. This discrepancy may be attributed to the utilization of the PRS algorithm [513] in [221], which can inaccurately model the DW dynamics at small-scale structures, as pointed out in [389].

Furthermore, there are other potential sources of this discrepancy. Firstly, ρ_3 encompasses not only the radiation from surface fluctuations of the DWs but also contributions from, for instance, horizon compact DW collapse that leads to the heating of axion clouds, as discussed in Sec.7.4.2. Secondly, in the later stages of the simulation, the observations of the scale of ρ_3 come close to the Nyquist frequency, which may result in considerable observational uncertainties, as discussed in Sec.7.6.

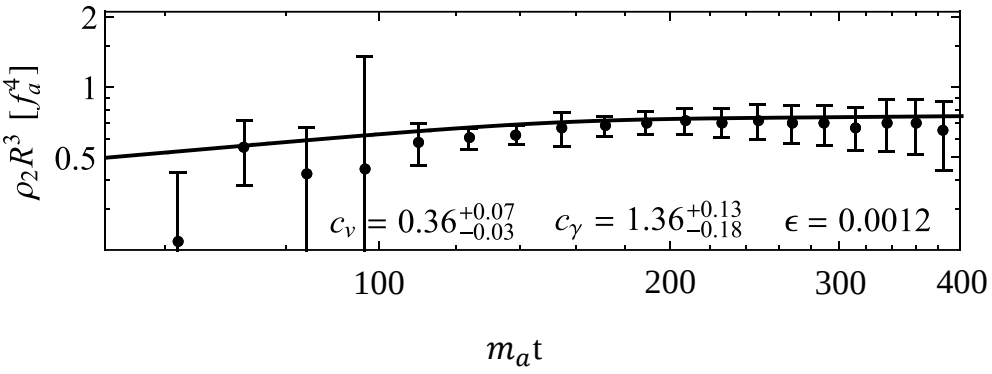

Figure 7.7: The energy density of the second Gaussian fitting function as given in Fig. 7.6 and Eq.(7.17) where we fix $\epsilon = 0.0012$. The black curve presents the prediction of energy loss model Eq.(7.21).

This section introduces coupled equations for DW network and free axions from DWs, using ρ_2 and ρ_3 from spectral analysis. The DW evolution equation, considering redshift effects and energy loss to ρ_2 and ρ_3, highlights the DW-axion relationship. Separate ρ_2 and ρ_3 equations detail DW self-chopping and axion cloud production. This illustrated free axion generation, which we delve into its application in the next section.

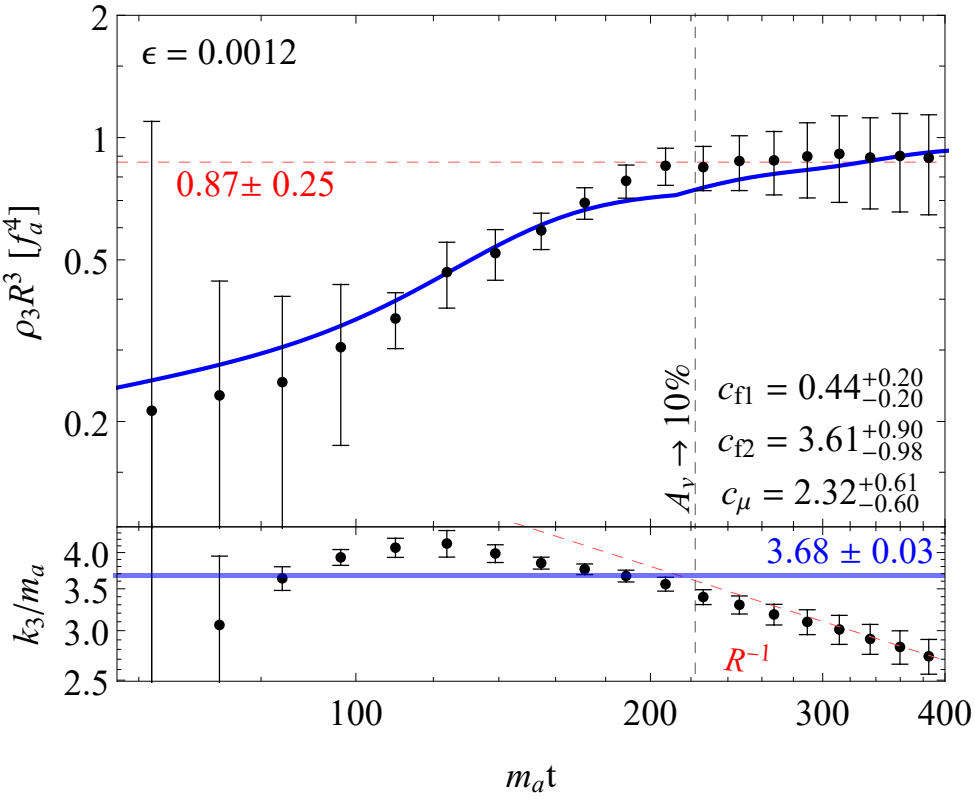

Figure 7.8: The energy density with $\epsilon = 0.0012$ for the third Gaussian fitting function as given in Fig. 7.6 and Eq.(7.17). The blue curve presents the prediction of energy loss model Eq.(7.27).

7.8 Cosmological implication

In this section, we will estimate the contribution of DWs to the relic density of axions based on the results obtained in earlier sections and present the viable parameter space of our model. We will apply our result to the $N_{DW} = 2$ ALP model (see Eq.(7.2)) with pre-inflationary PQ symmetry breaking as a concrete example. We then present an illustrative analysis that includes the contribution of cosmic strings to the axion relic abundance in the Appendix.7.9.

Furthermore, the contribution of the standard misalignment mechanism to the axion relic density is found to be ignorable ($\rho_{\rm mis}/\rho_{\rm DW} < 1\%$, where $\rho_{\rm mis}$ is axion energy density from misalignment mechanism, and $\rho_{\rm DW}$ is axion energy density from DW decay) compared to DW's contribution in our interested parameter space (see also [8]), we thus neglect its contribution in the subsequent discussion.

The DW contribution to relic axion is given by the solutions of the evolution equation of motion Eq.(7.21) and Eq. (7.27) in Eq.(7.26) and Eq. (7.31), respectively. The total axion energy density is $\rho_a = \rho_2 + \rho_3$, which reads

$$\Omega_{\rm a}^{\rm DW} h^2 \simeq 0.116 \left(\frac{m_a}{2\times 10^{-4}\,{\rm eV}}\right)^{-1.50^{+0.02}_{-0.02}} \times \left(\frac{\Lambda_{\rm QCD}}{400\,{\rm MeV}}\right)^{2} \left(\frac{\epsilon}{10^{-4}}\right)^{-1.87^{-0.35}_{+0.44}}. \tag{7.32}$$

As shown in Fig. 7.9 where assumed the DW formation at the QCD phase transition ($\Lambda = \Lambda_{\rm QCD}$) the parameter region that predicts the observed axion DM relic density $\Omega_{\rm a} = (0.12 \pm 0.0012)h^{-2}$ lies in the white area. We also considered the BBN constraint $t_{\rm decay} < 0.01$s [28, 29], and the CMB constraint that DW should decay before photon decoupling because the DW-produced particle represents DM. In addition, the region (above the black dashed-line) with a small biased parameter $\epsilon \lesssim 5\times 10^{-3}$ (see Fig. 7.20 in Appendix. 7.10) indicates that the DW network has sufficient time to transition into the scaling regime before its decay.

The limitations imposed upon ALP models are intricately tied to the interplay between axions and particles within the Standard Model (SM). As an illustration, when there is no interaction, the parameters m_a, Λ, and ϵ remain unconstrained. Hence, it

becomes justifiable to introduce an interaction, thereby enhancing the predictive capacity of the model. In this regard, we present two instances of ALP models under constraints, wherein interactions with SM particles have been incorporated.

To begin with, the introduction of an axion-photon conversion interaction $g_{a\gamma\gamma}aF_{\mu\nu}\tilde{F}^{\mu\nu}$, where $g_{a\gamma\gamma}$ denotes the coupling strength, leads to constraints determined by axion helioscopes such as the ongoing CAST experiment [528] and the prospective IAXO project [529]. These experiments serve to determine the characteristics of axions originating from the sun. The resulting bounds roughly limit m_a to $\lesssim$ 1,eV and $g_{a\gamma\gamma}$ to $\lesssim 10^{-10}$ GeV^{-1}. Given these restrictions, Figure 7.9 illustrates a region in the parameter space where the dark matter relic abundance exceeds $\epsilon \geq 3 \times 10^{-9}$.

Moving forward, a vector-like flavor violation interaction involving axions can be considered: $c_{e\mu}\frac{\partial_\nu a}{2f_a}\bar{f}_e\gamma^\nu f_\mu$, where f_e denotes the electron and f_μ represents the muon. With a naive assumption that the mixing coupling $c_{e\mu}$ approximate $\mathcal{O}(1)$. An upper limit on the muon decay channel $\mathrm{Br}(\mu^+ \to e^+ a) < 2.6 \times 10^{-6}$, established by the TRIUMF experiment [530], imposes a constraint on m_a of $\lesssim 0.1\,\mathrm{eV}$. This constraint results in the parameter space depicted in Figure 7.9, where the dark matter relic abundance is bounded by $\epsilon \gtrsim 3 \times 10^{-8}$. A comprehensive exploration of ALP constraints arising from particle physics experiments is presented in [183].

Fig. 7.9 also includes a comparison between the results from our study and those from the previous 2D simulation for the metastable DW by [8, 507]. We use the dashed blue curve to represent the predicted result [4] of DW contribution to the axion relic abundance

[4]The authors in [8] used a different notation compared to our Eq.(7.2), here we used a conversion: $\Xi \simeq \epsilon\frac{m_a^2}{2f_a^2 N_{\mathrm{DW}}^2}$, where Ξ is the bias parameter that used in Eq.(3.1) in [8].

as presented in [8]. Both studies have technical limitations that restrict their simulations to relatively large values of $\epsilon \gtrsim \mathcal{O}(10^{-3})$, and extrapolations are made to smaller ϵ and different m_a values.

Our estimate of the axion relic abundance at $\epsilon \sim 10^{-4}$ to 10^{-3} roughly agrees with that of [8], but a discrepancy becomes increasingly significant as ϵ decreases. This discrepancy may arise from the differences in the fitting models chosen for DW dynamics, especially the DW decay behavior A_v. This A_v controls the energy density of DW and explains its decaying process, and thus consequently influences the axion production. We adopt the fitting model described by Eq.(7.11), whereas [8] employs a power-law form $A_v \propto t^{1-p}$ with a pressure calibration parameter p. This power-law model was investigated in [523, 9]. They analyze the pressure gap between different vacuums, then conclude that the collapse of DWs occurs when the pressure in the true vacuum overcomes the one in the false vacuum, which takes place at $t_{\rm decay} \sim \sigma_{\rm DW}/\Delta V \propto \frac{\epsilon}{m_a}$, where ΔV represents the difference in potential between the vacua. However, the fitting model described by Eq.(7.11) and Eq.(7.12) in our work provides a much better fit to our simulation results. Those equations are inspired by the mean-field approximation method analysis in [509] as discussed in Sec.7.2.

In addition, a high non-zero axion field initial velocity ($\dot{a} \gg f_a$ at $3H(t) \simeq m_a$) in kinetic misalignment mechanism [257, 115] can delay the DW formation, and thus potentially increases the axion production from the DW network for given ϵ and m_a. Such a hypothesis can relax the BBN and CMB constraints.

7.9 The implication of QCD axion string-wall network

In order to estimate the axion energy density generated by cosmic strings, we employ a conservative estimation outlined in [30]. They simulated the QCD axion cosmic string evolution with a short-lived DW ($N_{\rm DW} = 1$) that formatted at the QCD phase transition. In this section, we consider a string-wall network which can be described by a combination of the string simulation [30, 111, 109] and the DW simulation in this study.

As discussed in Sec.7.3.2, our simulation result can be applied to the DW domination period in the QCD axion string-wall network if the two conditions are met:

(1) The DW dominates the string-wall network ($t > \mu/\sigma_{\rm DW}$, see Eq.(7.8)), then have enough time ($\Delta t \sim 10/m_a$) to enter the scaling region before its decay. This condition erases the string influence on the network and erases the initial field distribution effects after entering the attractive solution.

(2) Because the QCD axion domain wall thickness is time-dependent as Eq.(7.7) until cosmic temperature $T = \Lambda_{QCD}$, and our simulation considered a constant thickness. In order to be consistent, the second condition is that the DW network should be long-lived enough to enter the scaling region after $T = \Lambda_{QCD}$.

We will show these two conditions numerically in later paragraph.

The estimation of string-produced axion energy density in [30, 111, 109] considered two distinct contributions from cosmic strings: (1) the radiation emitted by cosmic strings during the evolutionary phase, and (2) the complete decay of the remaining cosmic strings at the QCD phase transition. The former contribution plays a more significant role in determining the axion relic abundance, as the production of a single lighter axion (as defined

in Eq.(7.7) that $m_a(T) \propto T^{-4}$) requires lower energy levels during earlier times. The latter contribution accounts for approximately 50% of the former [30]. It is worth noting that the string-wall network as we consider involves strings that are attached to walls, and not all of these strings decay at the QCD phase transition: some persist until later times. Therefore, the estimation presented in [30] may predict a higher axion abundance from strings in our specific case.

As shown in Fig. 7.10 that predicts the observed axion DM relic density $\Omega_{\rm a} = (0.12 \pm 0.0012)h^{-2}$ lies in the white area. The BBN and CMB constraints, scaling region, and a comparison to the early simulation work [521] are discussed in Fig. 7.9 and Sec.7.8. Furthermore, We present condition (1) as the red line, and condition (2) has been shown as the green dashed line in Fig. 7.10. The prediction of DW-produced axion relic abundance is given in Eq.(7.32). Due to the QCD axion string contribution, the constraint on m_a is strictly compared to the pure DW scenario.

7.10 Supplementary Data

In this section, we provide supplementary data for the following purposes:

• We present a simulation animation for a no biased potential $\epsilon = 0$ in Fig. 7.11. The right-most and the second-right snapshots clearly present the flattening motion of the DW.

• Axion kinetic energy density spectrum with benchmarks $\epsilon = 0$ and $\epsilon = 0.0012$ are given in Fig. 7.12 and Fig. 7.13, respectively.

• The model fits for ρ_3 with benchmarks $\epsilon = 0$, $\epsilon = 0.0011$, $\epsilon = 0.0013$, and $\epsilon = 0.0014$ are shown in Fig. 7.14, Fig. 7.15, Fig. 7.16, and Fig. 7.17, respectively.

• The model fits for ρ_2 with different benchmarks are shown in Fig. 7.18.

• Fig.7.19 displays the various potential model fit options for the DW velocity $\langle \gamma v \rangle$ when $\epsilon = 0$, which corresponds to fitting the first term in Eq.(7.14). The interpolation results for later times $m_a t \gg 1$ are significantly influenced by different assumptions made about the data, such as when the network enters the scaling regime. In this particular study, we assumed that the network enters the scaling regime when A_v becomes constant, i.e.$m_a t$, as shown in Fig. 7.2.

• We increase the bias parameter ϵ from 0.002 to 0.005 to verify a limitation of ϵ that whether the DW network enters into the scaling region before its decay in our simulation. Fig. 7.20.

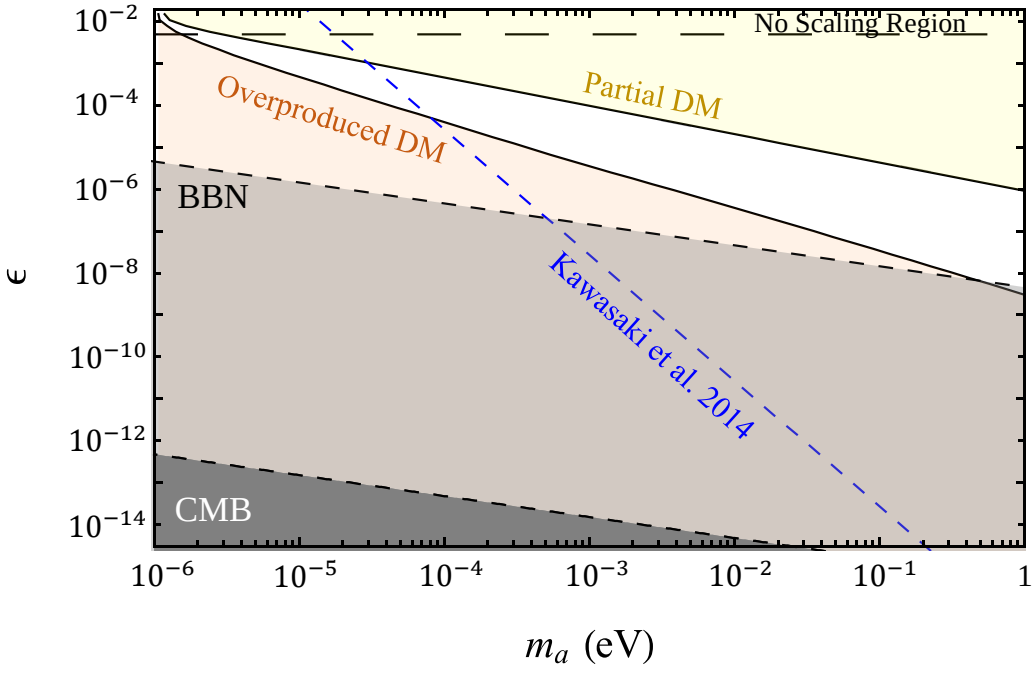

Figure 7.9: Viable parameter region of axion model considering the DW contribution to axion relic density as estimated by this work. The white region indicates that the axion relic abundance is sufficient to account for the observed dark matter as measured by the Planck Observatory ($\Omega_{\rm DM} = (0.12 \pm 0.0012)h^{-2}$) [11], taking into account both the misalignment mechanism and the DW. The width of the white region presents the uncertainty associated with extrapolation, which expands as ϵ decreases. Above the black-dashed horizontal line, the DW has not entered the scaling regime before its decay. The yellow area indicates that the produced axion partially contributes to dark matter, while the orange area indicates an overproduction of dark matter. The blue-dashed line represents the prediction $\Omega_a^{\rm DW} \propto \epsilon^{-1/2}$ from a previous simulation study [8]. The black areas have been excluded by CMB observation as the DWs must decay earlier than the CMB time. The gray region is excluded by BBN constraint $t_{\rm decay} < 0.01$s [28, 29].

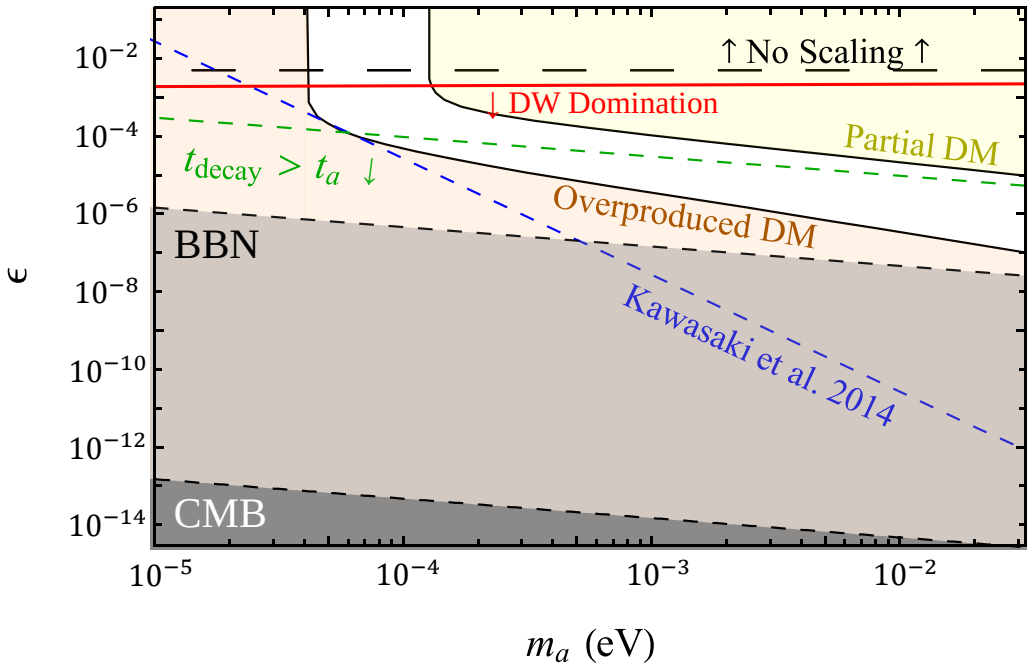

Figure 7.10: Viable parameter region of axion model considering the DW contribution to axion relic density as estimated by this work. The white region indicates that the axion relic abundance is sufficient to account for the observed dark matter as measured by the Planck Observatory ($\Omega_{\rm DW} = (0.12 \pm 0.0012)h^{-2}$) [11], taking into account both the misalignment mechanism, cosmic string [30], and the DW. Above the black-dashed horizontal line, the DW has not entered the scaling regime before its decay. Above the red-solid curve, if a cosmic string exists, string tension dominates the network until the DW decay. Below the green-dashed curve, the thickness of the QCD axion DWs stops contraction before its collapse, as given by Eq.(7.7). The yellow area indicates that the produced axion partially contributes to dark matter, while the orange area indicates an overproduction of dark matter. The blue-dashed line represents the prediction $\Omega_a^{\rm DW} \propto \epsilon^{-1/2}$ from a previous simulation study [8]. The gray areas have been excluded by CMB observation as the DWs must collapse earlier than the CMB time. The gray region is excluded by BBN constraint $t_{\rm decay} < 0.01$s [28, 29].

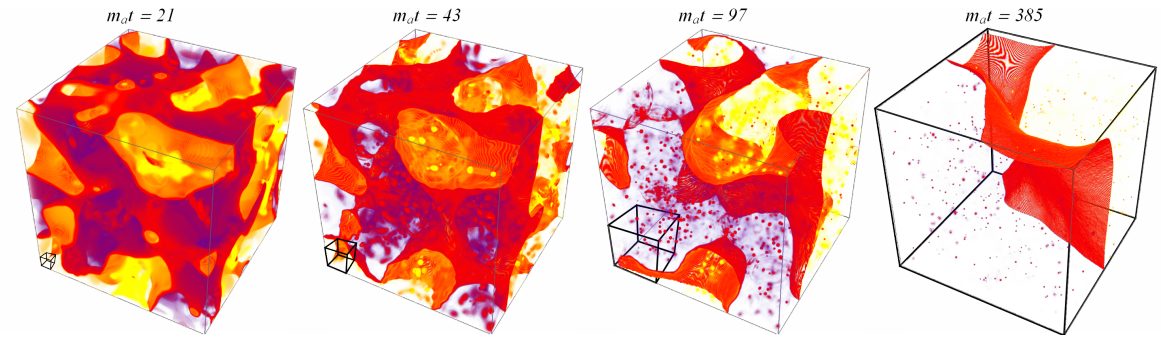

Figure 7.11: Virtualization of lattice simulation with no biased potential from early cosmic time to later (left to right). It is more clear to see the flattening motion of the DW on the right-most and second-right snapshots, in which the DW flats its surface curvature.

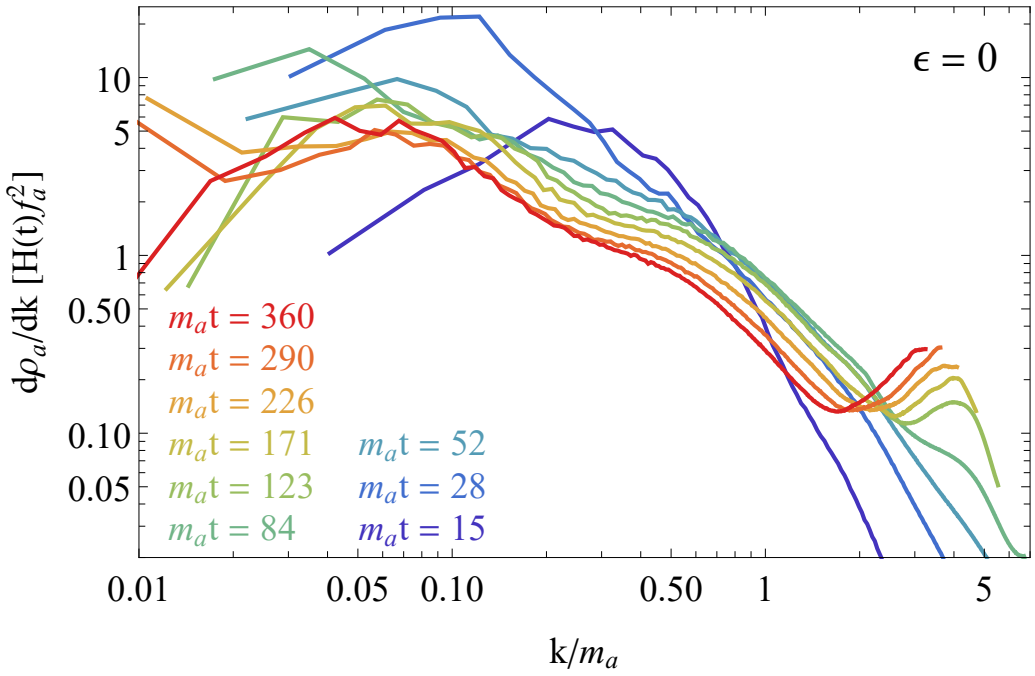

Figure 7.12: Axion energy density spectrum $\partial\rho_a/\partial k$ versus physical momentum k with no biased potential.

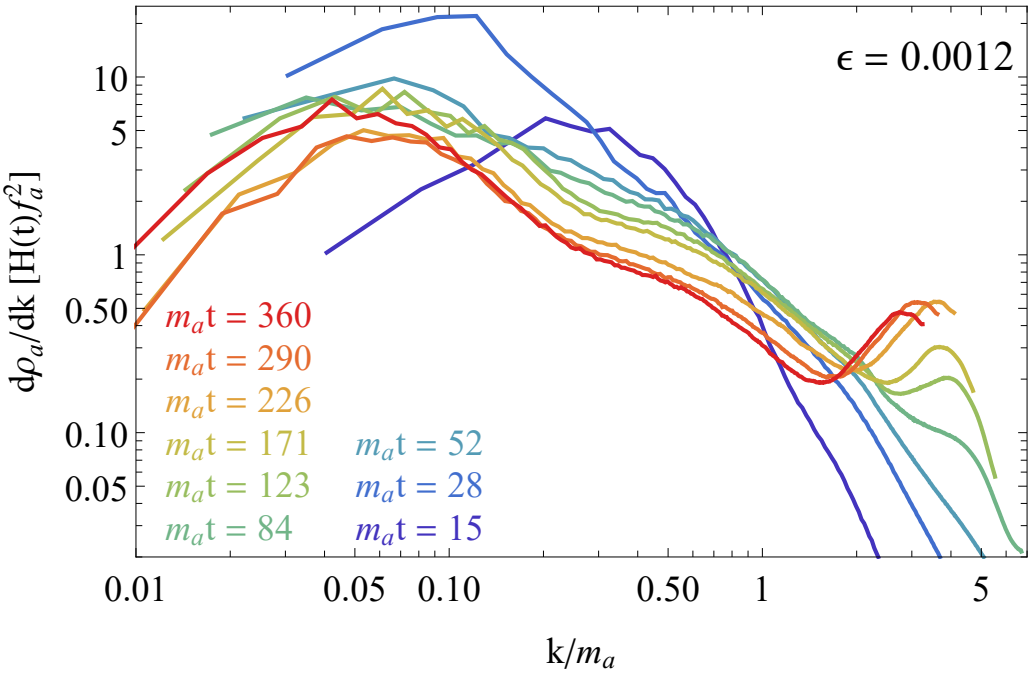

Figure 7.13: Axion energy density spectrum $\partial\rho_a/\partial k$ versus physical momentum k with bias parameter $\epsilon = 0.0012$.

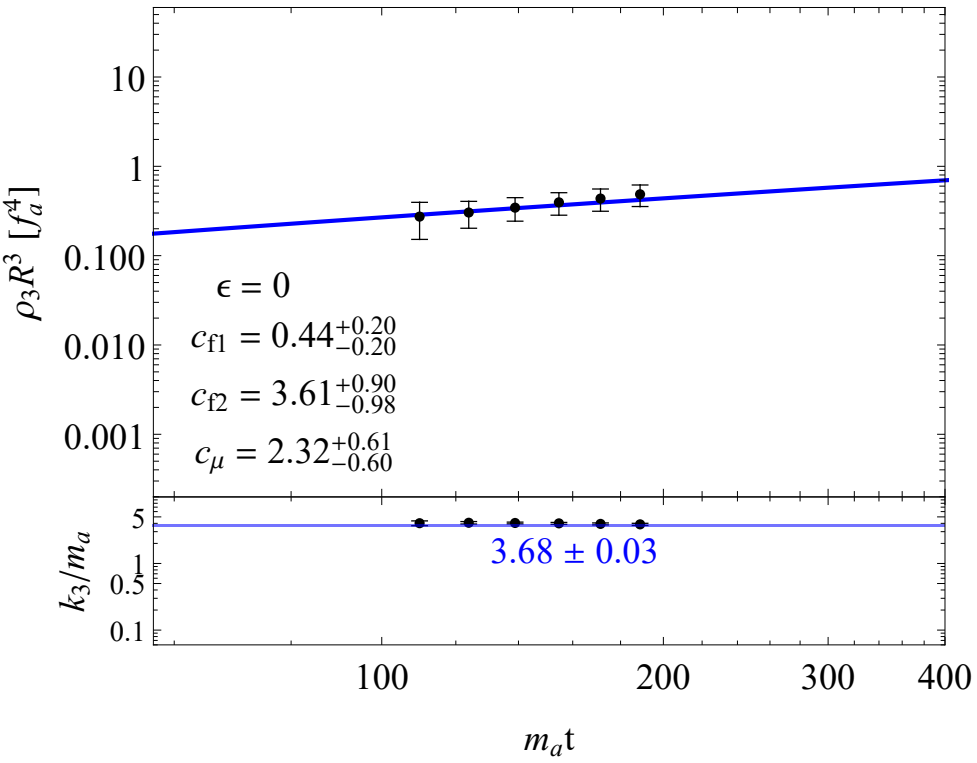

Figure 7.14: The energy density with $\epsilon = 0$ for the third Gaussian fitting function, see Eq.(7.17). The blue curve presents the prediction of energy loss model Eq.(7.27). We excluded the data from the early time $m_a t < 100$ because its amplitude is too small, and the fitting result has big uncertainty. The later time data $m_a t > 200$ has also been excluded because the peak of ρ_3 is out of $k_{\rm N_y}$, and we are thus not able to fit the model nicely.

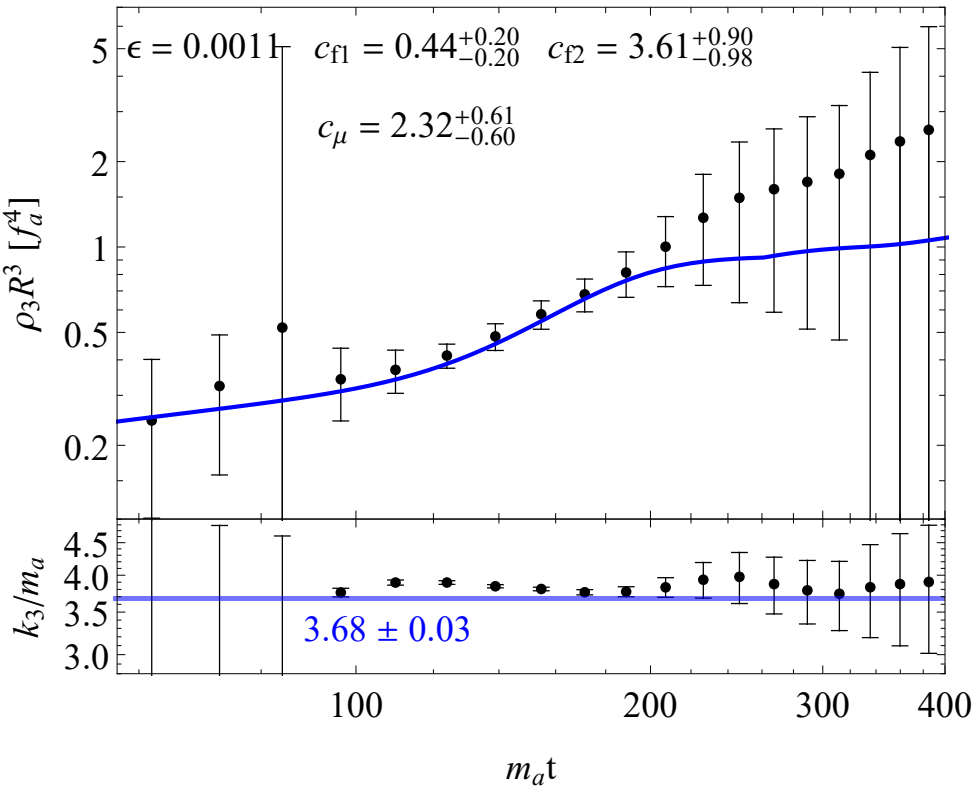

Figure 7.15: The energy density with $\epsilon = 0.0011$ for the third Gaussian fitting function as given in Eq.(7.17). The blue curve presents the prediction of energy loss model Eq.(7.27).

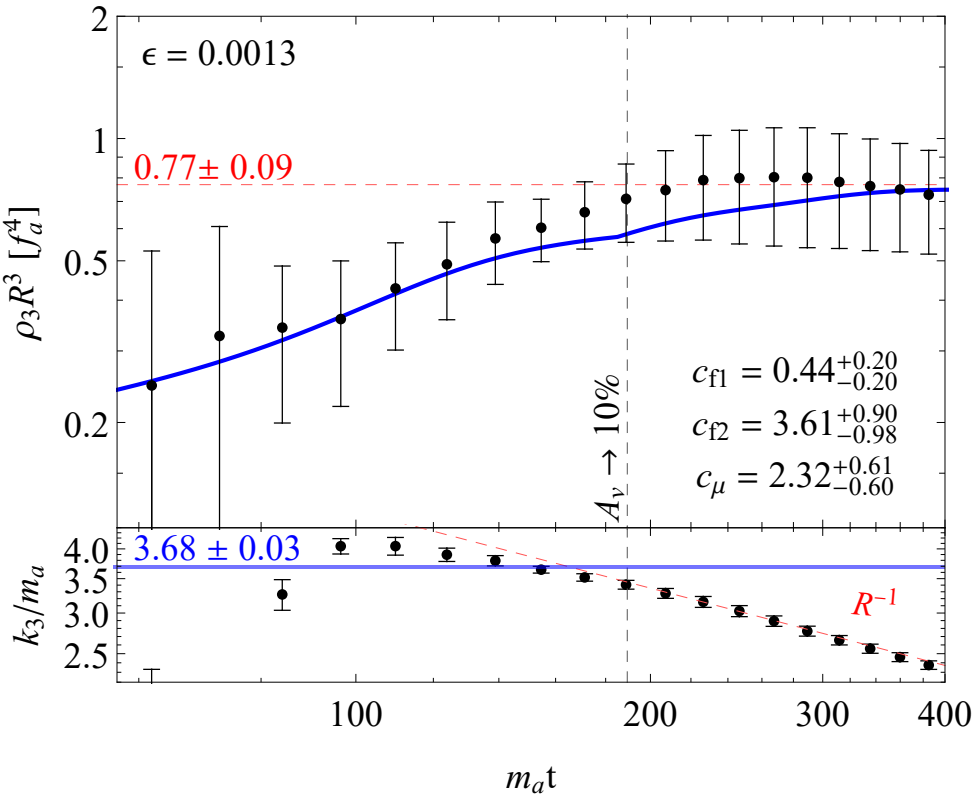

Figure 7.16: The energy density with $\epsilon = 0.0013$ for the third Gaussian fitting function as given in Eq.(7.17). The blue curve presents the prediction of energy loss model Eq.(7.27).

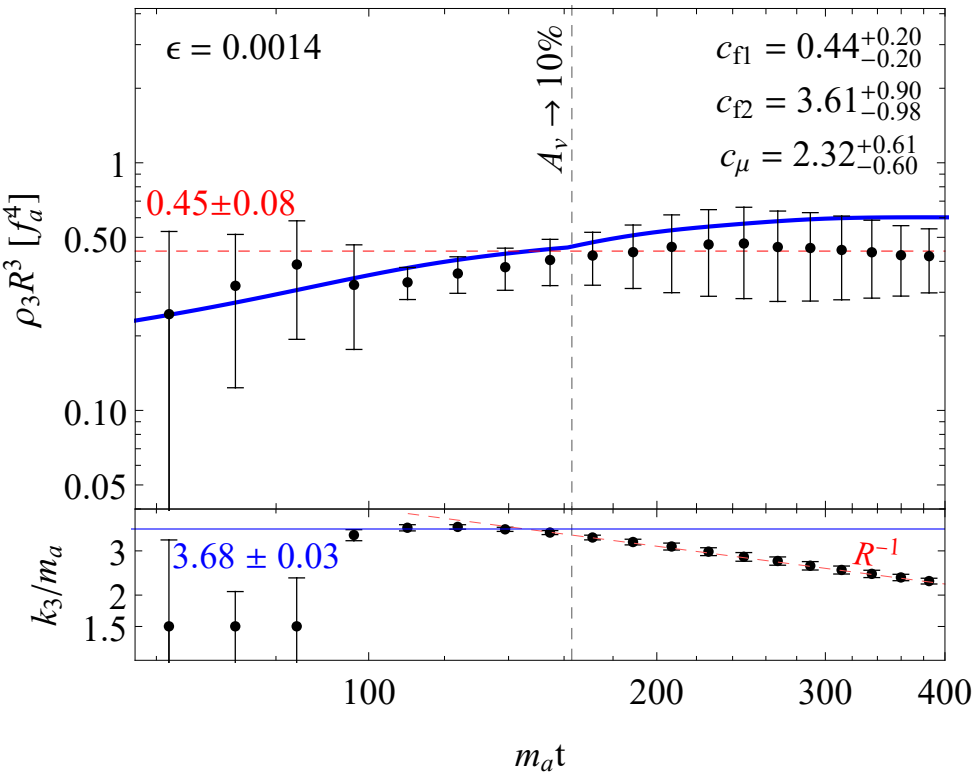

Figure 7.17: The energy density with $\epsilon = 0.0014$ for the third Gaussian fitting function as given in Eq.(7.17). The blue curve presents the prediction of energy loss model Eq.(7.27).

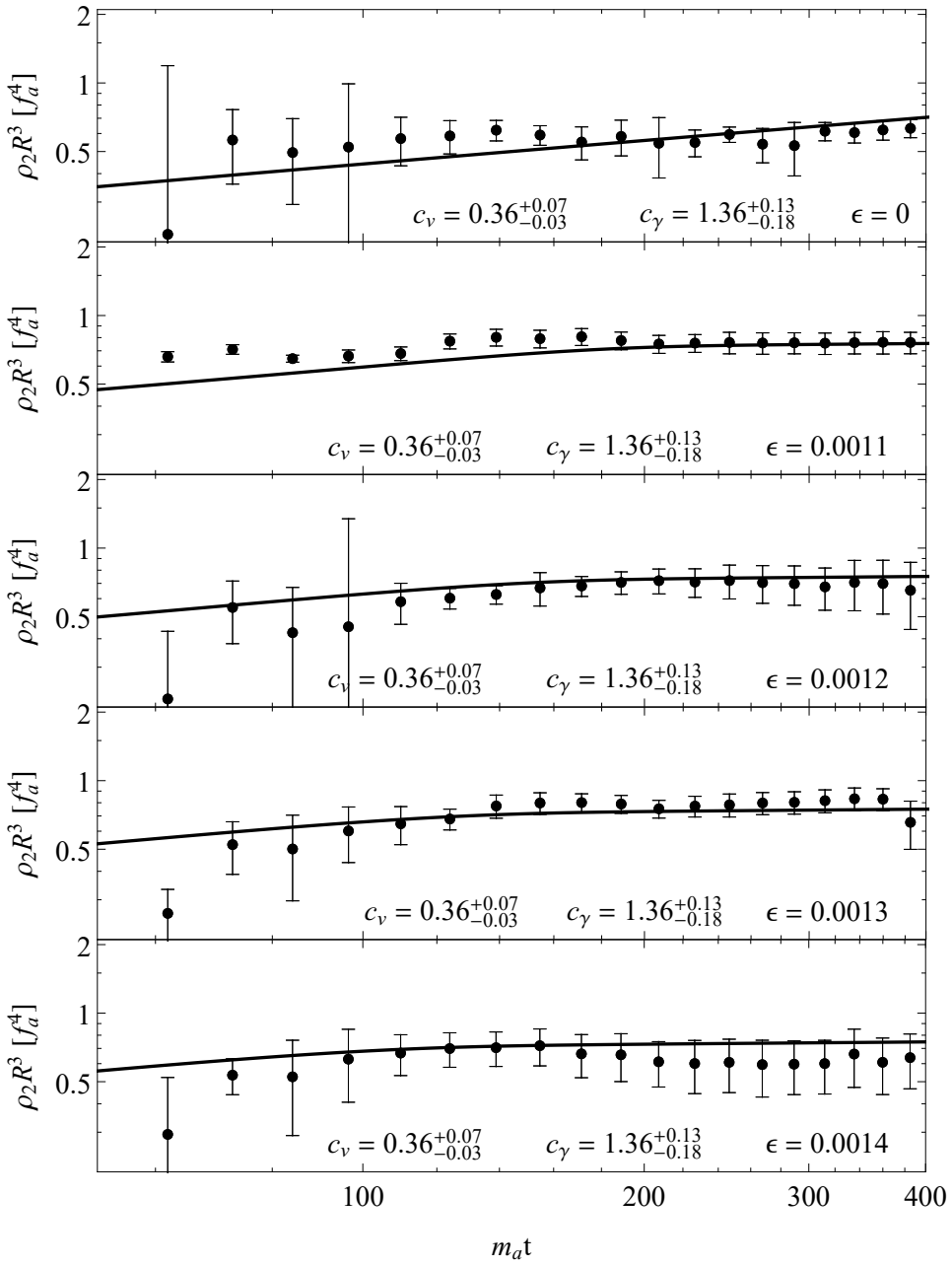

Figure 7.18: The energy density of the second Gaussian fitting function as given in Eq.(7.17) where we provide a variation of ϵ as marked in the figure. The black curve presents the prediction of energy loss model Eq.(7.21).

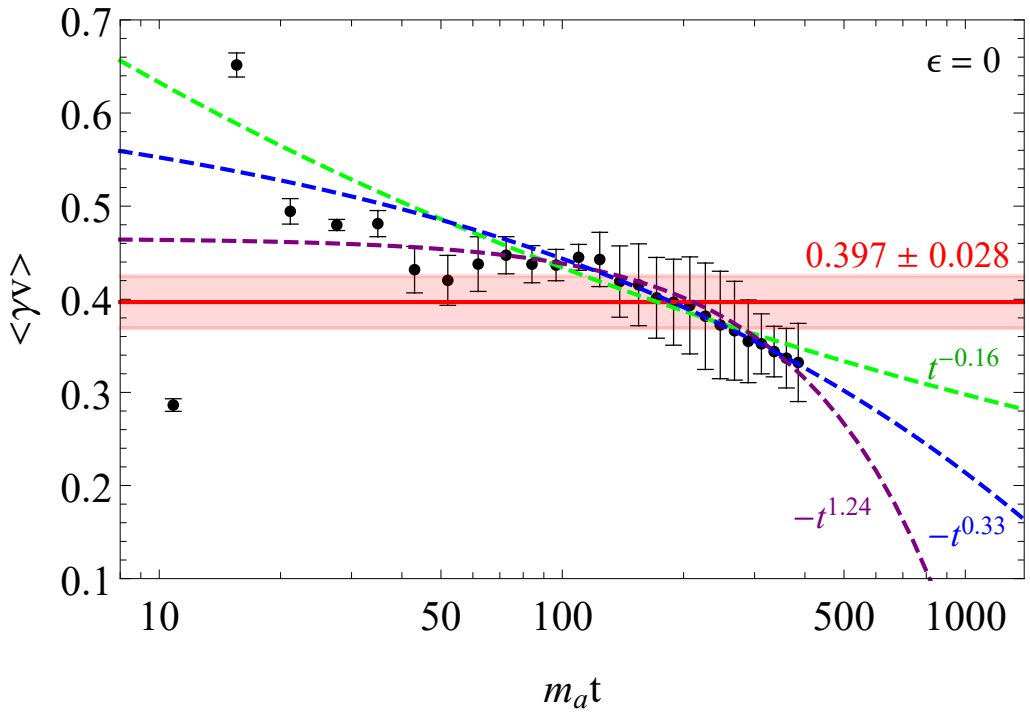

Figure 7.19: Averaged DW velocity with a relativistic factor $< \gamma v >$ versus $m_a t$ with benchmark $\epsilon = 0$. The black error bars are observation data in the simulation. The red area presents a constant fit. The dashed purple curve fits with whole time ranges. The dashed green curve fits with $m_a t \geq 15$ which corresponds to the scaling regime. And the dashed blue curve fits with $m_a t \geq 20$ that excludes the high-velocity data point at $m_a t \sim 15$ where the network just right entered the scaling regime (see Fig. 7.2, the A_v becomes a constant).

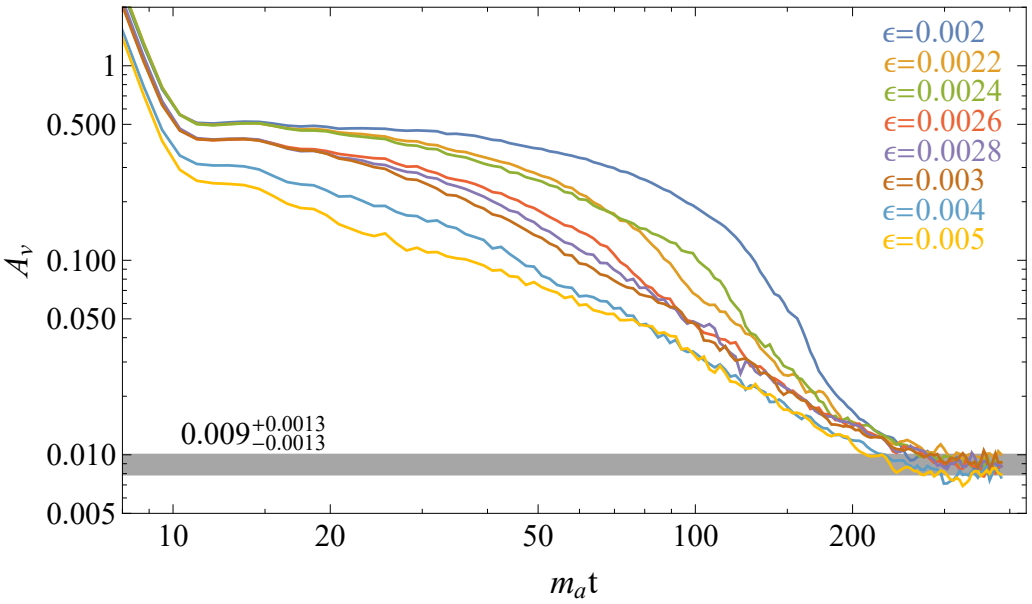

Figure 7.20: Domain wall area parameter to simulation cosmic time with varying bias parameter ϵ. All the benchmarks converge to $A_v = 0.009^{+0.0012}_{-0.0012}$. As the yellow curve, $\epsilon = 0.005$, the DW enters the scaling regime with a short period $11 \lesssim m_a t \lesssim 17$, then decays shortly after. We thus conclude that the DW has enough time to enter the scaling regime for $\epsilon \lesssim 0.005$.

Chapter 8

Conclusions

We propose a new misalignment mechanism where the axion initial velocity is non-zero and demonstrate its impact on axion relic abundance based on systematically classified benchmark cases with a UV model-independent approach. While in many cases Ω_a remains similar to the conventional prediction, it may be significantly enhanced with a large initial velocity $\dot{\theta}_i$ or suppressed when $\dot{\theta}_i$ and θ_i satisfy peculiar relations. As an outcome of this new scenario, new viable parameter space for the QCD axion DM opens up, allowing f_a both much above (in the special suppression region identified in IC-II) *and* much below (with sufficiently large $\dot{\theta}_i$) the conventional $\sim 10^{11}$ GeV scale (detailed relations given in Eqs. 3.10-3.12). Detailed realization of these initial conditions and phenomenological consequences for both QCD axion and general ALPs are worth further investigation (an example is given in Appendix. B). Meanwhile, a caveat for the scenario of post-inflationary PQ-breaking is that, as in conventional misalignment, topological defects' contribution to Ω_a may dominate over the misalignment contribution, and is worth revisiting to advance and complete our

understanding of the axion production mechanism [8, 156, 447, 109, 111]. In this thesis and the following conclusion paragraphs, we will discuss the axion phenomenologies on no only dark matter relic abundance, but also its topological defect evolution.

Global or axion cosmic strings are well-motivated sources of SGWB, and have attracted growing interest in the past few years. In this work, we applied the analytical VOS model in solving the evolution of a global string network over the course of cosmic history and illustrated the procedure of calculating the resultant GW signals with great detail. We demonstrated how our VOS model parameters were calibrated by simulation data which are most reliable for the early time of evolution $N \lesssim 7$, and commented on the compatibility between VOS model prediction and simulation results found by various groups. We found that the deviation from the scaling property as found by some simulation studies can be consistent with conventional VOS model prediction in the early regime of $3 \lesssim N \lesssim 7$, but the simple extrapolation of such a non-scaling behavior to large N or late times contradicts the conventional VOS model. Nevertheless, we also investigated how the SGWB signal would alter if the non-scaling does persist to late times, and suggested a possible revision to the VOS model that addresses this difference which can lead to a GW signal prediction consistent with that given in [15] based on simulation. While it will take time to resolve the discrepancies among different simulation data sets as well between VOS model prediction and some simulation results, our methodology of analysis and related discussions are timely complements to the literature and can be further improved/updated in light of future developments.

Our main results are presented following the standard VOS model and analytical calculation of SGWB by summing over harmonic modes and taking into account the significant effect of Goldstone emissions. In light of the recent findings on the important effect of high k modes for NG strings, we summed over 10^5 modes in all our analyses, leading to updated spectra relative to our earlier results in [156]. We first demonstrated the results assuming standard cosmology, and then considered the possible presence of a non-standard equation of state before BBN, e.g. an EMD or kination, which would lead to a drastic departure from the standard prediction at high f ranges. Since an indefinitely long kination period is subject to strong constraints on additional relic radiation energy density from CMB/BBN data due to a blue-tilted spectrum, we also considered an example where the kination epoch has a finite window of span and is preceded by an early stage of RD. We further demonstrated how the presence of new relativistic degrees of freedom in the early Universe can alter the GW spectrum. We showed the current and projected future sensitivities of GW detectors in detecting global string signals, and found that a detectable signal requires the corresponding spontaneous symmetry breaking scale $\eta > 2 \times 10^{14}\,\mathrm{GeV}$. Different from NG strings, GW amplitude from global strings is very sensitive to η ($\Omega_{\mathrm{GW}} \propto \eta^4$). The frequency-time (temperature) relation, which is the foundation for the method of GW cosmic archaeology, takes a very different form for global strings relative to its NG string counterpart. In particular, there is no $G\mu$ dependence in the f-T relation and the same f band corresponds to a much earlier emission time for global strings, which enables us to test the standard radiation era up to $T \sim 10^8$ GeV. We explained the physics behind the notable differences between SGWB from global strings and from NG strings, where the

strong rate of Goldstone emission and the consequent short lifetime of global string loops play an important role. As we have discussed in detail in the previous sections, the global string and its decay productions leave an abundant physics in dark matter and gravitational waves.

We further considered how the GW signal based on our baseline assumptions and model choices could vary with alternative possibilities. We studied the effects of different loop distribution patterns, the uncertainty in the radiation parameters (Γ, Γ_a), as well as a persisting non-scaling regime during the string network evolution. For example, by adopting the suggested non-scaling solution with $\xi \propto N$ while assuming $\bar{c}\bar{v}_\infty \propto N^{-1/2}$, we found that the predicted GW frequency spectrum (including the $\log^4$ relation) can be consistent with the simulation-based finding in [15]. We also briefly discussed the prospect of distinguishing a SGWB sourced by global strings from other cosmogenic sources or astrophysical background.

It is worth noting the importance of studying GWs from global/axion strings in light of its connection to axion physics (for QCD axion or general axion-like particles (ALPs)). Axion strings are indispensable companions of axion particles when the $U(1)_{\rm PQ}$ symmetry breaking occurs after inflation. The detection of axion particles is being actively pursued, but the prospect is model-dependent due to the uncertainty of the interaction between the SM and the axions. The prospect would be particularly dim in the case of the hidden axion scenario (e.g. motivated by the string axiverse [531]) where non-gravitational coupling is absent. Thus, the universal GW signal from axion strings could be the smoking-gun for the underlying axion physics. While our current work focused on the simpler case of

pure global strings with massless Goldstones, the methodology and results are relevant for the massive axion case. The GW spectrum from axion topological defects at high frequencies is expected to be dominated by cosmic strings, while at a low frequency corresponding to a QCD(-like) phase transition when the domain wall forms, the signal is expected to change form and die down. The recent work based on extrapolating simulation results to late times shows such a pattern [15]. It is intriguing to apply our analytical approaches to the more complex axion scenario including domain wall contributions, which will be pursued in future work.

We proposed that SGWB originating from the cosmic string network can be used to test the Hubble tension solution EDE. EDE behaves as dark energy in the early universe, then begins to dilute at the critical scaling factor $a_c \sim 10^{-4}$ with total energy density fraction $f_{\rm EDE} \gtrsim 1\%$. It influences cosmic string SGWB by accelerating and decelerating universe expansion rate $\dot{a}(t)$ due to a dark energy-like equation of state $\omega_\phi = -1$ and diluting faster than or equal to radiation-like component $\omega_\phi \geq 1/3$, respectively. The decelerated universe expansion rate locally increases cosmic string GW frequency spectra with magnitude 0.1% to 1% in the frequency range 10^{-5} to 10^{-3} Hz which is within LISA sensitivity. And on the other side, the acceleration reduces spectra with magnitude $\sim 5\%$ in the lower frequency region $f \sim 10^{-9}$ Hz, within the SKA search region. We also showed that EDE-influenced signals were stronger than LISA and SKA experimental noise background, and hence detectable. Such spectral shapes are distinguishable from other SGWBs sourced by cosmological or astrophysical objects. Thus, GW detection provides a possibility to probe EDE.

We demonstrated that in the framework of KMM there is a large parameter space of axion dark matter with $10^{-22}\text{eV} \lesssim m_a \lesssim 10^{-19}\text{eV}$ that can address the JWST excess while being compatible with all existing constraints. The delayed onset of the axion field oscillation in KMM allows for efficient axion field fragmentation at subhorizon scales. The fragmented axion field collapses into a large population of massive ACs, which leads to more massive galaxies at high redshift, and thus can potentially address the excess observed by JWST. Upcoming experiments can provide complementary probes for the ALP parameter range favored by the JWST excess. Near-future Lyman-α forest surveys such as Weave-QSO [532] or DESI [533, 534] will extend the scales on which the MPS can be measured by a further factor of $2-3$. Future surveys of strong lensing caustics could directly detect the predicted signature from small halos [535]. We also identified sizable gravitational scattering in our model parameter space, which enriches small-scale structure formation in our model that is worth further investigation [441, 442]. In addition to the complementary astrophysical probes related to structure formation, we demonstrated that the JWST excess favored parameter region can be probed by existing or planned axion search avenues, e.g. heterodyne, comagnetometer and storage ring experiments, assuming certain patterns of ALP-SM couplings (i.e. fixed $C_{a\gamma}$, C_{aN}). This study identifies new avenues for probing axion DM, and would stand as a worthwhile addition to the literature even if the current JWST excess resolves after further investigation.

We present an updated investigation into the dynamics and evolution of long-lived, metastable axion DWs with a DW number of $N_{\rm DW} = 2$ as a benchmark example. The study incorporates 3D lattice simulations and a semi-analytical approach based on the VOS model. Our analysis includes a detailed examination of the axion kinetic energy spectrum, based on which and monitoring the simulation snapshot, we infer the mechanisms of axion production sourced by the DWs and the corresponding energy loss mechanisms of the DWs.

In particular, based on the features in the axion energy spectrum obtained from our simulation (see Sec7.4.2), we identified two distinct components or kinetic energy regions of the axions: the shorter wave-length axion clouds with resonance around $k \sim 3.68\, m_a$, with larger impact on the small-scale region in the spectrum; and the longer wave-length axion ripples with $k \leq m_a$. These two features are sourced by different DW dynamics. The axion clouds primarily arise from the flattening motion of the horizon-scale DWs, which motion annihilated the fluctuations on the DW surface and then heats the background axion fields. On the other hand, the wave-like axion ripples are mostly generated by the collapse of the horizon-sized compact DWs which are formed by the self-chopping process of DWs.

Based on these identified features and the corresponding sources, we derive equations governing the evolution of the DWs, building upon the VOS model while extending it to incorporate the decay phase of the DWs. The DW equation is coupled to the axion evolution equations by energy conservation. By solving these equations, we determine the present-day relic abundance of axions. While our findings align with some earlier literature, notable differences arise and are thoroughly discussed. Particularly, our prediction

for $\Omega_a(m_a,\ \epsilon)$ takes a different form compared to the results found in [8, 507], as shown in Eq.(7.32) and Fig. 7.9. This discrepancy, which is caused by the mathematical fitting model for DW area evolution A_v, potentially has significant implications for axion dark matter physics and complementary probes. We predict more relic axion energy from the DW decay process on the $\epsilon \lesssim 10^{-6}$ range.

While we directly simulated the axion model using the potential described in Eq.(7.2), we have demonstrated that the results can be applied to ALP models and the QCD axion string-wall network, with a bias parameter $\epsilon \lesssim 10^{-3} - 10^{-4}$ that ensure DW thickness is a constant before DWs decay away, and can be generalized to more general ALPs, see discussion in Sec.7.3.2 for the application conditions, and Sec.7.8 and Appendix. 7.9 for a numerical result of the application for ALP DW and QCD axion string-wall networks, respectively.

Notably, our study improves upon existing literature by including the biased term in the 3D field simulation without relying on approximations such as the PRS algorithm. To ensure efficient simulation with this more accurate treatment, we focus on the benchmark case of $N_{\rm DW} = 2$ and decouple the radial mode, which is a reasonable assumption for the relevant time range of DW formation. It is worth exploring further by considering $N_{\rm DW} > 2$ and simulating the complex scalar field. The dynamics of DWs identified in this study can provide new insights into axion-like DWs and other types of DWs, such as those arising from GUT models. The updated results on axion DW dynamics presented here also have implications for astrophysical observables related to axion physics, including gravitational wave signals from axion DWs and the formation of axion minihalos as relic overdense energy.

8.1 Acknowledgments

Chapter 3 has been published in [257], Chapter 4 has been published in [321], and Chapter 5 has been published in [536].

Bibliography

[1] Jérémie Quevillon and Christopher Smith. Axions are blind to anomalies. *Eur. Phys. J. C*, 79(10):822, 2019.

[2] Giovanni Grilli di Cortona, Edward Hardy, Javier Pardo Vega, and Giovanni Villadoro. The qcd axion, precisely. *JHEP*, 1601:034, 2016. [arXiv:1511.02867 [hep-ph]].

[3] J. Moody and F. Wilczek. Phys. rev. d. 30:130, 1984.

[4] Masahiro Kawasaki and Kazunori Nakayama. Axions: Theory and cosmological role. *Ann.Rev.Nucl.Part.Sci.*, 63:69–95, 2013. [arXiv:1301.1123 [hep-ph]].

[5] David J. E. Marsh. Axion Cosmology. *Phys. Rept.*, 643:1–79, 2016.

[6] Edward W. Kolb and Michael S. Turner. *The Early Universe*, volume 69. 1990.

[7] Peter Graf and Frank Daniel Steffen. Thermal axion production in the primordial quark-gluon plasma. *Phys. Rev. D*, 83:075011, 2011.

[8] Masahiro Kawasaki, Ken'ichi Saikawa, and Toyokazu Sekiguchi. Axion dark matter from topological defects. *Phys. Rev.*, D91(6):065014, 2015.

[9] Takashi Hiramatsu, Masahiro Kawasaki, and Ken'ichi Saikawa. Evolution of String-Wall Networks and Axionic Domain Wall Problem. *JCAP*, 08:030, 2011.

[10] Takashi Hiramatsu, Masahiro Kawasaki, Ken'ichi Saikawa, and Toyokazu Sekiguchi. Axion cosmology with long-lived domain walls. *JCAP*, 1301:001, 2013. [arXiv:1207.3166 [hep-ph]].

[11] N. Aghanim et al. Planck 2018 results. VI. Cosmological parameters. 7 2018.

[12] Sophie Henrot-Versille et al. Improved constraint on the primordial gravitational-wave density using recent cosmological data and its impact on cosmic string models. *Class. Quant. Grav.*, 32(4):045003, 2015.

[13] Yanou Cui, Marek Lewicki, David E. Morrissey, and James D. Wells. Probing the pre-BBN universe with gravitational waves from cosmic strings. *JHEP*, 01:081, 2019.

[14] Yanou Cui, Marek Lewicki, David E. Morrissey, and James D. Wells. Cosmic Archaeology with Gravitational Waves from Cosmic Strings. *Phys. Rev.*, D97(12):123505, 2018.

[15] Marco Gorghetto, Edward Hardy, and Horia Nicolaescu. Observing Invisible Axions with Gravitational Waves. 1 2021.

[16] Vivian Poulin, Tristan L. Smith, Tanvi Karwal, and Marc Kamionkowski. Early Dark Energy Can Resolve The Hubble Tension. *Phys. Rev. Lett.*, 122(22):221301, 2019.

[17] Yanou Cui, Marek Lewicki, David E. Morrissey, and James D. Wells. Probing the pre-BBN universe with gravitational waves from cosmic strings. *JHEP*, 01:081, 2019.

[18] Solène Chabanier, Marius Millea, and Nathalie Palanque-Delabrouille. Matter power spectrum: from Lyα forest to CMB scales. *Mon. Not. Roy. Astron. Soc.*, 489(2):2247–2253, 2019.

[19] Nashwan Sabti, Julian B. Muñoz, and Diego Blas. New Roads to the Small-scale Universe: Measurements of the Clustering of Matter with the High-redshift UV Galaxy Luminosity Function. *Astrophys. J. Lett.*, 928(2):L20, 2022.

[20] Jens Chluba and Daniel Grin. CMB spectral distortions from small-scale isocurvature fluctuations. *Mon. Not. Roy. Astron. Soc.*, 434:1619–1635, 2013.

[21] Vid Iršič, Huangyu Xiao, and Matthew McQuinn. Early structure formation constraints on the ultralight axion in the postinflation scenario. *Phys. Rev. D*, 101(12):123518, 2020.

[22] Keir K. Rogers and Hiranya V. Peiris. Strong Bound on Canonical Ultralight Axion Dark Matter from the Lyman-Alpha Forest. *Phys. Rev. Lett.*, 126(7):071302, 2021.

[23] Yuichi Harikane, Masami Ouchi, Masamune Oguri, Yoshiaki Ono, Kimihiko Nakajima, Yuki Isobe, Hiroya Umeda, Ken Mawatari, and Yechi Zhang. A Comprehensive Study of Galaxies at z 9-16 Found in the Early JWST Data: Ultraviolet Luminosity Functions and Cosmic Star Formation History at the Pre-reionization Epoch. , 265(1):5, March 2023.

[24] Asimina Arvanitaki, Masha Baryakhtar, and Xinlu Huang. Discovering the QCD Axion with Black Holes and Gravitational Waves. *Phys. Rev. D*, 91(8):084011, 2015.

[25] Matthew J. Stott and David J. E. Marsh. Black hole spin constraints on the mass spectrum and number of axionlike fields. *Phys. Rev. D*, 98(8):083006, 2018.

[26] Caner Ünal, Fabio Pacucci, and Abraham Loeb. Properties of ultralight bosons from heavy quasar spins via superradiance. *JCAP*, 05:007, 2021.

[27] Derek F. Jackson Kimball and Karl van Bibber, editors. *The Search for Ultralight Bosonic Dark Matter*. Springer, 2022.

[28] Masahiro Kawasaki, Kazunori Kohri, and Takeo Moroi. Hadronic decay of late - decaying particles and Big-Bang Nucleosynthesis. *Phys. Lett. B*, 625:7–12, 2005.

[29] Masahiro Kawasaki, Kazunori Kohri, and Takeo Moroi. Big-Bang nucleosynthesis and hadronic decay of long-lived massive particles. *Phys. Rev. D*, 71:083502, 2005.

[30] Malte Buschmann, Joshua W. Foster, Anson Hook, Adam Peterson, Don E. Willcox, Weiqun Zhang, and Benjamin R. Safdi. Dark matter from axion strings with adaptive mesh refinement. *Nature Commun.*, 13(1):1049, 2022.

[31] C. J. A. P. Martins. Scaling properties of cosmological axion strings. *Phys. Lett.*, B788:147–151, 2019.

[32] Jihn E. Kim. Dark energy, qcd axion, and trans-planckian-inflaton decay constant. *Universe*, 3(4):68, 2017.

[33] R.D. Peccei. The strong cp problem and axions. *Lect.Notes Phys.*, 741:3–17, 2008. [arXiv:hep-ph/0607268].

[34] Weinberg. Qft volumeii chpater 19.7 and 19.10. Year.

[35] Matthew Schwartz. Quantum Field Theory and the Standard Model, Chapter 28.2. 2014.

[36] Weinberg. Phys.rev. d**11** (1975) 3583-3593. Year.

[37] G. 't Hooft. Phys. rev. lett. 37, 8 (1976); phys. rev. d14, 3432 (1976). Year.

[38] Jihn E. Kim and Gianpaolo Carosi. Axions and the strong cp problem. *Rev.Mod.Phys.*, 82:557–602, 2010. [arXiv:0807.3125 [hep-ph]].

[39] J. E. Kim. Phys. rept. 150:1, 1987.

[40] Kazuo Fujikama. Path integral for gauge theories with fermions. *PhysRevD*, 21:2848, 1980.

[41] M. Schwartz. Chapter 30.3 of qft. Year.

[42] Mikio Nakahara. *Geometry, Topology and Physics.*

[43] Matthew Schwartz. Quantum Field Theory and the Standard Model, Chapter 30.5.2. 2014.

[44] David B. Kaplan. Lectures on effective field theory.

[45] David B. Kaplan. Chiral Symmetry and Lattice Fermions. In *Les Houches Summer School: Session 93: Modern perspectives in lattice QCD: Quantum field theory and high performance computing*, pages 223–272, 12 2009.

[46] Siavash Golkar and Savdeep Sethi. Global Anomalies and Effective Field Theory. *JHEP*, 05:105, 2016.

[47] Hai-Yang Cheng. The Strong CP Problem Revisited. *Phys. Rept.*, 158:1, 1988.

[48] Kim. Other variants: composite axion, heavy axion, axiflavon, etc. *PRD 31 (1985)*, Year.

[49] J. C. Criado and M. Pérez-Victoria. Field redefinitions in effective theories at higher orders. *JHEP*, 03:038, 2019.

[50] S. Kamefuchi, L. O'Raifeartaigh, and Abdus Salam. Change of variables and equivalence theorems in quantum field theories. *Nucl. Phys.*, 28:529–549, 1961.

[51] G. 't Hooft. Phys. rev. d 14, 3432. 1976.

[52] S. Scherer and M. R. Schindler. A chiral perturbation theory primer. [arXiv:hep-ph/0505265].

[53] R.J. Crewther, P. Di Vecchia, G. Veneziano, and Edward Witten. Chiral estimate of the electric dipole moment of the neutron in quantum chromodynamics. *Phys.Lett.*, 88B:123, 1979. Erratum: Phys.Lett. 91B (1980) 487.

[54] C. A. Baker. Phys. rev. lett. 97:131801, Year.

[55] X.-G. He. Int. j. mod. phys. a. 23:3282, 2008.

[56] A. E. Nelson. Phys. lett. b. 136:387, 1984.

[57] D. Chang and W.-Y. Keung. Phys. rev. d. 70:051901, Year.

[58] Gustavo Castelo Branco, Luis Lavoura, and Joao Paulo Silva. Cp violation. Year.

[59] R. D. Peccei and H. R. Quinn. Phys. rev. lett. 38:1440, 1977.

[60] A. Vilenkin and E. P. S. Shellard. cosmic strings and other topological defects. Year.

[61] M. Srednicki. Nucl. phys. b. 260:689, 1985.

[62] Zhitnitsky. Sjnp 31 (1980). Year. Dine, Fischler, Srednicki PLB 104 (1981).

[63] Kim. Prl 43 (1979). Year.

[64] P. Di Vecchia and G. Veneziano. Chiral dynamics in the large n limit. *Nucl. Phys. B*, 171:253, 1980.

[65] S. Weinberg. A new light boson? *Phys. Rev. Lett.*, 40:223, 1978.

[66] Jr. C. G. Callan, R. Dashen, and D. J. Gross. Phys. rev. d. 17:2717, 1978.

[67] Pierre Sikivie. Axion Cosmology. *Lect. Notes Phys.*, 741:19–50, 2008.

[68] O. Wantz and E. P. S. Shellard. Phys. rev. d. 82:123508, 2010. [arXiv:0910.1066 [astro-ph.CO]].

[69] Alberto Diez-Tejedor and David J. E. Marsh. Cosmological production of ultralight dark matter axions. 2017.

[70] John Preskill, Mark B. Wise, and Frank Wilczek. Cosmology of the Invisible Axion. *Phys. Lett. B*, 120:127–132, 1983.

[71] L. F. Abbott and P. Sikivie. A Cosmological Bound on the Invisible Axion. *Phys. Lett. B*, 120:133–136, 1983.

[72] Michael Dine and Willy Fischler. The Not So Harmless Axion. *Phys. Lett. B*, 120:137–141, 1983.

[73] Daniel Baumann. cosmology lecture notes. 2014.

[74] Alan H. Guth, Mark P. Hertzberg, and C. Prescod-Weinstein. Do Dark Matter Axions Form a Condensate with Long-Range Correlation? *Phys. Rev. D*, 92(10):103513, 2015.

[75] Bohua Li, Paul R. Shapiro, and Tanja Rindler-Daller. Bose-Einstein-condensed scalar field dark matter and the gravitational wave background from inflation: new cosmological constraints and its detectability by LIGO. *Phys. Rev. D*, 96(6):063505, 2017.

[76] M. S. Turner. Phys. rev. d. 33:889, 1986.

[77] Kyu Jung Bae, Ji-Haeng Huh, and Jihn E. Kim. Update of axion CDM energy. *JCAP*, 09:005, 2008.

[78] Maria Beltran, Juan Garcia-Bellido, and Julien Lesgourgues. Isocurvature bounds on axions revisited. *Phys. Rev. D*, 75:103507, 2007.

[79] Eugenio Masso, Valentin Passemar, and Alejandro Redondo. Constraining the couplings of axion-like particles to photons with linearly polarized light. *Phys. Rev. Lett.*, 118:071802, 2017. [arXiv:1605.00644 [hep-ph]].

[80] Leesa M. Fleury and Guy D. Moore. Axion String Dynamics I: 2+1D. *JCAP*, 05:005, 2016.

[81] S. Borsanyi, M. Dierigl, Z. Fodor, S. D. Katz, S. W. Mages, D. Nogradi, J. Redondo, A. Ringwald, and K. K. Szabo. Axion cosmology, lattice QCD and the dilute instanton gas. *Phys. Lett. B*, 752:175–181, 2016.

[82] M. C. Huang and P. Sikivie. The Structure of Axionic Domain Walls. *Phys. Rev. D*, 32:1560, 1985.

[83] A. Vilenkin and E. P. S. Shellard. *Cosmic Strings and Other Topological Defects*. Cambridge University Press, 7 2000.

[84] P. Sikivie. Of Axions, Domain Walls and the Early Universe. *Phys. Rev. Lett.*, 48:1156–1159, 1982.

[85] Sebastian E. Larsson, Subir Sarkar, and Peter L. White. Evading the cosmological domain wall problem. *Phys. Rev. D*, 55:5129–5135, 1997.

[86] C. J. A. P. Martins. *Defect Evolution in Cosmology and Condensed Matter*. ISBN:978-3-319-44551-9.

[87] A. Vilenkin and E. P. S. Shellard. *Cosmic Strings and other topological Defects*. ISBN:0-521-65476-9.

[88] C.J.A.P. Martins, I.Yu. Rybak, A. Avgoustidis, and E.P.S. Shellard. Extending the velocity-dependent one-scale model for domain walls. *Phys.Rev. D*, 93(4):043534, 2016.

[89] L. Sousa and P. P. Avelino. The cosmological evolution of p-brane networks. *Phys. Rev. D*, 84:063502, 2011.

[90] A. Vilenkin and A. E. Everett. Cosmic strings and domain walls in models with goldstone and pseudo-goldstone bosons. *Physical Review Letters*, 48(26):1867, 1982.

[91] Alexander Vilenkin. Gravitational field of vacuum domain walls and strings. *Physical Review D*, 23(4):852, 1981.

[92] Alexander Vilenkin. Gravitational field of vacuum domain walls. *Physics Letters B*, 133(3-4):177–179, 1983.

[93] W. Rindler. Am. j. phys. 34:1174, 1966.

[94] A.H. Taub. Ann. math. 53:472, 1951.

[95] J. Ipser and P. Sikivie. Phys. rev. d. 30:712, 1984.

[96] Heling Deng, Jaume Garriga, and Alexander Vilenkin. Primordial black hole and wormhole formation by domain walls. *JCAP*, 1704:050, 2017.

[97] Hideo Kodama, Hideki Ishihara, and Hoshihisa Fujiwara. Does a domain wall emit gravitational waves? general relativistic perturbative treatment. *Phys.Rev. D*, 50:7292–7303, 1994.

[98] R. D. Peccei and Helen R. Quinn. CP Conservation in the Presence of Instantons. *Phys. Rev. Lett.*, 38:1440–1443, 1977. [,328(1977)].

[99] R. D. Peccei and Helen R. Quinn. Constraints Imposed by CP Conservation in the Presence of Instantons. *Phys. Rev.*, D16:1791–1797, 1977.

[100] Frank Wilczek. Problem of Strong P and T Invariance in the Presence of Instantons. *Phys. Rev. Lett.*, 40:279–282, 1978.

[101] Steven Weinberg. A New Light Boson? *Phys. Rev. Lett.*, 40:223–226, 1978.

[102] Igor G. Irastorza and Javier Redondo. New experimental approaches in the search for axion-like particles. *Prog. Part. Nucl. Phys.*, 102:89–159, 2018.

[103] P. Sikivie. Of Axions, Domain Walls and the Early Universe. *Phys. Rev. Lett.*, 48:1156–1159, 1982.

[104] Alexander Vilenkin. Cosmic Strings and Domain Walls. *Phys. Rept.*, 121:263–315, 1985.

[105] Richard Lynn Davis. Cosmic Axions from Cosmic Strings. *Phys. Lett.*, B180:225–230, 1986.

[106] Graham R. Vincent, Mark Hindmarsh, and Mairi Sakellariadou. Scaling and small scale structure in cosmic string networks. *Phys. Rev.*, D56:637–646, 1997.

[107] Alexander Vilenkin and Tanmay Vachaspati. Radiation of Goldstone Bosons From Cosmic Strings. *Phys. Rev.*, D35:1138, 1987.

[108] Vincent B. Klaer and Guy D. Moore. How to simulate global cosmic strings with large string tension. *JCAP*, 1710:043, 2017.

[109] Marco Gorghetto, Edward Hardy, and Giovanni Villadoro. Axions from Strings: the Attractive Solution. *JHEP*, 07:151, 2018.

[110] Masahiro Kawasaki, Toyokazu Sekiguchi, Masahide Yamaguchi, and Jun'ichi Yokoyama. Long-term dynamics of cosmological axion strings. *PTEP*, 2018(9):091E01, 2018.

[111] Malte Buschmann, Joshua W. Foster, and Benjamin R. Safdi. Early-Universe Simulations of the Cosmological Axion. 2019.

[112] Mark Hindmarsh, Joanes Lizarraga, Asier Lopez-Eiguren, and Jon Urrestilla. The scaling density of axion strings. 2019.

[113] C. J. A. P. Martins. Scaling properties of cosmological axion strings. *Phys. Lett.*, B788:147–151, 2019.

[114] Anson Hook. TASI Lectures on the Strong CP Problem and Axions. *PoS*, TASI2018:004, 2019.

[115] Raymond T. Co, Lawrence J. Hall, and Keisuke Harigaya. Kinetic Misalignment Mechanism. 2019.

[116] Ian Affleck and Michael Dine. A New Mechanism for Baryogenesis. *Nucl. Phys.*, B249:361–380, 1985.

[117] Michael Dine, Lisa Randall, and Scott D. Thomas. Supersymmetry breaking in the early universe. *Phys. Rev. Lett.*, 75:398–401, 1995.

[118] Michael Dine, Lisa Randall, and Scott D. Thomas. Baryogenesis from flat directions of the supersymmetric standard model. *Nucl. Phys.*, B458:291–326, 1996.

[119] Marc Kamionkowski and John March-Russell. Planck scale physics and the Peccei-Quinn mechanism. *Phys. Lett.*, B282:137–141, 1992.

[120] Peter W. Graham, David E. Kaplan, and Surjeet Rajendran. Cosmological Relaxation of the Electroweak Scale. *Phys. Rev. Lett.*, 115(22):221801, 2015.

[121] Giovanni Grilli di Cortona, Edward Hardy, Javier Pardo Vega, and Giovanni Villadoro. The QCD axion, precisely. *JHEP*, 01:034, 2016.

[122] Claudio Bonati, Massimo D'Elia, Guido Martinelli, Francesco Negro, Francesco Sanfilippo, and Antonino Todaro. Topology in full QCD at high temperature: a multicanonical approach. *JHEP*, 11:170, 2018.

[123] Peter Petreczky, Hans-Peter Schadler, and Sayantan Sharma. The topological susceptibility in finite temperature QCD and axion cosmology. *Phys. Lett.*, B762:498–505, 2016.

[124] Florian Burger, Ernst-Michael Ilgenfritz, Maria Paola Lombardo, and Anton Trunin. Chiral observables and topology in hot QCD with two families of quarks. *Phys. Rev.*, D98(9):094501, 2018.

[125] Marco Gorghetto and Giovanni Villadoro. Topological Susceptibility and QCD Axion Mass: QED and NNLO corrections. *JHEP*, 03:033, 2019.

[126] Michael Dine and Alexander Kusenko. The Origin of the matter - antimatter asymmetry. *Rev. Mod. Phys.*, 76:1, 2003.

[127] Kensuke Akita, Tatsuo Kobayashi, and Hajime Otsuka. Axion Inflation and Affleck-Dine Baryogenesis. *JCAP*, 1704(04):042, 2017.

[128] Kensuke Akita and Hajime Otsuka. Affleck-Dine baryogenesis in the SUSY Dine-Fischler-Srednicki-Zhitnitsky axion model without R-parity. *Phys. Rev.*, D99(5):055035, 2019.

[129] Luca Visinelli and Paolo Gondolo. Dark Matter Axions Revisited. *Phys. Rev.*, D80:035024, 2009.

[130] Alberto Diez-Tejedor and David J. E. Marsh. Cosmological production of ultralight dark matter axions. 2017.

[131] Pierre Salati. Quintessence and the relic density of neutralinos. *Phys. Lett.*, B571:121–131, 2003.

[132] Andrew R. Liddle and Robert J. Scherrer. A Classification of scalar field potentials with cosmological scaling solutions. *Phys. Rev.*, D59:023509, 1999.

[133] Daniel J. H. Chung, Lisa L. Everett, and Konstantin T. Matchev. Inflationary cosmology connecting dark energy and dark matter. *Phys. Rev.*, D76:103530, 2007.

[134] Vivian Poulin, Tristan L. Smith, Daniel Grin, Tanvi Karwal, and Marc Kamionkowski. Cosmological implications of ultralight axionlike fields. *Phys. Rev.*, D98(8):083525, 2018.

[135] Benjamin P Abbott et al. Exploring the Sensitivity of Next Generation Gravitational Wave Detectors. *Class. Quant. Grav.*, 34(4):044001, 2017.

[136] B. P. Abbott et al. Observation of Gravitational Waves from a Binary Black Hole Merger. *Phys. Rev. Lett.*, 116(6):061102, 2016.

[137] B. P. Abbott et al. Constraints on cosmic strings using data from the first Advanced LIGO observing run. *Phys. Rev.*, D97(10):102002, 2018.

[138] B. P. Abbott et al. GW150914: Implications for the stochastic gravitational wave background from binary black holes. *Phys. Rev. Lett.*, 116(13):131102, 2016.

[139] B. P. Abbott et al. Search for the isotropic stochastic background using data from Advanced LIGO's second observing run. *Phys. Rev.*, D100(6):061101, 2019.

[140] Pau Amaro-Seoane et al. Laser Interferometer Space Antenna. 2017.

[141] Nicola Bartolo et al. Science with the space-based interferometer LISA. IV: Probing inflation with gravitational waves. *JCAP*, 1612(12):026, 2016.

[142] Z. Arzoumanian et al. The NANOGrav 11-year Data Set: Pulsar-timing Constraints On The Stochastic Gravitational-wave Background. *Astrophys. J.*, 859(1):47, 2018.

[143] Zaven Arzoumanian et al. The NANOGrav 12.5 yr Data Set: Search for an Isotropic Stochastic Gravitational-wave Background. *Astrophys. J. Lett.*, 905(2):L34, 2020.

[144] Zaven Arzoumanian et al. Searching For Gravitational Waves From Cosmological Phase Transitions With The NANOGrav 12.5-year dataset. 4 2021.

[145] John Ellis and Marek Lewicki. Cosmic String Interpretation of NANOGrav Pulsar Timing Data. *Phys. Rev. Lett.*, 126(4):041304, 2021.

[146] Simone Blasi, Vedran Brdar, and Kai Schmitz. Has NANOGrav found first evidence for cosmic strings? *Phys. Rev. Lett.*, 126(4):041305, 2021.

[147] V. De Luca, G. Franciolini, and A. Riotto. NANOGrav Data Hints at Primordial Black Holes as Dark Matter. *Phys. Rev. Lett.*, 126(4):041303, 2021.

[148] Wilfried Buchmuller, Valerie Domcke, and Kai Schmitz. From NANOGrav to LIGO with metastable cosmic strings. *Phys. Lett. B*, 811:135914, 2020.

[149] Sunny Vagnozzi. Implications of the NANOGrav results for inflation. *Mon. Not. Roy. Astron. Soc.*, 502(1):L11–L15, 2021.

[150] Kazunori Kohri and Takahiro Terada. Solar-Mass Primordial Black Holes Explain NANOGrav Hint of Gravitational Waves. *Phys. Lett. B*, 813:136040, 2021.

[151] Nicklas Ramberg and Luca Visinelli. QCD axion and gravitational waves in light of NANOGrav results. *Phys. Rev. D*, 103(6):063031, 2021.

[152] Jose J. Blanco-Pillado, Ken D. Olum, and Jeremy M. Wachter. Comparison of cosmic string and superstring models to NANOGrav 12.5-year results. *Phys. Rev. D*, 103(10):103512, 2021.

[153] Christophe Grojean and Geraldine Servant. Gravitational Waves from Phase Transitions at the Electroweak Scale and Beyond. *Phys. Rev.*, D75:043507, 2007.

[154] Pedro Schwaller. Gravitational Waves from a Dark Phase Transition. *Phys. Rev. Lett.*, 115(18):181101, 2015.

[155] Robert R. Caldwell, Tristan L. Smith, and Devin G. E. Walker. Using a Primordial Gravitational Wave Background to Illuminate New Physics. *Phys. Rev.*, D100(4):043513, 2019.

[156] Chia-Feng Chang and Yanou Cui. Stochastic Gravitational Wave Background from Global Cosmic Strings. 2019.

[157] Yann Gouttenoire, Géraldine Servant, and Peera Simakachorn. BSM with Cosmic Strings: Heavy, up to EeV mass, Unstable Particles. *JCAP*, 07:016, 2020.

[158] Yanou Cui, Marek Lewicki, and David E. Morrissey. Gravitational Wave Bursts as Harbingers of Cosmic Strings Diluted by Inflation. *Phys. Rev. Lett.*, 125(21):211302, 2020.

[159] Wilfried Buchmuller, Valerie Domcke, Hitoshi Murayama, and Kai Schmitz. Probing the scale of grand unification with gravitational waves. *Phys. Lett. B*, 809:135764, 2020.

[160] Jeff A. Dror, Takashi Hiramatsu, Kazunori Kohri, Hitoshi Murayama, and Graham White. Testing the Seesaw Mechanism and Leptogenesis with Gravitational Waves. *Phys. Rev. Lett.*, 124(4):041804, 2020.

[161] David Dunsky, Lawrence J. Hall, and Keisuke Harigaya. Dark Matter, Dark Radiation and Gravitational Waves from Mirror Higgs Parity. *JHEP*, 02:078, 2020.

[162] Simone Blasi, Vedran Brdar, and Kai Schmitz. Fingerprint of low-scale leptogenesis in the primordial gravitational-wave spectrum. *Phys. Rev. Res.*, 2(4):043321, 2020.

[163] Camila S. Machado, Wolfram Ratzinger, Pedro Schwaller, and Ben A. Stefanek. Gravitational wave probes of axionlike particles. *Phys. Rev. D*, 102(7):075033, 2020.

[164] Chiara Caprini and Daniel G. Figueroa. Cosmological Backgrounds of Gravitational Waves. *Class. Quant. Grav.*, 35(16):163001, 2018.

[165] T. W. B. Kibble. Topology of Cosmic Domains and Strings. *J. Phys.*, A9:1387–1398, 1976.

[166] Holger Bech Nielsen and P. Olesen. Vortex Line Models for Dual Strings. *Nucl. Phys.*, B61:45–61, 1973.

[167] Tanmay Vachaspati and Alexander Vilenkin. Formation and Evolution of Cosmic Strings. *Phys. Rev. D*, 30:2036, 1984.

[168] A. Vilenkin and E. P. S. Shellard. *Cosmic Strings and Other Topological Defects*. Cambridge University Press, 2000.

[169] Stephen F. King, Silvia Pascoli, Jessica Turner, and Ye-Ling Zhou. Gravitational Waves and Proton Decay: Complementary Windows into Grand Unified Theories. *Phys. Rev. Lett.*, 126(2):021802, 2021.

[170] Wei-Chih Huang, Francesco Sannino, and Zhi-Wei Wang. Gravitational Waves from Pati-Salam Dynamics. *Phys. Rev. D*, 102(9):095025, 2020.

[171] Wei-Chih Huang, Manuel Reichert, Francesco Sannino, and Zhi-Wei Wang. Testing the Dark Confined Landscape: From Lattice to Gravitational Waves. 12 2020.

[172] Edmund J. Copeland, Robert C. Myers, and Joseph Polchinski. Cosmic F and D strings. *JHEP*, 06:013, 2004.

[173] Gia Dvali and Alexander Vilenkin. Formation and evolution of cosmic D strings. *JCAP*, 0403:010, 2004.

[174] Joseph Polchinski. Introduction to cosmic F- and D-strings. In *String theory: From gauge interactions to cosmology. Proceedings, NATO Advanced Study Institute, Cargese, France, June 7-19, 2004*, pages 229–253, 2004.

[175] Mark G. Jackson, Nicholas T. Jones, and Joseph Polchinski. Collisions of cosmic F and D-strings. *JHEP*, 10:013, 2005.

[176] S. H. Henry Tye, Ira Wasserman, and Mark Wyman. Scaling of multi-tension cosmic superstring networks. *Phys. Rev.*, D71:103508, 2005. [Erratum: Phys. Rev.D71,129906(2005)].

[177] Marco Gorghetto, Edward Hardy, and Giovanni Villadoro. More Axions from Strings. *SciPost Phys.*, 10:050, 2021.

[178] Daniel G. Figueroa, Mark Hindmarsh, Joanes Lizarraga, and Jon Urrestilla. Irreducible background of gravitational waves from a cosmic defect network: update and comparison of numerical techniques. *Phys. Rev. D*, 102(10):103516, 2020.

[179] Yousef Abou El-Neaj et al. AEDGE: Atomic Experiment for Dark Matter and Gravity Exploration in Space. *EPJ Quant. Technol.*, 7:6, 2020.

[180] Kent Yagi and Naoki Seto. Detector configuration of DECIGO/BBO and identification of cosmological neutron-star binaries. *Phys. Rev.*, D83:044011, 2011. [Erratum: Phys. Rev.D95,no.10,109901(2017)].

[181] Jonathan L. Feng. Dark Matter Candidates from Particle Physics and Methods of Detection. *Ann. Rev. Astron. Astrophys.*, 48:495–545, 2010.

[182] Tongyan Lin. Dark matter models and direct detection. *PoS*, 333:009, 2019.

[183] Luca Di Luzio, Maurizio Giannotti, Enrico Nardi, and Luca Visinelli. The landscape of QCD axion models. 2020.

[184] Hiren H. Patel and Michael J. Ramsey-Musolf. Baryon Washout, Electroweak Phase Transition, and Perturbation Theory. *JHEP*, 07:029, 2011.

[185] David E. Morrissey and Michael J. Ramsey-Musolf. Electroweak baryogenesis. *New J. Phys.*, 14:125003, 2012.

[186] Bharat Ratra and P. J. E. Peebles. Cosmological Consequences of a Rolling Homogeneous Scalar Field. *Phys. Rev.*, D37:3406, 1988.

[187] Andrei D. Linde. Inflationary Cosmology. *Lect. Notes Phys.*, 738:1–54, 2008.

[188] M. B. Hindmarsh and T. W. B. Kibble. Cosmic strings. *Rept. Prog. Phys.*, 58:477–562, 1995.

[189] Tanmay Vachaspati, Levon Pogosian, and Daniele Steer. Cosmic Strings. *Scholarpedia*, 10(2):31682, 2015.

[190] Adrienne L. Erickcek and Isaac Raj Waldstein. The early Universe's imprint on dark matter. *AIP Conf. Proc.*, 1900(1):040005, 2017.

[191] Kayla Redmond and Adrienne L. Erickcek. New Constraints on Dark Matter Production during Kination. *Phys. Rev. D*, 96(4):043511, 2017.

[192] Adrienne L. Erickcek, Pranjal Ralegankar, and Jessie Shelton. Cannibal domination and the matter power spectrum. *Phys. Rev. D*, 103(10):103508, 2021.

[193] Bruce Allen. The Stochastic gravity wave background: Sources and detection. In *Les Houches School of Physics: Astrophysical Sources of Gravitational Radiation*, 4 1996.

[194] Latham A. Boyle and Paul J. Steinhardt. Probing the early universe with inflationary gravitational waves. *Phys. Rev.*, D77:063504, 2008.

[195] Latham A. Boyle and Alessandra Buonanno. Relating gravitational wave constraints from primordial nucleosynthesis, pulsar timing, laser interferometers, and the CMB: Implications for the early Universe. *Phys. Rev.*, D78:043531, 2008.

[196] Vincent B. Klaer and Guy D. Moore. Global cosmic string networks as a function of tension. *JCAP*, 06:021, 2020.

[197] Graciela B. Gelmini, Anna Simpson, and Edoardo Vitagliano. Gravitational waves from axion-like particle cosmic string-wall networks. 3 2021.

[198] Leesa Fleury and Guy D. Moore. Axion dark matter: strings and their cores. *JCAP*, 01:004, 2016.

[199] Ayush Saurabh, Tanmay Vachaspati, and Levon Pogosian. Decay of Cosmic Global String Loops. *Phys. Rev. D*, 101(8):083522, 2020.

[200] Mark Hindmarsh, Joanes Lizarraga, Asier Lopez-Eiguren, and Jon Urrestilla. Approach to scaling in axion string networks. 2 2021.

[201] C. J. A. P. Martins, Patrick Peter, I. Yu Rybak, and E. P. S. Shellard. Generalized velocity-dependent one-scale model for current-carrying strings. *Phys. Rev. D*, 103(4):043538, 2021.

[202] Alejandro Vaquero, Javier Redondo, and Julia Stadler. Early seeds of axion miniclusters. *JCAP*, 04:012, 2019.

[203] C. J. A. P. Martins and E. P. S. Shellard. Quantitative string evolution. *Phys. Rev.*, D54:2535–2556, 1996.

[204] C. J. A. P. Martins and E. P. S. Shellard. Extending the velocity dependent one scale string evolution model. *Phys. Rev.*, D65:043514, 2002.

[205] C. J. A. P. Martins, J. N. Moore, and E. P. S. Shellard. A Unified model for vortex string network evolution. *Phys. Rev. Lett.*, 92:251601, 2004.

[206] J. R. C. C. C. Correia and C. J. A. P. Martins. Extending and Calibrating the Velocity dependent One-Scale model for Cosmic Strings with One Thousand Field Theory Simulations. *Phys. Rev. D*, 100(10):103517, 2019.

[207] C. J. A. P. Martins and M. M. P. V. P. Cabral. Physical and invariant models for defect network evolution. *Phys. Rev. D*, 93(4):043542, 2016. [Addendum: Phys.Rev.D 93, 069902 (2016)].

[208] Jose J. Blanco-Pillado, Ken D. Olum, and Benjamin Shlaer. The number of cosmic string loops. *Phys. Rev.*, D89(2):023512, 2014.

[209] Jose J. Blanco-Pillado and Ken D. Olum. Stochastic gravitational wave background from smoothed cosmic string loops. *Phys. Rev.*, D96(10):104046, 2017.

[210] Jose J. Blanco-Pillado, Ken D. Olum, and Xavier Siemens. New limits on cosmic strings from gravitational wave observation. *Phys. Lett. B*, 778:392–396, 2018.

[211] Mark Hindmarsh. Signals of Inflationary Models with Cosmic Strings. *Prog. Theor. Phys. Suppl.*, 190:197–228, 2011.

[212] Andreas Albrecht, Richard A. Battye, and James Robinson. Detailed study of defect models for cosmic structure formation. *Phys. Rev. D*, 59:023508, 1999.

[213] Levon Pogosian and Tanmay Vachaspati. Cosmic microwave background anisotropy from wiggly strings. *Phys. Rev. D*, 60:083504, 1999.

[214] Anastasios Avgoustidis, Edmund J. Copeland, Adam Moss, and Dimitri Skliros. Fast Analytic Computation of Cosmic String Power Spectra. *Phys. Rev. D*, 86:123513, 2012.

[215] Mark Hindmarsh, Joanes Lizarraga, Jon Urrestilla, David Daverio, and Martin Kunz. Scaling from gauge and scalar radiation in Abelian Higgs string networks. *Phys. Rev.*, D96(2):023525, 2017.

[216] Mark Hindmarsh, Joanes Lizarraga, Jon Urrestilla, David Daverio, and Martin Kunz. Type I Abelian Higgs strings: evolution and Cosmic Microwave Background constraints. *Phys. Rev. D*, 99(8):083522, 2019.

[217] Asier Lopez-Eiguren, Joanes Lizarraga, Mark Hindmarsh, and Jon Urrestilla. Cosmic Microwave Background constraints for global strings and global monopoles. *JCAP*, 1707:026, 2017.

[218] Masahide Yamaguchi and Jun'ichi Yokoyama. Quantitative evolution of global strings from the Lagrangian view point. *Phys. Rev. D*, 67:103514, 2003.

[219] Takashi Hiramatsu, Masahiro Kawasaki, Toyokazu Sekiguchi, Masahide Yamaguchi, and Jun'ichi Yokoyama. Improved estimation of radiated axions from cosmological axionic strings. *Phys. Rev. D*, 83:123531, 2011.

[220] Takashi Hiramatsu, Masahiro Kawasaki, Ken'ichi Saikawa, and Toyokazu Sekiguchi. Production of dark matter axions from collapse of string-wall systems. *Phys. Rev. D*, 85:105020, 2012. [Erratum: Phys.Rev.D 86, 089902 (2012)].

[221] C. J. A. P. Martins, I. Yu. Rybak, A. Avgoustidis, and E. P. S. Shellard. Extending the velocity-dependent one-scale model for domain walls. *Phys. Rev. D*, 93(4):043534, 2016.

[222] J. R. C. C. C. Correia and C. J. A. P. Martins. Quantifying the effect of cooled initial conditions on cosmic string network evolution. *Phys. Rev. D*, 102(4):043503, 2020.

[223] Pierre Auclair et al. Probing the gravitational wave background from cosmic strings with LISA. 2019.

[224] R. A. Battye and E. P. S. Shellard. Recent perspectives on axion cosmology. pages 554–579, 1997.

[225] A. Vilenkin. Gravitational radiation from cosmic strings. *Phys. Lett.*, 107B:47–50, 1981.

[226] Jose J. Blanco-Pillado, Ken D. Olum, and Benjamin Shlaer. Large parallel cosmic string simulations: New results on loop production. *Phys. Rev.*, D83:083514, 2011.

[227] Ken D. Olum and J. J. Blanco-Pillado. Field theory simulation of Abelian Higgs cosmic string cusps. *Phys. Rev. D*, 60:023503, 1999.

[228] Jose J. Blanco-Pillado, Ken D. Olum, and Benjamin Shlaer. Cosmic string loop shapes. *Phys. Rev. D*, 92(6):063528, 2015.

[229] Jose J. Blanco-Pillado, Ken D. Olum, and Jeremy M. Wachter. Gravitational backreaction simulations of simple cosmic string loops. *Phys. Rev. D*, 100(2):023535, 2019.

[230] Tanmay Vachaspati and Alexander Vilenkin. Gravitational Radiation from Cosmic Strings. *Phys. Rev. D*, 31:3052, 1985.

[231] C. J. Burden. Gravitational Radiation From a Particular Class of Cosmic Strings. *Phys. Lett. B*, 164:277–281, 1985.

[232] David Garfinkle and Tanmay Vachaspati. Radiation From Kinky, Cuspless Cosmic Loops. *Phys. Rev. D*, 36:2229, 1987.

[233] Sanghyeon Chang, C. Hagmann, and P. Sikivie. Studies of the motion and decay of axion walls bounded by strings. *Phys. Rev. D*, 59:023505, 1999.

[234] R. L. Davis and E. P. S. Shellard. GLOBAL STRING LIFETIMES: NEVER SAY FOREVER! *Phys. Rev. Lett.*, 63:2021, 1989.

[235] R. L. Davis. Relativistic Superfluids and Vortex Rings. *Phys. Rev. D*, 40:4033, 1989.

[236] Yann Gouttenoire, Géraldine Servant, and Peera Simakachorn. Beyond the Standard Models with Cosmic Strings. *JCAP*, 07:032, 2020.

[237] R. A. Battye and E. P. S. Shellard. Primordial gravitational waves: A Probe of the very early universe. 1996.

[238] J. Aasi et al. Advanced LIGO. *Class. Quant. Grav.*, 32:074001, 2015.

[239] Eric Thrane and Joseph D. Romano. Sensitivity curves for searches for gravitational-wave backgrounds. *Phys. Rev.*, D88(12):124032, 2013.

[240] R. van Haasteren et al. Placing limits on the stochastic gravitational-wave background using European Pulsar Timing Array data. *Mon. Not. Roy. Astron. Soc.*, 414(4):3117–3128, 2011. [Erratum: Mon. Not. Roy. Astron. Soc.425,no.2,1597(2012)].

[241] Paul D. Lasky et al. Gravitational-wave cosmology across 29 decades in frequency. *Phys. Rev.*, X6(1):011035, 2016.

[242] R. M. Shannon et al. Gravitational waves from binary supermassive black holes missing in pulsar observations. *Science*, 349(6255):1522–1525, 2015.

[243] B. P. Abbott et al. Prospects for Observing and Localizing Gravitational-Wave Transients with Advanced LIGO, Advanced Virgo and KAGRA. *Living Rev. Rel.*, 21(1):3, 2018.

[244] L. Badurina et al. AION: An Atom Interferometer Observatory and Network. *JCAP*, 05:011, 2020.

[245] M. Punturo et al. The Einstein Telescope: A third-generation gravitational wave observatory. *Class. Quant. Grav.*, 27:194002, 2010.

[246] S. Hild et al. Sensitivity Studies for Third-Generation Gravitational Wave Observatories. *Class. Quant. Grav.*, 28:094013, 2011.

[247] Gemma Janssen et al. Gravitational wave astronomy with the SKA. *PoS*, AASKA14:037, 2015.

[248] Andrii Neronov, Alberto Roper Pol, Chiara Caprini, and Dmitri Semikoz. NANOGrav signal from magnetohydrodynamic turbulence at the QCD phase transition in the early Universe. *Phys. Rev. D*, 103(4):041302, 2021.

[249] Jeffrey S. Hazboun, Joseph Simon, Xavier Siemens, and Joseph D. Romano. Model Dependence of Bayesian Gravitational-Wave Background Statistics for Pulsar Timing Arrays. *Astrophys. J. Lett.*, 905(1):L6, 2020.

[250] Tristan L. Smith, Marc Kamionkowski, and Asantha Cooray. Direct detection of the inflationary gravitational wave background. *Phys. Rev.*, D73:023504, 2006.

[251] Toshiya Namikawa, Shohei Saga, Daisuke Yamauchi, and Atsushi Taruya. CMB Constraints on the Stochastic Gravitational-Wave Background at Mpc scales. *Phys. Rev.*, D100(2):021303, 2019.

[252] Tristan L. Smith, Elena Pierpaoli, and Marc Kamionkowski. A new cosmic microwave background constraint to primordial gravitational waves. *Phys. Rev. Lett.*, 97:021301, 2006.

[253] Ken D. Olum and J. J. Blanco-Pillado. Radiation from cosmic string standing waves. *Phys. Rev. Lett.*, 84:4288–4291, 2000.

[254] Daniel G. Figueroa, Mark Hindmarsh, and Jon Urrestilla. Exact Scale-Invariant Background of Gravitational Waves from Cosmic Defects. *Phys. Rev. Lett.*, 110(10):101302, 2013.

[255] Christophe Ringeval and Teruaki Suyama. Stochastic gravitational waves from cosmic string loops in scaling. *JCAP*, 12:027, 2017.

[256] Greg Huey, Paul J. Steinhardt, Burt A. Ovrut, and Daniel Waldram. A Cosmological mechanism for stabilizing moduli. *Phys. Lett. B*, 476:379–386, 2000.

[257] Chia-Feng Chang and Yanou Cui. New Perspectives on Axion Misalignment Mechanism. 2019.

[258] G. S. F. Guedes, P. P. Avelino, and L. Sousa. Signature of inflation in the stochastic gravitational wave background generated by cosmic string networks. *Phys. Rev. D*, 98(12):123505, 2018.

[259] Z. Chacko, Hock-Seng Goh, and Roni Harnik. The Twin Higgs: Natural electroweak breaking from mirror symmetry. *Phys. Rev. Lett.*, 96:231802, 2006.

[260] Nima Arkani-Hamed, Timothy Cohen, Raffaele Tito D'Agnolo, Anson Hook, Hyung Do Kim, and David Pinner. Solving the Hierarchy Problem at Reheating with a Large Number of Degrees of Freedom. *Phys. Rev. Lett.*, 117(25):251801, 2016.

[261] Peter W. Graham, Ahmed Ismail, Surjeet Rajendran, and Prashant Saraswat. A Little Solution to the Little Hierarchy Problem: A Vector-like Generation. *Phys. Rev. D*, 81:055016, 2010.

[262] Jonathan L. Feng, Huitzu Tu, and Hai-Bo Yu. Thermal Relics in Hidden Sectors. *JCAP*, 10:043, 2008.

[263] Peter Adshead, Yanou Cui, and Jessie Shelton. Chilly Dark Sectors and Asymmetric Reheating. *JHEP*, 06:016, 2016.

[264] Matthew J. Strassler and Kathryn M. Zurek. Echoes of a hidden valley at hadron colliders. *Phys. Lett. B*, 651:374–379, 2007.

[265] H. M. Hodges. Mirror baryons as the dark matter. *Phys. Rev. D*, 47:456–459, 1993.

[266] Edward W. Kolb, D. Seckel, and Michael S. Turner. The Shadow World. *Nature*, 314:415–419, 1985.

[267] Christopher Brust, Yanou Cui, and Kris Sigurdson. Cosmological Constraints on Interacting Light Particles. *JCAP*, 08:020, 2017.

[268] Daniel Baumann, Daniel Green, Joel Meyers, and Benjamin Wallisch. Phases of New Physics in the CMB. *JCAP*, 01:007, 2016.

[269] Zackaria Chacko, Yanou Cui, Sungwoo Hong, and Takemichi Okui. Hidden dark matter sector, dark radiation, and the CMB. *Phys. Rev. D*, 92:055033, 2015.

[270] Christopher Brust, David E. Kaplan, and Matthew T. Walters. New Light Species and the CMB. *JHEP*, 12:058, 2013.

[271] David E. Kaplan and Riccardo Rattazzi. Large field excursions and approximate discrete symmetries from a clockwork axion. *Phys. Rev. D*, 93(8):085007, 2016.

[272] R. Foot. Mirror dark matter: Cosmology, galaxy structure and direct detection. *Int. J. Mod. Phys. A*, 29:1430013, 2014.

[273] B. P. Abbott et al. GW170817: Observation of Gravitational Waves from a Binary Neutron Star Inspiral. *Phys. Rev. Lett.*, 119(16):161101, 2017.

[274] B. . P. . Abbott et al. GW170608: Observation of a 19-solar-mass Binary Black Hole Coalescence. *Astrophys. J. Lett.*, 851:L35, 2017.

[275] Benjamin P. Abbott et al. GW170104: Observation of a 50-Solar-Mass Binary Black Hole Coalescence at Redshift 0.2. *Phys. Rev. Lett.*, 118(22):221101, 2017. [Erratum: Phys.Rev.Lett. 121, 129901 (2018)].

[276] Benjamin P. Abbott et al. GW170817: Implications for the Stochastic Gravitational-Wave Background from Compact Binary Coalescences. *Phys. Rev. Lett.*, 120(9):091101, 2018.

[277] Benjamin P. Abbott et al. Upper Limits on the Stochastic Gravitational-Wave Background from Advanced LIGO's First Observing Run. *Phys. Rev. Lett.*, 118(12):121101, 2017. [Erratum: Phys.Rev.Lett. 119, 029901 (2017)].

[278] Barry C. Barish, Simeon Bird, and Yanou Cui. The Impact of a Midband Gravitational Wave Experiment On Detectability of Cosmological Stochastic Gravitational Wave Backgrounds. 12 2020.

[279] B. P. Abbott et al. A gravitational-wave standard siren measurement of the Hubble constant. *Nature*, 551(7678):85–88, 2017.

[280] T. Regimbau, M. Evans, N. Christensen, E. Katsavounidis, B. Sathyaprakash, and S. Vitale. Digging deeper: Observing primordial gravitational waves below the binary black hole produced stochastic background. *Phys. Rev. Lett.*, 118(15):151105, 2017.

[281] Alexander C. Jenkins and Mairi Sakellariadou. Anisotropies in the stochastic gravitational-wave background: Formalism and the cosmic string case. *Phys. Rev. D*, 98(6):063509, 2018.

[282] Rory Smith and Eric Thrane. Optimal Search for an Astrophysical Gravitational-Wave Background. *Phys. Rev. X*, 8(2):021019, 2018.

[283] Nicola Bartolo, Valerie Domcke, Daniel G. Figueroa, Juan García-Bellido, Marco Peloso, Mauro Pieroni, Angelo Ricciardone, Mairi Sakellariadou, Lorenzo Sorbo, and Gianmassimo Tasinato. Probing non-Gaussian Stochastic Gravitational Wave Backgrounds with LISA. *JCAP*, 11:034, 2018.

[284] Yonadav Barry Ginat, Vincent Desjacques, Robert Reischke, and Hagai B. Perets. Probability distribution of astrophysical gravitational-wave background fluctuations. *Phys. Rev. D*, 102(8):083501, 2020.

[285] Quentin Baghi, Ira Thorpe, Jacob Slutsky, John Baker, Tito Dal Canton, Natalia Korsakova, and Nikos Karnesis. Gravitational-wave parameter estimation with gaps in LISA: a Bayesian data augmentation method. *Phys. Rev. D*, 100(2):022003, 2019.

[286] Chiara Caprini, Daniel G. Figueroa, Raphael Flauger, Germano Nardini, Marco Peloso, Mauro Pieroni, Angelo Ricciardone, and Gianmassimo Tasinato. Reconstructing the spectral shape of a stochastic gravitational wave background with LISA. *JCAP*, 11:017, 2019.

[287] Tristan L. Smith and Robert Caldwell. LISA for Cosmologists: Calculating the Signal-to-Noise Ratio for Stochastic and Deterministic Sources. *Phys. Rev. D*, 100(10):104055, 2019.

[288] Raphael Flauger, Nikolaos Karnesis, Germano Nardini, Mauro Pieroni, Angelo Ricciardone, and Jesús Torrado. Improved reconstruction of a stochastic gravitational wave background with LISA. *JCAP*, 01:059, 2021.

[289] Guillaume Boileau, Nelson Christensen, Renate Meyer, and Neil J. Cornish. Spectral separation of the stochastic gravitational-wave background for LISA: observing both cosmological and astrophysical backgrounds. *Phys. Rev. D*, 103:103529, 2021.

[290] Kai Schmitz. New Sensitivity Curves for Gravitational-Wave Signals from Cosmological Phase Transitions. *JHEP*, 01:097, 2021.

[291] Joseph D. Romano and Neil J. Cornish. Detection methods for stochastic gravitational-wave backgrounds: a unified treatment. *Living Rev. Rel.*, 20(1):2, 2017.

[292] Pierre Binetruy, Alejandro Bohe, Chiara Caprini, and Jean-Francois Dufaux. Cosmological Backgrounds of Gravitational Waves and eLISA/NGO: Phase Transitions, Cosmic Strings and Other Sources. *JCAP*, 1206:027, 2012.

[293] Sachiko Kuroyanagi, Takeshi Chiba, and Tomo Takahashi. Probing the Universe through the Stochastic Gravitational Wave Background. *JCAP*, 1811:038, 2018.

[294] Alexei A. Starobinsky. Spectrum of relict gravitational radiation and the early state of the universe. *JETP Lett.*, 30:682–685, 1979.

[295] Bruce Allen. The Stochastic Gravity Wave Background in Inflationary Universe Models. *Phys. Rev. D*, 37:2078, 1988.

[296] Ville Vaskonen and Hardi Veermäe. Did NANOGrav see a signal from primordial black hole formation? *Phys. Rev. Lett.*, 126(5):051303, 2021.

[297] S. Y. Khlebnikov and I. I. Tkachev. Relic gravitational waves produced after preheating. *Phys. Rev.*, D56:653–660, 1997.

[298] Richard Easther and Eugene A. Lim. Stochastic gravitational wave production after inflation. *JCAP*, 0604:010, 2006.

[299] Richard Easther, John T. Giblin, Jr., and Eugene A. Lim. Gravitational Wave Production At The End Of Inflation. *Phys. Rev. Lett.*, 99:221301, 2007.

[300] Juan Garcia-Bellido and Daniel G. Figueroa. A stochastic background of gravitational waves from hybrid preheating. *Phys. Rev. Lett.*, 98:061302, 2007.

[301] Edward Witten. Cosmic Separation of Phases. *Phys. Rev. D*, 30:272–285, 1984.

[302] CJ Hogan. Gravitational radiation from cosmological phase transitions. *Monthly Notices of the Royal Astronomical Society*, 218(4):629–636, 1986.

[303] Arthur Kosowsky, Michael S Turner, and Richard Watkins. Gravitational radiation from colliding vacuum bubbles. *Physical Review D*, 45(12):4514, 1992.

[304] Tommi Alanne, Thomas Hugle, Moritz Platscher, and Kai Schmitz. A fresh look at the gravitational-wave signal from cosmological phase transitions. *JHEP*, 03:004, 2020.

[305] Kai Schmitz. LISA Sensitivity to Gravitational Waves from Sound Waves. *Symmetry*, 12(9):1477, 2020.

[306] Marcelo Gleiser and Ronald Roberts. Gravitational waves from collapsing vacuum domains. *Phys. Rev. Lett.*, 81:5497–5500, 1998.

[307] Tanmay Vachaspati and Alexander Vilenkin. Gravitational radiation from cosmic strings. *Physical Review D*, 31(12):3052, 1985.

[308] RR Caldwell and Bruce Allen. Cosmological constraints on cosmic-string gravitational radiation. *Physical Review D*, 45(10):3447, 1992.

[309] Thibault Damour and Alexander Vilenkin. Gravitational radiation from cosmic (super)strings: Bursts, stochastic background, and observational windows. *Phys. Rev.*, D71:063510, 2005.

[310] Neil Bevis, Mark Hindmarsh, Martin Kunz, and Jon Urrestilla. CMB power spectrum contribution from cosmic strings using field-evolution simulations of the Abelian Higgs model. *Phys. Rev.*, D75:065015, 2007.

[311] B. P. Abbott et al. Observation of Gravitational Waves from a Binary Black Hole Merger. *Phys. Rev. Lett.*, 116(6):061102, 2016.

[312] B. P. Abbott et al. GW151226: Observation of Gravitational Waves from a 22-Solar-Mass Binary Black Hole Coalescence. *Phys. Rev. Lett.*, 116(24):241103, 2016.

[313] B. P. Abbott et al. GW170814: A Three-Detector Observation of Gravitational Waves from a Binary Black Hole Coalescence. *Phys. Rev. Lett.*, 119(14):141101, 2017.

[314] B. P. Abbott et al. Multi-messenger Observations of a Binary Neutron Star Merger. *Astrophys. J. Lett.*, 848(2):L12, 2017.

[315] Lucas Lombriser and Nelson A. Lima. Challenges to Self-Acceleration in Modified Gravity from Gravitational Waves and Large-Scale Structure. *Phys. Lett. B*, 765:382–385, 2017.

[316] Lucas Lombriser and Andy Taylor. Breaking a Dark Degeneracy with Gravitational Waves. *JCAP*, 03:031, 2016.

[317] Paolo Creminelli and Filippo Vernizzi. Dark Energy after GW170817 and GRB170817A. *Phys. Rev. Lett.*, 119(25):251302, 2017.

[318] Jose María Ezquiaga and Miguel Zumalacárregui. Dark Energy After GW170817: Dead Ends and the Road Ahead. *Phys. Rev. Lett.*, 119(25):251304, 2017.

[319] T. Baker, E. Bellini, P. G. Ferreira, M. Lagos, J. Noller, and I. Sawicki. Strong constraints on cosmological gravity from GW170817 and GRB 170817A. *Phys. Rev. Lett.*, 119(25):251301, 2017.

[320] Jeremy Sakstein and Bhuvnesh Jain. Implications of the Neutron Star Merger GW170817 for Cosmological Scalar-Tensor Theories. *Phys. Rev. Lett.*, 119(25):251303, 2017.

[321] Chia-Feng Chang and Yanou Cui. Gravitational Waves from Global Cosmic Strings and Cosmic Archaeology. 6 2021.

[322] Yanou Cui, Marek Lewicki, David E. Morrissey, and James D. Wells. Cosmic Archaeology with Gravitational Waves from Cosmic Strings. *Phys. Rev. D*, 97(12):123505, 2018.

[323] R. A. Battye and E. P. S. Shellard. Axion string constraints. *Phys. Rev. Lett.*, 73:2954–2957, 1994. [Erratum: Phys.Rev.Lett. 76, 2203–2204 (1996)].

[324] Suvodip Mukherjee, Guilhem Lavaux, François R. Bouchet, Jens Jasche, Benjamin D. Wandelt, Samaya M. Nissanke, Florent Leclercq, and Kenta Hotokezaka. Velocity correction for Hubble constant measurements from standard sirens. *Astron. Astrophys.*, 646:A65, 2021.

[325] V. Gayathri, J. Healy, J. Lange, B. O'Brien, M. Szczepanczyk, I. Bartos, M. Campanelli, S. Klimenko, C. Lousto, and R. O'Shaughnessy. Hubble Constant Measurement with GW190521 as an Eccentric Black Hole Merger. 9 2020.

[326] Suvodip Mukherjee, Archisman Ghosh, Matthew J. Graham, Christos Karathanasis, Mansi M. Kasliwal, Ignacio Magaña Hernandez, Samaya M. Nissanke, Alessandra Silvestri, and Benjamin D. Wandelt. First measurement of the Hubble parameter from bright binary black hole GW190521. 9 2020.

[327] Adam G. Riess et al. A 2.4% Determination of the Local Value of the Hubble Constant. *Astrophys. J.*, 826(1):56, 2016.

[328] Adam G. Riess et al. Milky Way Cepheid Standards for Measuring Cosmic Distances and Application to Gaia DR2: Implications for the Hubble Constant. *Astrophys. J.*, 861(2):126, 2018.

[329] Louise Breuval et al. The Milky Way Cepheid Leavitt law based on Gaia DR2 parallaxes of companion stars and host open cluster populations. *Astron. Astrophys.*, 643:A115, 2020.

[330] Adam G. Riess, Stefano Casertano, Wenlong Yuan, J. Bradley Bowers, Lucas Macri, Joel C. Zinn, and Dan Scolnic. Cosmic Distances Calibrated to 1% Precision with Gaia EDR3 Parallaxes and Hubble Space Telescope Photometry of 75 Milky Way Cepheids Confirm Tension with ΛCDM. *Astrophys. J. Lett.*, 908(1):L6, 2021.

[331] John Soltis, Stefano Casertano, and Adam G. Riess. The Parallax of ω Centauri Measured from Gaia EDR3 and a Direct, Geometric Calibration of the Tip of the Red Giant Branch and the Hubble Constant. *Astrophys. J. Lett.*, 908(1):L5, 2021.

[332] Wendy L. Freedman, Barry F. Madore, Taylor Hoyt, In Sung Jang, Rachael Beaton, Myung Gyoon Lee, Andrew Monson, Jill Neeley, and Jeffrey Rich. Calibration of the Tip of the Red Giant Branch (TRGB). 2 2020.

[333] V. Bonvin et al. H0LiCOW – V. New COSMOGRAIL time delays of HE 0435−1223: H_0 to 3.8 per cent precision from strong lensing in a flat ΛCDM model. *Mon. Not. Roy. Astron. Soc.*, 465(4):4914–4930, 2017.

[334] S. Birrer et al. H0LiCOW - IX. Cosmographic analysis of the doubly imaged quasar SDSS 1206+4332 and a new measurement of the Hubble constant. *Mon. Not. Roy. Astron. Soc.*, 484:4726, 2019.

[335] Philipp Denzel, Jonathan P. Coles, Prasenjit Saha, and Liliya L. R. Williams. The Hubble constant from eight time-delay galaxy lenses. *Mon. Not. Roy. Astron. Soc.*, 501(1):784–801, 2021.

[336] Tao Yang, Simon Birrer, and Bin Hu. The first simultaneous measurement of Hubble constant and post-Newtonian parameter from Time-Delay Strong Lensing. *Mon. Not. Roy. Astron. Soc.*, 497(1):L56–L61, 2020.

[337] S. Birrer et al. TDCOSMO - IV. Hierarchical time-delay cosmography – joint inference of the Hubble constant and galaxy density profiles. *Astron. Astrophys.*, 643:A165, 2020.

[338] M. Millon et al. TDCOSMO. I. An exploration of systematic uncertainties in the inference of H_0 from time-delay cosmography. *Astron. Astrophys.*, 639:A101, 2020.

[339] Eric J. Baxter and Blake D. Sherwin. Determining the Hubble Constant without the Sound Horizon Scale: Measurements from CMB Lensing. *Mon. Not. Roy. Astron. Soc.*, 501(2):1823–1835, 2021.

[340] K. Aylor et al. A Comparison of Cosmological Parameters Determined from CMB Temperature Power Spectra from the South Pole Telescope and the Planck Satellite. *Astrophys. J.*, 850(1):101, 2017.

[341] Simone Aiola et al. The Atacama Cosmology Telescope: DR4 Maps and Cosmological Parameters. *JCAP*, 12:047, 2020.

[342] Steve K. Choi et al. The Atacama Cosmology Telescope: a measurement of the Cosmic Microwave Background power spectra at 98 and 150 GHz. *JCAP*, 12:045, 2020.

[343] Stephen M. Feeney, Daniel J. Mortlock, and Niccolò Dalmasso. Clarifying the Hubble constant tension with a Bayesian hierarchical model of the local distance ladder. *Mon. Not. Roy. Astron. Soc.*, 476(3):3861–3882, 2018.

[344] Bonnie R. Zhang, Michael J. Childress, Tamara M. Davis, Natallia V. Karpenka, Chris Lidman, Brian P. Schmidt, and Mathew Smith. A blinded determination of H_0 from low-redshift Type Ia supernovae, calibrated by Cepheid variables. *Mon. Not. Roy. Astron. Soc.*, 471(2):2254–2285, 2017.

[345] Wilmar Cardona, Martin Kunz, and Valeria Pettorino. Determining H_0 with Bayesian hyper-parameters. *JCAP*, 03:056, 2017.

[346] C. L. Bennett, D. Larson, J. L. Weiland, and G. Hinshaw. The 1% Concordance Hubble Constant. *Astrophys. J.*, 794:135, 2014.

[347] D. W. Pesce et al. The Megamaser Cosmology Project. XIII. Combined Hubble constant constraints. *Astrophys. J. Lett.*, 891(1):L1, 2020.

[348] Kenneth C. Wong et al. H0LiCOW – XIII. A 2.4 per cent measurement of H0 from lensed quasars: 5.3σ tension between early- and late-Universe probes. *Mon. Not. Roy. Astron. Soc.*, 498(1):1420–1439, 2020.

[349] Caroline D. Huang, Adam G. Riess, Wenlong Yuan, Lucas M. Macri, Nadia L. Zakamska, Stefano Casertano, Patricia A. Whitelock, Samantha L. Hoffmann, Alexei V. Filippenko, and Daniel Scolnic. Hubble Space Telescope Observations of Mira Variables in the Type Ia Supernova Host NGC 1559: An Alternative Candle to Measure the Hubble Constant. 8 2019.

[350] Wendy L. Freedman et al. The Carnegie-Chicago Hubble Program. VIII. An Independent Determination of the Hubble Constant Based on the Tip of the Red Giant Branch. 7 2019.

[351] G. Fritz Benedict, Barbara E. McArthur, Michael W. Feast, Thomas G. Barnes, Thomas E. Harrison, Richard J. Patterson, John W. Menzies, Jacob L. Bean, and Wendy L. Freedman. Hubble Space Telescope Fine Guidance Sensor Parallaxes of Galactic Cepheid Variable Stars: Period-Luminosity Relations. *Astron. J.*, 133:1810–1827, 2007. [Erratum: Astron.J. 133, 2980 (2007)].

[352] E. M. L. Humphreys, Mark J. Reid, Jim M. Moran, Lincoln J. Greenhill, and Alice L. Argon. Toward a New Geometric Distance to the Active Galaxy NGC 4258. III. Final Results and the Hubble Constant. *Astrophys. J.*, 775:13, 2013.

[353] George Efstathiou. H0 Revisited. *Mon. Not. Roy. Astron. Soc.*, 440(2):1138–1152, 2014.

[354] M. Rigault et al. Confirmation of a Star Formation Bias in Type Ia Supernova Distances and its Effect on Measurement of the Hubble Constant. *Astrophys. J.*, 802(1):20, 2015.

[355] W. D'Arcy Kenworthy, Dan Scolnic, and Adam Riess. The Local Perspective on the Hubble Tension: Local Structure Does Not Impact Measurement of the Hubble Constant. *Astrophys. J.*, 875(2):145, 2019.

[356] David N. Spergel, Raphael Flauger, and Renée Hložek. Planck Data Reconsidered. *Phys. Rev. D*, 91(2):023518, 2015.

[357] Lloyd Knox and Marius Millea. Hubble constant hunter's guide. *Phys. Rev. D*, 101(4):043533, 2020.

[358] L. Verde, T. Treu, and A. G. Riess. Tensions between the Early and the Late Universe. *Nature Astron.*, 3:891, 7 2019.

[359] Kevin Aylor, MacKenzie Joy, Lloyd Knox, Marius Millea, Srinivasan Raghunathan, and W. L. Kimmy Wu. Sounds Discordant: Classical Distance Ladder \& ΛCDM -based Determinations of the Cosmological Sound Horizon. *Astrophys. J.*, 874(1):4, 2019.

[360] Tristan L. Smith, Vivian Poulin, and Mustafa A. Amin. Oscillating scalar fields and the Hubble tension: a resolution with novel signatures. *Phys. Rev. D*, 101(6):063523, 2020.

[361] Prateek Agrawal, Francis-Yan Cyr-Racine, David Pinner, and Lisa Randall. Rock 'n' Roll Solutions to the Hubble Tension. 4 2019.

[362] Tristan L. Smith, Vivian Poulin, José Luis Bernal, Kimberly K. Boddy, Marc Kamionkowski, and Riccardo Murgia. Early dark energy is not excluded by current large-scale structure data. 9 2020.

[363] Riccardo Murgia, Guillermo F. Abellán, and Vivian Poulin. Early dark energy resolution to the Hubble tension in light of weak lensing surveys and lensing anomalies. *Phys. Rev. D*, 103(6):063502, 2021.

[364] Meng-Xiang Lin, Wayne Hu, and Marco Raveri. Testing H_0 in Acoustic Dark Energy with Planck and ACT Polarization. *Phys. Rev. D*, 102:123523, 2020.

[365] Edmund J. Copeland, M. Sami, and Shinji Tsujikawa. Dynamics of dark energy. *Int. J. Mod. Phys. D*, 15:1753–1936, 2006.

[366] Eric V. Linder. The Dynamics of Quintessence, The Quintessence of Dynamics. *Gen. Rel. Grav.*, 40:329–356, 2008.

[367] R. R. Caldwell and Bruce Allen. Cosmological constraints on cosmic string gravitational radiation. *Phys. Rev. D*, 45:3447–3468, 1992.

[368] L. Lentati et al. European Pulsar Timing Array Limits On An Isotropic Stochastic Gravitational-Wave Background. *Mon. Not. Roy. Astron. Soc.*, 453(3):2576–2598, 2015.

[369] Zaven Arzoumanian et al. The NANOGrav 12.5 yr Data Set: Search for an Isotropic Stochastic Gravitational-wave Background. *Astrophys. J. Lett.*, 905(2):L34, 2020.

[370] Pau Amaro-Seoane et al. Laser Interferometer Space Antenna. 2 2017.

[371] Neil Turok. Grand Unified Strings and Galaxy Formation. *Nucl. Phys. B*, 242:520–541, 1984.

[372] Jean M. Quashnock and David N. Spergel. Gravitational Selfinteractions of Cosmic Strings. *Phys. Rev. D*, 42:2505–2520, 1990.

[373] C. J. A. P. Martins and E. P. S. Shellard. String evolution with friction. *Phys. Rev. D*, 53:575–579, 1996.

[374] P. P. Avelino and L. Sousa. Scaling laws for weakly interacting cosmic (super)string and p-brane networks. *Phys. Rev. D*, 85:083525, 2012.

[375] L. Sousa and P. P. Avelino. Stochastic Gravitational Wave Background generated by Cosmic String Networks: Velocity-Dependent One-Scale model versus Scale-Invariant Evolution. *Phys. Rev. D*, 88(2):023516, 2013.

[376] Ken'ichi Saikawa and Satoshi Shirai. Primordial gravitational waves, precisely: The role of thermodynamics in the Standard Model. *JCAP*, 05:035, 2018.

[377] Christopher J. Moore, Stephen R. Taylor, and Jonathan R. Gair. Estimating the sensitivity of pulsar timing arrays. *Class. Quant. Grav.*, 32(5):055004, 2015.

[378] Jeffrey S. Hazboun, Joseph D. Romano, and Tristan L. Smith. Realistic sensitivity curves for pulsar timing arrays. *Phys. Rev. D*, 100(10):104028, 2019.

[379] R. w. Hellings and G. s. Downs. UPPER LIMITS ON THE ISOTROPIC GRAVITATIONAL RADIATION BACKGROUND FROM PULSAR TIMING ANALYSIS. *Astrophys. J. Lett.*, 265:L39–L42, 1983.

[380] C. J. Moore, R. H. Cole, and C. P. L. Berry. Gravitational-wave sensitivity curves. *Class. Quant. Grav.*, 32(1):015014, 2015.

[381] Xavier Siemens, Justin Ellis, Fredrick Jenet, and Joseph D. Romano. The stochastic background: scaling laws and time to detection for pulsar timing arrays. *Class. Quant. Grav.*, 30:224015, 2013.

[382] Ilias Cholis. On the Gravitational Wave Background from Black Hole Binaries after the First LIGO Detections. *JCAP*, 06:037, 2017.

[383] Vuk Mandic, Simeon Bird, and Ilias Cholis. Stochastic Gravitational-Wave Background due to Primordial Binary Black Hole Mergers. *Phys. Rev. Lett.*, 117(20):201102, 2016.

[384] Matteo Bonetti and Alberto Sesana. Gravitational wave background from extreme mass ratio inspirals. *Phys. Rev. D*, 102(10):103023, 2020.

[385] Stanislav Babak, Jonathan Gair, Alberto Sesana, Enrico Barausse, Carlos F. Sopuerta, Christopher P. L. Berry, Emanuele Berti, Pau Amaro-Seoane, Antoine Petiteau, and Antoine Klein. Science with the space-based interferometer LISA. V: Extreme mass-ratio inspirals. *Phys. Rev. D*, 95(10):103012, 2017.

[386] Pau Amaro-Seoane, Jonathan R. Gair, Marc Freitag, M. Coleman Miller, Ilya Mandel, Curt J. Cutler, and Stanislav Babak. Astrophysics, detection and science applications of intermediate- and extreme mass-ratio inspirals. *Class. Quant. Grav.*, 24:R113–R169, 2007.

[387] Michael S. Turner, Martin J. White, and James E. Lidsey. Tensor perturbations in inflationary models as a probe of cosmology. *Phys. Rev. D*, 48:4613–4622, 1993.

[388] Ken'ichi Saikawa. A review of gravitational waves from cosmic domain walls. *Universe*, 3(2):40, 2017.

[389] Takashi Hiramatsu, Masahiro Kawasaki, and Ken'ichi Saikawa. On the estimation of gravitational wave spectrum from cosmic domain walls. *JCAP*, 1402:031, 2014.

[390] Chiara Caprini, Ruth Durrer, Thomas Konstandin, and Geraldine Servant. General Properties of the Gravitational Wave Spectrum from Phase Transitions. *Phys. Rev. D*, 79:083519, 2009.

[391] Mark Hindmarsh, Stephan J. Huber, Kari Rummukainen, and David J. Weir. Numerical simulations of acoustically generated gravitational waves at a first order phase transition. *Phys. Rev. D*, 92(12):123009, 2015.

[392] Stephan J. Huber and Thomas Konstandin. Gravitational Wave Production by Collisions: More Bubbles. *JCAP*, 09:022, 2008.

[393] David J. Weir. Revisiting the envelope approximation: gravitational waves from bubble collisions. *Phys. Rev. D*, 93(12):124037, 2016.

[394] Chiara Caprini, Ruth Durrer, and Geraldine Servant. The stochastic gravitational wave background from turbulence and magnetic fields generated by a first-order phase transition. *JCAP*, 12:024, 2009.

[395] Ivo Labbé, Pieter van Dokkum, Erica Nelson, Rachel Bezanson, Katherine A. Suess, Joel Leja, Gabriel Brammer, Katherine Whitaker, Elijah Mathews, Mauro Stefanon, and Bingjie Wang. A population of red candidate massive galaxies 600 Myr after the Big Bang. , 616(7956):266–269, April 2023.

[396] Hakim Atek, Marko Shuntov, Lukas J. Furtak, Johan Richard, Jean-Paul Kneib, Guillaume Mahler, Adi Zitrin, H. J. McCracken, Stéphane Charlot, Jacopo Chevallard, and Iryna Chemerynska. Revealing galaxy candidates out to $z \sim 16$ with JWST observations of the lensing cluster SMACS0723. , 519(1):1201–1220, February 2023.

[397] Steven L. Finkelstein, Micaela B. Bagley, Pablo Arrabal Haro, Mark Dickinson, Henry C. Ferguson, Jeyhan S. Kartaltepe, Casey Papovich, Denis Burgarella, Dale D. Kocevski, Marc Huertas-Company, Kartheik G. Iyer, Anton M. Koekemoer, Rebecca L. Larson, Pablo G. Pérez-González, Caitlin Rose, et al. A Long Time Ago in a Galaxy Far, Far Away: A Candidate $z \sim 12$ Galaxy in Early JWST CEERS Imaging. , 940(2):L55, December 2022.

[398] Larry D. Bradley, Dan Coe, Gabriel Brammer, Lukas J. Furtak, Rebecca L. Larson, Felipe Andrade-Santos, Rachana Bhatawdekar, Marusa Bradac, Tom Broadhurst, Adam Carnall, Christopher J. Conselice, Jose M. Diego, Brenda Frye, Seiji Fujimoto, Tiger Y. -Y Hsiao, et al. High-Redshift Galaxy Candidates at $z = 9 - 13$ as Revealed by JWST Observations of WHL0137-08. *arXiv e-prints*, October 2022.

[399] Yuichi Harikane, Kimihiko Nakajima, Masami Ouchi, Hiroya Umeda, Yuki Isobe, Yoshiaki Ono, Yi Xu, and Yechi Zhang. Pure Spectroscopic Constraints on UV Luminosity Functions and Cosmic Star Formation History From 25 Galaxies at $z_{\rm spec} = 8.61 - 13.20$ Confirmed with JWST/NIRSpec. *arXiv e-prints*, April 2023.

[400] Jonathan P. Gardner, John C. Mather, Mark Clampin, Rene Doyon, Matthew A. Greenhouse, Heidi B. Hammel, John B. Hutchings, Peter Jakobsen, Simon J. Lilly, Knox S. Long, Jonathan I. Lunine, Mark J. McCaughrean, Matt Mountain, John Nella, George H. Rieke, et al. The James Webb Space Telescope. , 123(4):485–606, April 2006.

[401] Pratika Dayal, Andrea Ferrara, James S. Dunlop, and Fabio Pacucci. Essential physics of early galaxy formation. , 445(3):2545–2557, December 2014.

[402] Pratika Dayal, Elena M. Rossi, Banafsheh Shiralilou, Olmo Piana, Tirthankar Roy Choudhury, and Marta Volonteri. The hierarchical assembly of galaxies and black holes in the first billion years: predictions for the era of gravitational wave astronomy. , 486(2):2336–2350, June 2019.

[403] L. Y. Aaron Yung, Rachel S. Somerville, Steven L. Finkelstein, Gergö Popping, Romeel Davé, Aparna Venkatesan, Peter Behroozi, and Harry C. Ferguson. Semi-analytic forecasts for JWST - IV. Implications for cosmic reionization and LyC escape fraction. , 496(4):4574–4592, August 2020.

[404] Peter Behroozi, Charlie Conroy, Risa H. Wechsler, Andrew Hearin, Christina C. Williams, Benjamin P. Moster, L. Y. Aaron Yung, Rachel S. Somerville, Stefan Gottlöber, Gustavo Yepes, and Ryan Endsley. The Universe at z > 10: predictions for JWST from the UNIVERSEMACHINE DR1. , 499(4):5702–5718, December 2020.

[405] Stephen M. Wilkins, Aswin P. Vijayan, Christopher C. Lovell, William J. Roper, Dimitrios Irodotou, Joseph Caruana, Louise T. C. Seeyave, Jussi K. Kuusisto, Peter A. Thomas, and Shedeur A. K. Parris. First light and reionization epoch simulations (FLARES) V: the redshift frontier. , 519(2):3118–3128, February 2023.

[406] Charlotte A. Mason, Michele Trenti, and Tommaso Treu. The brightest galaxies at cosmic dawn. , 521(1):497–503, May 2023.

[407] Christopher C. Lovell, Ian Harrison, Yuichi Harikane, Sandro Tacchella, and Stephen M. Wilkins. Extreme value statistics of the halo and stellar mass distributions at high redshift: are JWST results in tension with ΛCDM? , 518(2):2511–2520, January 2023.

[408] Michael Boylan-Kolchin. Stress Testing ΛCDM with High-redshift Galaxy Candidates. *arXiv e-prints*, 8 2022.

[409] Nashwan Sabti, Julian B. Muñoz, and Marc Kamionkowski. Insights from HST into Ultra-Massive Galaxies and Early-Universe Cosmology. *arXiv e-prints*, May 2023.

[410] Yangyao Chen, H. J. Mo, and Kai Wang. Massive Dark Matter Halos at High Redshift: Implications for Observations in the JWST Era. *arXiv e-prints*, 4 2023.

[411] Joe McCaffrey, Samantha Hardin, John Wise, and John Regan. No Tension: JWST Galaxies at $z > 10$ Consistent with Cosmological Simulations. *arXiv e-prints*, April 2023.

[412] Rahul Kannan, Volker Springel, Lars Hernquist, Rüdiger Pakmor, Ana Maria Delgado, Boryana Hadzhiyska, César Hernández-Aguayo, Monica Barrera, Fulvio Ferlito, Sownak Bose, Simon White, Carlos Frenk, Aaron Smith, and Enrico Garaldi. The MillenniumTNG Project: The galaxy population at $z \geq 8$. *arXiv e-prints*, October 2022.

[413] Avishai Dekel, Kartick S. Sarkar, Yuval Birnboim, Nir Mandelker, and Zhaozhou Li. Efficient Formation of Massive Galaxies at Cosmic Dawn by Feedback-Free Starbursts. *arXiv e-prints*, 3 2023.

[414] Ethan O. Nadler, Andrew Benson, Trey Driskell, Xiaolong Du, and Vera Gluscevic. Growing the first galaxies' merger trees. , 521(3):3201–3220, May 2023.

[415] Samuel Passaglia and Misao Sasaki. Primordial black holes from CDM isocurvature perturbations. *Phys. Rev. D*, 105(10):103530, 2022.

[416] Matteo Biagetti, Gabriele Franciolini, and Antonio Riotto. High-redshift JWST Observations and Primordial Non-Gaussianity. *Astrophys. J.*, 944(2):113, 2023.

[417] Boyuan Liu, Saiyang Zhang, and Volker Bromm. Effects of stellar-mass primordial black holes on first star formation. *Mon. Not. Roy. Astron. Soc.*, 514(2):2376–2396, 2022.

[418] Boyuan Liu and Volker Bromm. Accelerating Early Massive Galaxy Formation with Primordial Black Holes. *Astrophys. J. Lett.*, 937(2):L30, 2022.

[419] Gert Hütsi, Martti Raidal, Juan Urrutia, Ville Vaskonen, and Hardi Veermäe. Did JWST observe imprints of axion miniclusters or primordial black holes? *Phys. Rev. D*, 107(4):043502, 2023.

[420] Ronaldo C. Batista and Valerio Marra. Clustering dark energy and halo abundances. *JCAP*, 11:048, 2017.

[421] Anatoly Klypin, Vivian Poulin, Francisco Prada, Joel Primack, Marc Kamionkowski, Vladimir Avila-Reese, Aldo Rodriguez-Puebla, Peter Behroozi, Doug Hellinger, and Tristan L. Smith. Clustering and halo abundances in early dark energy cosmological models. , 504(1):769–781, June 2021.

[422] Hao Jiao, Robert Brandenberger, and Alexandre Refregier. Early Structure Formation from Cosmic String Loops in Light of Early JWST Observations. *arXiv e-prints*, 4 2023.

[423] Kathryn M. Zurek, Craig J. Hogan, and Thomas R. Quinn. Astrophysical Effects of Scalar Dark Matter Miniclusters. *Phys. Rev. D*, 75:043511, 2007.

[424] Bernard Carr and Joseph Silk. Primordial Black Holes as Generators of Cosmic Structures. *Mon. Not. Roy. Astron. Soc.*, 478(3):3756–3775, 2018.

[425] C. J. Hogan and M. J. Rees. AXION MINICLUSTERS. *Phys. Lett. B*, 205:228–230, 1988.

[426] Edward W. Kolb and Igor I. Tkachev. Axion miniclusters and Bose stars. *Phys. Rev. Lett.*, 71:3051–3054, 1993.

[427] Edward W. Kolb and Igor I. Tkachev. Nonlinear axion dynamics and formation of cosmological pseudosolitons. *Phys. Rev. D*, 49:5040–5051, 1994.

[428] Edward W. Kolb and Igor I. Tkachev. Large amplitude isothermal fluctuations and high density dark matter clumps. *Phys. Rev. D*, 50:769–773, 1994.

[429] Jens C. Niemeyer. Small-scale structure of fuzzy and axion-like dark matter. *arXiv e-prints*, 12 2019.

[430] Basabendu Barman, Nicolás Bernal, Nicklas Ramberg, and Luca Visinelli. QCD Axion Kinetic Misalignment without Prejudice. *Universe*, 8(12):634, 2022.

[431] Jonas Enander, Andreas Pargner, and Thomas Schwetz. Axion minicluster power spectrum and mass function. *JCAP*, 12:038, 2017.

[432] Malcolm Fairbairn, David J. E. Marsh, Jérémie Quevillon, and Simon Rozier. Structure formation and microlensing with axion miniclusters. *Phys. Rev. D*, 97(8):083502, 2018.

[433] Cem Eröncel, Ryosuke Sato, Geraldine Servant, and Philip Sørensen. ALP dark matter from kinetic fragmentation: opening up the parameter window. *JCAP*, 10:053, 2022.

[434] Cem Eröncel and Géraldine Servant. ALP dark matter mini-clusters from kinetic fragmentation. *JCAP*, 01:009, 2023.

[435] Timothy D. Brandt. Constraints on MACHO Dark Matter from Compact Stellar Systems in Ultra-faint Dwarf Galaxies. , 824(2):L31, June 2016.

[436] Savvas M. Koushiappas and Abraham Loeb. Dynamics of Dwarf Galaxies Disfavor Stellar-Mass Black Holes as Dark Matter. , 119(4):041102, July 2017.

[437] Asher Berlin, Raffaele Tito D'Agnolo, Sebastian A. R. Ellis, and Kevin Zhou. Heterodyne broadband detection of axion dark matter. *Phys. Rev. D*, 104(11):L111701, 2021.

[438] Peter W. Graham, Selcuk Hacıömeroğlu, David E. Kaplan, Zhanibek Omarov, Surjeet Rajendran, and Yannis K. Semertzidis. Storage ring probes of dark matter and dark energy. *Phys. Rev. D*, 103(5):055010, 2021.

[439] Itay M. Bloch, Yonit Hochberg, Eric Kuflik, and Tomer Volansky. Axion-like Relics: New Constraints from Old Comagnetometer Data. *JHEP*, 01:167, 2020.

[440] Sean Tulin and Hai-Bo Yu. Dark Matter Self-interactions and Small Scale Structure. *Phys. Rept.*, 730:1–57, 2018.

[441] Manoj Kaplinghat, Sean Tulin, and Hai-Bo Yu. Dark Matter Halos as Particle Colliders: Unified Solution to Small-Scale Structure Puzzles from Dwarfs to Clusters. *Phys. Rev. Lett.*, 116(4):041302, 2016.

[442] James S. Bullock and Michael Boylan-Kolchin. Small-Scale Challenges to the ΛCDM Paradigm. *Ann. Rev. Astron. Astrophys.*, 55:343–387, 2017.

[443] Pierre Auclair et al. Cosmology with the Laser Interferometer Space Antenna. *arXiv e-prints*, 4 2022.

[444] David Ellis, David J. E. Marsh, Benedikt Eggemeier, Jens Niemeyer, Javier Redondo, and Klaus Dolag. Structure of axion miniclusters. *Phys. Rev. D*, 106(10):103514, 2022.

[445] Huangyu Xiao, Ian Williams, and Matthew McQuinn. Simulations of axion minihalos. *Phys. Rev. D*, 104(2):023515, 2021.

[446] Benedikt Eggemeier, Javier Redondo, Klaus Dolag, Jens C. Niemeyer, and Alejandro Vaquero. First Simulations of Axion Minicluster Halos. *Phys. Rev. Lett.*, 125(4):041301, 2020.

[447] Chia-Feng Chang and Yanou Cui. In preparation. In preparation.

[448] Abraham Loeb. Effective Self-interaction of Dark Matter from Gravitational Scattering. *Astrophys. J. Lett.*, 929(2):L24, 2022.

[449] Michael Boylan-Kolchin, James S. Bullock, and Manoj Kaplinghat. Too big to fail? The puzzling darkness of massive Milky Way subhaloes. , 415(1):L40–L44, July 2011.

[450] Michael Boylan-Kolchin, James S. Bullock, and Manoj Kaplinghat. The Milky Way's bright satellites as an apparent failure of ΛCDM. , 422(2):1203–1218, May 2012.

[451] Mark Vogelsberger, Jesus Zavala, and Abraham Loeb. Subhaloes in self-interacting galactic dark matter haloes. , 423(4):3740–3752, July 2012.

[452] Miguel Rocha, Annika H. G. Peter, James S. Bullock, Manoj Kaplinghat, Shea Garrison-Kimmel, Jose Onorbe, and Leonidas A. Moustakas. Cosmological Simulations with Self-Interacting Dark Matter I: Constant Density Cores and Substructure. *Mon. Not. Roy. Astron. Soc.*, 430:81–104, 2013.

[453] J. Zavala, M. Vogelsberger, and M. G. Walker. Constraining self-interacting dark matter with the Milky way's dwarf spheroidals. , 431:L20–L24, April 2013.

[454] Annika H. G. Peter, Miguel Rocha, James S. Bullock, and Manoj Kaplinghat. Cosmological Simulations with Self-Interacting Dark Matter II: Halo Shapes vs. Observations. *Mon. Not. Roy. Astron. Soc.*, 430:105, 2013.

[455] Joe Wolf, Gregory D. Martinez, James S. Bullock, Manoj Kaplinghat, Marla Geha, Ricardo R. Muñoz, Joshua D. Simon, and Frank F. Avedo. Accurate masses for dispersion-supported galaxies. , 406(2):1220–1237, August 2010.

[456] Manoj Kaplinghat, Mauro Valli, and Hai-Bo Yu. Too Big To Fail in Light of Gaia. *Mon. Not. Roy. Astron. Soc.*, 490(1):231–242, 2019.

[457] Daneng Yang, Hai-Bo Yu, and Haipeng An. Self-Interacting Dark Matter and the Origin of Ultradiffuse Galaxies NGC1052-DF2 and -DF4. *Phys. Rev. Lett.*, 125(11):111105, 2020.

[458] Daneng Yang and Hai-Bo Yu. Self-interacting dark matter and small-scale gravitational lenses in galaxy clusters. *Phys. Rev. D*, 104(10):103031, 2021.

[459] Hannah C. Turner, Mark R. Lovell, Jesús Zavala, and Mark Vogelsberger. The onset of gravothermal core collapse in velocity-dependent self-interacting dark matter subhaloes. , 505(4):5327–5339, August 2021.

[460] Camila A. Correa, Matthieu Schaller, Sylvia Ploeckinger, Noemi Anau Montel, Christoph Weniger, and Shinichiro Ando. TangoSIDM: Tantalizing models of Self-Interacting Dark Matter. *arXiv e-prints*, 6 2022.

[461] Daneng Yang, Ethan O. Nadler, and Hai-Bo Yu. Strong Dark Matter Self-interactions Diversify Halo Populations Within and Surrounding the Milky Way. *arXiv e-prints*, November 2022.

[462] Wayne Hu, Rennan Barkana, and Andrei Gruzinov. Cold and fuzzy dark matter. *Phys. Rev. Lett.*, 85:1158–1161, 2000.

[463] R. A. Allsman et al. MACHO project limits on black hole dark matter in the 1-30 solar mass range. *Astrophys. J. Lett.*, 550:L169, 2001.

[464] P. Tisserand et al. Limits on the Macho Content of the Galactic Halo from the EROS-2 Survey of the Magellanic Clouds. *Astron. Astrophys.*, 469:387–404, 2007.

[465] L. Wyrzykowski, J. Skowron, S. Kozłowski, A. Udalski, M. K. Szymański, M. Kubiak, G. Pietrzyński, I. Soszyński, O. Szewczyk, K. Ulaczyk, R. Poleski, and P. Tisserand. The OGLE view of microlensing towards the Magellanic Clouds - IV. OGLE-III SMC data and final conclusions on MACHOs. , 416(4):2949–2961, October 2011.

[466] T. Blaineau, M. Moniez, C. Afonso, J. N. Albert, R. Ansari, E. Aubourg, C. Coutures, J. F. Glicenstein, B. Goldman, C. Hamadache, T. Lasserre, L. Le Guillou, E. Lesquoy, C. Magneville, J. B. Marquette, et al. New limits from microlensing on Galactic black holes in the mass range 10 $M\odot$ < M < 1000 $M\odot$. *Astron. Astrophys.*, 664:A106, 2022.

[467] Ivan Esteban, Annika H. G. Peter, and Stacy Y. Kim. Milky Way satellite velocities reveal the Dark Matter power spectrum at small scales. *arXiv e-prints*, 6 2023.

[468] I. L. Bogolyubsky and V. G. Makhankov. On the Pulsed Soliton Lifetime in Two Classical Relativistic Theory Models. *JETP Lett.*, 24:12, 1976.

[469] Edmund J. Copeland, M. Gleiser, and H. R. Muller. Oscillons: Resonant configurations during bubble collapse. *Phys. Rev. D*, 52:1920–1933, 1995.

[470] Gyula Fodor, Peter Forgacs, Philippe Grandclement, and Istvan Racz. Oscillons and Quasi-breathers in the phi**4 Klein-Gordon model. *Phys. Rev. D*, 74:124003, 2006.

[471] Pierre-Henri Chavanis. Mass-radius relation of Newtonian self-gravitating Bose-Einstein condensates with short-range interactions. I. Analytical results. , 84(4), August 2011.

[472] Hong Zhang. Axion Stars. *Symmetry*, 12(1):25, 2019.

[473] Derek Inman and Yacine Ali-Haïmoud. Early structure formation in primordial black hole cosmologies. *Phys. Rev. D*, 100(8):083528, 2019.

[474] P. Meszaros. The behaviour of point masses in an expanding cosmological substratum. , 37(2):225–228, December 1974.

[475] Veronica Dike, Daniel Gilman, and Tommaso Treu. Strong lensing constraints on primordial black holes as a dark matter candidate. *Mon. Not. Roy. Astron. Soc.*, 522(4):5434–5441, 2023.

[476] William H. Press and Paul Schechter. Formation of Galaxies and Clusters of Galaxies by Self-Similar Gravitational Condensation. , 187:425–438, February 1974.

[477] Ravi K. Sheth and Giuseppe Tormen. Large scale bias and the peak background split. *Mon. Not. Roy. Astron. Soc.*, 308:119, 1999.

[478] L. Y. Aaron Yung, Rachel S. Somerville, Steven L. Finkelstein, Stephen M. Wilkins, and Jonathan P. Gardner. Are the ultra-high-redshift galaxies at z $>$ 10 surprising in the context of standard galaxy formation models? *arXiv e-prints*, April 2023.

[479] Jordan Mirocha and Steven R. Furlanetto. Balancing the efficiency and stochasticity of star formation with dust extinction in z $\gtrsim$ 10 galaxies observed by JWST. , 519(1):843–853, February 2023.

[480] Yan Gong, Bin Yue, Ye Cao, and Xuelei Chen. Fuzzy Dark Matter as a Solution to Reconcile the Stellar Mass Density of High-z Massive Galaxies and Reionization History. *Astrophys. J.*, 947(1):28, 2023.

[481] Gary J. Feldman and Robert D. Cousins. A Unified approach to the classical statistical analysis of small signals. *Phys. Rev. D*, 57:3873–3889, 1998.

[482] Jihn E. Kim. Weak Interaction Singlet and Strong CP Invariance. *Phys. Rev. Lett.*, 43:103, 1979.

[483] Mikhail A. Shifman, A. I. Vainshtein, and Valentin I. Zakharov. Can Confinement Ensure Natural CP Invariance of Strong Interactions? *Nucl. Phys. B*, 166:493–506, 1980.

[484] Michael Dine, Willy Fischler, and Mark Srednicki. A Simple Solution to the Strong CP Problem with a Harmless Axion. *Phys. Lett. B*, 104:199–202, 1981.

[485] A. R. Zhitnitsky. On Possible Suppression of the Axion Hadron Interactions. (In Russian). *Sov. J. Nucl. Phys.*, 31:260, 1980.

[486] Jeff A. Dror and Jacob M. Leedom. Cosmological Tension of Ultralight Axion Dark Matter and its Solutions. *Phys. Rev. D*, 102(11):115030, 2020.

[487] Prateek Agrawal, JiJi Fan, Matthew Reece, and Lian-Tao Wang. Experimental Targets for Photon Couplings of the QCD Axion. *JHEP*, 02:006, 2018.

[488] Prateek Agrawal, Jiji Fan, and Matthew Reece. Clockwork Axions in Cosmology: Is Chromonatural Inflation Chrononatural? *JHEP*, 10:193, 2018.

[489] Alexandre Payez, Carmelo Evoli, Tobias Fischer, Maurizio Giannotti, Alessandro Mirizzi, and Andreas Ringwald. Revisiting the SN1987A gamma-ray limit on ultralight axion-like particles. *JCAP*, 02:006, 2015.

[490] Jae Hyeok Chang, Rouven Essig, and Samuel D. McDermott. Supernova 1987A Constraints on Sub-GeV Dark Sectors, Millicharged Particles, the QCD Axion, and an Axion-like Particle. *JHEP*, 09:051, 2018.

[491] Mikhail V. Beznogov, Ermal Rrapaj, Dany Page, and Sanjay Reddy. Constraints on Axion-like Particles and Nucleon Pairing in Dense Matter from the Hot Neutron Star in HESS J1731-347. *Phys. Rev. C*, 98(3):035802, 2018.

[492] Koichi Hamaguchi, Natsumi Nagata, Keisuke Yanagi, and Jiaming Zheng. Limit on the Axion Decay Constant from the Cooling Neutron Star in Cassiopeia A. *Phys. Rev. D*, 98(10):103015, 2018.

[493] Armen Sedrakian. Axion cooling of neutron stars. *Phys. Rev. D*, 93(6):065044, 2016.

[494] Tomohiro Fujita, Ryo Tazaki, and Kenji Toma. Hunting Axion Dark Matter with Protoplanetary Disk Polarimetry. *Phys. Rev. Lett.*, 122(19):191101, 2019.

[495] M. M. Ivanov, Y. Y. Kovalev, M. L. Lister, A. G. Panin, A. B. Pushkarev, T. Savolainen, and S. V. Troitsky. Constraining the photon coupling of ultra-light dark-matter axion-like particles by polarization variations of parsec-scale jets in active galaxies. *JCAP*, 02:059, 2019.

[496] Peter W. Graham, David E. Kaplan, Jeremy Mardon, Surjeet Rajendran, William A. Terrano, Lutz Trahms, and Thomas Wilkason. Spin Precession Experiments for Light Axionic Dark Matter. *Phys. Rev. D*, 97(5):055006, 2018.

[497] Tao Liu, George Smoot, and Yue Zhao. Detecting axionlike dark matter with linearly polarized pulsar light. *Phys. Rev. D*, 101(6):063012, 2020.

[498] S. Borsanyi, M. Dierigl, Z. Fodor, S. D. Katz, S. W. Mages, D. Nogradi, J. Redondo, A. Ringwald, and K. K. Szabo. Axion cosmology, lattice QCD and the dilute instanton gas. *Phys. Lett. B*, 752:175–181, 2016.

[499] Renée Hlozek, Daniel Grin, David J. E. Marsh, and Pedro G. Ferreira. A search for ultralight axions using precision cosmological data. *Phys. Rev. D*, 91(10):103512, 2015.

[500] Masahiro Kawasaki and Kazunori Nakayama. Axions: Theory and Cosmological Role. *Ann. Rev. Nucl. Part. Sci.*, 63:69–95, 2013.

[501] Dawid Brzeminski, Anson Hook, and Gustavo Marques-Tavares. Precision Early Universe Cosmology from Stochastic Gravitational Waves. 3 2022.

[502] Prateek Agrawal, Anson Hook, Junwu Huang, and Gustavo Marques-Tavares. Axion string signatures II: A cosmological plasma collider. 10 2020.

[503] Mudit Jain, Andrew J. Long, and Mustafa A. Amin. CMB birefringence from ultralight axion string networks. 3 2021.

[504] Mudit Jain, Ray Hagimoto, Andrew J. Long, and Mustafa A. Amin. Searching for axion-like particles through CMB birefringence from string-wall networks. *JCAP*, 10:090, 2022.

[505] Prateek Agrawal, Anson Hook, and Junwu Huang. A CMB Millikan experiment with cosmic axiverse strings. *JHEP*, 07:138, 2020.

[506] Christopher Dessert, Andrew J. Long, and Benjamin R. Safdi. No Evidence for Axions from Chandra Observation of the Magnetic White Dwarf RE J0317-853. *Phys. Rev. Lett.*, 128(7):071102, 2022.

[507] Takashi Hiramatsu, Masahiro Kawasaki, Ken'ichi Saikawa, and Toyokazu Sekiguchi. Axion cosmology with long-lived domain walls. *JCAP*, 01:001, 2013.

[508] Ya. B. Zeldovich, I. Yu. Kobzarev, and L. B. Okun. Cosmological Consequences of the Spontaneous Breakdown of Discrete Symmetry. *Zh. Eksp. Teor. Fiz.*, 67:3–11, 1974.

[509] Mark Hindmarsh. Analytic scaling solutions for cosmic domain walls. *Phys. Rev. Lett.*, 77:4495–4498, 1996.

[510] Mark Hindmarsh. Level set method for the evolution of defect and brane networks. *Phys. Rev. D*, 68:043510, 2003.

[511] J. R. C. C. C. Correia, I. S. C. R. Leite, and C. J. A. P. Martins. Effects of biases in domain wall network evolution. II. Quantitative analysis. *Phys. Rev. D*, 97(8):083521, 2018.

[512] J. R. C. C. C. Correia, I. S. C. R. Leite, and C. J. A. P. Martins. Effects of Biases in Domain Wall Network Evolution. *Phys. Rev. D*, 90(2):023521, 2014.

[513] William H. Press, Barbara S. Ryden, and David N. Spergel. Dynamical Evolution of Domain Walls in an Expanding Universe. *Astrophys. J.*, 347:590–604, 1989.

[514] C. J. A. P. Martins, I. Yu. Rybak, A. Avgoustidis, and E. P. S. Shellard. Stretching and Kibble scaling regimes for Hubble-damped defect networks. *Phys. Rev. D*, 94(11):116017, 2016. [Erratum: Phys.Rev.D 95, 039902 (2017)].

[515] P. P. Avelino, C. J. A. P. Martins, and J. C. R. E. Oliveira. One-scale model for domain wall network evolution. *Phys. Rev. D*, 72:083506, 2005.

[516] A. M. M. Leite and C. J. A. P. Martins. Scaling Properties of Domain Wall Networks. *Phys. Rev. D*, 84:103523, 2011.

[517] A. M. M. Leite, C. J. A. P. Martins, and E. P. S. Shellard. Accurate Calibration of the Velocity-dependent One-scale Model for Domain Walls. *Phys. Lett. B*, 718:740–744, 2013.

[518] Giovanni Grilli di Cortona, Edward Hardy, Javier Pardo Vega, and Giovanni Villadoro. The QCD axion, precisely. *JHEP*, 01:034, 2016.

[519] Peter W. Graham and Adam Scherlis. Stochastic axion scenario. *Phys. Rev. D*, 98(3):035017, 2018.

[520] Tommi Markkanen, Arttu Rajantie, Stephen Stopyra, and Tommi Tenkanen. Scalar correlation functions in de Sitter space from the stochastic spectral expansion. *JCAP*, 08:001, 2019.

[521] Marc Kamionkowski, Josef Pradler, and Devin G. E. Walker. Dark energy from the string axiverse. *Phys. Rev. Lett.*, 113(25):251302, 2014.

[522] D. Coulson, Z. Lalak, and Burt A. Ovrut. Biased domain walls. *Phys. Rev. D*, 53:4237–4246, 1996.

[523] Sebastian E. Larsson, Subir Sarkar, and Peter L. White. Evading the cosmological domain wall problem. *Phys. Rev. D*, 55:5129–5135, 1997.

[524] G. Hinshaw et al. First year Wilkinson Microwave Anisotropy Probe (WMAP) observations: The Angular power spectrum. *Astrophys. J. Suppl.*, 148:135, 2003.

[525] Sz. Borsanyi et al. Calculation of the axion mass based on high-temperature lattice quantum chromodynamics. *Nature*, 539(7627):69–71, 2016.

[526] T. W. B. Kibble. Evolution of a system of cosmic strings. *Nucl. Phys. B*, 252:227, 1985. [Erratum: Nucl.Phys.B 261, 750 (1985)].

[527] Tanmay Vachaspati, Allen E. Everett, and Alexander Vilenkin. Radiation From Vacuum Strings and Domain Walls. *Phys. Rev.*, D30:2046, 1984.

[528] V. Anastassopoulos et al. New CAST Limit on the Axion-Photon Interaction. *Nature Phys.*, 13:584–590, 2017.

[529] J. K. Vogel et al. IAXO - The International Axion Observatory. In *8th Patras Workshop on Axions, WIMPs and WISPs*, 2 2013.

[530] A. Jodidio et al. Search for Right-Handed Currents in Muon Decay. *Phys. Rev. D*, 34:1967, 1986. [Erratum: Phys.Rev.D 37, 237 (1988)].

[531] Asimina Arvanitaki, Savas Dimopoulos, Sergei Dubovsky, Nemanja Kaloper, and John March-Russell. String Axiverse. *Phys. Rev.*, D81:123530, 2010.

[532] M. M. Pieri, S. Bonoli, J. Chaves-Montero, I. Pâris, M. Fumagalli, J. S. Bolton, M. Viel, P. Noterdaeme, J. Miralda-Escudé, N. G. Busca, H. Rahmani, C. Peroux, A. Font-Ribera, and S. C. Trager. WEAVE-QSO: A Massive Intergalactic Medium Survey for the William Herschel Telescope. In C. Reylé, J. Richard, L. Cambrésy, M. Deleuil, E. Pécontal, L. Tresse, and I. Vauglin, editors, *SF2A-2016: Proceedings of the Annual meeting of the French Society of Astronomy and Astrophysics*, pages 259–266, December 2016.

[533] Naim Göksel Karaçaylı, Paul Martini, Julien Guy, Corentin Ravoux, Marie Lynn Abdul Karim, Eric Armengaud, Michael Walther, J. Aguilar, S. Ahlen, S. Bailey, J. Bautista, S. F. Beltran, D. Brooks, L. Cabayol-Garcia, S. Chabanier, et al. Optimal 1D Lyα Forest Power Spectrum Estimation – III. DESI early data. *arXiv e-prints*, page arXiv:2306.06316, June 2023.

[534] Corentin Ravoux, Marie Lynn Abdul Karim, Eric Armengaud, Michael Walther, Naim Göksel Karaçaylı, Paul Martini, Julien Guy, Jessica Nicole Aguilar, Steven Ahlen, Stephen Bailey, Julian Bautista, Sergio Felipe Beltran, David Brooks, Laura Cabayol-Garcia, Solène Chabanier, et al. The Dark Energy Spectroscopic Instrument: One-dimensional power spectrum from first Lyman-α forest samples with Fast Fourier Transform. *arXiv e-prints*, page arXiv:2306.06311, June 2023.

[535] Tansu Daylan and Simon Birrer. Searching for dark matter substructure: a deeper wide-area community survey for Roman. *arXiv e-prints*, page arXiv:2306.12864, June 2023.

[536] Chia-Feng Chang. Imprint of early dark energy in stochastic gravitational wave background. *Phys. Rev. D*, 105(2):023508, 2022.

[537] Volker Koch. Aspects of chiral symmetry. *Int.J.Mod.Phys. E*, 6:203–250, 1997. [arXiv:nucl-th/9706075].

[538] David J. E. Marsh. Axion cosmology. *Phys.Rept.*, 643:1–79, 2016. [arXiv:1510.07633 [astro-ph.CO]].

[539] David H. Lyth and Ernest D. Stewart. Cosmology and axion. *Phys. Rev. Lett.*, 75:201, 1995.

[540] Chia-Min Lin, Masahiro Kawasaki, Kazunori Nakayama, and Toyokazu Sekiguchi. Axion models with high-scale inflation. *JCAP*, 1307:035, 2013. [arXiv:1303.3756 [hep-ph]].

[541] Takeshi Kobayashi, Fuminobu Takahashi, and Toyokazu Sekiguchi. Axion dark matter from topological defects. *Phys. Rev. D*, 94:023519, 2016. [arXiv:1604.08614 [astro-ph.CO]].

[542] Peter Svrcek and Edward Witten. Axions in string theory. *JHEP*, 0606:051, 2006. [arXiv:hep-th/0605206].

[543] Manuel A. B. do Vale, Alex G. Dias, and C. A. de S. Pires. On the vacuum alignment in the dfsz axion model. *Eur. Phys. J. C*, 78:5, 2018. [arXiv:1709.09014 [hep-ph]].

[544] Masahiro Kawasaki, Fuminobu Takahashi, and Masaki Yamada. Large hadron collider test of gravitational effects on the axion. *Phys. Lett. B*, 743:66, 2015. [arXiv:1412.0789 [hep-ph]].

[545] Ryo Namba and Fuminobu Takahashi. Gravitational waves from axion monodromy. *JHEP*, 1604:022, 2016. [arXiv:1512.06239 [hep-ph]].

[546] Naoya Kitajima and Fuminobu Takahashi. Gravitational waves induced by axion oscillations. *JCAP*, 1705:008, 2017. [arXiv:1612.05268 [hep-ph]].

[547] Masahiro Kawasaki, Naoya Kitajima, Fuminobu Takahashi, and Toyokazu Sekiguchi. Isocurvature perturbations of axion and curvaton. *JCAP*, 1802:026, 2018. [arXiv:1712.05037 [astro-ph.CO]].

[548] Yohei Ema, Kazunori Nakayama, and Masaki Yamada. Peccei-quinn symmetry in the universe: A review. *PTEP*, 2016:12B01, 2016. [arXiv:1609.06351 [hep-ph]].

[549] Tetsutaro Higaki, Yohei Ema, and Kazunori Nakayama. Axion model with extra colored particles. *JHEP*, 1705:019, 2017. [arXiv:1703.04627 [hep-ph]].

[550] R. J. Thompson and M. J. Duncan. The cosmic axion spin precession experiment (casper). *Annalen Phys.*, 525:793, 2013. [arXiv:1203.3408 [hep-ph]].

[551] R. Barbieri and G. Raffelt. Axion cosmology in the early universe. *Phys. Lett. B*, 166:123, 1986.

[552] Sz. Borsányi, Z. Fodor, J. Guenther, and K. K. Szabó. Calculation of the axion mass based on high-temperature lattice quantum chromodynamics. *Nature*, 539:69, 2016. [arXiv:1606.07494 [hep-lat]].

[553] Alessio Caputo, Alessandro Gruppuso, Carlo Burigana, and Sabino Matarrese. Probing axion-like particle properties with polarized cmb measurements. *Phys. Rev. D*, 94:023525, 2016. [arXiv:1603.03034 [astro-ph.CO]].

[554] C. Q. Geng and D. Huang. Constraints on the axion-photon coupling constant from the gamma-ray observations of the black hole binary system lmc x-3. *Phys. Rev. D*, 92:014005, 2015. [arXiv:1501.06185 [hep-ph]].

[555] David Alesini, Mauro Nuvolari, and Fabrizio Villa. A high-resolution spectrometer for axion research. *Nucl. Instrum. Meth. A*, 959:163444, 2020. [arXiv:2003.01308 [physics.ins-det]].

[556] D. Horns, M. Meyer, and M. Raue. The universe as a source of high-energy gamma-ray photons. *Phys. Rev. D*, 78:123015, 2008. [arXiv:0810.4940 [astro-ph]].

[557] P. Arias, D. Cadamuro, M. Goodsell, J. Jaeckel, and J. Redondo. Wispy cold dark matter. *JCAP*, 1606:013, 2016. [arXiv:1601.00008 [hep-ph]].

[558] R. Bahre et al. Any light particle search ii—technical design report. *JINST*, 8:T09001, 2013. [arXiv:1302.5647 [physics.ins-det]].

[559] T. Braine et al. Axion searches with helioscopes: Calibration of the cern axion solar telescope (cast) using synchrotron radiation. *JCAP*, 1403:024, 2014. [arXiv:1401.3233 [physics.ins-det]].

[560] M. Arik et al. Design, construction, operation and performance of the cms electromagnetic calorimeter. *Eur. Phys. J. C*, 9:1, 1999.

[561] T. Stolarczyk et al. Physics performance of the cast solar telescope. *JINST*, 3:P08001, 2008.

[562] K. Barth et al. Microwave cavity search for dark-matter axions. *ApJ*, 818:106, 2016. [arXiv:1506.01378 [astro-ph.CO]].

[563] Benjamin T. McAllister, Thomas R. Primack, and Joseph H. Taylor. New constraint on cpt violation from clock-comparison experiments. *Phys. Rev. D*, 94:082001, 2016. [arXiv:1609.02504 [hep-ph]].

[564] Steven Abel, Jonathan Jaeckel, Valentin V. Khoze, and Michel Spannowsky. Kinetic mixing of the photon with hidden u(1)s in string phenomenology. *Phys. Lett. B*, 661:201, 2008. [arXiv:0707.2958 [hep-ph]].

[565] N. Aghanim et al. Planck 2015 results. xi. cmb power spectra, likelihoods, and robustness of parameters. *AA*, 594:A11, 2016. [arXiv:1507.02704 [astro-ph.CO]].

[566] A. Aguilar-Arevalo et al. Determination of the charge of the pion fluctuations in the numi near detector. *Phys. Rev. D*, 91:051101, 2015. [arXiv:1412.3825 [hep-ex]].

[567] S. Andriamonje et al. An improved limit on the axion-photon coupling from the cast experiment. *JCAP*, 0704:010, 2007. [arXiv:astro-ph/0701164].

[568] E. Armengaud et al. Axion helioscopes as solar magnetometers. *Nat. Phys.*, 13:591, 2017. [arXiv:1703.03688 [astro-ph.SR]].

[569] S. J. Asztalos et al. An improved rf cavity search for halo axions. *Phys. Rev. D*, 69:011101, 2004. [arXiv:astro-ph/0310042].

[570] D. Budker et al. Proposal for a cosmic axion spin precession experiment (casper). *Phys. Rev. X*, 4:021030, 2014. [arXiv:1310.7534 [physics.atom-ph]].

[571] R. Barbieri et al. An axion-like particle search with a liquid xenon detector. *Phys. Rev. D*, 87:032006, 2013. [arXiv:1206.2955 [hep-ph]].

[572] D. Cadamuro et al. New constraints on sub-gev hidden sector gauge bosons from a search for heavy neutrino decays. *Phys. Rev. D*, 101:115042, 2020. [arXiv:1912.00868 [hep-ph]].

[573] D. Cadamuro et al. Search for axion-like particles with the cern axion solar telescope. *JCAP*, 1808:011, 2018. [arXiv:1805.12028 [hep-ex]].

[574] L. Capparelli et al. New constraints on ultralight scalar and pseudoscalar axion-like particles from ultraviolet quasar spectra. *Phys. Rev. Lett.*, 120:151301, 2018. [arXiv:1710.08901 [hep-ph]].

[575] A. S. Chou et al. Search for axionlike dark matter through nuclear spin precession in electric and magnetic fields. *Phys. Rev. Lett.*, 100:080402, 2008. [arXiv:0710.3783 [hep-ex]].

[576] W. DeRocco et al. Searching for axion dark matter with a liquid-state nuclear spin comagnetometer. *Phys. Rev. Lett.*, 118:161801, 2017. [arXiv:1611.05022 [hep-ph]].

[577] R. J. Hill et al. Axion induced oscillating electric dipole moments. *Phys. Rev. D*, 97:095034, 2018. [arXiv:1801.03293 [hep-ph]].

[578] I. G. Irastorza et al. Towards a new generation axion helioscope: the international axion observatory (iaxo). *JCAP*, 1404:001, 2014. [arXiv:1308.3633 [physics.ins-det]].

[579] E. Izaguirre et al. New electron beam-dump experiments to search for mev to 10's of gev dark matter. *Phys. Rev. D*, 89:114015, 2014. [arXiv:1310.4484 [hep-ph]].

[580] J. Jaeckel et al. Probing axions with dilaton-like domain walls. *Phys. Rev. Lett.*, 114:101802, 2015. [arXiv:1408.4808 [hep-ph]].

[581] A. Aguilar et al. Axion searches with the edelweiss-ii experiment. *Phys. Lett. B*, 716:1, 2012. [arXiv:1202.1292 [astro-ph.CO]].

[582] S. Archambault et al. Constraints on light hidden sector gauge bosons from supernova cooling. *Phys. Rev. D*, 91:065019, 2015. [arXiv:1412.3828 [hep-ph]].

[583] M. Arik et al. Ksvz axion search by helioscope at cern. *JCAP*, 0902:008, 2009. [arXiv:0810.4482 [hep-ex]].

[584] M. Arik et al. Search for solar axions by the cern axion solar telescope with 3he buffer gas: Closing the hot dark matter gap. *Phys. Rev. D*, 92:021101, 2015. [arXiv:1502.01591 [astro-ph.CO]].

[585] M. Spalinski. CHIRAL CORRECTIONS TO THE AXION MASS. *Z. Phys.*, C41:87–90, 1988.

[586] J. Aasi et al. Characterization of the LIGO detectors during their sixth science run. *Class. Quant. Grav.*, 32(11):115012, 2015.

[587] P. A. R. Ade et al. Improved Constraints on Cosmology and Foregrounds from BICEP2 and Keck Array Cosmic Microwave Background Data with Inclusion of 95 GHz Band. *Phys. Rev. Lett.*, 116:031302, 2016.

[588] B. P. Abbott et al. GW170817: Observation of Gravitational Waves from a Binary Neutron Star Inspiral. *Phys. Rev. Lett.*, 119(16):161101, 2017.

[589] F. Acernese et al. Advanced Virgo: a second-generation interferometric gravitational wave detector. *Class. Quant. Grav.*, 32(2):024001, 2015.

[590] Heather Audley et al. Laser Interferometer Space Antenna. 2017.

[591] Kent Yagi and Naoki Seto. Detector configuration of DECIGO/BBO and identification of cosmological neutron-star binaries. *Phys. Rev.*, D83:044011, 2011. [Erratum: Phys. Rev.D95,no.10,109901(2017)].

[592] Marc Kamionkowski, Arthur Kosowsky, and Michael S. Turner. Gravitational radiation from first order phase transitions. *Phys. Rev.*, D49:2837–2851, 1994.

[593] David J. Weir. Gravitational waves from a first order electroweak phase transition: a brief review. *Phil. Trans. Roy. Soc. Lond.*, A376(2114):20170126, 2018.

[594] Tom Charnock, Anastasios Avgoustidis, Edmund J. Copeland, and Adam Moss. CMB constraints on cosmic strings and superstrings. *Phys. Rev.*, D93(12):123503, 2016.

[595] N. Aghanim et al. Planck 2018 results. VI. Cosmological parameters. 2018.

[596] Y. Akrami et al. Planck 2018 results. X. Constraints on inflation. 2018.

[597] M. Tanabashi et al. Review of Particle Physics. *Phys. Rev.*, D98(3):030001, 2018.

[598] Mark P Hertzberg, Max Tegmark, and Frank Wilczek. Axion Cosmology and the Energy Scale of Inflation. *Phys. Rev.*, D78:083507, 2008.

[599] G. W. Gibbons and S. W. Hawking. Cosmological Event Horizons, Thermodynamics, and Particle Creation. *Phys. Rev.*, D15:2738–2751, 1977.

[600] T. S. Bunch and P. C. W. Davies. Quantum Field Theory in de Sitter Space: Renormalization by Point Splitting. *Proc. Roy. Soc. Lond.*, A360:117–134, 1978.

[601] Bruce A. Bassett, Shinji Tsujikawa, and David Wands. Inflation dynamics and reheating. *Rev. Mod. Phys.*, 78:537–589, 2006.

[602] Pierre Salati. Quintessence and the relic density of neutralinos. *Phys. Lett.*, B571:121–131, 2003.

[603] Yanou Cui, Stephen P. Martin, David Edgar Morrissey, and James Daniel Wells. Cosmic Strings from Supersymmetric Flat Directions. *Phys. Rev.*, D77:043528, 2008.

[604] Yanou Cui and David E. Morrissey. Non-Thermal Dark Matter from Cosmic Strings. *Phys. Rev.*, D79:083532, 2009.

[605] Steen Hannestad. What is the lowest possible reheating temperature? *Phys. Rev.*, D70:043506, 2004.

[606] Vincent B.. Klaer and Guy D. Moore. The dark-matter axion mass. *JCAP*, 1711(11):049, 2017.

[607] Christophe Ringeval, Daisuke Yamauchi, Jun'ichi Yokoyama, and Francois R. Bouchet. Large scale CMB anomalies from thawing cosmic strings. *JCAP*, 1602(02):033, 2016.

[608] Marco Gorghetto, Edward Hardy, and Giovanni Villadoro. Axions from Strings: the Attractive Solution. *JHEP*, 07:151, 2018.

[609] G. S. F. Guedes, P. P. Avelino, and L. Sousa. Signature of inflation in the stochastic gravitational wave background generated by cosmic string networks. 2018.

[610] Masahiro Kawasaki, Koichi Miyamoto, and Kazunori Nakayama. Cosmological Effects of Decaying Cosmic String Loops with TeV Scale Width. 2011.

[611] Kohei Kamada, Yuhei Miyamoto, Daisuke Yamauchi, and Jun'ichi Yokoyama. Effects of cosmic strings with delayed scaling on CMB anisotropy. *Phys. Rev.*, D90(8):083502, 2014.

[612] Kohei Kamada, Yuhei Miyamoto, and Jun'ichi Yokoyama. Evading the pulsar constraints on the cosmic string tension in supergravity inflation. *JCAP*, 1210:023, 2012.

[613] Ken'ichi Saikawa. A review of gravitational waves from cosmic domain walls. *Universe*, 3(2):40, 2017.

[614] R. A. Battye and E. P. S. Shellard. Primordial gravitational waves: A Probe of the very early universe. 1996.

[615] Ann E. Nelson and Huangyu Xiao. Axion Cosmology with Early Matter Domination. *Phys. Rev.*, D98(6):063516, 2018.

[616] R. A. Battye and E. P. S. Shellard. Radiative back reaction on global strings. *Phys. Rev.*, D53:1811–1826, 1996.

[617] R. A. Battye and E. P. S. Shellard. Global string radiation. *Nucl. Phys.*, B423:260–304, 1994.

[618] Edmund J. Copeland, D. Haws, and M. Hindmarsh. Classical theory of radiating strings. *Phys. Rev.*, D42:726–730, 1990.

[619] Atish Dabholkar and Jean M. Quashnock. Pinning Down the Axion. *Nucl. Phys.*, B333:815–832, 1990.

[620] Takeo Moroi and Lisa Randall. Wino cold dark matter from anomaly mediated SUSY breaking. *Nucl. Phys.*, B570:455–472, 2000.

[621] Daiju Matsunami, Levon Pogosian, Ayush Saurabh, and Tanmay Vachaspati. Decay of Cosmic String Loops Due to Particle Radiation. *Phys. Rev. Lett.*, 122(20):201301, 2019.

[622] P. S. Bhupal Dev, Francesc Ferrer, Yiyang Zhang, and Yongchao Zhang. Gravitational Waves from First-Order Phase Transition in a Simple Axion-Like Particle Model. 2019.

[623] Malcolm Fairbairn, Edward Hardy, and Alastair Wickens. Hearing without seeing: gravitational waves from hot and cold hidden sectors. *JHEP*, 07:044, 2019.

[624] Andrew J. Long and Lian-Tao Wang. Dark Photon Dark Matter from a Network of Cosmic Strings. *Phys. Rev.*, D99(6):063529, 2019.

[625] Francesc Ferrer, Eduard Masso, Giuliano Panico, Oriol Pujolas, and Fabrizio Rompineve. Primordial Black Holes from the QCD axion. *Phys. Rev. Lett.*, 122(10):101301, 2019.

[626] C. Hagmann and P. Sikivie. Computer simulations of the motion and decay of global strings. *Nucl. Phys.*, B363:247–280, 1991.

[627] Asier Lopez-Eiguren, Joanes Lizarraga, Mark Hindmarsh, and Jon Urrestilla. Cosmic Microwave Background constraints for global strings and global monopoles. *JCAP*, 1707:026, 2017.

[628] P. A. R. Ade et al. Planck 2015 results. XIII. Cosmological parameters. *Astron. Astrophys.*, 594:A13, 2016.

[629] Elisa Fenu, Daniel G. Figueroa, Ruth Durrer, and Juan Garcia-Bellido. Gravitational waves from self-ordering scalar fields. *JCAP*, 0910:005, 2009.

[630] Nicklas Ramberg and Luca Visinelli. Probing the Early Universe with Axion Physics and Gravitational Waves. *Phys. Rev.*, D99(12):123513, 2019.

[631] Lisa Randall. Composite axion models and Planck scale physics. *Phys. Lett.*, B284:77–80, 1992.

[632] Benjamin Lillard and Tim M. P. Tait. A High Quality Composite Axion. *JHEP*, 11:199, 2018.

[633] Masahide Yamaguchi, M. Kawasaki, and Jun'ichi Yokoyama. Evolution of axionic strings and spectrum of axions radiated from them. *Phys. Rev. Lett.*, 82:4578–4581, 1999.

[634] Tomasz Krajewski, Jan Henryk Kwapisz, Zygmunt Lalak, and Marek Lewicki. Stability of domain walls in models with asymmetric potentials. 3 2021.

[635] Tomasz Krajewski, Zygmunt Lalak, Marek Lewicki, and Paweł Olszewski. Domain walls and gravitational waves in the Standard Model. *JCAP*, 12:036, 2016.

[636] Tomasz Krajewski, Zygmunt Lalak, Marek Lewicki, and Paweł Olszewski. Domain walls in the extensions of the Standard Model. *JCAP*, 05:007, 2018.

[637] Michael Dine, Nicolas Fernandez, Akshay Ghalsasi, and Hiren H. Patel. Comments on Axions, Domain Walls, and Cosmic Strings. 12 2020.

[638] A. Vilenkin and A. E. Everett. Cosmic Strings and Domain Walls in Models with Goldstone and PseudoGoldstone Bosons. *Phys. Rev. Lett.*, 48:1867–1870, 1982.

[639] Hajime Fukuda, Aneesh V. Manohar, Hitoshi Murayama, and Ofri Telem. Axion strings are superconducting. 10 2020.

[640] Yoshihiko Abe, Yu Hamada, and Koichi Yoshioka. Electroweak axion string and superconductivity. 10 2020.

[641] Masahiro Ibe, Shin Kobayashi, Yuhei Nakayama, and Satoshi Shirai. On Stability of Superconducting Current in Cosmic String. 2 2021.

[642] Mark Hindmarsh, Joanes Lizarraga, Ander Urio, and Jon Urrestilla. Loop decay in Abelian-Higgs string networks. 3 2021.

[643] Adam G. Riess et al. Observational evidence from supernovae for an accelerating universe and a cosmological constant. *Astron. J.*, 116:1009–1038, 1998.

[644] S. Perlmutter et al. Measurements of Ω and Λ from 42 high redshift supernovae. *Astrophys. J.*, 517:565–586, 1999.

[645] Malcolm Hicken, W. Michael Wood-Vasey, Stephane Blondin, Peter Challis, Saurabh Jha, Patrick L. Kelly, Armin Rest, and Robert P. Kirshner. Improved Dark Energy Constraints from 100 New CfA Supernova Type Ia Light Curves. *Astrophys. J.*, 700:1097–1140, 2009.

[646] N. Suzuki et al. The Hubble Space Telescope Cluster Supernova Survey: V. Improving the Dark Energy Constraints Above z¿1 and Building an Early-Type-Hosted Supernova Sample. *Astrophys. J.*, 746:85, 2012.

[647] Daniel J. Eisenstein et al. Detection of the Baryon Acoustic Peak in the Large-Scale Correlation Function of SDSS Luminous Red Galaxies. *Astrophys. J.*, 633:560–574, 2005.

[648] Will J. Percival et al. Baryon Acoustic Oscillations in the Sloan Digital Sky Survey Data Release 7 Galaxy Sample. *Mon. Not. Roy. Astron. Soc.*, 401:2148–2168, 2010.

[649] Shadab Alam et al. The clustering of galaxies in the completed SDSS-III Baryon Oscillation Spectroscopic Survey: cosmological analysis of the DR12 galaxy sample. *Mon. Not. Roy. Astron. Soc.*, 470(3):2617–2652, 2017.

[650] Pauline Zarrouk et al. The clustering of the SDSS-IV extended Baryon Oscillation Spectroscopic Survey DR14 quasar sample: measurement of the growth rate of structure from the anisotropic correlation function between redshift 0.8 and 2.2. *Mon. Not. Roy. Astron. Soc.*, 477(2):1639–1663, 2018.

[651] Victoria de Sainte Agathe et al. Baryon acoustic oscillations at z = 2.34 from the correlations of Lyα absorption in eBOSS DR14. *Astron. Astrophys.*, 629:A85, 2019.

[652] Pierre Sikivie. Axion Cosmology. *Lect. Notes Phys.*, 741:19–50, 2008.

[653] Pierre Sikivie. Invisible Axion Search Methods. *Rev. Mod. Phys.*, 93(1):015004, 2021.

[654] D. N. Spergel et al. First year Wilkinson Microwave Anisotropy Probe (WMAP) observations: Determination of cosmological parameters. *Astrophys. J. Suppl.*, 148:175–194, 2003.

[655] E. Komatsu et al. Seven-Year Wilkinson Microwave Anisotropy Probe (WMAP) Observations: Cosmological Interpretation. *Astrophys. J. Suppl.*, 192:18, 2011.

[656] D. A. Kirzhnits and Andrei D. Linde. Symmetry Behavior in Gauge Theories. *Annals Phys.*, 101:195–238, 1976.

[657] L. Dolan and R. Jackiw. Symmetry Behavior at Finite Temperature. *Phys. Rev.*, D9:3320–3341, 1974.

[658] Steven Weinberg. Gauge and Global Symmetries at High Temperature. *Phys. Rev.*, D9:3357–3378, 1974.

[659] Alan H. Guth. The Inflationary Universe: A Possible Solution to the Horizon and Flatness Problems. *Phys. Rev.*, D23:347–356, 1981. [Adv. Ser. Astrophys. Cosmol.3,139(1987)].

[660] K. Sato. First Order Phase Transition of a Vacuum and Expansion of the Universe. *Mon. Not. Roy. Astron. Soc.*, 195:467–479, 1981.

[661] K. Sato. Cosmological Baryon Number Domain Structure and the First Order Phase Transition of a Vacuum. *Phys. Lett.*, 99B:66–70, 1981. [Adv. Ser. Astrophys. Cosmol.3,134(1987)].

[662] Alexei A. Starobinsky. A New Type of Isotropic Cosmological Models Without Singularity. *Phys. Lett.*, 91B:99–102, 1980. [Adv. Ser. Astrophys. Cosmol.3,130(1987)].

[663] J. Aasi et al. Characterization of the LIGO detectors during their sixth science run. *Class. Quant. Grav.*, 32(11):115012, 2015.

[664] Andrei D. Linde. A New Inflationary Universe Scenario: A Possible Solution of the Horizon, Flatness, Homogeneity, Isotropy and Primordial Monopole Problems. *Phys. Lett.*, 108B:389–393, 1982. [Adv. Ser. Astrophys. Cosmol.3,149(1987)].

[665] Andreas Albrecht and Paul J. Steinhardt. Cosmology for Grand Unified Theories with Radiatively Induced Symmetry Breaking. *Phys. Rev. Lett.*, 48:1220–1223, 1982. [Adv. Ser. Astrophys. Cosmol.3,158(1987)].

[666] Andrei D. Linde. Chaotic Inflation. *Phys. Lett.*, 129B:177–181, 1983.

[667] Chia-Feng Chang and Yanou Cui. In preparation.

[668] C.J.A.P. Martins. *Defect Evolution in Cosmology and Condensed Matter: Quantitative Analysis with the Velocity-Dependent One-Scale Model*. Springer International Publishing, 2016.

[669] T. W. B. Kibble. Some Implications of a Cosmological Phase Transition. *Phys. Rept.*, 67:183, 1980.

[670] Takashi Hiramatsu, Masahiro Kawasaki, and Ken'ichi Saikawa. Gravitational Waves from Collapsing Domain Walls. *JCAP*, 05:032, 2010.

[671] Daniel G. Figueroa and Francisco Torrenti. Gravitational wave production from preheating: parameter dependence. *JCAP*, 10:057, 2017.

[672] Daniel G. Figueroa, Juan García-Bellido, and Francisco Torrentí. Gravitational wave production from the decay of the standard model Higgs field after inflation. *Phys. Rev. D*, 93(10):103521, 2016.

[673] Daniel G. Figueroa and Tuukka Meriniemi. Stochastic Background of Gravitational Waves from Fermions – Theory and Applications. *JHEP*, 10:101, 2013.

[674] Rong-Gen Cai, Zhoujian Cao, Zong-Kuan Guo, Shao-Jiang Wang, and Tao Yang. The Gravitational-Wave Physics. *Natl. Sci. Rev.*, 4(5):687–706, 2017.

[675] David J. Weir. Gravitational waves from a first order electroweak phase transition: a brief review. *Phil. Trans. Roy. Soc. Lond. A*, 376(2114):20170126, 2018.

[676] Chiara Caprini et al. Science with the space-based interferometer eLISA. II: Gravitational waves from cosmological phase transitions. *JCAP*, 04:001, 2016.

[677] Thibault Damour and Alexander Vilenkin. Gravitational wave bursts from cosmic strings. *Phys. Rev. Lett.*, 85:3761–3764, 2000.

[678] Thibault Damour and Alexander Vilenkin. Gravitational wave bursts from cusps and kinks on cosmic strings. *Phys. Rev. D*, 64:064008, 2001.

[679] Edward W. Kolb and Michael S. Turner. *The Early Universe*, volume 69. 1990.

[680] Howard Baer, Ki-Young Choi, Jihn E. Kim, and Leszek Roszkowski. Dark matter production in the early Universe: beyond the thermal WIMP paradigm. *Phys. Rept.*, 555:1–60, 2015.

[681] Csaba Csáki and Philip Tanedo. Beyond the Standard Model. In *2013 European School of High-Energy Physics*, 2015.

[682] Virgo and Kagra. Constraints on the cosmic expansion history from GWTC-3. 11 2021.

[683] Naoki Seto, Seiji Kawamura, and Takashi Nakamura. Possibility of direct measurement of the acceleration of the universe using 0.1-Hz band laser interferometer gravitational wave antenna in space. *Phys. Rev. Lett.*, 87:221103, 2001.

[684] S. Kawamura et al. The Japanese space gravitational wave antenna DECIGO. *Class. Quant. Grav.*, 23:S125–S132, 2006.

[685] Vitaly Vanchurin, Ken D. Olum, and Alexander Vilenkin. Scaling of cosmic string loops. *Phys. Rev. D*, 74:063527, 2006.

[686] Ken D. Olum and Vitaly Vanchurin. Cosmic string loops in the expanding Universe. *Phys. Rev. D*, 75:063521, 2007.

[687] C. J. A. P. Martins and E. P. S. Shellard. Fractal properties and small-scale structure of cosmic string networks. *Phys. Rev. D*, 73:043515, 2006.

[688] Christophe Ringeval, Mairi Sakellariadou, and Francois Bouchet. Cosmological evolution of cosmic string loops. *JCAP*, 02:023, 2007.

[689] Jose J. Blanco-Pillado, Ken D. Olum, and Benjamin Shlaer. Large parallel cosmic string simulations: New results on loop production. *Phys. Rev. D*, 83:083514, 2011.

[690] Toshikazu Ebisuzaki, Junichiro Makino, Takeshi Go Tsuru, Yoko Funato, Simon F. Portegies Zwart, Piet Hut, Steve McMillan, Satoki Matsushita, Hironori Matsumoto, and Ryohei Kawabe. Missing link found? – the "runaway" path to supermassive black holes. *Astrophys. J. Lett.*, 562:L19, 2001.

[691] Ryusuke Jinno and Masahiro Takimoto. Gravitational waves from bubble collisions: An analytic derivation. *Phys. Rev. D*, 95(2):024009, 2017.

[692] Sunny Vagnozzi. New physics in light of the H_0 tension: An alternative view. *Phys. Rev. D*, 102(2):023518, 2020.

[693] Sunny Vagnozzi. Consistency tests of ΛCDM from the early integrated Sachs-Wolfe effect: Implications for early-time new physics and the Hubble tension. 5 2021.

[694] Gen Ye and Yun-Song Piao. Is the Hubble tension a hint of AdS phase around recombination? *Phys. Rev. D*, 101(8):083507, 2020.

[695] Leonardo Badurina, Oliver Buchmueller, John Ellis, Marek Lewicki, Christopher McCabe, and Ville Vaskonen. Prospective Sensitivities of Atom Interferometers to Gravitational Waves and Ultralight Dark Matter. 8 2021.

[696] Gen Ye, Jun Zhang, and Yun-Song Piao. Resolving both H_0 and S_8 tensions with AdS early dark energy and ultralight axion. 7 2021.

[697] Osamu Seto and Yo Toda. Comparing early dark energy and extra radiation solutions to the Hubble tension with BBN. *Phys. Rev. D*, 103(12):123501, 2021.

[698] Eleonora Di Valentino, Olga Mena, Supriya Pan, Luca Visinelli, Weiqiang Yang, Alessandro Melchiorri, David F. Mota, Adam G. Riess, and Joseph Silk. In the realm of the Hubble tension—a review of solutions. *Class. Quant. Grav.*, 38(15):153001, 2021.

[699] Michele Maggiore. Gravitational wave experiments and early universe cosmology. *Phys. Rept.*, 331:283–367, 2000.

[700] Seiji Kawamura et al. The Japanese space gravitational wave antenna: DECIGO. *Class. Quant. Grav.*, 28:094011, 2011.

[701] Seiji Kawamura et al. Current status of space gravitational wave antenna DECIGO and B-DECIGO. *PTEP*, 2021(5):05A105, 2021.

[702] Shuichi Sato et al. The status of DECIGO. *J. Phys. Conf. Ser.*, 840(1):012010, 2017.

[703] Jeff Crowder and Neil J. Cornish. Beyond LISA: Exploring future gravitational wave missions. *Phys. Rev. D*, 72:083005, 2005.

[704] Vincent Corbin and Neil J. Cornish. Detecting the cosmic gravitational wave background with the big bang observer. *Class. Quant. Grav.*, 23:2435–2446, 2006.

[705] G. M. Harry, P. Fritschel, D. A. Shaddock, W. Folkner, and E. S. Phinney. Laser interferometry for the big bang observer. *Class. Quant. Grav.*, 23:4887–4894, 2006. [Erratum: Class.Quant.Grav. 23, 7361 (2006)].

[706] Chris L. Carilli and S. Rawlings. Science with the Square Kilometer Array: Motivation, key science projects, standards and assumptions. *New Astron. Rev.*, 48:979, 2004.

[707] A. Weltman et al. Fundamental physics with the Square Kilometre Array. *Publ. Astron. Soc. Austral.*, 37:e002, 2020.

[708] Francoise Combes. Science with SKA. In *Semaine de l'astrophysique française 2021*, 7 2021.

[709] Hideaki Kudoh, Atsushi Taruya, Takashi Hiramatsu, and Yoshiaki Himemoto. Detecting a gravitational-wave background with next-generation space interferometers. *Phys. Rev. D*, 73:064006, 2006.

[710] Sachiko Kuroyanagi, Kazunori Nakayama, and Jun'ichi Yokoyama. Prospects of determination of reheating temperature after inflation by DECIGO. *PTEP*, 2015(1):013E02, 2015.

[711] Sachiko Kuroyanagi, Shinji Tsujikawa, Takeshi Chiba, and Naoshi Sugiyama. Implications of the B-mode Polarization Measurement for Direct Detection of Inflationary Gravitational Waves. *Phys. Rev. D*, 90(6):063513, 2014.

[712] Atsushi Nishizawa, Atsushi Taruya, Kazuhiro Hayama, Seiji Kawamura, and Masaaki Sakagami. Probing non-tensorial polarizations of stochastic gravitational-wave backgrounds with ground-based laser interferometers. *Phys. Rev. D*, 79:082002, 2009.

[713] Bruce Allen and Joseph D. Romano. Detecting a stochastic background of gravitational radiation: Signal processing strategies and sensitivities. *Phys. Rev. D*, 59:102001, 1999.

[714] Shane L. Larson, William A. Hiscock, and Ronald W. Hellings. Sensitivity curves for spaceborne gravitational wave interferometers. *Phys. Rev. D*, 62:062001, 2000.

[715] Melissa Anholm, Stefan Ballmer, Jolien D. E. Creighton, Larry R. Price, and Xavier Siemens. Optimal strategies for gravitational wave stochastic background searches in pulsar timing data. *Phys. Rev. D*, 79:084030, 2009.

[716] Curt Cutler. Angular resolution of the LISA gravitational wave detector. *Phys. Rev. D*, 57:7089–7102, 1998.

[717] Neil J. Cornish. Detecting a stochastic gravitational wave background with the Laser Interferometer Space Antenna. *Phys. Rev. D*, 65:022004, 2002.

[718] Sydney J. Chamberlin, Jolien D. E. Creighton, Xavier Siemens, Paul Demorest, Justin Ellis, Larry R. Price, and Joseph D. Romano. Time-domain Implementation of the Optimal Cross-Correlation Statistic for Stochastic Gravitational-Wave Background Searches in Pulsar Timing Data. *Phys. Rev. D*, 91(4):044048, 2015.

[719] Rutger van Haasteren and Yuri Levin. Understanding and analysing time-correlated stochastic signals in pulsar timing. *Mon. Not. Roy. Astron. Soc.*, 428:1147, 2013.

[720] K. J. Lee, C. G. Bassa, R. Karuppusamy, M. Kramer, R. Smits, and B. W. Stappers. The optimal schedule for pulsar timing array observations. *Mon. Not. Roy. Astron. Soc.*, 423:2642, 2012.

[721] Mauro Pieroni and Enrico Barausse. Foreground cleaning and template-free stochastic background extraction for LISA. *JCAP*, 07:021, 2020. [Erratum: JCAP 09, E01 (2020)].

[722] C. Cutler and J. Harms. BBO and the neutron-star-binary subtraction problem. *Phys. Rev. D*, 73:042001, 2006.

[723] Alison J. Farmer and E. Sterl Phinney. The gravitational wave background from cosmological compact binaries. *Mon. Not. Roy. Astron. Soc.*, 346:1197, 2003.

[724] Pierre-Henri Chavanis. Phase transitions between dilute and dense axion stars. *Phys. Rev. D*, 98(2):023009, 2018.

[725] Thomas Helfer, David J. E. Marsh, Katy Clough, Malcolm Fairbairn, Eugene A. Lim, and Ricardo Becerril. Black hole formation from axion stars. *JCAP*, 03:055, 2017.

[726] Eric Cotner, Alexander Kusenko, Misao Sasaki, and Volodymyr Takhistov. Analytic Description of Primordial Black Hole Formation from Scalar Field Fragmentation. *JCAP*, 10:077, 2019.

[727] Zainab Nazari, Michele Cicoli, Katy Clough, and Francesco Muia. Oscillon collapse to black holes. *JCAP*, 05:027, 2021.

[728] Andrei Khmelnitsky and Valery Rubakov. Pulsar timing signal from ultralight scalar dark matter. *JCAP*, 02:019, 2014.

[729] Ivan De Martino, Tom Broadhurst, S. H. Henry Tye, Tzihong Chiueh, Hsi-Yu Schive, and Ruth Lazkoz. Recognizing Axionic Dark Matter by Compton and de Broglie Scale Modulation of Pulsar Timing. *Phys. Rev. Lett.*, 119(22):221103, 2017.

[730] Gabriella Agazie et al. The NANOGrav 15 yr Data Set: Evidence for a Gravitational-wave Background. *Astrophys. J. Lett.*, 951(1):L8, 2023.

[731] Adeela Afzal et al. The NANOGrav 15 yr Data Set: Search for Signals from New Physics. *Astrophys. J. Lett.*, 951(1):L11, 2023.

[732] Jan Ollé, Oriol Pujolàs, and Fabrizio Rompineve. Oscillons and Dark Matter. *JCAP*, 02:006, 2020.

[733] J. Antoniadis et al. The second data release from the European Pulsar Timing Array I. The dataset and timing analysis. 6 2023.

[734] J. Antoniadis et al. The second data release from the European Pulsar Timing Array III. Search for gravitational wave signals. 6 2023.

[735] Daniel J. Reardon et al. Search for an Isotropic Gravitational-wave Background with the Parkes Pulsar Timing Array. *Astrophys. J. Lett.*, 951(1):L6, 2023.

[736] Heng Xu et al. Searching for the Nano-Hertz Stochastic Gravitational Wave Background with the Chinese Pulsar Timing Array Data Release I. *Res. Astron. Astrophys.*, 23(7):075024, 2023.

[737] Andrew Zic et al. The Parkes Pulsar Timing Array Third Data Release. 6 2023.

[738] Gabriella Agazie et al. The NANOGrav 15 yr Data Set: Observations and Timing of 68 Millisecond Pulsars. *Astrophys. J. Lett.*, 951(1):L9, 2023.

[739] Jeff A. Dror, Harikrishnan Ramani, Tanner Trickle, and Kathryn M. Zurek. Pulsar Timing Probes of Primordial Black Holes and Subhalos. *Phys. Rev. D*, 100(2):023003, 2019.

[740] Jai-chan Hwang and Hyerim Noh. Axion as a Cold Dark Matter candidate. *Phys. Lett. B*, 680:1–3, 2009.

[741] Maya Silverman, James S. Bullock, Manoj Kaplinghat, Victor H. Robles, and Mauro Valli. Motivations for a large self-interacting dark matter cross-section from Milky Way satellites. *Mon. Not. Roy. Astron. Soc.*, 518(2):2418–2435, 2022.

[742] Felix Kling and Arvind Rajaraman. Towards an Analytic Construction of the Wavefunction of Boson Stars. *Phys. Rev. D*, 96(4):044039, 2017.

[743] Felix Kling and Arvind Rajaraman. Profiles of boson stars with self-interactions. *Phys. Rev. D*, 97(6):063012, 2018.

[744] Camila A. Correa, J. Stuart B. Wyithe, Joop Schaye, and Alan R. Duffy. The accretion history of dark matter haloes – I. The physical origin of the universal function. *Mon. Not. Roy. Astron. Soc.*, 450(2):1514–1520, 2015.

[745] Joshua D. Simon. The Faintest Dwarf Galaxies. , 57:375–415, August 2019.

[746] Juna A. Kollmeier, Gail Zasowski, Hans-Walter Rix, Matt Johns, Scott F. Anderson, Niv Drory, Jennifer A. Johnson, Richard W. Pogge, Jonathan C. Bird, Guillermo A. Blanc, Joel R. Brownstein, Jeffrey D. Crane, Nathan M. De Lee, Mark A. Klaene, Kathryn Kreckel, et al. SDSS-V: Pioneering Panoptic Spectroscopy. *arXiv e-prints*, November 2017.

[747] Atınç Çağan Şengül and Cora Dvorkin. Probing dark matter with strong gravitational lensing through an effective density slope. *Mon. Not. Roy. Astron. Soc.*, 516(1):336–357, 2022.

[748] Željko Ivezić et al. LSST: from Science Drivers to Reference Design and Anticipated Data Products. *Astrophys. J.*, 873(2):111, 2019.

[749] N. Afshordi, P. McDonald, and D. N. Spergel. Primordial black holes as dark matter: The Power spectrum and evaporation of early structures. *Astrophys. J. Lett.*, 594:L71–L74, 2003.

[750] Daniel Egana-Ugrinovic, Rouven Essig, Daniel Gift, and Marilena LoVerde. The Cosmological Evolution of Self-interacting Dark Matter. *JCAP*, 05:013, 2021.

[751] Minos Axenides, Robert H. Brandenberger, and Michael S. Turner. Development of Axion Perturbations in an Axion Dominated Universe. *Phys. Lett. B*, 126:178–182, 1983.

[752] Andrei D. Linde. Generation of Isothermal Density Perturbations in the Inflationary Universe. *Phys. Lett. B*, 158:375–380, 1985.

[753] D. Seckel and Michael S. Turner. Isothermal Density Perturbations in an Axion Dominated Inflationary Universe. *Phys. Rev. D*, 32:3178, 1985.

[754] David H. Lyth. A Limit on the Inflationary Energy Density From Axion Isocurvature Fluctuations. *Phys. Lett. B*, 236:408–410, 1990.

[755] Peter W. Graham, Igor G. Irastorza, Steven K. Lamoreaux, Axel Lindner, and Karl A. van Bibber. Experimental Searches for the Axion and Axion-Like Particles. *Ann. Rev. Nucl. Part. Sci.*, 65:485–514, 2015.

[756] Francesca Chadha-Day, John Ellis, and David J. E. Marsh. Axion dark matter: What is it and why now? *Sci. Adv.*, 8(8):abj3618, 2022.

[757] Michael S. Turner and Frank Wilczek. Inflationary axion cosmology. *Phys. Rev. Lett.*, 66:5–8, 1991.

[758] Andrea Caputo, Laura Sberna, Miguel Frias, Diego Blas, Paolo Pani, Lijing Shao, and Wenming Yan. Constraints on millicharged dark matter and axionlike particles from timing of radio waves. *Phys. Rev. D*, 100(6):063515, 2019.

[759] Michael A. Fedderke, Peter W. Graham, and Surjeet Rajendran. Axion Dark Matter Detection with CMB Polarization. *Phys. Rev. D*, 100(1):015040, 2019.

[760] Ippei Obata, Tomohiro Fujita, and Yuta Michimura. Optical Ring Cavity Search for Axion Dark Matter. *Phys. Rev. Lett.*, 121(16):161301, 2018.

[761] Teng Wu et al. Search for Axionlike Dark Matter with a Liquid-State Nuclear Spin Comagnetometer. *Phys. Rev. Lett.*, 122(19):191302, 2019.

[762] Antoine Garcon et al. Constraints on bosonic dark matter from ultralow-field nuclear magnetic resonance. *Sci. Adv.*, 5(10):eaax4539, 2019.

[763] Raymond T. Co, Francesco D'Eramo, and Lawrence J. Hall. Supersymmetric axion grand unified theories and their predictions. *Phys. Rev. D*, 94(7):075001, 2016.

[764] David I. Dunsky, Anish Ghoshal, Hitoshi Murayama, Yuki Sakakihara, and Graham White. Gravitational Wave Gastronomy. 11 2021.

[765] Peter Svrcek and Edward Witten. Axions In String Theory. *JHEP*, 06:051, 2006.

[766] T. Vachaspati, A. E. Everett, and A. Vilenkin. Phys. rev. d. 30:2046, 1984.

[767] S. Weinberg. Gauge and global symmetries at high temperature. *PRD*, 9(12):3357, 1974.

[768] Kazunori Nakayama, Fuminobu Takahashi, and Norimi Yokozaki. Gravitational waves from domain walls and their implications. *Phys. Lett. B*, 770:500–506, 2017.

[769] Naoya Kitajima and Fuminobu Takahashi. Gravitational waves from Higgs domain walls. *Phys. Lett. B*, 745:112–117, 2015.

[770] Jose J. Blanco-Pillado, Daniel Jiménez-Aguilar, and Jon Urrestilla. Exciting the domain wall soliton. *JCAP*, 01:027, 2021.

[771] R. MacKenzie. TOPOLOGICAL STRUCTURES ON DOMAIN WALLS. *Nucl. Phys. B*, 303:149–171, 1988.

[772] Tanmay Vachaspati. *Kinks and domain walls: An introduction to classical and quantum solitons*. Cambridge University Press, 4 2010.

[773] M. C. Huang and P. Sikivie. The Structure of Axionic Domain Walls. *Phys. Rev. D*, 32:1560, 1985.

[774] Sanghyeon Chang, C. Hagmann, and P. Sikivie. The Cold axion populations. In *2nd International Heidelberg Conference on Dark Matter in Astro and Particle Physics*, pages 471–498, 7 1998.

[775] Ciaran A. J. O'Hare, Giovanni Pierobon, Javier Redondo, and Yvonne Y. Y. Wong. Simulations of axionlike particles in the postinflationary scenario. *Phys. Rev. D*, 105(5):055025, 2022.

[776] C. Abel et al. Measurement of the Permanent Electric Dipole Moment of the Neutron. *Phys. Rev. Lett.*, 124(8):081803, 2020.

[777] Diego Harari and P. Sikivie. On the Evolution of Global Strings in the Early Universe. *Phys. Lett. B*, 195:361–365, 1987.

[778] Ciaran A. J. O'Hare, Andrea Caputo, Alexander J. Millar, and Edoardo Vitagliano. Axion helioscopes as solar magnetometers. *Phys. Rev. D*, 102(4):043019, 2020.

[779] Amelia Drew and E. P. S. Shellard. Radiation from global topological strings using adaptive mesh refinement: Methodology and massless modes. *Phys. Rev. D*, 105(6):063517, 2022.

[780] Kiwoon Choi, Sang Hui Im, and Chang Sub Shin. Recent Progress in the Physics of Axions and Axion-Like Particles. *Ann. Rev. Nucl. Part. Sci.*, 71:225–252, 2021.

[781] Manuel Meyer, Dieter Horns, and Martin Raue. First lower limits on the photon-axion-like particle coupling from very high energy gamma-ray observations. *Phys. Rev. D*, 87(3):035027, 2013.

[782] Alejandro H. Córsico, Alejandra D. Romero, Leandro G. Althaus, Enrique García-Berro, Jordi Isern, S. O. Kepler, Marcelo M. Miller Bertolami, Denis J. Sullivan, and Paul Chote. An asteroseismic constraint on the mass of the axion from the period drift of the pulsating DA white dwarf star L19-2. *JCAP*, 07:036, 2016.

[783] Kazunori Kohri and Hideo Kodama. Axion-Like Particles and Recent Observations of the Cosmic Infrared Background Radiation. *Phys. Rev. D*, 96(5):051701, 2017.

[784] Jihn E. Kim and Gianpaolo Carosi. Axions and the Strong CP Problem. *Rev. Mod. Phys.*, 82:557–602, 2010. [Erratum: Rev.Mod.Phys. 91, 049902 (2019)].

[785] R. F. Ling. On the theory and construction of k-clusters. *The Computer Journal*, 15:4, 326–332, 1972.